Experimental and Computational Micromechanical Investigations for Developing Mechanically Competent 3D Printable Nanocomposite Biomaterials

by

Sanaz Saadatmand Hashemi

A thesis
presented to the University of Waterloo
in fulfillment of the
thesis requirement for the degree of
Doctor of Philosophy
in
Systems Design Engineering

Waterloo, Ontario, Canada, 2023

©Sanaz Saadatmand Hashemi 2023

Examining Committee Membership

The following served on the Examining Committee of this thesis. The decision of the Examining Committee is by majority vote.

External Examiner:	François Barthelat, Ph.D. Professor, University of Colorado
Supervisor:	Thomas L. Willett, Ph.D. Associate Professor, University of Waterloo
Co-Supervisor:	John Montesano, Ph.D. Associate Professor, University of Waterloo
Internal Member:	Maud Gorbet, Ph.D. Associate Professor, University of Waterloo
Internal Member:	Nima Maftoon, Ph.D. Assistant Professor, University of Waterloo
Internal-External Examiner:	Cliff Butcher, Ph.D. Assistant Professor, University of Waterloo

Author's Declaration

This thesis consists of material all of which I authored or co-authored: see Statement of Contributions included in the thesis. This is a true copy of the thesis, including any required final revisions, as accepted by my examiners. I understand that my thesis may be made electronically available to the public.

Statement of Contributions

I would like to acknowledge my co-authors who contributed to this thesis:

Prof. Thomas L. Willett: Conceptualization, Methodology, Data Interpretation, Data Curation, Investigation, Resources, Writing – Review & Editing, Supervision, Project Administration, Funding Acquisition.

Prof. John Montesano: Conceptualization, Methodology, Investigation, Data Interpretation, Data Curation, Writing – Review & Editing, Supervision, Project Administration.

Dr. Dibakar Mondal: Conceptualization (Section 5.2.2, Section 6.2.2), Methodology, Data Collection, Data Interpretation, Investigation, Review.

Joe Deering: Data Collection, Data Interpretation, Visualization, Writing (Sections 6.3.3)

Haresh Patil: Investigation, Visualization, Writing (Section 4.2.3.2)

Prof. Kathrine Grandfield: Enabled the contributions made by Joe Deering, including access to state-of-the-art instrumentation.

The following published (submitted) peer-reviewed journal papers, book chapters and conference papers have been used in writing this thesis:

- Mondal, D., **Hashemi, S. S.**, Diederichs, E., Patil, H., & Willett, T. L. (2023). 3D printing of biopolymer composites and nanocomposites. *Additive Manufacturing of Biopolymers*, 135-166.
- **Hashemi, S. S.**, Mondal, D.,Patil, H., Montesano, J., Willett, T.L (2023). "Effect of Increased Shear during Extrusion-Based 3D Printing on the Mechanical Properties of 3D Printable Nanocomposite Biomaterials", *Additive manufacturing*, Elsevier. (Under review)
- **Hashemi, S. S.**, Mondal, D., Montesano, J., Willett, T.L (2022). "Effects of Biopolymer Functionalization and Nanohydroxyapatite Heat Treatment on the Tensile and Thermomechanical Properties of Bone-Inspired 3D Printable Nanocomposite Biomaterials", *Materials & Design*, 225,111587.
- **Hashemi, S. S.**, Mondal, D., H., Deering, J., Grandfield, K., Montesano, J., Willett, T.L (2023). "Enhanced Dispersion and Interfacial Bonding of Nanoparticles in 3D Printable Nanocomposite Materials: Innovative Surface Functionalization and Processing Techniques for Nanohydroxyapatite Particles". (To be submitted by the end of July 2023)
- **Hashemi, S. S.**, Montesano, J., Willett, T.L (2023). "Micromechanical Elastoplastic Modeling and Characterization of 3D Printable Biopolymer Nanocomposites Using Developed Realistic RVEs". (To be submitted by the end of July 2023).

- **Hashemi, S. _S.,** J. Montesano and T. L. Willett. (Sep 2023). "Effect of Nanohydroxyapatite Particle Orientation and Distribution on Orthotropic Properties of Bone-Inspired 3D Printable Nanocomposites", *The International Conference on Biofabrication, Saskatoon, Canada.*
- **Hashemi, S. _S.,** D. Mondal, J. Montesano and T. L. Willett. (May 2022). "Biopolymer Functionalization and Nanohydroxyapatite Heat Treatment Affect the Mechanical Properties of Bone-Inspired Extrusion 3D Printed Nanocomposites", *37th Annual Meeting of the Canadian Biomaterials Society, Banf, Calgary, Canada*.
- **Hashemi, S. _S.,** D. Mondal, J. Montesano and T. L. Willett. (May 2021). "Influence of flow shear stress on the mechanical properties of an extrusion-based 3D printed bone-inspired nanocomposite biomaterial", *36th Annual Meeting of the Canadian Biomaterials Society, Virtual, Waterloo, Canada, Virtual.*
- **Hashemi, S. S.,** D. Mondal, J. Montesano and T. L. Willett. (2020 Oct). "Tailoring Shear Stress During Extrusion-based 3D-Printing to Enhance the Mechanical Properties of a Novel Nanocomposite Biomaterial", *2020 BMES Virtual Annual Meeting, USA.*
- **Hashemi, S. S.,** D. Mondal, J. Montesano and T. L. Willett. (2020 July)." The Fracture Strength of Nanocomposite Biomaterial Improved by Higher Shear Stresses During Extrusion-based 3D Printing", *42nd Annual International Conferences of the IEEE Engineering in Medicine and Biology Society in conjunction with the 43rd Annual Conference of the Canadian Medical and Biological Engineering Society, Montreal, Canada, Virtual*.

Abstract

The development of mechanically competent biomaterials that can also facilitate new bone formation is a major challenge in the field of bone repair, especially critically-sized bone defect reconstruction. 3D printed synthetic bone grafts are a possible alternative to conventional bone-substitutes if engineered to provide appropriate structure with adequate mechanical properties and biocompatibility. Nanocomposites may provide better mechanical properties and cell-material interactions compared to other classes of biomaterials due to their nano-scale reinforcements with advantageous surface-to-volume ratio and surface chemistry. In the context of 3D printed bone grafts, nanohydroxyapatite (nHA)-based biopolymer nanocomposites are attractive. The biopolymer matrix component represents the organic phase of natural bone, while nHA, the primary constituent of bone mineral, represents the mineral phase. The mechanical properties of these 3D printable biopolymer nanocomposites can be enhanced through different strategies such as optimizing the processing and manufacturing techniques, biopolymer matrix selection and optimization, surface functionalization of nanoparticles and improved dispersion and interfacial bonding between matrix and nanoparticle, all of which are attributed to improving the mechanical behavior at the micron and sub-micron scales. The focus of the current thesis was to conduct experimental and computational micromechanical investigations toward the development of mechanically competent 3D printable nanocomposite biomaterials (with a focus on strength). The objective was to enhance the mechanical properties of these nanocomposites at the nano-to-micro scales. To achieve this goal, various strategies were employed, including optimizing material design and fabrication techniques. Using a custom-designed direct ink writing (DIW) 3D printer, shear stress was varied during extrusion to force the nHA nanoparticles and/or polymer chains into alignment. The high shear extrusion led to improved mechanical properties through the formation of polymer chain crystallites and nanoconfined thermoset crystallinity phenomena, while no nHA alignment was observed. Another approach focused on optimizing the composition of the matrix by additional functionalization of the biopolymer matrix as well as heat-treating the nHA particles to remove absorbed moisture to improve the dispersion. The high shear extruded functionalized biopolymer nanocomposite system demonstrated Young's modulus of 6.6 GPa and ultimate tensile strength of 75.5 MPa, providing a strength safety factor of approximately 1.5 against the minimum required standard mechanical properties for bone cement according to ISO standard 5833. It also improved the shape-holding properties of ink, making it suitable for printing objects using the DIW printing system. As part of the effort to enhance the mechanical properties, a novel processing technique and surface functionalization

were introduced to achieve a homogeneous dispersion of nHA particles and enhance the interfacial bonding between nHA and the biopolymer matrix. This new approach significantly improved the nHA dispersion with few sub-micron scale agglomerations detected. Additionally, interfacial bonding was improved. Interestingly, the enhanced dispersion and interface properties resulted in greater ductility. Finally, an elastoplastic micromechanical computational model as a design tool was developed and biopolymer matrix characterization experiments were conducted to calibrate the elastoplastic material model used for predicting the elastoplastic behaviour of the biopolymer matrix. The model was developed to provide a design tool for virtual investigations of the effect of nHA distribution and orientation on the elastoplastic properties of the nanocomposite systems reported in this thesis. The model was validated using data from tensile tests conducted on these nanocomposite systems. The findings of the current thesis may pave the way for the fabrication of mechanically competent 3D printable nanocomposite grafts for use in bone reconstruction technology.

Acknowledgements

I would like to express my deepest gratitude and appreciation to all those who have contributed to the completion of this thesis.

First and foremost, I am immensely grateful to my supervisors, Prof. Thomas L. Willett and Prof. John Montesano, whose guidance, expertise, and unwavering support have been invaluable throughout this research journey. Their insightful feedback, encouragement, and dedication to my academic growth have played a pivotal role in shaping this thesis. I am also indebted to the members of my thesis examining committee for their time, valuable input, and scholarly guidance.

I would like to thank my colleagues in both WCBS and CRG groups for the fruitful discussions I had with them through working on my research. I am especially grateful to Dr. Mondal for his advisory guidance during my material design experiments. I am thankful to Mr. Pierre-Yves Lavertu for his valuable guidance in designing my Representative Volume Elements (RVEs). I would like to express my appreciation to Dr. Pedram Samadian for his insightful discussions throughout the computational modelling and material characterization phases of my research. I would like to thank Mr. Yu Zeng for generously sharing his knowledge and experience in polymer characterization experiments. I also want to thank Dr. Mouhanad Babi for his help with my PLM imaging, Dr. Joe Deering for his help and contribution to my TEM imaging and Mr. Binh Minh for his help with the DMA testing and Elena Kathleen Damus (URA student) for her contribution in surface functionalization of nHA particles.

To my friends in Canada and Iran, thank you for standing by my side and cheering me on throughout this journey. To my parents and my family, thank you for always being there for me and providing a nurturing and supportive environment that allowed me to pursue my academic and research goals. Your belief in me, constant encouragement and understanding have given me the confidence to overcome obstacles and persevere in the face of adversity. And finally, last but certainly not least, I want to express my deepest gratitude to my best friend, my beloved husband, for being my biggest cheerleader and for his immeasurable support, patience, and understanding during this journey.

I would like to acknowledge the financial support from the Natural Science and Engineering Research Council of Canada (NSERC), Canadian Institutes of Health Research (CIHR), Ontario Centre for Innovation and the University of Waterloo.

Dedication

To my beloved parents, and my lovely husband.

Table of Contents

Examining Committee Membership ii
Author's Declaration iii
Statement of Contributions iv
Abstract vi
Acknowledgements viii
Dedication ix
List of Figures xvi
List of Tables xx
List of Abbreviations xvi
Chapter 1: Introduction 1
1.1. Motivation 1
1.2. Thesis Outline 5
Chapter 2: Background and Literature Review 6
2.1. Natural Composites 6
2.2. Bone Structure and Mechanical Properties 6
2.3. Bio-Inspired Composite Materials 8
2.4. Overview of Fabrication Techniques 10
2.4.1. Material Extrusion 11
2.4.2. Vat Polymerization 12
2.5. Types of Nanocomposite Inks for three-dimensional printing 14
2.5.1. Metal-embedded Polymer Nanocomposites 15
2.5.2. Ceramic-embedded Polymer Nanocomposites 17
2.6. Mechanically Competent 3D Printable Nanocomposite Ink Design, and Characterization 20
2.6.1. Rheology 20
2.6.2. Shear Flow and Mechanics of Extrusion 21
2.6.3. Biopolymer Crystallinity 25

2.6.4. Cure depth 26
2.6.5. Nanoparticle Dispersion 27
2.6.6. Physical principles of miscibility 29
2.6.7. Phase Functionalization 29
2.7. Computational Modeling of Nanocomposite Materials 32
2.7.1. Constitutive Material Model for elastoplastic deformation of Polymer Matrix 36
2.7.2. Polymer Characterization Experiments 40
Chapter 3: Research Objectives and Hypothesis 43
3.1. Objectives and Hypothesis 43
3.2. Scope of Work 45
Chapter 4: The Effects of Shear Stress on the Micromechanical Properties of 3D Printable Biopolymer Nanocomposites using a Custom-Designed Extrusion-Based 3D Printer 47
4.1. Introduction 47
4.2. Materials and Methods 50
4.2.1. Preparation of 3D printable Nanocomspoite Ink 51
4.2.2. Characterization of Nanocomposites 51
4.2.2.1. Nanocomposite Ink Rheology 51
4.2.2.2. Fourier Transform Infrared Spectroscopy (FTIR) 52
4.2.2.3. Thermogravimetric Analysis (TGA) 52
4.2.2.4. Differential scanning calorimetry (DSC) 52
4.2.2.5. Scanning electron microscopy (SEM) 53
4.2.2.6. Polarized Light Microscopy Imaging 54
4.2.3. DIW of Nanocomposite Filaments 54
4.2.3.1. Mechanics of Extrusion-Based 3D printing 54
4.2.3.2. Printing Nanocomposite Filaments using Custom-Built Skeleprinter 55
4.2.4. Mechanical Testing of Nanocomposite Filaments 60
4.2.5. Dynamic Mechanical Analysis (DMA) 61
4.2.6. Statistical Analyses 62
4.3. Results 62

4.3.1. Nanocomposite inks characterization 62
4.3.2. Microstructure Imaging of Different Extruded Nanocomposite Filaments 65
4.3.2.1. Scanning Electron Microscopy (SEM) 65
4.3.2.2. Polarized Light Microscopy Images 66
4.3.3. Mechanical Properties of Nanocomposite Filaments 67
4.3.4. DMA 69
4.4. Discussion 69
4.5. Conclusions 72
Chapter 5: Effects of Biopolymer Functionalization and Nanohydroxyapatite Heat Treatment on the Tensile and Thermomechanical Properties of Bone-Inspired 3D Printable Nanocomposite Biomaterials 73
5.1. Introduction 73
5.2. Materials and Method 77
5.2.1. Ink Composition 77
5.2.2. Ink Preparation 77
5.2.2.1. Preparation of mAESO 77
5.2.2.2. Heat Treatment of nHA Particles 78
5.2.2.3. Mixing the biopolymer matrix and nHA particles 78
5.2.3. Preparation of 3D printed nanocomposite filaments 79
5.2.4. Characterization of Nanocomposites 80
5.2.4.1. Rheology of the nanocomposite inks 80
5.2.4.2. Cure Depth Analysis 80
5.2.4.3. Fourier-Transform Infrared Spectroscopy (FTIR) 81
5.2.4.4. Thermo-Gravimetric Analysis (TGA) 81
5.2.5. Mechanical Testing and Strain Measurements of Nanocomposite Filaments 82
5.2.6. Imaging of nHA dispersion and filament fracture surfaces 83
5.2.6.1. Image analysis of nHA dispersion 84
5.2.7. Differential scanning calorimetry (DSC) 84
5.2.8. Dynamic Mechanical Analysis (DMA) 85
5.2.9. Statistical Analyses 85

5.3. Results 85
5.3.1. Characterization of nanocomposite 85
5.3.2. DSC analysis 89
5.3.3. Dispersion of nHA in the nanocomposites 90
5.3.4. Tensile Testing of Nanocomposite Filaments 92
5.3.5. DMA Results 93
5.4. Discussion 95
5.5. Conclusion 98
Chapter 6: Improved Dispersion and Interfacial Bonding of Nanoparticles in 3D Printable Nanocomposite Biomaterials via Innovative Surface Modification and Processing of Nanohydroxyapatite Particles 99
6.1. Introduction 99
6.2. Materials and Method 102
6.2.1. Ink Composition 102
6.2.2. Ink Preparation 102
6.2.2.1. nHA Purification 102
6.2.2.2. Surface Functionalization of nHA 103
6.2.2.3. Preparation of Functionalized Biopolymer Matrix 104
6.2.2.4. Preparation of Nanocomposite Ink 104
6.2.2.5. Rheology 104
6.2.3. 3D Printing of Nanocomposite Inks 104
6.2.4. Mechanical Testing of Biopolymer Matrix and Nanocomposite Sample 105
6.2.5. Characterization of 3D printed Nanocomposite 107
6.2.5.1. Thermo-Gravimetric Analysis (TGA) 107
6.2.5.2. Fourier Transform Infrared Spectroscopy (FTIR) 107
6.2.5.3. Scanning Electron Microscopy (SEM) 107
6.2.5.4. EDX 108
6.2.6. TEM Characterization 108
6.3. Results 108
6.3.1. TGA 108

6.3.2. Surface Functionalization and Interfacial Bonding Assessment 109
6.3.3. TEM Surface Characterization of Functionalized and NonFunctionalized nHA Nanorods 110
6.3.4. FTIR Results 113
6.3.5. nHA Dispersion in Developed Nanocomposite Systems 114
6.3.5.1. Quantitative Comparison of nHA Dispersion 116
6.3.6. Effect of nHA dispersion on Ink rheology 116
6.3.7. Tensile Testing of 3D-Printed Nanocompsoite Inks 117
6.3.8. Fracture Surfaces 118
6.4. Discussion 119
6.5. Conclusion 124
Chapter 7: Micromechanical Elastoplastic Modeling and Characterization of 3D Printable Biopolymer Nanocomposites Using Realistic RVEs 125
7.1. Introduction 125
7.2. Materials and Method 128
7.2.1. Preparation of Functionalized Biopolymer Matrix 128
7.2.2. 3D Printing of the Functionalized Biopolymer Matrix 128
7.2.2.1. Tensile Test Specimens 128
7.2.2.2. Compression Test Specimens 129
7.2.2.3. Uniaxial Shear Test Specimens 129
7.2.3. Mechanical Testing of the Biopolymer Matrix 130
7.2.3.1. Tensile testing of 3D Printed Biopolymer Matrix and Nanocomposite Specimens 130
7.2.3.2. Compression Testing 131
7.2.3.3. Uniaxial Shear Testing 132
7.2.4. Material models 133
7.2.4.1. Drucker-Prager Elastoplastic Constitutive Model for the Biopolymer Matrix 133
7.2.4.2. Hardening Properties 134
7.2.5. Realistic RVE Generation 134
7.2.5.1. RVE Size Definition 136
7.2.5.2. Orientation Tensors 136
7.2.5.3. Length Distribution 138

7.2.5.4. Agglomerations 139
7.2.6. Application of Periodic Boundary Condition on 3D Periodic RVEs 139
7.2.7. Homogenization and Mesh Sensitivity Analysis 140
7.3. Results and Discussion 142
7.3.1. Material Model Calibration and Verification 142
7.3.1.1. Hardening Properties 145
7.3.2. Micromechanical Simulations 145
7.3.2.1. Nanorod Alignment Effect 147
7.3.2.2. Nanorod Length and aspect ratio effect 148
7.3.2.3. Nanorod length distribution 150
7.3.2.4. RVEs with length distribution and agglomerations 151
7.3.2.5. Orthotropic properties of generated RVEs 153
7.3.3. Elasto-Plastic Micromechanical Modeling of RVEs 155
7.4. Conclusion 159
Chapter 8: Conclusion 161
8.1. Ideas for Future Work 163
Letter of Copy Right Permissions 166
References 174
Appendices 206

List of Figures

Fig. 1.1. Schematic illustration of bone-inspired nanocomposite materials 1

Fig. 1.2. A segmental bone defect and its reconstruction with bone allograft and stabilization by bridging plate .. 2

Fig. 1.3. The hierarchical structure of cortical bone 3

Fig. 2.1. Material-property chart and projections for natural and synthetic materials 7

Fig. 2.2. AM fabrication method classifications 11

Fig. 2.3. Methods for extruding materials for 3D printing 12

Fig. 2.4. Laser SLA, DLP-SLA, and mSLA process differentiation 14

Fig. 2.5. Example of three-dimensional printed nanocomposite bone models using masked stereolithography 3D Printing technique printed in WCBS lab 14

Fig. 2.6. Illustration showing a sample loaded between two plates 21

Fig. 2.7. Illustration of the potential reactions of various microstructures to the application of shear 22

Fig. 2.8. Velocity, shear rate and shear stress profiles for flow through a round tube 23

Fig. 2.9.Shear stress profile and measurement in a printing needle. 23

Fig. 2.10. The different filler alignment techniques used in AM biopolymer composites 24

Fig. 2.11. Schematics presenting the anisotropic particles' alignment due to shear at the dispensing nozzle 24

Fig. 2.12. Semi-crystalline molecular structure for a thermoplastic polymer 25

Fig. 2.13. Wetting of different fluids 29

Fig. 2.14. Silane grafting of nHA particles 31

Fig. 2.15. Steps involved in micromechanical FEM modelling of nanocomposite systems 35

Fig. 2.16. Stress-strain curves in compression at various hydrostatic pressures for a glassy polymer 38

Fig. 2.17. Mohr-Coulomb and Drucker-Prager yield criterion in principal coordinates 38

Fig. 2.18. A representative compressive stress-strain curve for glassy polymers 42

Fig. 4.1. Schematic of the preparation of AESO-based 3D printable nanocomposite inks 51

Fig. 4.2. The velocity distribution profile in a simple shear flow of Newtonian fluid between two parallel plates .. 55

Fig. 4.3. Shear stress distribution profiles for laminar flow through a round tube with a maximum at the tube wall and zero at the centre. 55

Fig. 4.4. Schema of the experimental set-up using the custom-built extrusion-based SkelePrint 3D printer for extruding the filaments with controlled shear stress during extrusion. 56
Fig. 4.5. SkelePrint's components 57
Fig. 4.6. Adjustable UV lamp mounting configurations to accommodate different angular layup sequencing 58
Fig. 4.7. Concentrically layered 3D printed sample structures printed using the custom-designed Skeleprint 59
Fig. 4.8. Nanocomposite filament test specimen preparation 60
Fig. 4.9. Representative viscosity vs shear strain rate and shear stress vs shear strain rate 63
Fig. 4.10. Melting enthalpy for the four extruded nanocomposite filaments and cast specimen as a control 64
Fig. 4.11. Representative SEM images of extruded filaments 65
Fig. 4.12. Polarized light microscopy images 67
Fig. 4.13. Representative stress-strain curves 68
Fig. 4.14. Representative SEM images extruded filaments' fracture surfaces after tensile testing 68
Fig. 4.15. Dynamic mechanical properties of an extruded thin film nanocomposite (14 kPa) compared to a cast nanocomposite thin film specimen. 69
Fig. 5.1. 3D printable nanocomposite ink preparation 79
Fig. 5.2. 3D printed samples with developed nanocomposite inks 80
Fig. 5.3. Nanocomposite filament extrusion, sample preparation process and tensile test configuration 83
Fig. 5.4. Rheological data of the three nanocomposite inks over a variety of shear strain rates 86
Fig. 5.5. Cure depth vs. UV energy dosage for SP30, SP30h, mSP30 and mSP30h nanocomposites 88
Fig. 5.6. DSC data 89
Fig. 5.7. Representative SEM images of longitudinal sections of extruded filaments 90
Fig. 5.8. Distribution of nanoparticle agglomerations for D>1 μm 91
Fig. 5.9. Representative stress-strain curves, strength, elastic modulus, fracture strain of the four novel 3D printable nanocomposites in this study 92
Fig. 5.10. Representative SEM images of fracture surfaces of extruded filaments after tensile tests 93
Fig. 5.11. DMA results of AESO and mAESO based neat resins and SP30, SP30h, mSP30 and mSP30h nanocomposites 94
Fig. 6.1. nHA purification procedure and functionalization process 103

Fig. 6.2. Printing dogbone samples and tensile testing 106
Fig. 6.3. SEM EDX results of non-functionalized and functionalized nHA 109
Fig. 6.4. HAADF-STEM images and EDX mapping of a hydroxyapatite nanorod grafted with sulfopropyl methacrylate 110
Fig. 6.5. HAADF-STEM images and EDX mapping of a hydroxyapatite nanorod 111
Fig. 6.6. EDS line scans across the minor and major axes of a functionalized nanoparticle 112
Fig. 6.7. EDS line scans across the minor and major axes of a nanoparticle without functionalization 112
Fig. 6.8. FTIR Spectra for non-functionalized and functionalized SPM-nHA 113
Fig. 6.9. SEM images of different processed nanocomposite systems 114
Fig. 6.10. HAADF-STEM images of hydroxyapatite nanorod aggregation 115
Fig. 6.11. Distribution of nanoparticle agglomerations for the three nanocomposite systems 116
Fig. 6.12. Rheological data of three developed nanocomposite inks at different shear strain rates 117
Fig. 6.13. Representativestress–strain curves, Elastic modulus, Fracture Strength, Fracture strain of the three developed 3D printable nanocomposites in this study 118
Fig. 6.14. SEM images of fracture surfaces of tensile tested nanocomposite samples 119
Fig. 7.1. 3D printed mini-shear samples with final beam support design 130
Fig. 7.2. Biopolymer matrix Dogbone tensile test set-up 131
Fig. 7.3. Biopolymer matrix compression test set-up 132
Fig. 7.4. Uniaxial shear test setup 132
Fig. 7.5. Drucker-Prager yield criterion in principal stresses, π-plane and meridian plane 133
Fig. 7.6. RVE generation algorithm using Digimt-FE 135
Fig. 7.7. Nanoparticle oriented in 3D with unit vector p along its axis of a revolution described with two spherical angles θ and ϕ. 137
Fig. 7.8. Gaussian probability distribution vs size of rod-shaped nanoparticle in the matrix. 138
Fig. 7.9. 3D periodic RVEs 139
Fig. 7.10. Heterogeneous periodic microstructure and RVE of the composite structure with matrix and inclusions. 141
Fig. 7.11. Single element verification test models for the biopolymer matrix under tension. 143

Fig. 7.12. Single element verification test models for the biopolymer matrix under compression. 144

Fig. 7.13. Experimental and single-element quasi-static test results for the biopolymer matrix tested in shear. 144

Fig. 7.14. Comparison the Digimat-FE tensile single-element and averaged experimental quasi-static test results for the biopolymer matrix using derived material and hardening properties. 145

Fig. 7.15. RVE size sensitivity analysis. RVE size was increased in all three directions while keeping the volume fraction of particles constant at 5% in all RVEs. 146

Fig. 7.16. Represented RVEs generated with different percentages of aligned particles at a constant volume fraction. 148

Fig. 7.17. Represented RVEs with different length scales of nHA particles with randomly dispersed randomly oriented and 100 % aligned particles. 149

Fig. 7.18. Randomly dispersed, randomly oriented, length distributed RVE, Representative generated RVE and Comparison of the length distribution of generated RVE with inputted reference microstructure. 151

Fig. 7.19. Randomly dispersed, randomly oriented, length-distributed RVEs with nanoscale agglomerations. 152

Fig. 7.20. Elastic stress contours (σ_{vm}) in the matrix and inclusion through five class of RVEs 154

Fig. 7.21. Elasto-plastic stress-strain response of five classes of generated RVEs compared with the average experimental stress-strain response of our novel nanocomposite. 155

Fig. 7.22. Shear stress (σ_{13}) contour in the matrix and normal stress (σ_1) contour in the inclusion of five class of generated RVEs 157

Fig. 7.23. Von mises stress contour in the regions of agglomerations; the matrix demonstrates higher stress levels and may act as stress concentration regions for the onset of local failure. 158

Fig. 7.24. Stress contours (σ_{vm}) in RVEs of randomly dispersed, randomly oriented, length-distributed inclusions with random clusters through different increments of deformation 159

List of Tables

Table 2.1. Thermosets vs Thermoplastics features 41

Table 4.1. Viscosity, shear yield strength and TGA results of the as-prepared nanocomposite ink 63

Table 4.2. The relative degree of crystallinity obtained for different shear extruded cases 64

Table 4.3. Number and size of spherulites detected in specific ROI of POM micrographs for different cases 66

Table 5.1. Nomenclature of the four 3D printable nanocomposites according to their constituents 78

Table 5.2. Viscosity and shear yield strength results of as-prepared nanocomposite inks 86

Table 5.3. Cure depth material constants for the nanocomposite inks 87

Table 5.4. Peak temperatures of derivative loss weight vs temperature curves for studied nanocomposites obtained from TGA 88

Table 6.1. TGA analysis results, volume fraction calculated for each nanocomposite system 109

Table 6.2. EDX-SEM Atomic percentage of non-functionalized raw nHA and SPM functionalized nHA 110

Table 6.3. Viscosity and shear yield strength results of nanocomposite inks 117

Table 7.1. The assumed elastic properties of nHA and measured biopolymer matrix properties 142

Table 7.2. Calibrated hardening parameters 145

Table 7.3. RVE size sensitivity analysis results 147

Table 7.4. The elastic modulus of representative RVEs with increasing particle alignment in the uniaxial loading direction 148

Table 7.5. The elastic modulus (E_{11}) of represented RVEs with increased nHA aspect ratio in randomly oriented and 100% aligned inclusions in the loading direction 150

Table 7.6. The elastic modulus (E_{11}) of represented RVEs with increased volume fraction of agglomerations in randomly oriented, randomly dispersed, length distributed RVEs 152

Table 7.7. The orthotropic mechanical properties for five representative classes of generated RVEs 153

List of Abbreviations

AESO	Acrylated Epoxidized Soybean Oil
AM	Additive Manufacturing
ANOVA	Analysis of Variance
CAD	Computer-Aided Design
DIC	Digital Image Correlation
DIW	Direct Ink Writing
DLP	Digital Light Projection
DMA	Dynamic Mechanical Analysis
DSC	Differential Scanning Calorimetry
EDS	Energy Dispersive Spectrometer
EDX	Energy-Dispersive X-ray Spectroscopy
FDM	Fused Deposition Modelling
FEM	Finite Element Modeling
FTIR	Fourier-Transform Infrared Spectroscopy analysis
MAA	Methacrylic Anhydride
mAESO	Methacrylated Acrylated Epoxidized Soybean Oil
MD	Molecular Dynamics
ME	Material Extrusion
mSLA	masked Stereolithography
nHA	nanohydroxyapatite
PBF	Powder Bed Fusion
PEGDA	Polyethylene Glycol Diacrylate
PLA	Poly Lactic Acid
PLM	Polarized Light Microscopy
RVE	Representative Volume Element
SEM	Scanning Electron Microscopy
SLS	Selective Laser Sintering
SPM	Sulfopropyl Methacrylate
TEM	Transmission Electron Microscopy
TGA	Thermogravimetric Analysis
VP	Vat Polymerization

Chapter 1

Introduction

1.1. Motivation

Natural composites such as bone, wood and shells are lightweight materials with high specific strength and toughness characteristics that exceed that of their constituents [1]. Modern characterization techniques and modelling tools provide an opportunity for researchers to decode the effect of the complex and hierarchical structure of these natural composites on their mechanical performance by enabling analysis from nano to macroscopic length scales. These analyses are invaluable in the pursuit of understanding the underlying mechanisms that result in the exhibited mechanical properties of these natural and biological materials. Furthermore, they provide valuable information for developing bio-inspired composite material systems such as nanocomposites [2–4]. It has been discovered that by manipulating the structure of nanocomposites – which has become feasible only recently due to advancements in nanotechnology and nanoscale engineering - opportunities will be opened to develop new bio-inspired nanocomposite systems (Fig. 1.1). However, there are still some obstacles that inhibit the control of nano-scale characteristics of materials during their fabrication. Choosing appropriate material composition and processing methods will help to overcome some of these obstacles and pave the way for emerging bioinspired nanocomposite materials.

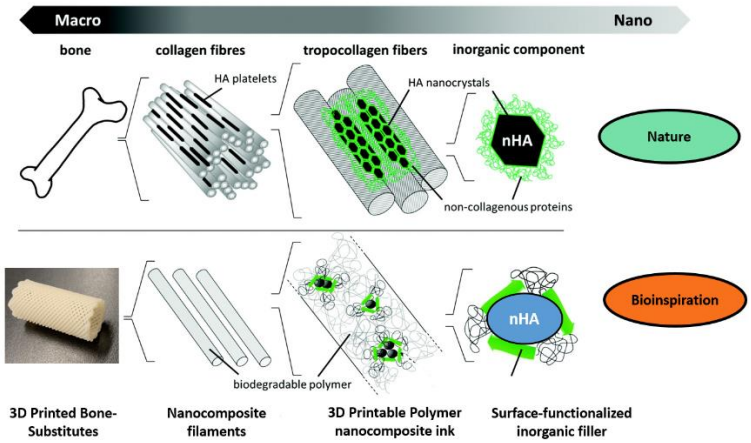


Fig. 1.1. Schematic illustration of bone-inspired nanocomposite materials: Top (left to right) demonstrates natural bone structure demonstrates engineered interface of nanohydroxyapatite(nHA) with non-collagenous proteins compatible with collagen matrix; Bottom (right to left): bone-mimetic surface functionalized nanocomposite ink designed for 3D printing bone substitutes (Images obtained and customized [5],[6])

Bioinspired composites may have different applications in various strategic fields, such as medicine, transportation, and manufacturing. The field of medicine has seen growth in the application of bioinspired composites for the treatment of diseases [7]. A potential application for bioinspired nanocomposite materials is using them in advanced bone reconstruction. In recent years, the demand for bone tissue replacements has been on the rise. This is primarily due to factors such as an aging population and an increase in patients dealing with sports injuries, traffic accidents, or bone cancer. [8]. As a biological tissue, bone has the ability to remodel itself, which is an astounding feature that can repair small gaps. However, when the gaps are too large, such as for segmental bone defects in human long bones where gaps are >2.5 cm [9] (Fig. 1.2), the bone does not heal effectively. These large gaps are termed critically-sized bone defects (CSBDs) and can be caused by traumatic injury or surgical treatment of infections or tumours. Every year over 2.2 million people in the world receive bone grafting surgery to repair large bone defects [10]. Grafting is a surgical procedure that replaces the diseased bone and is used to aid bone reconstruction in segmental bone losses.



Fig. 1.2. A segmental bone defect and its reconstruction with bone allograft and stabilization by bridging plate [11].

There are two popular approaches in current treatment methods for segmental bone defects: allografts and synthetic bone substitutes. Allografts are the bone taken from a deceased person who has donated their bone. Synthetic bone substitutes such as implants are artificially made of synthetic materials such as polymers, metals or ceramic composites. Although these current methods help patients to recover some functionality, they have disadvantages, such as the need for at least two or three revision surgeries, mechanical failures, stress shielding, immune rejection, and disease transfer, all of which provide poor quality of life for the patient during the treatment period [12–14]. Hence, there is an increasing demand for new technologies for fabricating long-lasting implants [15].

Bone-inspired biopolymer nanocomposite grafts, with their osteoconductive and biocompatible features, are a new alternative to conventional bone substitutes with the potential to overcome some of the aforementioned disadvantages. In constructing bone-inspired composites, various features such as chemical composition, nano/microstructure, and hierarchical architecture can be inspired by the bone tissue itself. Bone is a major structural tissue of the human body which supports and protects various organs, stores minerals and produces bone marrow cells. Bone can be considered a natural nanocomposite that is comprised of two main nano-phases, including collagen fibrils and hydroxyapatite nanocrystals. The properties and the hierarchical structure arrangement of the nanohydroxyapatite (nHA) particles and collagen (Fig. 1.3) interact synergistically with other trace components (i.e. non-collagenous proteins) to define the biomechanical properties of bone [16].

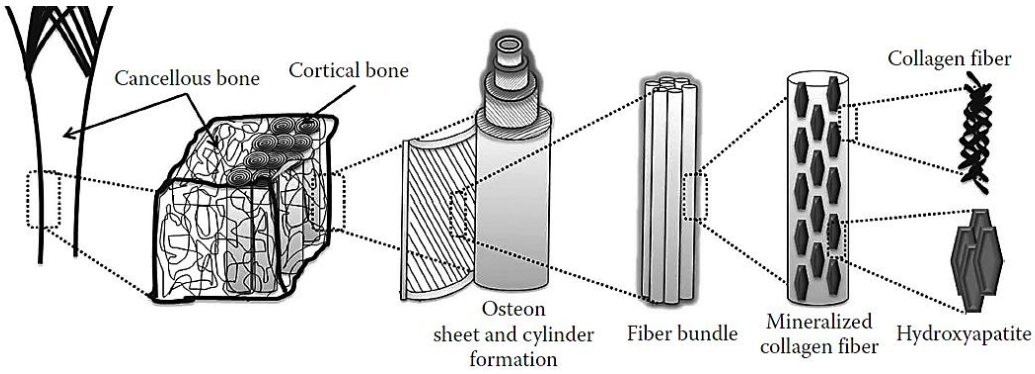


Fig. 1.3. The hierarchical structure of cortical bone [17].

A primary concern in designing bone-inspired composites is material selection. These materials should provide mechanical properties that can mimic the mechanical properties of bone as well as overcome the *in vivo* challenges, such as biocompatibility and osteoconductivity to be used as bone-substitutes in critically sized segmental bone defects [18].

In bone tissue, nHA particles are homogeneously dispersed within the collagen fibers. This uniform distribution ensures that the mechanical load is efficiently transferred throughout the material. Additionally, the interface between the nHA particles and collagen fibres is coated with non-collagenous proteins which play a crucial role in enhancing the compatibility between the nHA particles and the collagen matrix at the nanoscale [5]. They assist in maintaining the structural integrity of the bone. At the macro scale, the arrangement of the collagen fibers and nHA particles

follows a hierarchical pattern. This hierarchical arrangement contributes to the overall strength and toughness of the bone. The collagen fibres provide flexibility and resistance to tension, while the nHA particles enhance the strength of the material. To fabricate a mechanically competent nanocomposite system, it is essential to consider and replicate these nano-macro features of the bone structure. This means incorporating a homogeneous dispersion of nanoparticles within the matrix material and engineering interfaces that enhance compatibility and load transfer. Additionally, mimicking the hierarchical arrangement of the nanocomposite structure can contribute to achieving the desired mechanical properties in the fabricated system. Due to the *in vivo* challenges and the limitations in manufacturing nano-scale hierarchical architectures, research on designing these bone-mimetic nanocomposites has been largely overlooked. A distinctive feature of natural composites is their hierarchical structure, which is thought to provide superior mechanical properties like strength and fracture toughness. Clearly, arrangement and structure will play a key role in enhancing the mechanical properties even without changing the composite's chemical composition.

To develop a bone-like nanostructure, the fabrication procedure must control the arrangement of nano-scale inclusion orientations as well as the layers of the structure at larger length scales. Direct Ink Writing (DIW) is an extrusion-based 3D printing method that can be used to fabricate biomimetic nanocomposites. The advantage of this free-form additive manufacturing method compared to other fabrication techniques is that custom-designed materials with complex hierarchical structures can be fabricated accurately with good reproducibility [19]. It has been demonstrated that the use of a DIW method can improve the mechanical properties (strength specifically) of some nanocomposite materials as a result of fewer defects and increased crystallinity in the polymer matrix [20]. Moreover, the orientation of the polymeric and particulate phases along the fibre/extrusion axis can be tailored during the extrusion process [21], which could also lead to better mechanical properties. Therefore, the design of mechanically competent 3D printable nanocomposite inks requires a comprehensive study that encompasses various considerations. Factors such as nanoparticle selection, dispersion, matrix material choice, interfacial bonding, and optimization of printing process parameters all play roles in ensuring the successful fabrication of bone–inspired nanocomposite structures with the desired mechanical properties.

For the widespread adoption of bone-mimetic and other biomimetic composites, it is pivotal to develop the ability to tailor their elaborate architectures and assess their corresponding material performance. To achieve this goal, it is necessary to develop robust high-fidelity design tools. Through the use of validated computational methods, such as micromechanical analysis, it is possible to assess different material systems and compositions virtually by predicting the mechanical properties and the failure processes. Such a design tool will help biomaterial engineers to better understand the underlying failure mechanisms of bone-mimetic nanocomposites and establish general design guidelines to achieve more mechanically competent nanocomposite systems. It will pave the way for designers to develop new bone-mimetic nanocomposite grafts for use in advanced bone reconstruction.

1.2. Thesis Outline

In Chapter 2, the relevant theoretical background and literature review of bone-inspired nanocomposite systems, fabrication methods of biological and bioinspired composite materials, considerations for designing mechanically competent 3D printable nanocomposite inks and finally, elastoplastic micromechanical modelling of polymer nanocomposite systems are described to understand the required knowledge and realize limitations, gaps, and shortcomings in this area. Chapter 3 describes the main objective and hypothesis of the current thesis, along with the scope of work for each objective. Chapters 4 to 7 of the thesis consist of the published or submitted peer-reviewed papers that the candidate authored as the first author and is responsible for the conceptualization, methodology, development, data collection, data curation and analysis of the results presented in these chapters. The content of these chapters has been adjusted to ensure cohesiveness with the broader perspective of the thesis. In Chapter 8, the thesis concludes with the presentation of overall conclusions drawn from the research and provides recommendations for future directions in the field. The rest of the thesis comprises an appendix which has been referred to in Chapter 7. Finally, a dedicated list of references has been provided at the end of the thesis.

Chapter 2

Background and Literature Review

2.1. Natural Composites

Nature creates diverse types of composites from limited ingredients and constituents. Natural composites are typically comprised of hard and soft phases with a complex hierarchical structure [1]. Polymeric materials such as proteins or polysaccharides often make up the matrix phase, and ceramic minerals such as calcium salts, silica, or hydroxyapatite are often the reinforcement phase [22,23]. Animal tissues are examples of natural composites and are comprised of collagen, elastin, keratin, chitin, and minerals such as calcium phosphate or silica. Other examples include wood and bamboo, which consist of cellulose fibres in a lignin hemicellulose matrix, dentine and enamel which are mainly comprised of hydroxyapatite, and bone and antler that are formed from hydroxyapatite and collagen. [24].

From a mechanical point of view, the individual phases of natural composites do not have remarkable mechanical properties. However, the resultant properties of these composites are high, surpassing the mechanical properties of their individual constituents. Understanding *the structure* and *arrangement* of reinforcement phases, as well as the *properties* and *volume fractions* of different phases, is crucial for achieving superior mechanical properties in natural composites. Various examples, such as cartilage, tendons, ligaments, and bone tissues, demonstrate how the structural characteristics impact the mechanical performance of these materials. While all these natural composites share similar components, their unique fractions and arrangements result in distinct mechanical properties which enable them to effectively fulfill their specific functions [24]. Therefore, to develop engineered nanocomposites that can mimic natural tissues, it is essential to thoroughly comprehend their properties and structural characteristics.

2.2. Bone Structure and Mechanical Properties

Having a better understanding of the structure, composition, and mechanical properties of bone will help lead us to an ideal design for tissue-engineered biomimetic nanocomposites suitable for use in bone reconstruction technologies and in aiding the bone healing process.

Bone is a natural nanocomposite, and its majority of mass includes Hydroxyapatite (~60%), Carbonate (~5 %), Collagen (~20%), Water (~9%), Non-collagenous proteins (~3%), other minerals(~1%) [25]. Bone has two main nano-phases; One phase consists of collagen fibrils made from type-I collagen molecules (~300 nm long, ~1.5 nm in diameter), while the other consists of hydroxyapatite nanocrystals ($Ca_{10}(PO_4)_6(OH)_2$, plate-shaped, 50 nm × 25 nm in size, 1.5–4 nm thick) which are distributed along the collagen fibrils. It's important to note that the exact nature of bone mineral can vary, and it may exhibit some calcium deficiencies and substitutions, resulting in a slightly modified chemical formula. The properties and structural arrangement of the nanohydroxyapatite (nHA) particles and collagen interact collaboratively with other trace components (i.e. non-collagenous proteins) to define the biomechanical properties of bone [26]. The mechanical properties of bone are intricately determined by the interactions and combination of its various components during growth and synthesis. Throughout the process of bone formation, a complex interplay occurs between different components, including cells, extracellular matrix proteins (such as collagen), and mineralized deposits (such as hydroxyapatite). These interactions at the molecular and microstructural levels play a crucial role in shaping the mechanical behavior of bone. [1].

Natural materials like bone are multifunctional. Their mechanical, biological and other functions are combined to present an optimum design solution for a set of demands. Ashby devised a material property chart which presents the specific performance, fracture toughness and multi-directional properties of each section. The plots help identify regions or clusters where materials with desirable combinations of properties reside (Fig. 2.1.) [24].

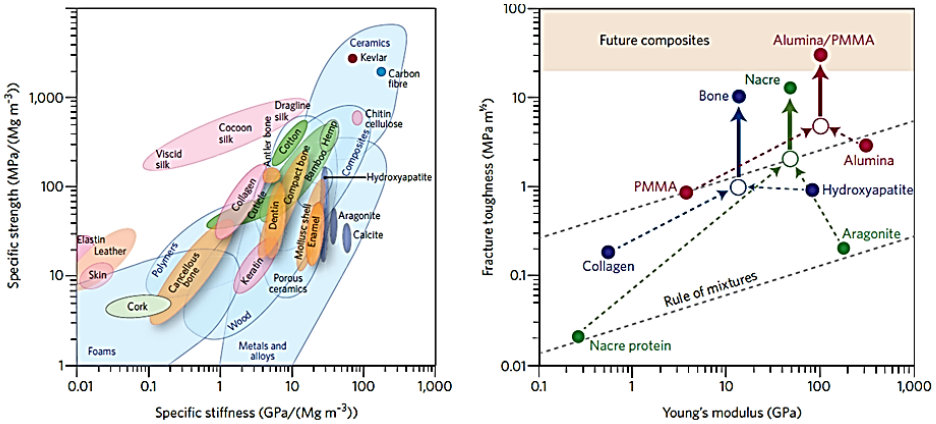


Fig. 2.1. Material-property chart and projections for natural and synthetic materials (Adapted with permission [1]).

The constituent materials of bone have limited mechanical properties, while as a natural nanocomposite, bone has superior properties partially due to its hierarchical structure [1]. The tensile (compression) yield strength, tensile (compression) ultimate strength and elastic modulus of cortical bone in humans are 71.56 ± 10.19 (115.06 ± 16.36) MPa, 135 ± 15.6 (205 ± 17.3) MPa and 17.9 ± 3.9 GPa respectively. [27][28] The fracture toughnesses (K_c) values in the human cortical bone MPa $m^{1/2}$ have been reported to range between 2 to 12 MPa $m^{1/2}$[29]. Through applying biomimicry and using synthetic constituents, various high-performance composite material systems may be generated, leading to a new generation of composites named bio-inspired composites [30]. Benchmark mechanical property values for bone substitute materials should aim to match the mechanical properties of the natural bone they are intended to replace. The mentioned values can vary depending on factors like age, gender, bone type, and location in the body. Additionally, the specific requirements of the application, such as load-bearing capacity, articulation, or non-load-bearing, will influence the prioritization of these properties. There are three requirements for the conventional bone cements: compressive strength (minimum of 70 MPa), bending modulus (minimum of 1800 MPa) and bending strength (minimum of 50 MPa) require according to ISO 5833. When designing new bone substitute materials, it's important to strike a balance between mimicking natural bone properties and fulfilling the intended functional requirements and will require further assessing other mechanical properties including fracture toughness, hardness and density to prevent sudden failures during healing procedure.

2.3. Bio-Inspired Composite Materials

Various research groups have developed and fabricated bioinspired composites by mimicking the features of natural materials in order to investigate the structure-property relationships for different applications. Grossman et al. [31] produced a nacre-like brick-and-mortar structure that was interconnected with submicron interplate mineral bridges. They produced inorganic scaffolds, which were hot-pressed and infiltrated with an organic phase. This structure led to the creation of a strong and tough composite. Martin et al. [32] recreated complex bioinspired reinforcement architectures that enhanced material performance. They reported an increase in stiffness, Vickers hardness, and failure strain. Their complex structures were developed using 3D magnetic printing technology. Erb et al. [33] produced a self-shaping composite with programmable bioinspired microstructures. Using a new approach, they replicated the unusual shape-changing mechanism of

natural systems. They remotely controlled the orientation of inorganic particles in the composite by using a weak external magnetic field. Yaraghi et al. [34] generated biomimetic composites inspired by the dactyl segments of mantis shrimp, which had helicoid and herringbone microstructure to customize the impact resistance. They reported that in the helicoid structure, critical shear strains were possible, which were not possible in the herringbone structure. Thus, the herringbone structure had superior impact resistance. Mirkhalaf et al. [35] mimicked various topological interlocked structures to obtain superior mechanical properties. In each structure, they tested the maximum load capacity and energy absorption under static and impact loading. Lewis et al. [36] developed various geometries of cellular structures that were reinforced via rod-shape whiskers trying to mimic the strength and stiffness of these material systems. Zhang et al. [37] focused on the development of bio-inspired staggered composites with improved energy dissipation characteristics. The authors employed a numerical-experimental approach to investigate and optimize the performance of these composites. Libonati et al. [38] focused on the development of a bone-inspired fiber composite with improved fracture toughness. The researchers aimed to synergistically activate the characteristic toughening mechanisms of fiber-reinforced composites to fabricate advanced structural materials.

Although encouraging results were reported for the mechanical properties of some of these composites, there are some deficiencies in the function of some of the aforementioned biomimetic composites, which originate in either the material structure or the manufacturing process. Most of these composites had micro-scale inclusions while, as mentioned above, to get the high-performance properties of natural and biological composites and specifically to mimic the bone structure, nano-scale bio-inspired structures will be essential [4,39]. The orientation and alignment of nano-scale inclusions cannot be controlled in most of their manufacturing processes. Nano-scale physical and chemical bonding has not yet sufficiently been developed in these materials. Further, a lack of adequate interfacial interaction between the inorganic particles and the polymer matrix can drastically influence the mechanical properties of the biomimetic composites as they will limit the reinforcement effect due to stress concentrations and hinder load transfer between matrix and inclusion, respectively [6]. Therefore, it can be expected that to achieve superior mechanical properties for mimicking a natural composite like bone, nano-scale arrangements are necessary and polymer nanocomposites for bone reconstruction applications could potentially ameliorate some of the aforementioned deficiencies.

2.4. Overview of Fabrication Techniques

One of the key aspects in enhancing the mechanical properties of materials is the arrangement of the constituents and structure. Fabrication techniques for bio-inspired composites aim to mimic the hierarchical structure of natural composites, which will be very useful in modifying their mechanical properties. There have been several fabrication methods in the literature for producing bioinspired composites, such as casting [40], layer-by-layer assembly [41], freeze casting [42], ink-jet printing [43], gel casting [44], hot pressing [44], magnetic alignment [45], magnetically assisted slip casting [46], hot-press assisted slip casting [47], and robocasting [48]. Although encouraging results were reported when using these methods, their main disadvantage is their lack of control over the microstructure to produce hierarchical as well as complex structures like natural composites. Moreover, in some of the aforementioned methods, significant manufacturing defects occur.

Additive manufacturing (AM) technologies, particularly 3D printing, are an adaptable technique for the cost-effective fabrication of on-demand customized products. There are various AM (Additive Manufacturing) processes available that are used for rapid prototyping applications (Fig. 2.2). These processes can be categorized into three groups based on their working principles: powder bed fusion (PBF), material extrusion (ME), vat polymerization (VP), and hybrid methods. Computer-aided design (CAD) models are typically used in AM technologies [49]. These designated AM techniques may process polymer materials and their composites in various raw material types, such as powders, solid filaments, pastes, or liquids. Selective laser sintering (SLS) and fused deposition modelling (FDM) are used in additive manufacturing (AM) to process "thermoplastic" biopolymers (like Polylactic Acid (PLA)) and their composites. On the other hand, photopolymerization AM techniques, such as material extrusion and vat polymerization techniques, are typically used to print "thermoset" biopolymers and their composites.

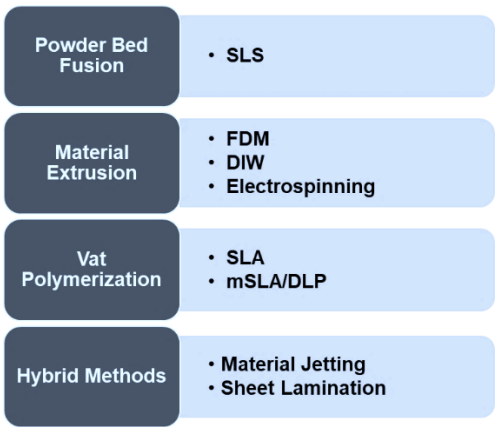


Fig. 2.2. AM fabrication method classifications (Adapted with Permission [49]).

2.4.1. Material Extrusion

Parts are created by layer-wise material deposition from droplets or filaments when employing material extrusion techniques [50,51]. In extrusion-based approaches, the material is subjected to pressure and expelled using either air pressure or mechanical displacement by a piston. This methodology can be divided into two main forms: fused deposition modelling (FDM) and direct ink writing (DIW) (Fig. 2.3), and the subsequent sections provide further details on these techniques. When compared to other manufacturing methods, extrusion printing has some drawbacks. Components produced through material extrusion additive manufacturing (AM) often exhibit subpar surface finish [52]. The overlapping of deposited filament in material extrusion AM can lead to the formation of voids in the fabricated parts. These defects can vary depending on the infill structure within the fabricated component, resulting in significant variations in the mechanical properties of the printed parts. Additional factors that might affect the inclusion of defects include print resolution (extruded filament size), printing speed, bed and nozzle temperature, and cooling rate [50,52]. The advantage of material extrusion AM is that it gives you the freedom to have control over the microstructure and mechanical properties by adjusting the filament deposition and its internal structure. The majority of thermoplastics and their composites are fabricated with the method known as fused deposition modelling (FDM). To print each sliced layer, a filament is heated to a molten state and extruded into a thin filament [50,51]. The filament is then placed in a programmed pattern in the XY plane on a flat print bed. During printing, molten thermoplastic filaments fuse with nearby fibres, and concurrent cooling hardens them so they maintain their form [50,51]. The primary benefits of this AM technique over alternatives are its

lower cost and widespread adoption [53]. FDM printing is most frequently used to create composites and copolymers of commercial thermoplastic biopolymers like PLA. However, thermoset biopolymers and their composites cannot be processed using this technique.

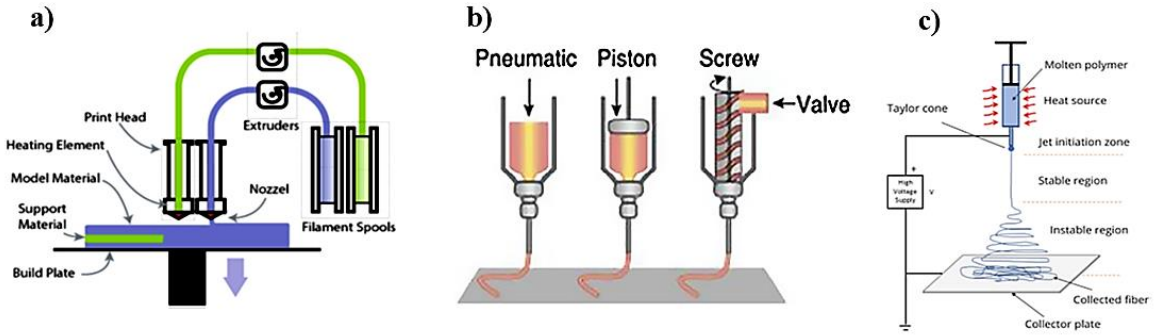


Fig. 2.3. Methods for extruding materials for 3D printing include a) the FDM printing technique for thermoplastic filaments and b) the DIW printing technique for viscous, curable resins. (c) Material is extruded between dielectric charges using the electrospinning technique (Adapted with Permission [49]).

The Direct Ink Writing (DIW) method utilizes thermoset biopolymers and their composites, which are in the form of viscous paste-like inks extruded through the needle/nozzle in a layer-by-layer scheme to create complex 3D multi-scale structures with design-specific features [20]. These layers are then polymerized or cured simultaneously using UV light, resulting in the formation of solid structures [50,51,54]. The versatility of DIW in processing various biopolymers and their composites, without requiring specific process control, has led researchers to explore its potential applications in tissue regeneration, biofabrication, 3D bioprinting to name a few. Moreover, another important advantage of DIW is that the mechanical properties of the material can also be enhanced during the extrusion process.

2.4.2. Vat Polymerization

Vat polymerization AM techniques create a component by selectively curing layers of photocurable polymers (Fig. 2.4). Stereolithography (SLA) is the name given to it most frequently. The majority of the monomers, oligomers, and photoinitiators found in photocurable resins are based on methacrylates and acrylates [55]. The photoinitiator catalyzes a free-radical polymerization reaction, generating chain formation by crosslinking the monomers and oligomers upon exposure to specified wavelengths of light. The most common wavelength used in SLA is in the ultraviolet range, typically around 355 nm. In addition to UV light, some SLA systems utilize

visible light wavelengths, typically in the range of 405 nm or 450 nm. Through photopolymerization, the crosslinking converts the exposed resin into a solid [51,55]. The 3D shape is created by sequentially exposing the ink to UV light and curing them in a pattern of sliced layers [50,51]. After a layer has been cured, the print platform is raised slightly, allowing for a new layer of liquid resin to flow over the cured layer. The process is repeated, layer by layer, with the platform moving up and down inside the vat, each time exposing the new layer to the curing light. This layer-by-layer approach continues until the entire object is printed [50,51]. With a minimum layer thickness of 10 μm, SLA can create parts of excellent quality and more precise geometries compared to other techniques [56]. For objects with overhangs or complex geometries, support structures are often necessary to provide stability during printing. These supports are also printed layer by layer and can be removed or dissolved after the printing process is complete. Once the object is fully printed, it is removed from the resin vat. The printed part may require post-processing steps such as cleaning to remove excess resin, curing under UV light to complete the polymerization process, and potentially surface finishing (e.g., sanding or polishing) for desired aesthetics. SLA components exhibit mechanical characteristics that are almost isotropic [52]. This technology is divided into three categories according to how the light is delivered: laser SLA, digital light projection SLA (DLP-SLA), and masked SLA (mSLA).

Laser SLA employs a conventional technique of vat polymerization, utilizing a UV laser as the sole light source for curing each layer. UV light projection is controlled by two motor-driven mirrors to scan the 2D layer pattern on the vat bed. In *DLP-SLA*, a projector is employed to project a single UV light image of a layer onto the vat bed. The quality and precision of the printed object rely on the resolution of the projector and optical components, as the curing process is carried out based on the pixelized projected image [49]. *mSLA* utilizes an LED array as the light source, along with an LCD photomask. The LCD photomask selectively deactivates individual pixels, allowing the LED light to pass through and form a 2D pattern. The accuracy and resolution of the projected image are determined by the size of the deactivated pixels on the LCD photomask.

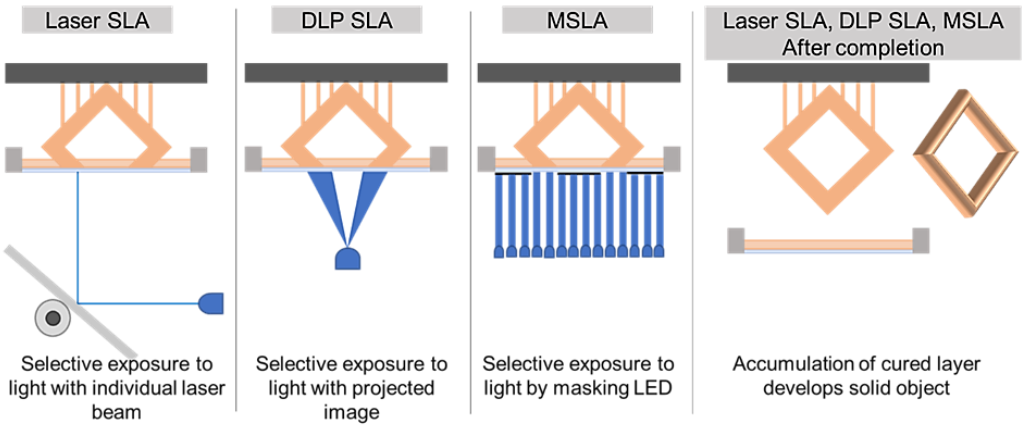


Fig. 2.4. Laser SLA, DLP-SLA, and mSLA process differentiation (Adapted with Permission [49]).

This method involves using low-viscosity inks placed in a resin tank. The build plate moves down to a level that matches the intended layer height, creating space, and then UV light is directed onto precise coordinates through a transparent film made of fluorinated ethylene propylene (FEP). This process solidifies each layer. Once a layer is printed, the build plate rises, breaking the surface tension between the cured layer and the FEP sheet. This allows new ink to fill the gap before forming the next layer [49]. Using this approach, it is possible to fabricate objects with intricate geometry and high resolution [57].



Fig. 2.5. Example of three-dimensional printed nanocomposite bone models using masked stereolithography 3D Printing technique printed in WCBS lab (Adapted with Permission [57]).

2.5. Types of Nanocomposite Inks for three-dimensional printing

Most particulate composites are comprised of two phases: the matrix phase and the reinforcement phase. The primary role of the reinforcement phase is to carry applied loads, and it is the main contributor to composite strength and stiffness [58]. Multiphase materials with at least one phase that is at the nanoscale are considered nanocomposites. The classification of nanocomposites is based on the materials they contain as matrix and inclusion components.

Polymer nanocomposite, which involves the dispersion of nanoparticles within an organic polymer (thermoplastic/thermosets) matrix, is most well-known in the field of 3D printing of synthetic bone materials. They have more adaptability in designing specific properties because there is better control of interactions between nanoparticles and polymers in these composites [59]. In these materials, the inorganic ceramic phase brings strength and stiffness, and the toughness and ductility come from the polymer matrix. The biopolymer utilized can fall into either the category of thermoplastic or thermoset polymers. With the inclusion of a curing agent (activated by photo, chemical, or heat), functionalized bio-derived monomers or prepolymers can undergo polymerization, resulting in the formation of thermoset matrices. The high level of crosslinking in thermoset biopolymers prevents them from being melted or dissolved for recycling purposes. In contrast, thermoplastic polymers can be melted above their melting temperature, enabling extrusion or injection molding, and they are generally recyclable. Lack of functional sites for interfacial or interphase bonding with reinforcing fillers may be the main drawback of thermoplastic biopolymers; however, this issue can be fixed by adding required functional groups to the polymer chains or on the nanoparticles [60]. To create thermoset biopolymers, bio-derived polymers (like cellulose, chitin, etc.) or monomers (sugar alcohols, vegetable oils, etc.) can be functionalized with vinyl groups (i.e., acrylated or methacrylated) to allow covalent cross-linking (curing) [6,61–64]. This makes it possible to print these materials using AM. Thermoset and thermoplastic biopolymers used in bone grafts and in developing bone graft composites are either synthetic or naturally derived biopolymers. The most popular synthetic biopolymers include poly (glycolic acid) (PGA), poly (lactic acid) (PLA), poly (lactic-co-glycolic acid) (PLGA), poly (caprolactone) (PCL), poly (propylene fumarate) (PPF), and poly (ethylene glycol) (PEG). Natural biopolymers could be derived from plants or animals. Some of the most common natural biopolymers are collagen, silk, fibrin, hyaluronic acid, chitosan, and alginate [65–68]. The nanoparticles used in 3D printing biopolymer nanocomposites for bone reconstruction technologies can be metallic, ceramic, or polymeric. Ceramics and metal nanoparticles are, respectively, the most commonly used in the fabrication of nanocomposites for bone healing.

2.5.1. Metal-embedded Polymer Nanocomposites

Due to their antibacterial properties, metals, including silver, gold, iron, and copper, are frequently employed in nanocomposites for bone tissue engineering. By forming bonds with the

electronegative phospholipid bilayers of the bacterial cell wall, electropositive metal nanoparticles can limit bacterial development and eventually force the bacterium into death [69,70]. Adding metal nanoparticles to nanocomposites at low concentrations (ranging from 0.1% to 4%) is a viable method to hinder infections and curb bacterial growth within living organisms [71]. The utilization of such minimal concentrations of metal ions is advantageous due to their ability to decrease metal erosion and toxicity risks. There are various approaches to 3D printing metal-embedded nanocomposites. In the case of the FDM technique, it is possible to combine thermoplastic polymers with metal nanoparticles, resulting in the fabrication of nanocomposite filaments through melt blending or solvent-casting processes [72]. By employing mechanical mixers, metal nanoparticles can be blended with solid thermoplastic polymer powder. Subsequently, the resulting mixture can be 3D printed using the SLS (Selective Laser Sintering) technique [73]. Additionally, thermosetting nanocomposites containing antibacterial metal nanoparticles have been successfully 3D printed using methods such as DIW (Direct Ink Writing), SLA (Stereolithography), DLP (Digital Light Processing), or mSLA (Masked-Stereolithography). In these methods, the nanoparticles are initially dispersed into a monomer or prepolymer solution using a homogenizer to create nanocomposite inks. These inks are then deposited layer-by-layer through the process of photopolymerization. Metal nanoparticles can be readily integrated into nanocomposite inks and efficiently 3D printed into customized shapes. Nevertheless, additional research is essential before advancing to clinical trials or commercializing these metal/polymer nanocomposites. The evaluation of their effectiveness has primarily relied on in vitro assessments, overlooking significant factors like inflammation. Furthermore, the long-term effects of metal nanoparticles on the human body remain uncertain [74]. In order to address these difficulties within living organisms, it is necessary to achieve a controlled release of these nanoparticles [75]. Furthermore, incorporating metal nanoparticles into 3D printed thermoplastics often entails a complex, multi-stage procedure. For instance, it involves the synthesis of nanoparticles, their homogeneous dispersion into the polymer matrix, and, ultimately, the 3D printing process. This not only raises the overall manufacturing cost but also poses potential risks to the quality of the 3D print, including the formation of filler defects, inadequate interphase adhesion, particle agglomeration, and uneven distribution. In order to address these difficulties within living organisms, it is necessary to achieve a controlled release of these nanoparticles [75]. Furthermore, incorporating metal nanoparticles into 3D printed thermoplastics often entails a complex, multi-

stage procedure. For instance, it involves the synthesis of nanoparticles, their homogeneous dispersion into the polymer matrix, and, ultimately, the 3D printing process. This not only raises the overall manufacturing cost but also poses potential risks to the quality of the 3D print, including the formation of filler defects, inadequate interphase adhesion, particle agglomeration, and uneven distribution.

2.5.2. Ceramic-embedded Polymer Nanocomposites

Various nanoscale ceramic particles, including silica (SiO2), bioactive glass (BG), hydroxyapatite (HA), zirconia (ZrO2), tricalcium phosphate, and alumina (Al2O3), have been incorporated into polymer matrices to create nanocomposite inks for bone applicaitons. These ceramic-based nanocomposites have demonstrated improved mechanical strength and bioactivity. It is worth noting that natural bone itself is a nanocomposite primarily composed of HA. Researchers presented [76] a biomimetic approach for cross-linking nano-HAp with a PLA-co-PEG polymer network. It was found that the inclusion of glutamic acid (Glu), a negatively charged peptide, as a cross-linker led to an increased shear modulus. Interestingly, when micro-HAp was used instead of nano-HAp, no significant difference in the mechanical properties was observed with or without the Glu cross-linker. This study provides further evidence that the size of the added particles plays a significant role in enhancing mechanical properties. In a similar investigation [77], PLLA/nano-HAp nanocomposites were studied. The results showed that these nanocomposites exhibited higher mechanical properties compared to their micro-composite counterparts. Additionally, the incorporation of nano-HAp improved protein adhesion. The nanocomposites demonstrated approximately a twofold increase in compressive modulus when 50 wt% of nano-HAp was added to pure PLLA. The integration of well-dispersed ceramic nanoparticles within biopolymer matrices, coupled with a hierarchical microstructure, holds significant promise for bone tissue engineering applications. Nano-hydroxyapatite (nHA) possesses physical and chemical properties that closely resemble those of natural bone minerals. Crystalline HA is a calcium phosphate with the slowest degradation rate and good stability in the body compared to the other calcium phosphate phases because of having the lowest dissolution rate [78]. Another key feature of HA is its biocompatibility. These characteristics make HA a good candidate for use in bone mimicking nanocomposites. The incorporation of HA with the polymer matrix, i.e. nanoparticle dispersion as well their favourable adhesion to the polymer matrix, is the main aspect that affects the mechanical

properties of such composite materials. Another feature of HA which makes it a proper selection is its osteoconductivity which interacts with natural tissue without obtaining any inflammation [79,80]. Extensive research has been conducted over the past few decades to evaluate the biocompatibility of nHA in both in vitro and in vivo settings. Due to its high surface-area-to-volume ratio and nanostructure, nHA plays a crucial role in the interaction between cells and materials in vitro [61]. Therefore, embedding nHA in polymer matrices can enhance the chemical, mechanical, and biological attributes of nanocomposites. By acting as both the organic and mineral phases, nano-inks that are 3D printed into strong grafts may mimic genuine bone. When implanted with human mesenchymal stem cells (hMSCs), scaffolds created by FDM printing of nHA-containing polylactide (PLA) nanocomposites showed good adhesion, proliferation, and osteogenesis [81]. The incorporation of nHA into SLS-printed poly(lactic-co-glycolic acid) (PLGA)-nHA nanocomposites at increasing weight percentages (from 0 to 20 wt%) resulted in improved compressive modulus and strength [81]. In addition, polyester urea [82] and polycaprolactone [83] were combined with nHA and 3D printed to create scaffolds for bone tissue engineering. Ceramic-based nanocomposites have been utilized as bioinks for 3D bioprinting applications in bone regeneration. For instance, hMSC cultures were mixed with polyethylene glycol dimethacrylate (PEGDMA), nHA, and bioactive glass (BG) and then printed into 3D constructs, exhibiting high cell viability (>85%), collagen production, alkaline phosphatase activity, and increased compressive modulus [63]. This research also demonstrated that nHA outperformed BG in promoting hMSC-mediated osteogenesis within bioprinted bone constructs. The combination of nHA with acrylated epoxidized soybean oil and polyethylene glycol diacrylate resulted in improved mechanical properties when using extrusion-based Direct Ink Writing (DIW) [20]. These enhancements can be attributed to the reduced presence of defects and the promotion of crystallinity within the polymer matrix, facilitated by extrusion through small gauge needles. Scaffolds and grafts made from these nanocomposites, printed using DIW and masked stereolithography (mSLA) techniques respectively, exhibited exceptional characteristics such as strong cell adhesion, proliferation, and osteogenic differentiation [63,84]. Additionally, the integration of nHA into a gelatin-methacrylate (GelMA) and triethyleneglycol dimethacrylate system not only improved printability but also demonstrated favourable interactions between cells and the biomaterial, making it suitable for bone repair applications [85,86]. The addition of ceramic nanoparticles has beneficial impacts on the mechanical properties of nanocomposites,

specifically in terms of fracture strength and hardness. By refining the microstructure, the size of flaws is reduced, leading to improved strength and enhanced reliability of structural composite ceramics.

Although polymer nanocomposites are heterogeneous materials like other particulate composites, they usually have a more complicated structure, which can increase the complexity of predicting their mechanical properties. The behaviour of the nanocomposite polymers can be affected by various factors, including the properties and size of the particles, particle concentration and dispersion, phase interfacial quality and polymer matrix crystallinity. For example, the particles can aggregate and not be uniformly dispersed in the matrix, and the orientation of particles may be random and/or aligned. Also, due to the large particle/matrix interfacial area, the interfacial interactions between phases may play a more important role compared to other particulate composites [87]. The design of mechanically competent 3D printable nanocomposite inks requires careful consideration of multiple factors, which necessitate comprehensive study and analysis. These considerations play a crucial role in ensuring the desired mechanical properties and performance of the printed nanocomposite structures. Firstly, the selection and dispersion of nanoparticles within the ink formulation are critical. It is important to choose nanoparticles with suitable properties that can enhance the mechanical strength, stiffness, and toughness of the printed structures. Achieving a homogeneous dispersion of nanoparticles within the ink is essential to ensure consistent mechanical properties and biocompatibility throughout the printed object. Secondly, the choice of matrix material is crucial. The matrix should possess properties such as appropriate viscosity, adhesion, biodegradiblity, mechanical properties and compatibility with the nanoparticles to facilitate effective printing and achieve desired mechanical performance. The matrix material should also have good mechanical properties to complement the reinforcement provided by the nanoparticles. Furthermore, the interaction and interfacial bonding between the nanoparticles and matrix should be considered. This includes suitable surface functionalization of nanoparticles to promote strong bonding with the matrix and prevent particle agglomeration. Effective interfacial bonding is crucial for load transfer and to ensure the integrity and mechanical stability of the printed nanocomposite. Additionally, the printing process parameters need to be optimized to achieve the desired mechanical propertiesand. Factors such as printing speed, shear stress during extrusion, temperature, and layer thickness can significantly influence the final mechanical performance of the printed structure. Comprehensive study and experimentation are

necessary to determine the optimal printing parameters for achieving mechanically competent nanocomposite structures.

2.6. Mechanically Competent 3D Printable Nanocomposite Ink Design, and Characterization

2.6.1. Rheology

Ink engineering is a fundamental area of research within additive manufacturing (AM). Understanding the rheology of 3D printable nanocomposite inks is crucial because it directly impacts the ability to print, the resulting mechanical properties, and the overall performance of the printed parts [88–90]. The ink's rheological properties can be influenced by various factors, including the concentration and type of nanoparticles, polymer matrix viscosity, and printing conditions such as temperature, pressure, and applied shear stress or shear strain rate. In order to ensure successful printing, the 3D printable nanocomposite ink needs to have specific rheological properties compatible with the chosen printing technique. Specifically, for direct ink writing (DIW), the ink should possess appropriate viscosity to flow easily through the printing nozzle while retaining enough yield strength to hold its shape once printed. It must be such that it can be extruded into filaments and maintain its shape until it is cured. Additionally, the ink should have adequate yield stress to prevent it from collapsing or sagging during the printing process. The ideal ink for DIW is a Bingham plastic fluid, which is extrudable with moderate stress and low viscosity, but also possesses some yield shear strength to hold its shape before curing [57]. This can be achieved through the addition of interfacial interactions among the phases or deflocculant in the particle suspension [91]. For SLA, DLP, and mSLA-based printing techniques, it is crucial that the ink viscosity is kept below 5 Pa s to prevent the formation of voids or defects during the rapid recoating of each new ink layer and allow for up-down movement of the print bed [92]. This viscosity requirement limits the amount of nanoparticles that can be added to the nanocomposite ink or necessitates additional dilution of the resin for successful print [84].

Rheometry is the technique used to characterize the rheological properties of the 3D printable nanocomposite ink. This method measures the flow and deformation behavior of the ink under various conditions [93]. Understanding the rheology of the ink aids in optimizing the printing process and ideally, designing 3D printed structures with superior properties. There are two fundamental forms of flow: extensional flow and shear flow. Fluid components go past one another

in shear flow whereas they move away from or towards one another in extensional flow. Shear flow is the most prevalent flow behaviour and can be measured on a rotating disc, capillary and cone and plate rheometer or viscometers.

2.6.2. Shear Flow and Mechanics of Extrusion

Shear flow can be expressed as fluid layers sliding on top of one another, each layer moving faster than the layer beneath it [94]. All materials flow when given enough time. The distinguishing feature of polymeric materials is that their processing times for extrusion are usually in the same order as their time constants for flow. Viscosity, which represents the resistance to shearing of material to flow [95], is the most important flow property. Referring to Fig. 2.6, the viscosity is defined as the ratio of the imposed shear stress (force F, applied tangentially and divided by the area A) and the shear rate (velocity V, divided by the gap h):

$$\eta = \frac{Shear\ Stress}{Shear\ rate} = \frac{F/A}{V/h} = \frac{\tau}{\dot{\gamma}} \tag{2.1}$$

Where τ and $\dot{\gamma}$ are conventionally used to designate the shear stress and shear rate, respectively. To measure shear viscosity with a single head (stress-regulated) rotating rheometer and parallel plate measurement equipment, the sample is loaded between the plates at a given gap (h), as illustrated in Fig. 2.6 [94].

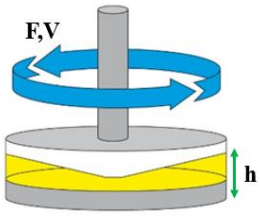


Fig. 2.6. Illustration showing a sample loaded between two plates, the cone rotates while the lower plate is stationary (Adapted with permission [94]).

Rheometers with a single head have the ability to function in either a controlled stress mode or a controlled rate mode. This implies that it is possible to either apply a torque and measure the rotational speed or apply a rotational speed and measure the torque necessary to sustain that speed. When operating in controlled stress mode, a rheometer generates torque via a motor, which is then transformed into a force (F) acting over the plate's surface area (A), leading to the development of shear stress (F/A). If a liquid-like sample is subjected to shear stress, it will flow with a shear rate

determined by its viscosity. If the measurement gap (h) is accurately known, the shear rate (V/h) can be determined from the measured angular velocity (ω) of the upper plate, which is determined by high-precision position sensors, and its radius (r) since V = r ω. Different measuring systems, such as cone-plate and concentric cylinders, are frequently employed to measure viscosity, with cone-plate being preferred since the shear rate is consistent across the sample [94].

Newtonian materials respond linearly to shear rate with no change in viscosity. Non-Newtonian materials exhibit viscosity changes in response to shear rate changes. Shear thinning or pseudoplastic flow is a behaviour in which fluid viscosity reduces with increasing shear [94]. Fluids that exhibit significant shear-thinning properties may also display yield stress, whereby the viscosity becomes infinite and similar to that of a solid material when exposed to a specific critical stress level. This phenomenon is referred to as plastic flow and is identified by a viscosity increase as the shear rate decreases without any visible plateau. Some experts prefer the term "apparent yield stress" because some materials that seem to exhibit yield stress behavior over a limited range of shear rates may exhibit a viscosity plateau at extremely low shear rates [94]. Fig. 2.7 demonstrates how various microstructures behave under the application of shear.

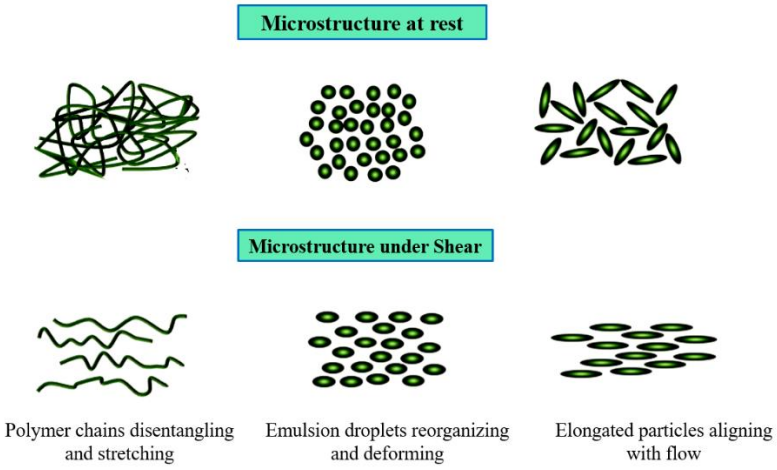


Fig. 2.7. Illustration of the potential reactions of various microstructures to the application of shear [93].

A shear rate can only be created after the shear yield strength has been surpassed for fluids with yield stresses. The shear stress vs shear rate curves for these fluids will intercept the stress axis at a non-zero value. The term "Bingham plastic" refers to a material that exhibits a yield strength which follows the Bingham model:

$$\sigma = \sigma_y + \eta_B \dot{\gamma}$$

Where σ_y denotes the yield stress and η_B denotes the Bingham viscosity, which is represented as the slope of shear stress vs shear rate in the Newtonian zone, post yield [94].

The shear rate changes along the central axis varies nonlinearly from zero to a maximum in the wall where as the shear stress along the central axis changes linearly from zero to a maximum value along the wall. The velocity has a quasi-parabolic profile with a maximum at the plane of symmetry and zero at the wall (Fig. 2. 8). [95].

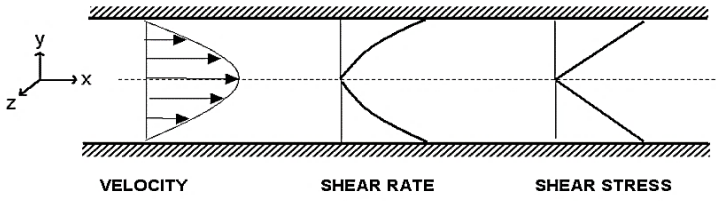


Fig. 2.8. Velocity, shear rate and shear stress profiles for flow through a round tube [95].

In capillary viscometers, the shear stress is measured through the pressure applied by a piston.

$$\tau = \frac{\Delta p r}{2l} \tag{2.2}$$

where Δp is a pressure drop, l is length, and r is the radius of capillary (Fig. 2.9).

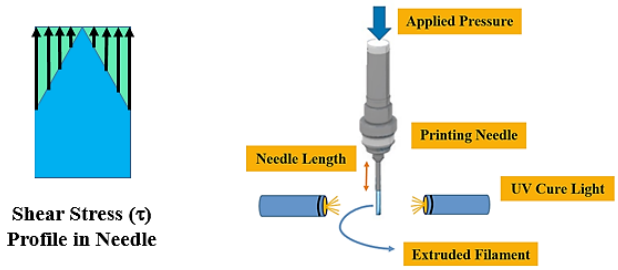


Fig. 2.9. Shear stress profile and measurement in a printing needle.

According to the literature, extruding short-fiber polymer composites through a needle can apply shear force to align polymer chains and fibers, resulting in reduced defect density [32,96–99]. Particle alignment in the flow direction can be encouraged by DIW, which is similar to other extrusion methods [100]. In order to leverage the shear for alignment of their nanofibers during the 3D printing of their nanocomposites, Yunus et al. integrated linear oscillatory actuation mechanisms with SLA devices [101]. According to Narimissa et al. their polylactide-nanographite platelets biopolymer composites' shear-thing behaviour was enhanced by the shear-induced alignment of nanographene platelets [102]. Other techniques rather than shear extrusion have been

investigated in the literature to control fiber alignments to improve the mechanical properties. Magnetic [103,104], electric [105], and acoustic fields [106] are some of the other approaches used to control the fillers' directions in the resin (Fig. 2.10).

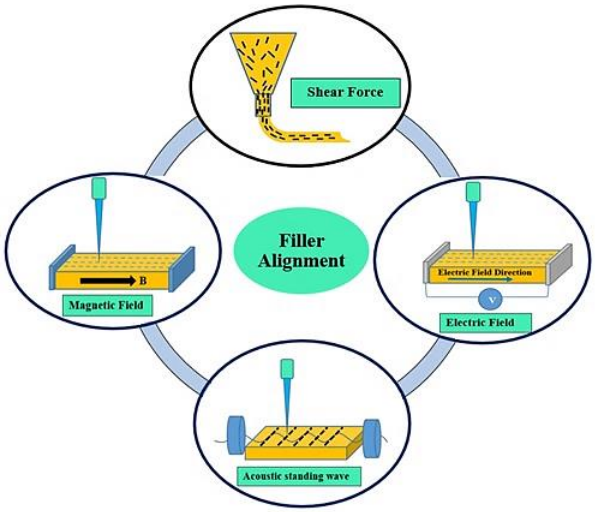


Fig. 2.10. The different filler alignment techniques used in AM biopolymer composites. Using a shear-induced alignment mechanism and electric, acoustic, and magnetic fields to drive the fillers.

Studies have shown that shear stresses leading to alignment are most concentrated near the nozzle wall [30]. Lewicki et al. [107] observed that the fiber phase in their carbon fiber (CF)-loaded ink began as randomly dispersed fibers. However, after undergoing microextrusion through a DIW print head, the fibers became aligned. This finding was also noted by Lewis and Tekinalp [108,109] (Fig. 2.11). The aspect ratio of fibers is one of the crucial factor in inducing shear alignment. However, most of the literature focuses on microfibers, while only two studies [101],[102] have explored the impact of shear-induced alignment in nanocomposites. Furthermore, there is a lack of research investigating how increased shear during extrusion affects nanoparticle and polymer chain alignment in a thermoset biopolymer matrix.

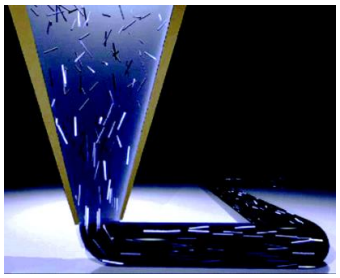


Fig. 2.11. Schematics presenting the anisotropic particles' alignment due to shear at the dispensing nozzle (Adapted with Permission [30]).

2.6.3. Biopolymer Crystallinity

It is uncommon for polymers to exhibit complete crystallinity due to the inability to align all polymer chains in all areas [110]. As a result, the structured sections are bordered by areas of amorphousness (Fig. 2.12).

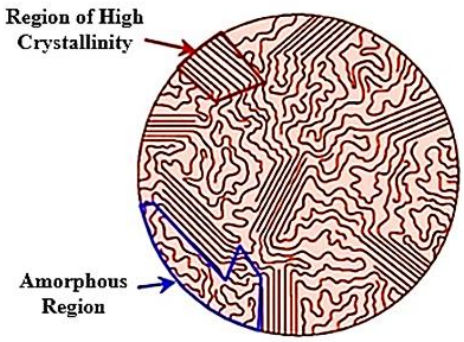


Fig. 2.12. Semi-crystalline molecular structure for a thermoplastic polymer (Modified from [111]).

The degree of crystallinity has an impact on various properties of polymers, including their optical, mechanical, thermal, and chemical properties. Polymers with higher crystallinity are stronger and tougher due to the increased presence of intermolecular bonding in the crystalline regions [49]. The degree of crystallinity in a nanocomposite system is influenced by various factors such as the intrinsic properties of the nanofillers, the matrix, and the dispersion state of the fillers. The intrinsic properties of the nanofillers and the matrix, such as their chemical composition, molecular weight and the interactions between the two can strongly influence the degree of crystallinity in a nanocomposite [112]. The composition of a nanocomposite can be modified to control the degree of crystallinity. For example, the addition of certain types of nanofillers, such as clay nanoparticles, can increase the degree of crystallinity in a polymer matrix. Alternatively, modifying the matrix composition, such as by changing the molecular weight or introducing comonomers, can also impact the degree of crystallinity. Finally, the fabrication technique used to produce a nanocomposite can also impact its degree of crystallinity. For example, using a technique like DIW (direct ink writing) can improve the degree of crystallinity by reducing the presence of defects and promoting a more ordered structure within the matrix [20]. This can ultimately result in improved mechanical properties, such as increased strength. The extrusion of short-fiber polymer composites through a needle can align the polymer chains and fibers, as well as reduce defects in the material [32,96,97]. Extrusion-based 3D printing has been shown to have an impact on the microstructural

characteristics of thermoplastic polymer composites and polymer matrix crystallinity in several studies [113–115] but further research is needed to determine how extrusion impacts the micromechanical characteristics of thermoset polymer composites. Achieving crystallinity in thermosets can be challenging due to their highly crosslinked structure, and crystallization may only occur in confined regions such as nanophase domains. Techniques such as extrusion and nanoconfinement may promote crystallization and improve the properties of thermoset composites [116,117].

2.6.4. Cure depth

The cure depth analysis in 3D printing is a critical step in the production of high-quality, functional parts with desirable mechanical and physical properties. In photopolymerization-based AM processes, the layer thickness of cured materials influences the resolution of a 3D printed item [118]. Maximum layer thickness in AM may be calculated using cure depth data as a function of UV dosage. In photopolymerization-based 3D printing processes, achieving a uniform microstructure requires proper curing of each freshly printed layer. To measure the cure-depth relationships, the classic cure-depth equation, also known as Jacob's equation, is used [118].

$$Z_c = D_p \ln\left(\frac{E}{E_c}\right)$$

where Z_c denotes the cure depth (mm), E_{max} the energy dosage per unit area (J/mm^2), E_c the critical energy dosage (J/mm^2) required to commence the curing process, and D_p the depth of penetration (mm). The constant parameters in this equation, such as the critical UV dose and D_p for particular nanocomposite inks, are computed by fitting the equation to a set of experimental data with a known UV intensity and measuring the cured depth [49].

Delamination is a significant problem with 3D printed scaffolds for bone tissue creation. Inhomogeneous microstructure and blocked pores in printed items will occur if the freshly printed layer does not bind with neighbouring layers and is not fully cured due to a lack of energy necessary to become fully polymerized [57]. To avoid delamination and defects, the layer thickness should be larger than the cure depth value of that specific nanocomposite ink for the incident light dosage [119]. Fourier-Transform Infrared Spectroscopy analysis FTIR is a method which commonly used to evaluate the effectiveness of curing in 3D printed nanocomposite parts

made from UV-cured biopolymers. This technique is employed to investigate the chemical composition of the cured material and to identify any remaining C=C peaks, which may indicate incomplete curing of the biopolymer nanocomposite system [6].

2.6.5. Nanoparticle Dispersion

Two crucial factors in achieving nanocomposites with desirable mechanical properties are the homogeneous dispersion of fillers within polymer matrices and the establishment of strong interfacial adhesion between inorganic fillers and organic polymer matrices [120]. Achieving a homogeneous dispersion of nanoparticles within the polymer matrix at the nanoscale is the primary challenge in preparing 3D printable nanocomposite inks. Dispersion can affect the printability of the ink. It is highly challenging to disperse nanoparticles in polymers as the particles have a high tendency to agglomerate due to their surface chemistry, high surface area, and interparticle forces [121–123]. Furthermore, hydrophilic nanoparticles and hydrophobic polymers are incompatible in nature, resulting in poor interfacial contact which can lead to an increased tendency of agglomerations, decreasing the overall mechanical properties through defects and stress concentrations [124]. The agglomerations result in an uneven distribution of nanoparticles within the polymer matrix, leading to changes in ink rheology properties, making it difficult to achieve accurate deposition of the ink during printing. The uneven distribution of nanoparticles within the polymer matrix also compromises the mechanical properties of the printed object [57]. Agglomerates can create weak points, reducing the overall strength and structural integrity of the nanocomposite material and leading to potential bulk degradation of the nanocomposites as a whole. Furthermore, the presence of agglomerates can lead to localized variations in material properties and stress concentration affecting the performance and functionality of the printed object as well as the mechanical properties and performance of the material. Moreover nanoparticle aggregates are very friable, they are unable to withstand stress and hence have a negative impact on the mechanical properties of polymeric nanocomposites [124]. It has been shown that the tendency of agglomeration in polymer nanocomposites rises as nanoparticle size decreases [125]. Understanding and mitigating the impact of agglomeration is crucial for the development of high-performance nanocomposites. Depending on the nature of the polymers, their rheology, and the volume percentage of nanoparticles, several techniques are used to disperse nanoparticles into polymer matrices [57,126,127]. Mechanical mixing/ball miling [128,129],

magnetic stirring, ultrasonication or a combination of these technologies are commonly utilized. Mechanical mixing employs high-shear homogenization to push the mixture to run through a fast-moving rotor, breaking up the aggregates. Ultrasonic homogenizers generate shear and shock waves to rip apart agglomerates. While these high-energy aided mixing procedures can create nanoscale emulsions as nanocomposite inks, they can also shatter nanoparticles, lowering their aspect ratio [130]. Due to the high inter-nanoparticle interaction, the shear force generated by traditional mixing facilities frequently fails to disperse the nanoparticle agglomerates in either polymer melt or solution [131][124]. All of these shortcomings prevent the efficient use of inorganic nanoparticles in polymer nanocomposites.

nHA crystals as the main mineral component of bone are evenly distributed within collagen fibers. In order to replicate these natural materials [132], it is advantageous to create highly uniform and stable dispersions of nHA as intermediate products. These dispersions should exhibit close interaction with the organic component. Subsequently, they can be shaped into final structures intended to function as bone substitutes [133]. Like other polymer nanocomposites, the nHA particles also have the tendency to agglomerate and depending on the size and aspect ratio of the nanoparticles, this tendency may be affected. Although some promising results have been achieved through the addition and dispersing of nHA particles into biopolymer matrices [20,63,84,133–136], achieving a homogeneous dispersion of nHA particles still remains a significant challenge in the field. Thorough investigation and study are necessary to address this challenge and improve the homogeneity of nHA particle dispersion. Therefore, addressing the issue of agglomeration is crucial in the development of 3D printable nanocomposite inks to ensure uniformity, stability, and optimal performance of the printed objects. By mitigating the agglomeration issue, the mechanical properties, bioactivity, and overall performance of the nanocomposite may be significantly improved, leading to better bone substitute materials and tissue engineering scaffolds. To date, various techniques have been explored to disperse nanoparticles into polymer matrices, which can be broadly categorized into physical dispersing techniques and surface pretreatment approaches. While some studies propose that conventional mixing may lack the sufficient shear force to effectively break up nanoparticles, suggesting a greater focus on surface treatment technologies, it is important to acknowledge that a comprehensive approach combining both techniques is necessary to fully harness the reinforcing effects of nanoparticle fillers, even in situations where achieving uniform dispersion of nanoparticles in polymers may be challenging.

2.6.6. Physical principles of miscibility

The strength of the interface between the filler and polymer plays a critical role in the development of nHA/polymer nanocomposites. Insufficient adhesion between the two phases can lead to premature failure at the interface, resulting in a decrease in mechanical properties, particularly tensile strength [137].

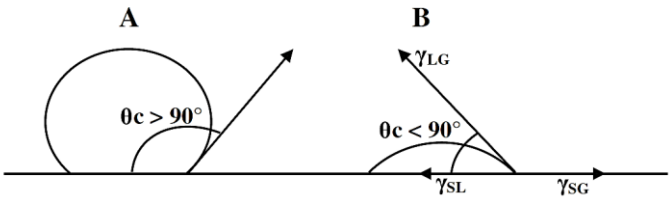


Fig. 2.13. Wetting of different fluids: A) Hydrophobic surface with contact angle >90°, B) Hydrophilic surface with contact angle angle <90°(Adapted with permission [137]).

The process of wetting is crucial for achieving strong bonding and adhesion between the filler surface and the polymer, and this is influenced by the hydrophilicity or polarity of the filler and the presence of polar groups on the polymer. Hydrophilicity is the property of a molecule to have a temporary bonding ability with water through hydrogen bonding. On the other hand, hydrophobic substances primarily interact with themselves and other substances through van der Waals forces, lacking the capacity to readily form hydrogen bonds [138]. The phenomenon of wetting is influenced by the surface energies, or surface tensions, of the interfaces involved, with the objective of minimizing the total energy. The extent of wetting is described by the contact angle, denoted as θc, which represents the angle formed between the liquid-gas interface γ_{LG} and the solid-liquid interface γ_{SL} (as shown in Fig. 2.13). When the contact angle is less than 90 degrees, the liquid will spread over a larger surface area, indicating a wettable surface that is often referred to as hydrophilic [137,139]. Conversely, a contact angle of 90 degrees or greater characterizes a non-wettable surface, commonly known as hydrophobic.

2.6.7. Phase Functionalization

In nanocomposites, the interphase refers to the region between the matrix and the nanoparticles or filler materials and interface referes to boundary or contact region between nanoparticle and the matrix. It plays a crucial role in determining the overall properties and performance of the nanocomposite material. Although various polymer nanocomposites have been studied to obtain

bone substitutes with improved mechanical properties and bioactivities [140–144], when it comes to enhancing the properties of nanocomposites, researchers are still struggling with filler-matrix interface adhesion and filler dispersion in the polymer matrix [145,146]. By employing phase functionalization techniques, it is possible to modify the interphase of nanocomposite materials and enhance bonding between nanoparticles and matrix. This involves introducing additional functional groups to both the polymer matrix and the surfaces of nanoparticles, which can result in enhancing interfacial bonding between the components, leading to improve the dispersion of nanoparticles within the matrix. This approach has the potential to significantly enhance the mechanical properties of the developed nanocomposite materials. By incorporating different chemical groups through functionalization, it is possible to customize the strength, biocompatibility, and biodegradability of biopolymers according to specific requirements and desired properties [147,148]. Depending on the type of functional groups, functionalizing polymer matrices can improve mechanical properties through various mechanisms. This includes promoting better dispersion and bonding with reinforcing materials, introducing crosslinking sites or reactive groups to enhance intermolecular forces, incorporating toughening mechanisms for improved resistance to crack propagation and fracture toughness, and modifying the molecular structure to affect chain mobility and crystallinity, ultimately leading to enhanced mechanical properties in nanocomposites. Plant or vegetable oil-derived biopolymers are preferable to animal-derived natural polymers because of their greater availability and potential to reduce carbon emissions [149–151]. They have demonstrated remarkable promise for the production of a wide range of polymers, including polyesters, polyolefins, and polyurethanes [152,153]. For example, acrylated epoxidized soybean oil (AESO) is created by first adding epoxides to the unsaturated triglyceride chains of soybean oil and then replacing the epoxides with acrylate groups [154–156]. These functionalized acrylates may be polymerized using light-assisted free radical polymerization to produce a variety of multifunctional thermosets [157–159]. The remaining hydroxyl groups (2–3 -OH groups per molecule) from AESO's acrylate functionalization, however, cause less robust cross-linking and increase viscosity through hydrogen bonding. It is beneficial to substitute these -OH groups with additional acrylate/methacrylate groups that may be polymerized by comparable procedures in order to increase processing simplicity and degree of crosslinking which may result in enhanced mechanical properties [160]. Furthermore, the strength of polymerized AESO is rather

low, which encourages additional functionalization to increase crosslinking and increase the strength of the resultant thermosets [161].

Surface modification of inorganic nanoparticles has attracted a great deal of attention because the covalent attachment modifier resists desorption from the particle surface [124]. Furthermore, a fine adjustment of interfacial properties in nanocomposites with chemically prepared nanoparticles may be accomplished by inserting modifiers containing reactive groups, which aid in the formation of chemical bonds between the fillers and the matrix polymer. Among the numerous procedures, coupling agent treatment is the most common to implement which may help produce nanocomposites with robust interfacial bonds between polymer matrices and nanoparticles. To increase the adhesion and interface between inorganic fillers and polymer matrices a range of coupling agents such as silane, titanate, and zirconate have been utilized [5,123,124,162–165]. To achieve bone-like properties in nanocomposites, two crucial factors are important. First, there needs to be a strong interfacial adhesion between organic polymers and inorganic hydroxyapatite (HAp). This contributes to enhanced mechanical properties. Second, the uniform dispersion of HAp at the nano-level within the polymer matrix is essential. This not only improves biocompatibility but also facilitates cell adhesion and proliferation due to the increased specific surface area and favorable mechanical properties [133,166,167]. To enhance these properties, various coupling agents and polymers have been employed to modify the surface of HAp nano-crystals, representing ongoing efforts in this field [167–182][135]. Although successful nHA grafting was demonstrated within the studied coupling agents (Fig. 2.14), it should be noted that not all compositions may be suitable for load-bearing applications. Additionally, certain coupling agents may exhibit limited biocompatibility, making them unsuitable for use in bone reconstruction technologies. Furthermore, some of the coupling agents may lack sufficient rheological properties required for 3D printing purposes after nHA grafting.

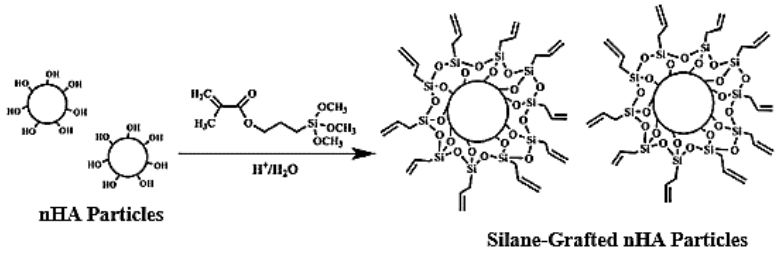


Fig. 2.14. Silane grafting of nHA particles (Adapted with permission [183]). Silanized nanohydroxyapatite (Si-nHA) has been shown to improve bioactivity more than nHA [184,185].

Furthermore, the impact of surface functionalization of nHA on the resulting mechanical properties as well as dispersion within the polymer matrix, has received limited attention in the existing literature. This knowledge gap poses a significant challenge in the field of developing nHA-based biopolymer nanocompsoites. Therefore, there is a clear need for further research and development in order to create a nHA polymer nanocomposite system that exhibits improved interfacial properties and enhanced dispersion. Such advancements are crucial for the successful development of a mechanically robust bone-inspired 3D printable nanocomposite system suitable to be used in bone reconstruction technologies.

2.7. Computational Modeling of Nanocomposite Materials

Due to the use of polymer nanocomposites in demanding industrial and consumer applications (such as automotive, electronics, aviation and biomedical fields), a reliable product design depends on the accurate prediction of the deformation and failure of these materials [186]. Conducting experiments at the nanoscale is costly, and a proper design of experiments and determining the correlation between process, microstructure, and property for these materials is challenging for early design purposes. On the other hand, formulating analytical models can be challenging, and solving them can be complex. Furthermore, analytical models have limitations in accurately describing the intricate microstructure of nanocomposites, their nonlinear material behavior, and assessing local failures within these systems and they struggle to capture the complexity of nanocomposite structures [187,188]. Numerical modelling may serve as a valuable tool for investigating the properties of polymer nanocomposites across various length scales. These models offer valuable insights into the mechanical, thermal, electronic, and optical properties of nanocomposites [187–189]. Numerical modeling aids engineers and scientists in optimizing the design and performance of nanocomposites for specific applications, by simulating their behavior under different circumstances. One particular approach to numerical modeling of nanocomposites involves molecular dynamics simulations[190–192]. These simulations employ classical mechanics to simulate the behavior of individual atoms and molecules within a nanocomposite. By simulating the interactions between these particles, molecular dynamics simulations can provide information on the mechanical properties of a nanocomposite, including its strength and elasticity [187,191,193]. One drawback of molecular dynamics (MD) simulations of nanocomposites compared is the limitation in scale. MD simulations typically operate at the atomic

or molecular level, providing detailed information about the interactions and behavior of individual particles. However, this level of detail comes at the cost of limited system size, making it challenging to capture larger-scale structural behavior. FEM computational micromechanical modelling of nanocomposites is another simulation approach which can provide an opportunity to broadly observe and investigate the behaviour of these materials and to predict the mechanical properties and failure process for different material systems. Since the local stress/strain fields in the constituent materials can be determined, local failure can also be simulated for multiple loading conditions using computational micromechanics [187]. Nevertheless, micromechanical modelling can be computationally expensive. Computational micromechanics is often used as a design tool to tailor a material system for a specific application, and once the material is designed, the mechanical properties can be verified with experiments. Several components must be considered in computational micromechanics, including effective representative volume elements (RVE), applying an appropriate constitutive model for describing the mechanical behaviour of each constituent, their required material constants and employing appropriate periodic boundary conditions.

Computational micromechanics analysis allows for the accurate depiction of the reinforcement phase size, geometry, and spatial dispersion, which can lead to improved prediction of effective mechanical properties (i.e. homogenization) when compared to analytical models that require several assumptions to be made [194]. Several studies have investigated the micromechanical modeling of different nanocomposite systems. A 3D FE micromechanical model was introduced by Aghdam et al. in order to examine the impact of thermal residual stress, fiber coating, and interface bonding on the transverse behavior of MMC (Metal Matrix Composite) under various loading conditions such as unidirectional, biaxial, and shear loading [195–197]. Wagih et al. [25] utilized a 3D finite element (FE) model to predict the microhardness and the strengthening mechanisms in Al-SiC nanocomposites. Ahmadi et al. [198] conducted an examination of the mechanical properties of a polyethylene matrix reinforced with carbon nanotubes and carbon fibers. They employed a stochastic finite element (FE) method and molecular dynamics (MD) simulations for their analysis. Mirkhalaf and Barthelat developed an RVE-FEM model to evaluate the longitudinal performance of nacre-mimetic composites [199]. Mesfin et al. [200] investigated the elastic properties of carbon nanotube (CNT) reinforced polymer nanocomposites and validated them with experimental work. Malgorzata et al. [187] studied the influence of carbon nanotube

(CNT) arrangements on the elastic properties of CNT-based nanocomposites using the finite-element method (FEM) and representative volume element (RVE) approach. Liu and Chen [201,202] also employed RVE approach to investigate the elastic properties of CNT-reinforced polymer nanocomposites under two loading cases. There are several more studies in the literature which employed micromechanical modeling to study effect of different parameters on the elastic properties of polymer nanocomposites, especially CNT polymer nanocomposites [203–209]. The findings of these investigations demonstrate that the FEM micromechanical modelling is capable of predicting the mechanical properties of nanocomposite systems. While it is crucial to employ micromechanical modeling to predict the elastic properties of polymer nanocomposites as an initial and essential step in their characterization, in order to use these models as a more precise design tool, it is important to consider their nonlinear elastoplastic behavior to comprehend failure, strength, damage initiation and evolution [210]. Bao et al. [211] investigated the role of non-deformed particles in reinforcing ductile matrix materials against the plastic flow was investigated theoretically. To determine how particle size affects plastic behaviour under uniaxial tension in nanocomposites, Qu et al. [212] employed theories of strain-gradient plasticity. Wang and Huang [213] introduced comparative analytical micromechanics models to investigate the elastoplastic behavior of long fibrous composites. Asiri et al. [214] presented a finite element (FE) model to simulate the nanoindentation process on elastoplastic nanocomposites, encompassing loading and unloading phases. Thanh et al. [215] introduced a nonlinear numerical model aimed at capturing the influence of small-scale effects on the geometrically nonlinear behaviors of micro-plates composed of carbon nanotube-reinforced composite materials.

In recent years, there has been a notable increase in attention towards the field of nano-hydroxyapatite (nHA) based polymer nanocomposites, which is actively being researched for its applications in bone reconstruction technologies. While numerous studies have investigated the experimental aspects of the mechanical properties of nHA-based polymer nanocomposites [5,77,160,216,217], there is a noticeable scarcity of research focusing on computational modeling of these material systems [218,219]. Computational models play a crucial role in providing detailed insights into the behavior and properties of these nanocomposites, offering valuable predictions and understanding of their performance. To bridge this gap, there is a pressing requirement for comprehensive FEM micromechanical modelling approaches that can accurately

capture the behavior of nHA-based polymer nanocomposites. Such models would enable researchers to delve deeper into the material's mechanical response, predict its behavior under different loading conditions, and optimize its design for specific applications in bone reconstruction. By developing robust computational models, researchers can conduct virtual experiments, simulate the nanocomposites' response to various external factors, and assess their long-term performance. This detailed micromechanical modelling approach would facilitate a better understanding of the complex interplay between these nanocomposite constituents, the nonlinear behavior of polymer matrix, interface interactions, and elastoplastic mechanical properties.

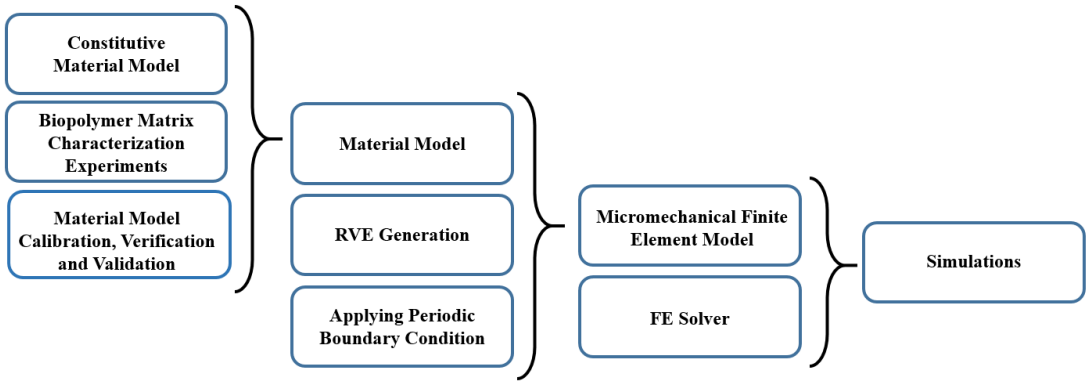


Fig. 2.15. Steps involved in micromechanical FEM modelling of nanocomposite systems.

In commercial finite element (FE) software, material constitutive models and their associated parameters are utilized to simulate and capture the behavior of materials during simulations. To obtain these material constants, various characterization experiments are conducted on the material being studied. The obtained data is then used to calibrate, verify, and validate the constitutive models, ensuring their accuracy in predicting the material's behavior (Fig. 2.15). In computational micromechanics, it is important to define the appropriate volume of the material that will allow for accurate prediction of the effective (macroscopic) response. The volume (V) must be large enough to include a sufficient number of reinforcements and must statistically represent the material microstructure while respecting the randomness of phases, phase volume fraction and size [220]. However, the RVE must be small enough to be considered a material point in an effectively homogeneous continuum for continuum-based analysis [221]. Additionally, practical computational costs must be taken into account, ensuring that the size of the RVE remains feasible for computational simulations [220].

Computational micromechanics can be used to define the effective mechanical properties of the material, where either a homogeneous displacement (strain) or stress is imposed on the surface of the RVE. Several types of boundary conditions can be prescribed on the RVE surface [222]. The underlying assumption is that the averaged stresses/strains over the RVE are equivalent to the related macroscopic values (i.e. the imposed homogeneous stresses/strains). If the RVE is subjected to an imposed macroscopically homogeneous stress or displacement field on its surface, without any body forces, then the volume-averaged stresses, $\{\bar{\sigma}_{ij}\}$, and strains, $\{\bar{\varepsilon}_{ij}\}$, are defined as:

$$\bar{\sigma}_{ij} = \frac{1}{V}\int_V^1 \sigma_{ij} dV, \qquad \bar{\varepsilon}_{ij} = \frac{1}{V}\int_V^1 \varepsilon_{ij} dV \tag{2.3}$$

Where σ_{ij} are the local or micro stresses, and ε_{ij} are the local strain components. The development of an effective numerical tool to predict the properties of nanocomposites based on their complex multi-phase and multiscale structure is still at an early stage [223]. In the context of nanocomposites, developing a realistic RVE is essential for accurate micromechanical modelling of nanocomposites. The RVE requires careful consideration of the microstructural features and should accurately capture the spatial distribution, particles' orientation, size distribution and interactions of the nanoparticles within the matrix. This requires careful consideration of factors such as particle size, shape, volume fraction, and interfacial properties. While creating truly realistic RVEs in nanocomposite modelling is challenging, it is feasible to enhance the realism of RVEs to capture the microstructure studied nanocomspoite system by utilizing experimental data, such as microscopy images or characterization techniques, to capture the material's microstructure. Sophisticated image analysis techniques can help extract relevant information about the distribution and arrangement of nanoparticles within the matrix. In addition to the geometric aspects, incorporating realistic material properties within the RVE is also crucial. This includes accurately representing the mechanical properties of the matrix, nanoparticles, as well as the interfacial properties between the matrix and nanoparticles.

2.7.1. Constitutive Material Model for elastoplastic deformation of Polymer Matrix

For particulate-reinforced polymer composites, computational micromechanical analysis requires an accurate representation of the polymer matrix phase. The mechanical properties of solid

polymers are a consequence of their chemical composition and their structure at the molecular and supermolecular levels [224]. It is demonstrated that the basic plastic deformation mechanisms in polymers occur when polymer chains tend to untangle and reorient [225]. At this stage, the polymer chains start to slide past each other, leading to the formation of permanent molecular rearrangements. In classical plasticity theory, several assumptions have often been included regarding the yield behaviour of different solids. These are: the material is isotropic and homogeneous, yielding is not influenced by the hydrostatic component of the stress state, tensile and compressive yield strengths are equal, and deformation proceeds under constant volume. Although these assumptions are reasonable for ductile metals, they are incorrect for polymers. Each yield criterion corresponds to a specific surface in the principal coordinate. For example, a cylindrical surface corresponds to the Von Mises yield criterion, and a hexagonal prism represents the Tresca criterion, both applicable to materials whose plastic flow is independent of hydrostatic pressure, such as some metals. A hexagonal pyramid is a modified version of the Tresca criterion and represents the Mohr-Coulomb yield criterion.

Polymers have different yield strengths under compression, tension, and shear, and also exhibit pressure sensitivity. There have been several detailed investigations conducted on the influence of hydrostatic pressure on the yield behaviour of polymers [226–232]. In contrast to many crystalline materials where shear deformations are typically unaffected by hydrostatic pressure, the shear stress-strain behavior of most polymers can be influenced by their hydrostatic stress [233] (Fig. 2.16). When subjected to compressive normal stresses, polymer materials generally exhibit increased elastic modulus and yield strength [234]. This pressure-dependent behavior of deformation can be attributed to the reduction of free volume within the polymer, resulting in enhanced resistance to molecular mobility [235].

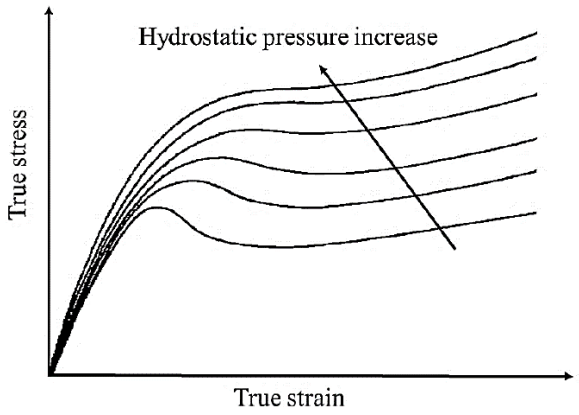


Fig. 2.16. Stress-strain curves in compression at various hydrostatic pressures for a glassy polymer [234].

The Drucker-Prager model is a constitutive model commonly used to describe the elastoplastic behavior of polymers [236–242]. It is particularly applicable to materials that exhibit pressure-dependent plasticity and are subject to compressive loading conditions. The Drucker-Prager model was developed by smoothing the surface described by the Mohr-Coulomb yield criterion and making modifications to the Von Mises yield criterion [243–245].

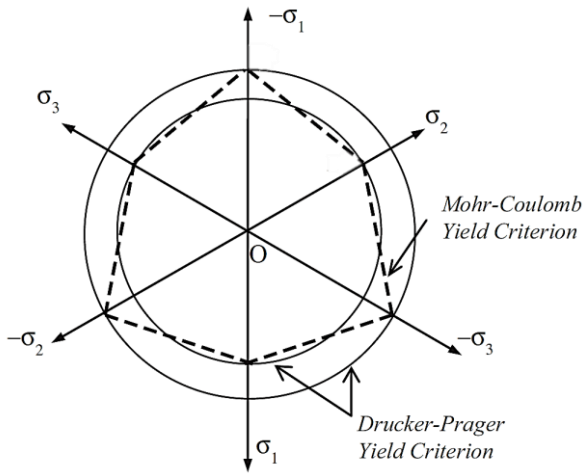


Fig. 2.17. Mohr-Coulomb and Drucker-Prager yield criterion in principal coordinates (Adapted with permission [244]).

This model considers both the dilatational and deviatoric components of stress and can capture phenomena such as plastic yielding, strain hardening, and the influence of hydrostatic pressure on the material's behavior [243].

Von Mises yield criterion does not explicitly consider pressure and assumes that yielding depends solely on the deviatoric stresses. It is most commonly used for materials like metals. The Drucker-Prager model accounts for pressure dependency by including the hydrostatic pressure terms in the yield function, which makes it more complex due to these additional parameters (Fig. 2.18). So, it can model materials with various pressure sensitivities such as polymers and cohesive soils.

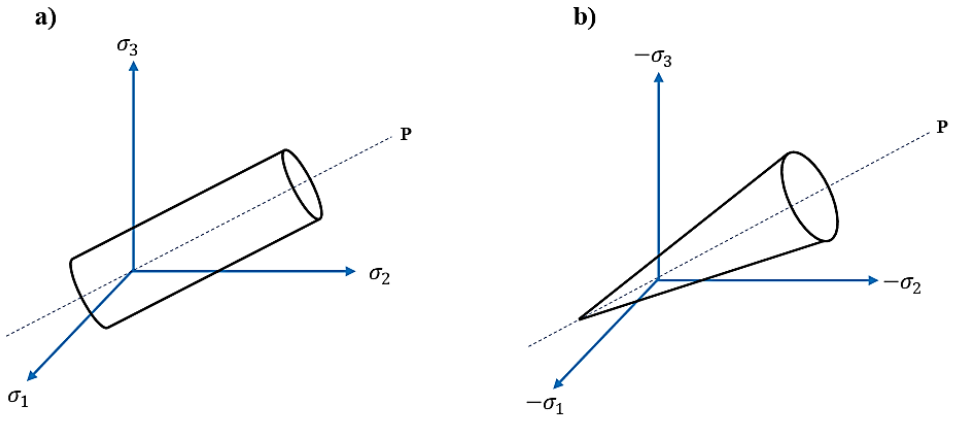


Fig. 2.18. a) The von Mises yield criterion b) The Drucker-Prager yield criterion. σ_1, σ_2, σ_3 denote the principal stresses and $P = (\sigma_1 + \sigma_2 + \sigma_3) / 3$ is the hydrostatic pressure. The von-Mises yield surface is constant while it changes with pressure in the Drucker-Prager model.

The corresponding yield function is defined by:

$$\Phi(\sigma, \sigma_c, \sigma_t) = \sqrt{J_2} + \alpha I_1 - \beta \tag{2.4}$$

Where α and β are material parameters defined as follows:

$$\alpha = \frac{\sigma_{yc} - \sigma_{yt}}{\sqrt{3}(\sigma_{yc} + \sigma_{yt})}$$

$$\beta = \frac{2\sigma_{yc}\sigma_{yt}}{\sqrt{3}(\sigma_{yc} + \sigma_{yt})} \tag{2.5}$$

where σ_c and σ_t are the compressive and tensile yield stresses, respectively, J_2 is the second invariant of the deviatoric stress tensor, and I_1 is the first invariant of the stress tensor (i.e. mean stress). This criterion includes the above-mentioned dependency on hydrostatic pressure and different yield stresses in tension and compression. This scalar function restricts the region in the

stress space where any point inside the surface, $\Phi < 0$, is in the elastic domain and any point on the surface, $\Phi = 0$, corresponds to plastic yielding and the material begins suffering permanent plastic strains the material. The material can also undergo hardening, i.e. the yield stress increases as the plastic strains accumulate. As the hardening variables increase in value, so the yield surface expands. This effect is known as isotropic hardening. In the most general case, the surface can even change its shape or translate in the stress space which in this case is known as kinematic hardening. Another important component in constitutive modelling of plasticity is defining a proper flow rule that can be used to determine the amount of plastic deformation in the material and is used to describe the relationship between the strain increment and deviatoric stress tensor for the plastic behaviour of materials [246].

The Drucker-Prager model can be further modified to account for additional effects, such as strain rate dependency, temperature effects, and different loading conditions [236]. Modifications can be made by introducing additional terms or modifying the parameters in the model equations. To apply the Drucker-Prager model to polymer materials, specific material parameters such as the friction angle (ϕ) and cohesion (c) need to be determined through experimental testing or obtained from existing literature.

2.7.2. Polymer Characterization Experiments

Synthetic polymers consist of long repeating molecules formed through synthesis and organic polymers contain carbon-based molecules [247]. Polymers have some advantages over the other matrixes, e.g they can be manufactured into complex shapes through near-net shaping processing at low costs, they have low density; high strength-to-weight ratio, they are corrosive resistant, they have low electrical and thermal conductivity [247]. On the other hand, they have some disadvantages like low-temperature limits (up to 300° C, but typically < 150° C), susceptibility to moisture degradation, low stiffness, and high thermal expansion coefficient (not desirable for composite processing). Polymers are categorized into three different types: *thermoplastics*, *thermosets*, and *elastomers*. The first two types are most common in composites. The main physical differences between thermosets and thermoplastics are that the thermoplastics can be remelted back into a liquid, whereas thermoset plastics always remain in a permanent solid-state [248]. Table 2.1. summarizes the differences between thermosets and thermoplastics briefly. Thermoset polymer materials which are the focus of the current study, are extensively used in the

fabrication of composite materials and as structural adhesives, making them highly prevalent in various applications [249]. Consequently, the stress-strain behavior of these materials has been extensively documented in the literature.

Table 2.1. Thermosets vs Thermoplastics features

Thermosets	Thermoplastics
• They soften and flow for processing when heated	• Solid materials at RT, but soften or melt when heated which allows for economical shaping of parts
• High temperatures produce a chemical reaction that hardens and permanently sets the material into a solid (i.e., curing)	• Can be subjected to repeated heating and cooling cycles without significant degradation (reversible process)
• If reheated after curing, thermosets decompose and char rather than melt	• Allows for economical shaping of parts
• As a result, they are not re-shapable or recyclable	• Beneficial for reshaping or recycling
• Curing involves an irreversible chemical process that changes the molecular structure of the polymer which forms strong covalent bonds between molecules	• Molecules are held together by weak bonds that soften when exposed to heat and return to their original condition when cooled back down to room temperature

The mechanical properties of thermoset polymers are influenced by several internal factors, such as the chemical structure, curing agent, the polymerization degree, and crosslink density [250–253]. When subjected to quasi-static uniaxial compressive loading, a highly cross-linked epoxy material follows a representative stress-strain curve, exhibiting four distinct deformation stages (Fig 2.19): elastic, initiation of plastic flow, strain-softening, and either strain hardening or re-hardening [254]. In the second stage of deformation (stage II), the transition from elastic to plastic deformation takes place, marked by the onset of plastic flow. Determining the yield point (yield stress) traditionally involves identifying the stress value at which the material's deformation is no longer fully reversible. However, in the case of many polymers, distinguishing between elastic and plastic deformation is often not straightforward [255]. As a convention, the yield point can be defined as the point where the stress no longer increases with increasing strain, commonly referred to as the local stress maximum [256].

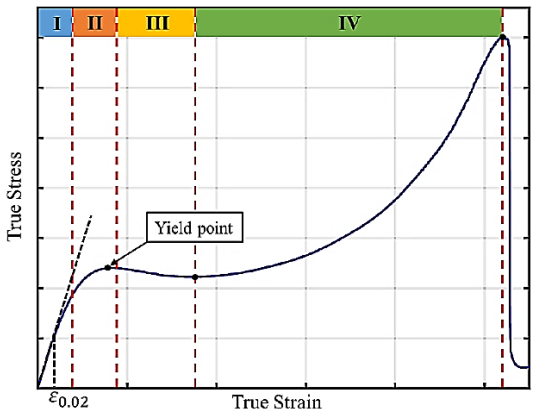


Fig. 2.19. A representative compressive stress-strain curve for glassy polymers [249].

To gain a deeper understanding of how a newly developed polymer system behaves under stress and determine its yield strengths, several mechanical tests are necessary. To define the material parameters for the Drucker-Prager model, it is essential to establish the tensile and compression yield strengths to calibrate the constitutive model for the current studied polymer system. Achieving accurate results in micromechanical simulations relies on *verifying* and *validating* the material models employed [249][247]. Material model *verification* ensures that the implementation of the model aligns correctly with the constitutive equations. This involves virtually testing the material parameters obtained from associated experiments and comparing the finite element (FE) results with the experimental data. By performing single element simulations using a commercial finite element code, the constitutive model parameters can be verified and adjusted to match the measured experimental data [247]. On the other hand, material model *validation* is crucial to ensure that the constitutive model accurately represents the behavior of real-world materials. During this process, the proposed material model parameters are validated by comparing the results of independent experiments conducted on test specimens with those obtained from a computational model that incorporates the calibrated constitutive model.

Chapter 3

Research Objectives and Hypothesis

3.1. Objectives and Hypothesis

The design of bone-inspired nanocomposites for advanced bone reconstruction technologies reveals that it is important to have biocompatibility and bioactivity as well as adequate mechanical properties to bear physiological loads similar to those experienced by cortical bone. Hence, a thorough investigation is required to study all the mentioned features in any material system designed for this purpose. To facilitate the design and production of bone-inspired nanocomposite systems for future use in bone reconstruction technologies, it is necessary to conduct a comprehensive study aimed at further modifying the 3D printable nHA-reinforced AESO-based polymer nanocomposite inks previously developed in the Waterloo Composite Biomaterial Systems Lab. The current thesis focuses on an important aspect of this comprehensive study, which involves enhancing the mechanical properties of the nanocomposite so that it can withstand the physiological loads exerted on the cortical bone following grafting. To achieve this goal, it is necessary to further characterize and modify these new material systems and develop robust design tools for assessing the mechanical performance of these bio-inspired nanocomposites.

Enhancing the mechanical properties of 3D printed bone-inspired nanocomposite grafts can be achieved by addressing various length scales, ranging from the nano to macro scale. Key factors that significantly influence the mechanical performance of these 3d printable nanocomposite grafts include nanoparticle selection, dispersion, matrix material choice, interfacial bonding, and optimization of printing process parameters. These factors operate at the nano-micro scale and play a critical role in the successful fabrication of nanocomposite structures with the desired mechanical properties. In addition, by implementing suitable micromechanical computational modelling, it becomes possible to gain further insights into the mechanisms that can enhance the mechanical properties of these bone-inspired nanocomposites to help engineers in the early design stage of these materials. This research endeavour aims to contribute to the long-term goal of developing a mechanically competent nanocomposite system by pursuing four main objectives.

Objective 1: The primary objective of this research was to conduct a process study aimed at investigating the impact of enhanced shear during extrusion-based 3D printing on the mechanical

properties of a 3D printable bone-inspired nHA-reinforced AESO-based biopolymer nanocomposite and how the morphology of the thermoset biopolymer matrix will change under high shear extrusion. The hypothesis was that higher applied shear stress during extrusion would result in polymer chain alignments and increased crystallinity in the biopolymer matrix, more particle alignment and fewer defects, and thus greater tensile strength.

Objective 2: The second objective of this project was to investigate the impact of augmenting the AESO biopolymer matrix with methacrylate groups, along with heat treatment of nHA particles on mechanical properties. The goal was to examine how these modifications influence the dispersion, ink rheology, and mechanical properties of 3D printed nanocomposite filaments extruded under high shear conditions. Our hypothesis posits that heating nHA would enhance the dispersion of nHA, and the additional functionalization of the biopolymer matrix would result in increased cross-linking, all leading to improved tensile and thermo-mechanical properties of the developed nanocomposite system.

Objective 3: The third objective was to develop a new approach for improving the interfacial bonding and achieving nanoscale dispersion of nHA particles within our nanocomposite system. Our aim was to integrate a novel mechanical dispersion process and an innovative surface functionalization technique to achieve nanoscale dispersion and enhanced interfacial bonding between nanohydroxyapatite (nHA) and the biopolymer matrix which would lead to improved mechanical properties of the nanocomposite system. The decision to use of mSLA 3D printing in the continuation of the current research was made due to the manufacturing defects generated by DIW 3D printing. The volume fraction of nHA was lowered to 5% due to the different mechanism involved with this type of additive manufacturing, requiring low viscosity inks while maintaining the same ink components. It should be emphasized that the nHA functionalization technique developed in this objective can also be used with inks with higher volume fractions.

Objective 4: The fourth objective was focused on developing a computational tool to enable the prediction of the elastoplastic mechanical performance of newly developed bone-inspired 3D printable nano-composite. The micromechanical FE model would enable accurate prediction of the plastic failure response of these nano-composites. The ability to comprehensively and precisely predict the nonlinear response at the sub-micron-scale would depend on an accurate and realistic geometrical representation of the distribution and randomness of the inclusions in the matrix

material and on the definition and implementation of a proper constitutive model for each constituent of the nano-composite. To calibrate the constitutive model for the functionalized-AESO biopolymer matrix, mechanical characterization experiments were required.

3.2. Scope of Work

Initially, a process study was conducted to investigate the effects of applied shear stress during extrusion-based 3D printing on the mechanical properties of the AESO-PEGDA-nHA nanocomposite biomaterial (Task 1.1). The shear stress during extrusion was controlled by changing needles' length and applying pressure. Tensile tests were conducted on different cases to study the effect of applied shear stress ranging from 3.5 kPa-14 kPa on the mechanical properties of extruded nanocomposite filaments (Task 1.2). To interpret the changes in the mechanical properties of the nanocomposite, differential scanning calorimetry (DSC), scanning electron microscopy (SEM) and Polarized Light Microscopy (PLM) images were obtained (Task 1.3).

Two groups of novel ink compositions (mSP30-mSP30h) (functionalized biopolymer matrix with and without nHA heat treatment) were developed for the first time in the WCBS lab by further functionalizing the biopolymer matrix and nanocomposite filaments were extruded with the highest shear condition obtained in the first objective (Task 2.1). Tensile tests and dynamic mechanical analysis were conducted on extruded nanocomposite filaments (Task 2.2). To interpret the mechanical properties, further DSC and TGA characterization along with further SEM image analysis was conducted to investigate the effect of nHA heat treatment and functionalization on the dispersion and morphological properties of the nanocomposites.

Following several trials of methods for surface functionalization of nHA, a new series of inks was prepared by incorporating modified nHA particles with the functionalized AESO as a biopolymer matrix. To refine the raw nHA, centrifugation was performed in multiple steps, followed by further reaction with Barium as the multi-valent cation and functionalization with sulfopropyl methacrylate (Task 3.1). The effects of these modifications on nHA dispersion and nHA-matrix interfacial bonding were investigated through multiple characterization techniques, including EDX, FTIR, TGA, EDS, rheology analysis, and advanced image analysis using TEM (Task 3.2). To assess the influence of nHA dispersion and SPM functionalization on the mechanical properties of the nanocomposite system, dogbone samples were mSLA printed. These samples were

subjected to tensile testing and served as validation data for comparison with computational micromechanical results (Task 3.3).

Realistic representative volume elements (RVE) were developed for precise finite element modelling using commercial Digimat software which facilitated the generation of RVEs capturing the microstructure of the phase-functionalized nanocomposite system such as the shape, size, aspect ratio, random dispersion, size distribution, and nanoscale agglomerations of the nHA particles (Task 4.1). Polymer characterization experiments were conducted, including tensile, compression and shear tests on mSLA-printed functionalized biopolymer dogbone, cylinder and shear butterfly samples (Task 4.2). The Drucker-Prager elastoplastic constitutive model was calibrated, verified and validated for the developed functionalized biopolymer matrix (Task 4.3). The generated RVEs were imported into Digimat-FE, with periodic boundary conditions applied, to perform micromechanical simulations. The initial objective was to validate the elastic properties of the developed RVEs by comparing them with experimental data. Parametric studies were also conducted to explore the influence of nHA dispersion on the orthotropic elastic properties. Subsequently, the elastoplastic Drucker-Prager material model was applied to the generated RVEs, to compare the micromechanical model's predicted elastoplastic behaviour with experimental results (Task 4.4).

Chapter 4

The Effects of Shear Stress on the Micromechanical Properties of 3D Printable Biopolymer Nanocomposites Using a Custom-Designed Extrusion-Based 3D Printer

4.1. Introduction

Various materials are used for bone regeneration, including autografts, allografts, and synthetic bone substitutes. The known issues with the current methods, such as immune rejection, revision surgeries, stress shielding, mechanical failures, and disease transfer, which all lead to poor life quality of the patient during the treatment period, hamper their widespread clinical applicability [13,14,257]. Therefore, the development of alternate effective bone substitutes is imperative. Bone-inspired biopolymer nanocomposite grafts with biocompatiblity and osteoconductive features are new alternatives to traditional bone substitutes, with the potential to overcome some of the aforementioned disadvantages [18,258]. Bone-inspired polymer nanocomposite biomaterials offer several benefits over conventional biomaterials such as metals, ceramics, polymers, and their composites [259–264]. Their nanoparticle reinforcements provide high surface-area-to-volume ratios, which improve mechanical properties and load-bearing features [20,84]. Moreover, nano-scale hydroxyapatite mimics bone minerals and improves biocompatibility [63,84].

It has been discovered that modifying the structure of polymer nanocomposites,opens up new opportunities for bio-inspired material systems. However, there are still obstacles that inhibit control of the nano-scale characteristics of these materials during fabrication. Owing to the limitations in manufacturing nano-scale hierarchical architectures while addressing the biocompatibility of materials, research on the design of bio-inspired nanocomposite biomaterials has received relatively little attention. Choosing an appropriate material composition and manufacturing method will help overcome some of these obstacles and pave the way for emerging bio-inspired nanocomposite biomaterials with superior mechanical properties and biocompatibility [7,136] that can be used in various biomedical applications, including bone reconstruction.

In the fabrication of bone substitutes, various features, such as chemical composition, nano/microstructure, and hierarchical structure, can be inspired by the bone tissue. A broad range of polymers, hydrogels, inclusions, and manufacturing procedures, such as gel casting, freeze casting, hot pressing, and slip casting, have been studied for the design and manufacturing of bio-inspired composite materials, including bone-mimetic composites [44,46,48,96,265–270]. Although some of these fabrication techniques have produced promising results, their main drawback is a lack of control over the microstructure, which prevents them from producing hierarchical and complex structures like those found in natural composites. Moreover, conventional biomaterials have disadvantages in that they either lack sufficient mechanical properties or are unable to assist in the production of new bone (osteoconduction and osteoinduction), making them inadequate for bone repair [271–273].

Additive manufacturing techniques such as 3D printing have recently aided advances in tissue engineering for the regeneration and healing of damaged tissues, including bone tissue, owing to their particular manufacturing features such as the development of precise and patient-specific structures [274]. Direct Ink Writing (DIW), which is an extrusion-based 3D printing technique, can be used to fabricate bone-inspired nanocomposites with the ability to regulate how nanoscale inclusion orientations are arranged and layers of the structure at greater length scales [275]. DIW is an adaptable technique for cost-effective fabrication of customized on-demand products. Although it is not possible to achieve a precise and sophisticated structure of natural biological systems with human-made technologies, the aforementioned features suggest that DIW offers an exciting means for the fabrication of synthetic heterogeneous materials and hierarchal structures with increasing complexity and performance [19–21]. Therefore, developing a material composition in conjunction with an efficient manufacturing technique capable of mimicking the bone structure from the micro-to macroscale is of great interest. Bone is a nanocomposite on the microscale with a cylindrical hierarchal structure on the macro scale, all of which contribute to the superior mechanical properties of bone. Clearly, the arrangement and structure play key roles in enhancing the mechanical properties of bone-inspired nanocomposites, even with keeping the chemical composition of the composite. Using a layer-by-layer procedure, continuous "ink" filaments are extruded via a needle or nozzle using the DIW technology in order to produce complex 3D multiscale structures with design-specific properties [276], [20]. Current additive manufacturing (AM) technologies often do not use a rotating axis, limiting their use in the

manufacture of tubular structures [277]. Few custom-built extrusion-based mandrel-bed 3D printers for printing concentric layered structures using hydrogels or thermoplastic materials have been reported in the literature, with printing structures restricted to two concentric layers [277–282]. A mandrel-bed DIW 3D printer, which deposits nanocomposite filaments in concentric layers, can help produce bone-inspired structures that mimic bone features at different length scales and provide the opportunity to improve mechanical properties at both micro and macro scales. Zhang et. al [283] fabricated microscale fibrous tissue scaffolds on a rotational madrel using melt electro writing (MEW) additive manufacturing method. According to the best of the authors' knowledge, there is no custom-designed 3D printer in the literature that has demonstrated the possibility of printing multilayered hierarchal tubular bone-inspired structures using 3D printable nanocomposite biomaterials with the ability to adjust the shear stress during extrusion along with the flow rate. To begin designing such bone-inspired structures, it is necessary to first understand the microstructure of the extruded nanocomposite biomaterial filaments and their contribution towards enhancing the mechanical properties. A key technical challenge for successful DIW is the composition of inks for optimum rheological behavior [284]. The ink must have sufficient viscosity to permit smooth flow during extrusion, while simultaneously exhibiting shear yield stress and elasticity to prevent deformation and flow of the deposited material after deposition and before solidification or curing.

It has been shown that the application of the DIW approach provides an opportunity to enhance the mechanical properties (especially strength) of various nanocomposite materials as a result of fewer defects and a rise in the degree of crystallinity of the biopolymer matrix. [20]. Moreover, the particulate and polymeric phases' molecular alignment along the fiber/extrusion axis during the extrusion process can lead to improved mechanical properties [21]. Although some studies have demonstrated the effect of extrusion-based 3D printing on the microstructural features of thermoplastic polymer composites [113–115], the extrusion effects on the micromechanical properties of thermoset polymer composites are yet to be studied. Gue et al. first reported the crystallization of epoxy thermosets in a nano-scale confined environment [285]. Later, other studies demonstrated the creation of nanophase crystals in nanostructured thermosets owing to confined crystallization [116,117]. It has been reported that the extrusion of short-fiber polymer composites through a needle can force the shear alignment of polymer chains, as well as align the fibers and reduce the density of defects [32,96,97]. DIW, like any other extrusion process, has a

significant driving force for promoting particle alignment in the flow direction. [100]. The shear stresses causing alignment were more pronounced close to the nozzle wall [30]. Lewicki et al. [107] demonstrated that the fibre phase in their carbon fibre (CF)-loaded ink was formed up of randomly aligned dispersed carbon fibres at the start. They found that upon microextrusion through a DIW print head, alignment of the fiber phase was induced. This effect was also reported by Compton and Lewis [108] and Tekinalp [109]. Mondal et al. [20] produced filaments of acrylated epoxidized soybean oil (AESO)/polyethylene glycol diacrylate (PEGDA)/nano-hydroxyapatite (nHA)-based nanocomposites by using a commercial extrusion-based 3D printer. They demonstrated that by extruding ink through narrower needles, which limits the number of possible defects according to the Griffith effect [286], the mechanical properties such as the strength, modulus, and toughness, of the extruded nanocomposite filaments were improved.

In this study, anAESO- PEGDA based 3D printable nanocomposite ink with good in vitro bone cell compatibility [20,63,84] was extruded using a custom-designed air-pressure-driven extrusion-based 3D printer with a post-extrusion UV curing system. To eliminate the Griffith effect [286] on the mechanical properties of the nanocomposite filaments and to better correlate the extrusion shear effect with the mechanical properties, the diameter of the extrusion needle was kept constant during this study. The system allowed the control and measurement of the pressure drop along the needle during extrusion, thus allowing control of the shear stress in the needle during extrusion. To tailor the influence of extrusion shear on the final mechanical properties of the nanocomposites, single filaments were extruded using a controlled shear stress range of 3.5 kPa to 14 kPa by manipulating the applied pressure and needle length, while keeping the needle diameter constant. It was hypothesized that the increased shear stress during extrusion would enhance the mechanical properties, presumably because of the formation of polymer chain crystallites and/or nanoparticle alignment.

4.2. Materials and Methods

The nanocomposite material studied herein comprised a mixture of room temperature printable AESO, PEGDA (250 MW), and the photoinitiator phenylibis (2, 4, 6-trimethyl benzoyl) phosphine oxide (Irgacure 819) (all purchased from Sigma Aldrich Co.), which was reinforced with rod-shaped nanohydroxyapatite powder (nHA) (~120 nm in length, and 30-40 nm in diameter)

(MKnano Inc., Mississauga, Canada). These nHA particles are calcium-deficient with a 1.52 ratio of calcium to phosphorous, a crystallinity index of 0.52–0.54 and a specific gravity of 2.92 [219].

4.2.1. Preparation of 3D printable Nanocomspoite Ink

After dissolving AESO in ethanol, nHA particles were gradually added to the AESO-ethanol mixture (Fig. 4.1). At each step of the nHA particle addition, an ultrasonic homogenizer (Branson Sonifier 450, Emerson Inc., USA) was used for 5 min to disperse the particles until the required quantity of nHA particles was attained (Fig. 4.1).

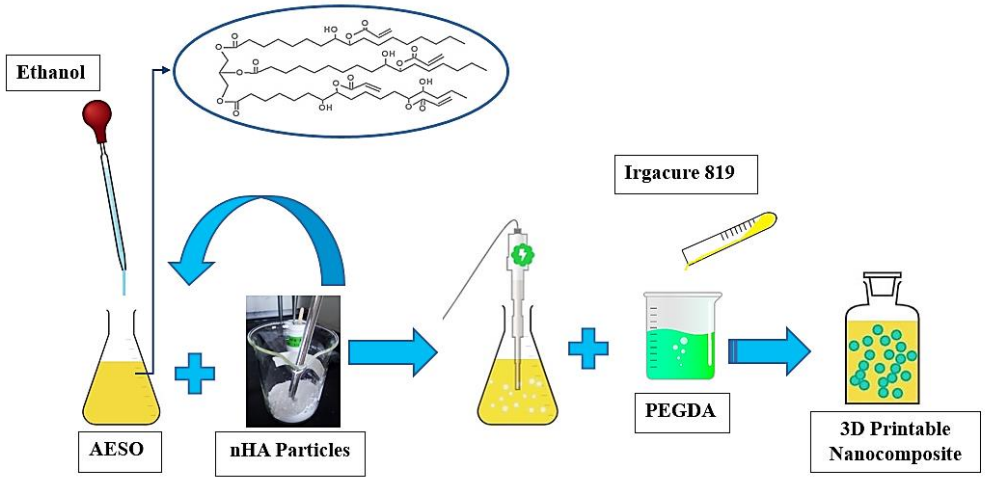


Fig. 4.1. Schematic of the preparation of AESO-based 3D printable nanocomposite inks

PEGDA was subsequently added to the mixture, which was homogenized for 15 min. The ink composition was 30 vol% nHA (30) with 49 vol% AESO (S) and 21 vol% PEGDA (P). This composition was denoted as SP30. Finally, Irgacure 819 was mixed in 10% w/v acetone and added to the ink composition at a volume ratio of 1. %. Ethanol and acetone were evaporated in a vacuum chamber. During this period, the ink was homogenized for approximately 10 min per day to maintain particle dispersion.

4.2.2. Characterization of Nanocomposites

4.2.2.1. Nanocomposite Ink Rheology

To obtain the rheological characteristics of the nanocomposite ink, a new batch of ink was prepared following the same procedure mentioned in Section 2.1, except that the Irgacure 819 photoinitiator

was not included to avoid curing. A Bohlin CS Rheometer with a cone-and-plate arrangement (150 μm spacing) system was used to measure viscosity and shear yield strength of the inks (n = 3) [63]. The experiments were carried out at 25 °C with shear rates ranging from 0.01 s^{-1} to 100 s^{-1}. At 10^{-} second intervals, the viscosity was measured for each shear rate.

4.2.2.2. Fourier Transform Infrared Spectroscopy (FTIR)

Fourier-transform infrared spectroscopy (FTIR) was performed on the surfaces of the cured nanocomposite specimens (n=3) to measure their curing and conversion efficiencies. A Nicolet 6700 FT-IR Spectrometer (Thermo Scientific, USA) with a resolution of 4 cm^{-1} and a sample scan of 32 was conducted to collect FTIR spectra. All spectra were analyzed using OMNIC series software [136].

4.2.2.3. Thermogravimetric Analysis (TGA)

Using thermogravimetric analysis (TGA), 3D printed nanocomposites' organic-inorganic ratios and heat degradation properties were examined. Ten to fifteen milligrammes of each nanocomposite specimen (n = 3) were heated and burned using a TA Q500 device (TA Instruments Inc., New Castle, DE, USA). A rate of 10 °C/min to 800 °C was applied to the samples during air heating. The specimens were allowed to equilibrate at 40 °C for 5 min prior to heating. The residual mass obtained at 800 °C was used to calculate organic-inorganic ratio of the nanocomposites.

4.2.2.4. Differential scanning calorimetry (DSC)

The absorbed energy (endotherm) or released (exotherm) as a function of temperature or time was measured using DSC which can obtain material properties, such as melting temperature, crystallization temperature, crystallinity, and glass transition temperature. DSC analysis was performed on different cases of extruded filaments to investigate how the heat capacity and, consequently, the enthalpy of melting, which is directly related to the degree of crystallinity in polymers [117,287], changed with shear stress. The nanocomposite filaments were weighed (averaging 7±1 mg) before being sealed in Tzero Aluminum Hermetic pans. The prepared pans were then loaded onto an autosampler and DSC was performed. The specimens were heated to 25 °C at a rate of 10 °C/min for 5 min prior to equilibration. The specimens were then chilled to -25 °C at 10 °C/min before being heated to 350 °C at 5 °C/min. The decomposition temperature

recorded in the thermogravimetric analysis in [20] was used to determine the maximum temperature for DSC experiments. Specific heat capacity data were calculated by dividing the heat capacity data by the specimen mass. The degree of crystallinity for semi-crystalline polymers can be obtained according to Equation 4.1 [287]:

$$X_{\mathrm{C,DSC}} = \frac{\Delta H_m}{\Delta H_m^0} \tag{4.1}$$

where $X_{\mathrm{C,DSC}}$ is the degree of crystallinity, ΔH_m^0 is the specific melting enthalpy for a 100% crystalline polymer matrix, which in this study is the AESO/PEGDA polymer matrix [288,289] and ΔH_m is the enthalpy of melting which the area beneath the melting endotherm zone of the specific heat capacity data vs. temperature graphs used to measure it. Because we did not have information on the value of ΔH_m^0 for our polymer matrix, we were unable to calculate the degree of crystallinity in our nanocomposite filaments. Instead, the relative degree of crystallinity was established by comparing the crystallinity in the different extruded shear cases with that of the cast specimen. The compositions of the cast and extruded nanocomposite specimens were the same; therefore, the value of ΔH_m^0 for all cases was the same. The relative degree of crystallinity was computed using Equation 4.2 by dividing the determined enthalpy of melting for each case by the enthalpy of melting calculated for the cast specimen as a control.

$$X_{\mathrm{r}} = \frac{X_{\mathrm{C,DSC,Extrude}}}{X_{\mathrm{C,DSC,Cast}}} = \frac{\Delta H_{m,Extrude} \Big/ \Delta H_m^0}{\Delta H_{m,Cast} \Big/ \Delta H_m^0} = \frac{\Delta H_{m,Extrude}}{\Delta H_{m,Cast}} \tag{4.2}$$

Where X_{r} refers to the relative degree of crystallinity, $\Delta H_{m,Extrude}$ is the enthalpy of melting for each extruded case, and $\Delta H_{m,Cast}$ is the enthalpy of melting for a cast specimen.

4.2.2.5. Scanning electron microscopy (SEM)

Further SEM and backscattered electron microscopy (BSE) specimens were prepared to observe the microstructures of the printed filaments. The longitudinal and transverse cross-sections of the filaments were imaged after they were embedded in a cylindrical mold using an epoxy resin. After 24 h, the resin-embedded filaments were polished sequentially with diamond pastes of 6 μm, 0.05 μm and 0.01 μm particle size diamond pastes [136]. SEM examination was performed in low-vacuum mode using a Quanta FEG 250 (ThermoFisher Scientific, USA). Both SEM and BSE

analyses of high-resolution microscopy are complementary; however, unlike SEM, BSE detects atomic number variations using high-energy electrons. BSE analysis is highly dependent on the atomic number of the specimen [290]. As the calcium-deficient nHA particles have a higher atomic number than the carbon atoms in the matrix, they give off much more intense signals and generate high-contrast images of our nanocomposite compared with SEM. For fractographic purposes, the fractured filaments were mounted on SEM stubs without modification and the fracture surfaces were imaged.

4.2.2.6. Polarized Light Microscopy Imaging

Polarized light microscopy (PLM) with reflected polarization was employed for further investigation of shear-induced crystallinity in various extrusion cases and cast specimens. The specimen preparation procedure for POM was the same as that described in section 2.2.5. A Nikon Eclipse LV-100 upright reflected polarized light microscope obtained the images of the bulk specimens. Cross-polarization was selected for the polarizer and analyzer. Illumination was achieved using a Lumencore LED light source, and images were captured using an Infinity 1 color camera after passing through a quarter-wavelength retardation plate. After capturing the POM micrographs for further investigation and quantitative comparison of the nucleated crystallinity sites in different cases, the number and size of the spherulites were measured using ImageJ software. To ensure consistency, after calibrating the images, a specified ROI of 70 μm × 90 μm was chosen, and the triangle threshold and bandpass filtering configuration were used for all specimens before the measurements were performed.

4.2.3. DIW of Nanocomposite Filaments

4.2.3.1. Mechanics of Extrusion-Based 3D printing

All materials flow when given a sufficient time. The distinguishing feature of polymeric materials is that their processing times for extrusion are usually of the same order as their time constants for flow [48]. Viscosity, which represents the material resistance to flow due to the applied shear stress [291], is the most important flow property. Referring to Fig. 4.2, viscosity is defined as the ratio of the imposed shear stress to the shear rate, according to Equation 4.3:

$$\eta = \frac{Shear\ Stress}{Shear\ rate} = \frac{F/_A}{V/_h} = \frac{\tau}{\dot{\gamma}} \quad (4.3)$$

where τ and $\dot{\gamma}$ are the shear stress and strain rates, respectively. Where F, V, A, and h are force, velocity, area, and gap distance, respectively.

For the flow in the tube, the shear stress changed linearly from zero at the central axis to a maximum value along the wall (Fig. 4.2).

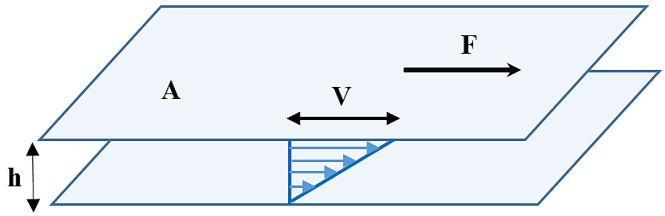


Fig. 4.2. The velocity distribution profile in a simple shear flow of Newtonian fluid between two parallel plates

The shear stress distribution in a tube with laminar flow (Fig. 4.3) [291] was calculated using the applied pressure [292] according to Equation 4.4:

$$\tau = \frac{\Delta p r}{2l} \quad (4.4)$$

where Δp denotes the pressure drop along length l, and r is the radius of the tube. In this study, the maximum applied shear stress on the wall during extrusion-based 3D printing was calculated using Equation 4.4.

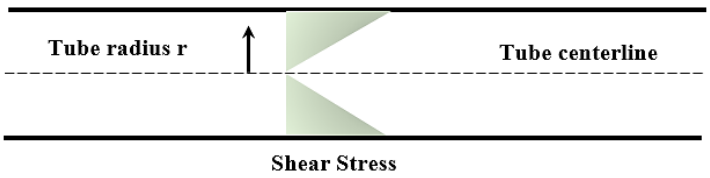


Fig. 4.3. Shear stress distribution profiles for laminar flow through a round tube with a maximum at the tube wall and zero at the centre.

4.2.3.2. Printing Nanocomposite Filaments using Custom-Built Skeleprinter

After the evaporation of the solvents, the prepared nanocomposite ink was used to extrude filaments using a custom-designed DIW 3D printing system called SkelePrint. SkelePrint is a

mandrel-bed 3D printing system developed at the University of Waterloo by a group of Systems Design Engineering (SYDE) undergraduate students as part of their capstone project. This system is developed to produce 3D printed components by depositing extruded filaments on the mandrel bed in concentric layers, contradictory to commercially available flatbed 3D printing systems. A schematic view and experimental setup of the custom-designed SkelePrint are shown in Fig. 4.4 and 4.5(A, B), respectively.

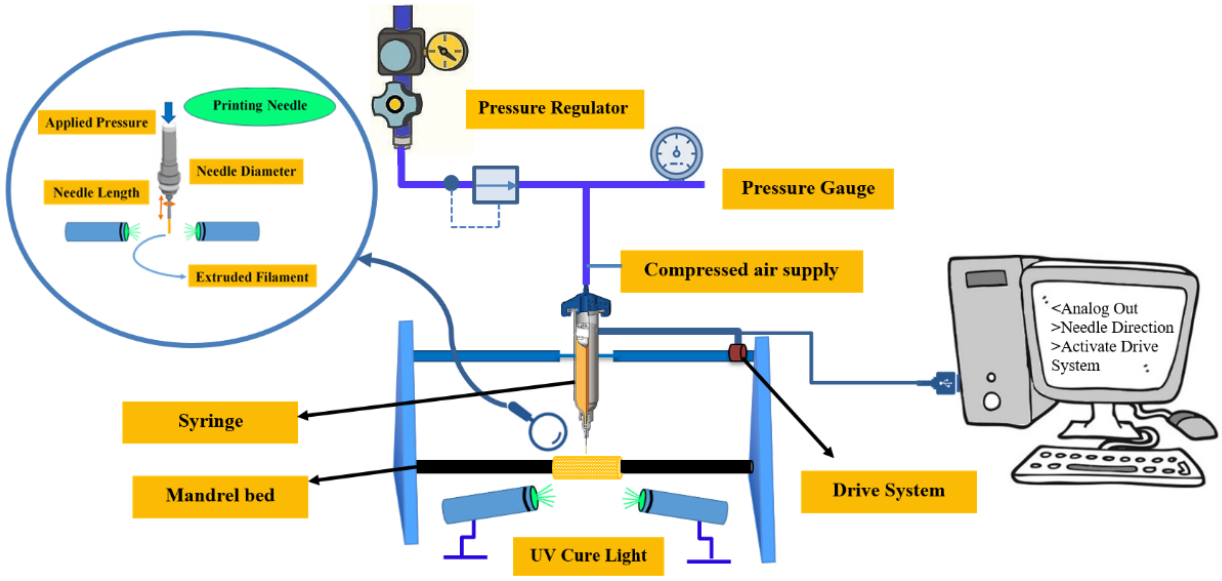


Fig. 4.4. Schema of the experimental set-up using the custom-built extrusion-based SkelePrint 3D printer for extruding the filaments with controlled shear stress during extrusion.

As shown in Fig. 4.5. B, the SkelePrint system was primarily composed of a mechanical frame (Fig. 4.5. B-h), three-stepper motor-actuated drive system (Fig. 4.5. A), a pneumatic actuator (98623-05, 12VDC, 4.5w, 125PSI max pressure, Parker), UV curing mounting arrangement (Fig. 4.5. B-c) and pressure gauges (Fig. 4.5. B-i), mechanical transmission components, and an Arduino microcontroller (Fig. 4.5. B-e), the CNC control package, and the user interface.

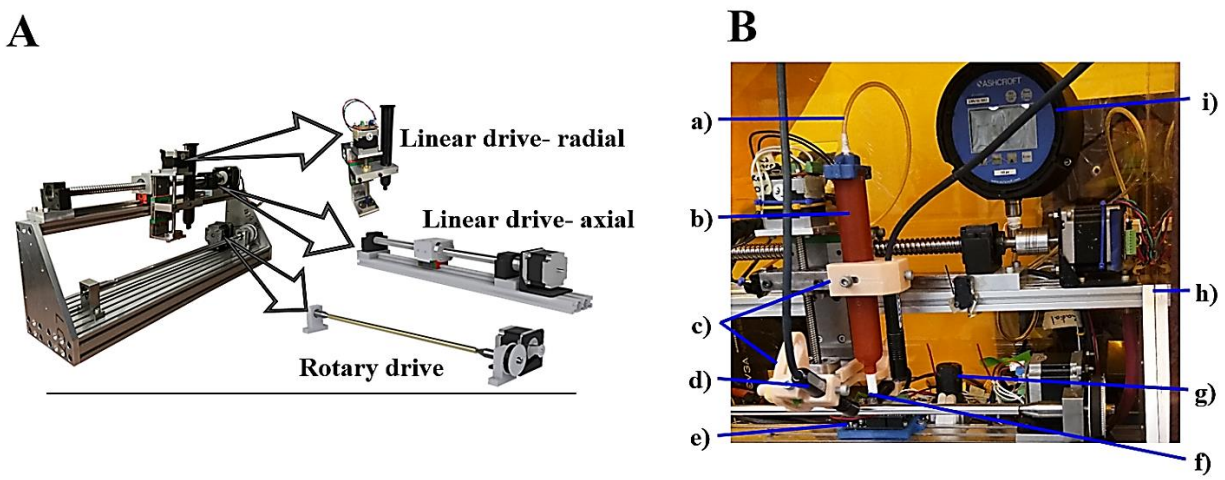


Fig. 4.5. SkelePrint's components: A. SkelePrint drive systems: Linear drive system for radial displacement, the linear drive system for axial displacement, and rotary displacement; B a) air pressure line, b) syringe barrel, c) UV lamp mounts, d) UV lamp, e) Arduino microcontroller, f) dispensing tip and cap, g) pressure regulator, h) chassis, i) pressure gauge.

The linear drive assemblies are shown in Fig. 4.5. A. They drive linear motion in both the axial and radial directions, respectively. The third drive assembly is illustrated in Fig. 4.5. A drives rotary motion about the mandrel axis. The material dispensing holder assembly of the system was designed to load the print head (Fig. 4.5 B-b) (Optimum dispensing syringe, EFD, Nordson, USA), which was connected to a solenoid-controlled actuator that actuated the flow of preset pressurized air (Fig. 4.5. B-a) for material extrusion. The printing parameters, feed rate, print bed diameter, print length, extruded filament size, final print diameter, and helix angle, were input into the user interface to generate the G-code. The CNC controller of SkelePrint interprets the G-code and actuates each drive system using an Arduino microcontroller (Fig. 4.5. B-e) to 3D print the part.

The print head was raised vertically in the radial direction by a predefined layer height (filament diameter) to print successive concentric layers on the mandrel print bed. The SkelePrint is equipped with an adjustable mounting arrangement (Fig. 4.5. B-c) for UV lamps (Fig. 4.5. B-d) (385 nm, at 175 mW/cm^2 intensity, BlueWave® QX4® LED Spot-Curing System, Dymax Corp., USA). The UV lamp mount was intended to allow the UV lamp position to be manually adjusted linearly along the length of the print bed axis, radially around the mandrel bed axis, and normally towards the print bed axis (Fig. 4.6). These mounting arrangements provide controlled exposure

of the extruded nanocomposite filaments to UV light while 3D printing a complex microstructural layup.

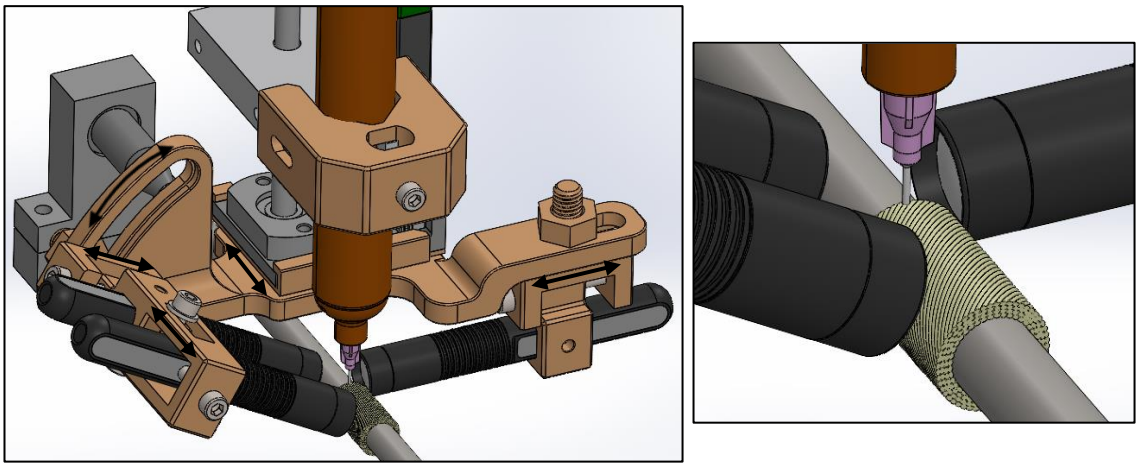


Fig. 4.6. Adjustable UV lamp mounting configurations to accommodate different angular layup sequencing

SkelePrint programming allows complex microstructure layup sequences during the fabrication of multilayer hierarchical structures. Fig. 4.7. (a)–(d) show some examples of dense and porous 3D printed microstructures with SkelePrint in two arrangements: Crisscross (45°) and Bouligand (change in angular orientation for each deposited layer from 0°-90° with 15° angular increment) [293,294] which were manufactured using extruded nanocomposite filaments with one of the UV mounting configurations. As a result, SkelePrint and its customizable UV mounting arrangements enabled the fabrication of both dense and porous multilayer microstructures. Pneumatically actuated extrusion allows better control of the material feed rate by altering the pneumatic pressure than mechanical piston-driven extrusion [295].

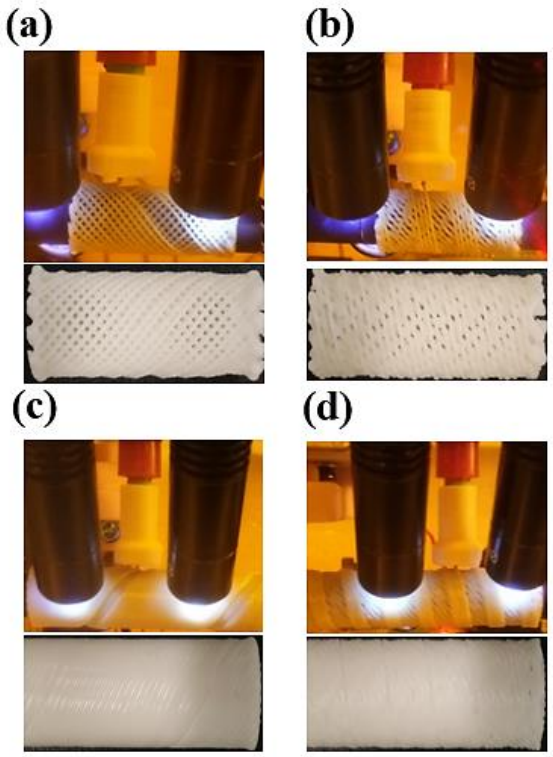


Fig. 4.7. Concentrically layered 3D printed sample structures printed using the custom-designed Skeleprint: a) Porous Crisscross structure, b) Porous Bouligand structure, c) Dense Crisscross structure, and d) Dense Bouligand structure.

The SkelePrint system is equipped with a pressure regulator (Fig. 4.5. B-g) controlling the applied pneumatic pressure for extrusion, which allows the calculation of the shear stress applied in the needle during extrusion according to Equation 4.4, knowing the needle (precision stainless steel tips, Nordson, EFD, USA) specifications (needle length and inner diameter). Single filaments were extruded by varying the shear stress from 3.5kPa to 14kPa by adjusting the needle length and applying pressure while maintaining a constant needle diameter. To extrude the filaments, an optimum dispensing syringe fitted with a 0.25" long 20ga (0.6 mm) optimum general-purpose dispensing tip (EFD, Nordson, USA) was used as the printhead on the SkelePrint.

For printing the filaments, first the compressed air pressure was adjusted using a regulator and a pressure gauge to set a predefined value. The valve was then opened by executing the relevant G-code for filament extrusion at the set pressure values. The extruded filament was exposed to parallel UV curing (385 nm, at 175 mW/cm^2 intensity, BlueWave® QX4® LED Spot-Curing System, Dymax Corp., USA) post-extrusion (Fig. 4.4), which was arranged to emit UV light on the sidewalls of the extruded filament, resulting in an efficient curing process.

4.2.4. Mechanical Testing of Nanocomposite Filaments

After curing, single extruded filaments were tensile tested to determine their mechanical properties. The trapezoidal end tabs were designed and manufactured using masked stereolithography (mSLA) to bind the ends of the filament. The end tabs featured a cylindrically formed depression [219] to match the cross-sectional geometry of the filament (Fig. 4.8) [20]. The trapezoidal pieces were adhered using an epoxy glue (7 mm in length) to each filament head. The filaments were cut consistently at 2 cm lengths to preserve a consistent 6 mm gauge length. Another trapezoidal end tab was bonded to each filament head's opposite side to hold the samples firmly in place and prevent the filaments from separating from the adhesive throughout the test. All tensile tests were conducted with a Psylotech µTS mechanical testing frame (Psylotech Inc., Evanston, IL, USA) on a vibration isolation table (Vision Isostation, Newport Corp., California, USA). The instrument is equipped with a 1.6kN load cell with a windowing function that provides greater load signal resolution and sensitivity over the 0N–100N range. During the test, strain measurements were performed using a microscope-enabled Digital Image Correlation (DIC) system. A microscope with a digital camera (BXFM, Olympus Corp., Center Valley, PA, USA, Point Grey, 5 MP, 2/3" detector) was employed in order to acquire magnified images of the gauge length during testing. The tests were performed under displacement control at a rate of 16 µm/s, with resulted average strain rate of 0.0016 s^{-1}.

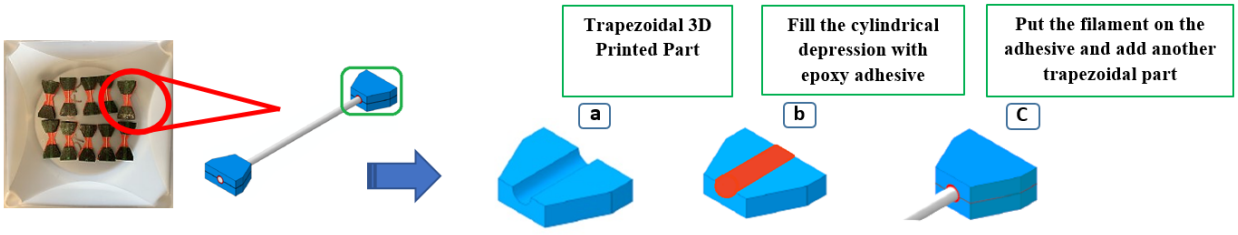


Fig. 4.8. Nanocomposite filament test specimen preparation (Obtained and modified from [6]).

Prior to image acquisition, distortion correction was performed to correct for measurement corruption caused by the optical path. All mechanical data and image acquisition were performed at 5 Hz rate, and at room temperature. To accurately measure the deformation using DIC, a speckle pattern is required to the surface of the specimen. atomizer jar loaded with high-resolution toner

powder (Xerox Phaser 6000 laser toner cartridge) were used to spray test specimens (Fig. 4.8). The toner particles had a diameter of 4–5 μm, making them appropriate for DIC with a 5x microscope objective in our system. The spatial resolution is 729 pixels/mm (1 pixel=1.37 micron). The strain was measured by analyzing the recorded pictures from the tensile test in the DIC analysis program Vic 2D (DIC; Vic 2D 6, Correlated Solutions Inc., USA) to estimate the strain based on deformation in the AOI (Area of Interest, 4.03 mm long, 0.4-0.5 mm wide).

Each experiment was set with a 150-pixel subset window and a 7-pixel step size. To ensure consistency in the strain measurements, virtual extensometers were used to measure the average engineering strain values from DIC. over the length of the AOI in each specimen. By dividing the applied force by the filament's initial cross-sectional area, engineering stress values were determined. The slope of the first linear elastic section of the stress-strain curves and ultimate stress, respectively, were used to compute the elastic modulus and tensile strength. The area under the stress-strain curves was used to calculate the toughness values.

4.2.5. Dynamic Mechanical Analysis (DMA)

Thermal parameters such as the glass transition temperature (Tg) can be assessed using DMA. The thermal properties of the nanocomposites were measured to investigate the effects of the high-shear extrusion. Extruded film-like specimens (5.5 ± 0.1 *w*, 0.62 ± 0.3 *t*, 5.5±0.1 *l*) were prepared using the printing parameters of our highest shear case. Cast film specimens were also fabricated with similar dimensions using the same ink, enabling comparison with high-shear extruded specimens. Because the SkelePrint print bed is a mandrel, printing flat specimens for DMA testing is not possible with this device. Therefore, a commercial System 30M (Hyrel, Georgia, USA) 3D printer with a Volcano metal syringe print head and curing system using a UV lamp (385 nm, at 175 mW/cm^2 intensity, BlueWave® QX4® LED Spot-Curing System, Dymax Corp., USA) with a flat printing bed was utilized to fabricate the extruded thin film specimens for DMA purposes. The flow rate of the highest shear extrusion on SkelePrint was measured for consistency assurance, and then by trying different feed rates on the Hyrel printer and measuring the flow rate of the ink for every feed rate. A feed rate of 1.2 mm/min provided the same flow rate as SkelePrint's high-shear extrusion. The G-code was written accordingly to print a one-layer 0.6 mm thick film made up of continuously deposited filaments. The cast specimens were prepared using a thin mold with a similar thickness. Then, both sides of the specimen were cured for 10 min in an LED light-cure

box with a light energy intensity of > 15 mW/cm². DMA was conducted on a Q800 (TA Instruments, USA) at a temperature range of -20 °C to 120 °C, an oscillation frequency of 1 Hz, and a strain amplitude of 0.02% at 3 °C /min using fixtures for tensile testing films.

4.2.6. Statistical Analyses

Means and standard deviations were used to represent the data (mean±SD). SigmaStat (version 4.0, Systat Software Inc., CA, USA) was used to analyze the data. To compare means, one-way analysis of variance (ANOVA) was employed, followed by Tukey's multiple comparison test. Mean differences were considered statistically significant at $p<0.05$.

4.3. Results

4.3.1. Nanocomposite inks characterization

The rheological properties of our nanocomposite ink contribute to its ability to flow smoothly during extrusion-based 3D printing of filaments and hold their shape prior curing. Fig. 4.9 (a) shows representative viscosity vs. shear rate and shear stress plots. The ink exhibited shear yield strength and shear thinning behavior, which are required for effective DIW 3D printing. The rheological properties of the samples are listed in Table 4.1. No peak at 1630 cm^{-1} (related to the stretching vibration of C=C) and at 806 cm^{-1} (for the asymmetric vibration of out-of-plane vinyl groups) were observed at the FTIR spectra of the cured SP30 nanocomposites [20,296] (Fig. 4.9. (b)). This suggests that unreacted monomers were not present in the cured nanocomposites. The ratio of nHA to the AESO/PEGDA resin in the 3D-printed nanocomposites was verified using TGA. After burnout, the nHA volume fractions of SP30 were calculated, and a volume fraction of 29.6 ± 0.3 ($n = 3$) was obtained, which was close to the targeted 30% (Fig. 4.9 (c)).

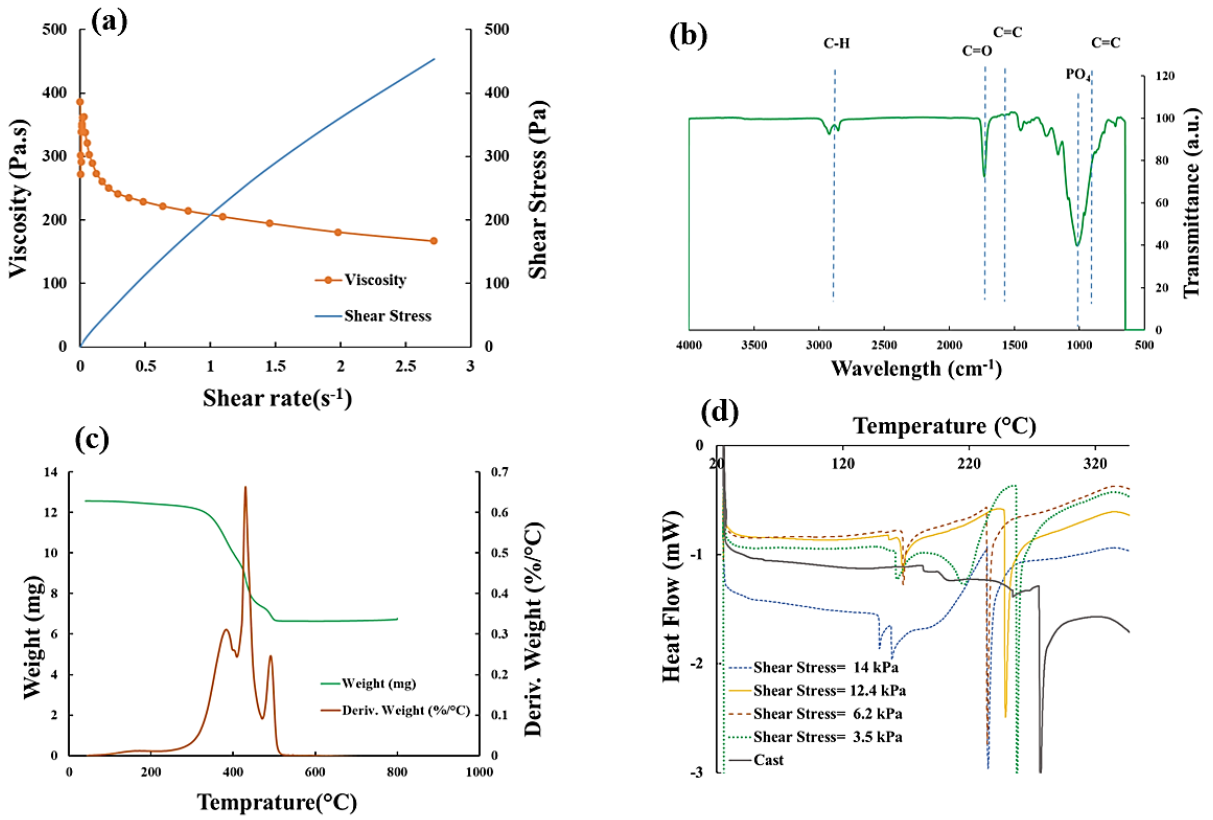


Fig. 4.9. a) Representative viscosity vs shear strain rate and shear stress vs shear strain rate (n=3). b) FTIR spectrum of cured SP30 nanocomposite. c) Representative TGA and DTG thermograms of cured SP30 nanocomposites, d) Representative DSC thermograms of extruded SP30 nanocomposites filaments with varied shear flow conditions. (n=3)

Table 4.1. Viscosity, shear yield strength and TGA results of the as-prepared nanocomposite ink. (n = 3; data are presented as mean ± SD).

Nanocomposite Ink	Viscosity (Pa.s)	Shear Yield Strength (Pa)	TGA Volume fraction (V_f)
SP30	157 ± 13	10.38 ± 0.27	29.62 ± 0.31

Representative DSC thermograms of extruded filaments and cast specimens are shown in Fig. 4.9. (d). The extruded specimens exhibited a similar trend, with two endothermic peaks visible in their thermograms. The cast specimen also exhibits two endothermic peaks, with the first peak being very small. The second peak demonstrating specimen melting is in the 240-260 °C range, which is similar across all cases, suggesting that there is no change in the melting or glass transition temperature between different cases.

Fig. 4.10 shows the average value of the melting enthalpy (a measure of crystallinity) for each group of extruded filaments as well as the cast specimen, which was measured using the area under the second melting endotherm zone-specific heat capacity vs. temperature curves across the same temperature range. The enthalpy increased from 7.8±1.4 mJ/mg to 28.32±3.3 mJ/mg by increasing the shear stress during extrusion from 3.5 kPa to 14 kPa. Moreover, the enthalpy of melting through high-shear extrusion compared with casting increased by more than four times. The relative degree of crystallinity for each extruded filament was calculated using Equation 4.2, and is listed in Table 4.2. Increasing the shear stress during extrusion increased the relative degree of crystallinity. Statistically significant differences were observed between the cases with a larger change in shear flow during extrusion.

Table 4.2. The relative degree of crystallinity obtained for different shear extruded cases according to Equation 4.2. (Dissimilar letters imply a statistically significant difference in means ($p<0.05$))

	Cast	**τ = 3.5 kPa**	**τ = 6.2 kPa**	**τ = 12.4 kPa**	**τ = 14 kPa**
Relative degree of crystallinity (Xr)	1 ± 0.12^{a}	1.38 ± 0.25^{a}	1.81 ± 0.04^{a}	3.68 ± 0.22^{b}	5.02 ± 0.60^{c}

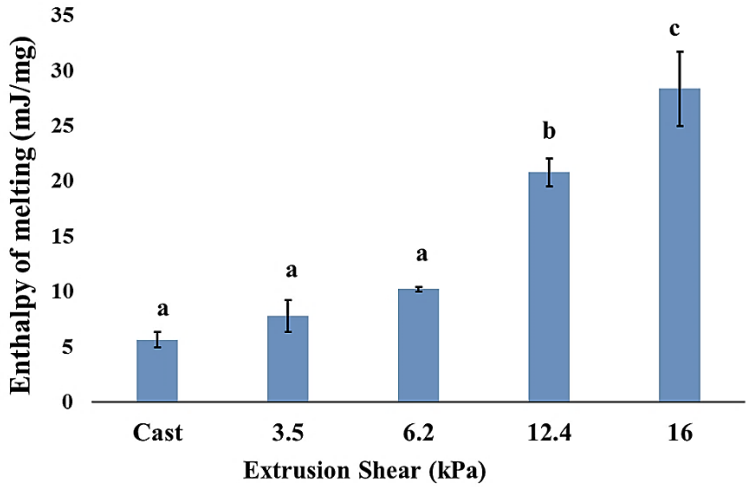


Fig. 4.10. Melting enthalpy for the four extruded nanocomposite filaments and cast specimen as a control. Evidently, crystallinity increased with greater applied shear stress during extrusion. Dissimilar letters imply a statistically significant difference in means ($p<0.05$).

4.3.2. Microstructure Imaging of Different Extruded Nanocomposite Filaments

4.3.2.1. Scanning Electron Microscopy (SEM)

Representative SEM images of the longitudinal sections of extruded filaments from the four groups are shown in Fig. 4.11. (a-e).

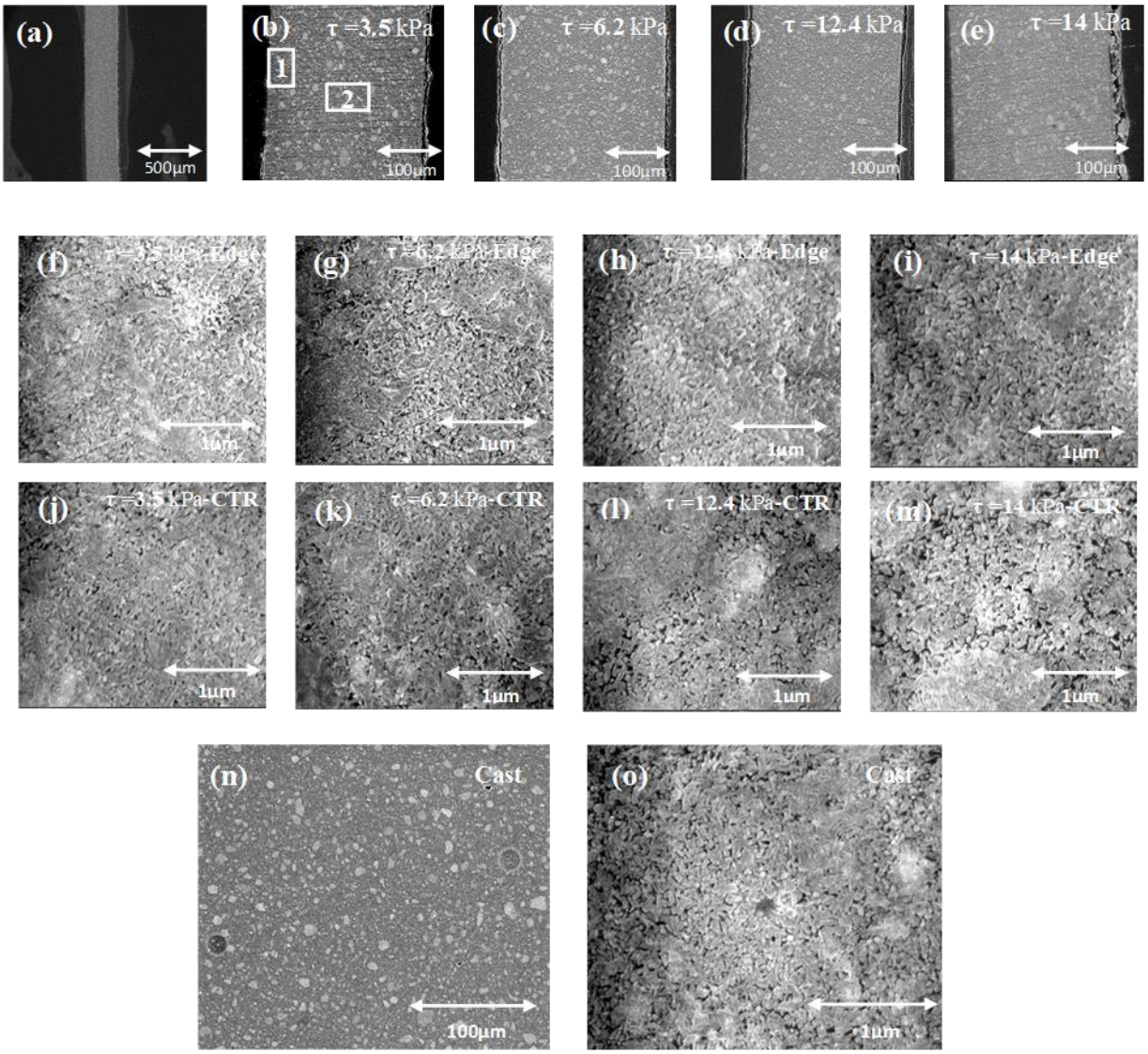


Fig. 4.11. Representative SEM images of extruded filaments. a-e) longitudinal cross-sections (250x magnification). f-i) Region-1(Edge of filaments) in higher magnification (40000x magnification). j-m) Region-2 (Centre of filaments) in higher magnification (40000x magnification). n-o) Cast specimen in low (250x) and high (40000) magnification.

To further assess the particle alignment in different cases, the regions at the center and edge of each filament (shown in Fig. 4.11. (b)) were selected, and the high-magnification images (Fig.

4.11. (f)–(o)) were captured. The nHA nanoparticles are densely dispersed in the matrix and no specific pattern change in the particle distribution and orientation were observed in different shear extrusions compared to cast sample as control. No particle alignment was detected in the high-magnification images of all extruded cases (either in the edge or in the center regions of filaments in which the shear stress during extrusion was maximum and minimum, respectively).

They revealed nHA particle dispersion, with some agglomerations detected on the scale of tens of micrometers. There were no noticeable differences in the dispersion or alignment of the nHA particles as shear stress was increased during extrusion. The extruded filaments' SEM images, demonstrated that the filaments were dense, whereas the cast specimen had some spherical defects. This was most likely caused by entrapped air bubbles that acted as stress concentrations, reducing the cast specimens' strength.

4.3.2.2. Polarized Light Microscopy Images

Using PLM images, the effect of increasing shear stress during extrusion on the polymer matrix crystallinity was further investigated. POM images of filaments extruded with shear stress 3.5 kPa, 6.2 kPa, 12.4 kPa and 14 kPa are shown in Fig. 4.12 (b-e), along with a cast specimen as a control micrograph (Fig. 4.12 (a)). As shown in these images, filaments extruded under high shear exhibited a morphology with an increased number of crystalline sites and detected spherulites. While the crystallinity sites and spherulites increased in cases with greater shear stress during extrusion, the low-shear extruded cases did not exhibit a significant difference in the observed crystallinity sites and spherulites compared to the cast specimen. This is consistent with the DSC results and relative degrees of crystallinity measurements. Further investigations using ImageJ to quantitatively compare the shear-induced crystallinity in the PLM images of different cases and cast specimens are presented in Table 4.3.

Table 4.3. Number and size of spherulites detected in specific ROI of PLM micrographs for different cases (Dissimilar letters shows a statistically detectable difference in the means ($p<0.05$))

	Cast	**τ=3.5 kPa**	**τ=6.2 kPa**	**τ=12.4 kPa**	**τ=14 kPa**
Number of detected spherulites in ROI	**5**	**8**	**15**	**38**	**148**
Size of detected spherulites (µm) (Data are presented as mean ± SD)	0.38 ± 0.20^{a}	0.37 ± 0.14^{a}	$0.47\pm0.22^{a,b}$	$0.61\pm0.56^{b,c}$	0.71 ± 0.63^{c}

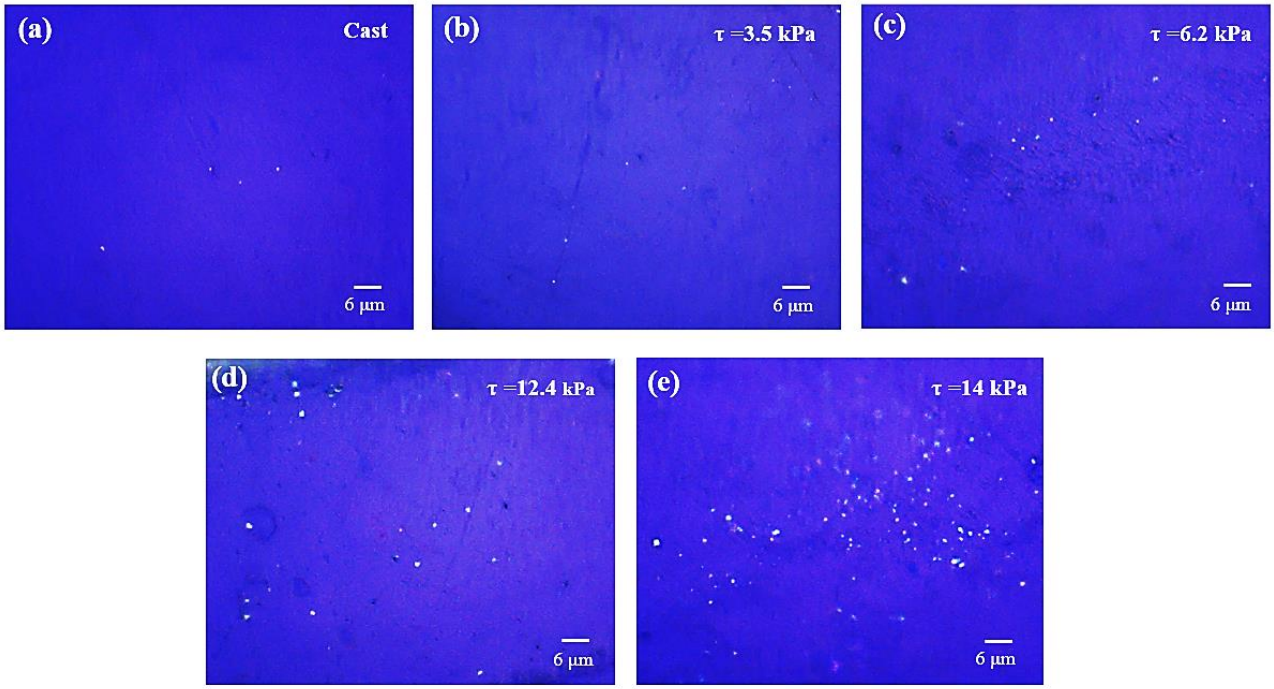


Fig. 4.12. Polarized light microscopy images a) Micrographs of cast specimen, b-e) Micrographs of extruded filaments with different shear flow

4.3.3. Mechanical Properties of Nanocomposite Filaments

Stress-strain curves and plots of ultimate tensile strength, elastic modulus, toughness, and fracture strain for each of the extruded nanocomposite filament groups are shown in Fig. 4.13 (a)–(e). As shown in these plots, the strength, elastic modulus, and toughness of the nanocomposites were enhanced by increasing the shear stress applied during the extrusion. The ultimate strength increased from 12.07 ±1.8 MPa to 35.6 ±3.7 MPa by increasing the shear during extrusion from 3.5 kPa to 14 kPa respectively. The elastic modulus and toughness also increased from 0.5 ± 0.26 GPa and 0.31 ± 0.13 MPa to 1.8 ± 0.47 GPa and 1.03 ± 0.46 MPa respectively. There were no significant differences in the fracture strain data for the different extrusion shear cases.

The SEM images of the fracture surfaces of the filaments after tensile testing are shown in Fig. 4.14. The filaments had a smooth and circular cross-section. The filament fracture surfaces featured a rough morphology, and SEM showed that the surfaces of the filaments extruded with high shear were rougher than those extruded with low shear.

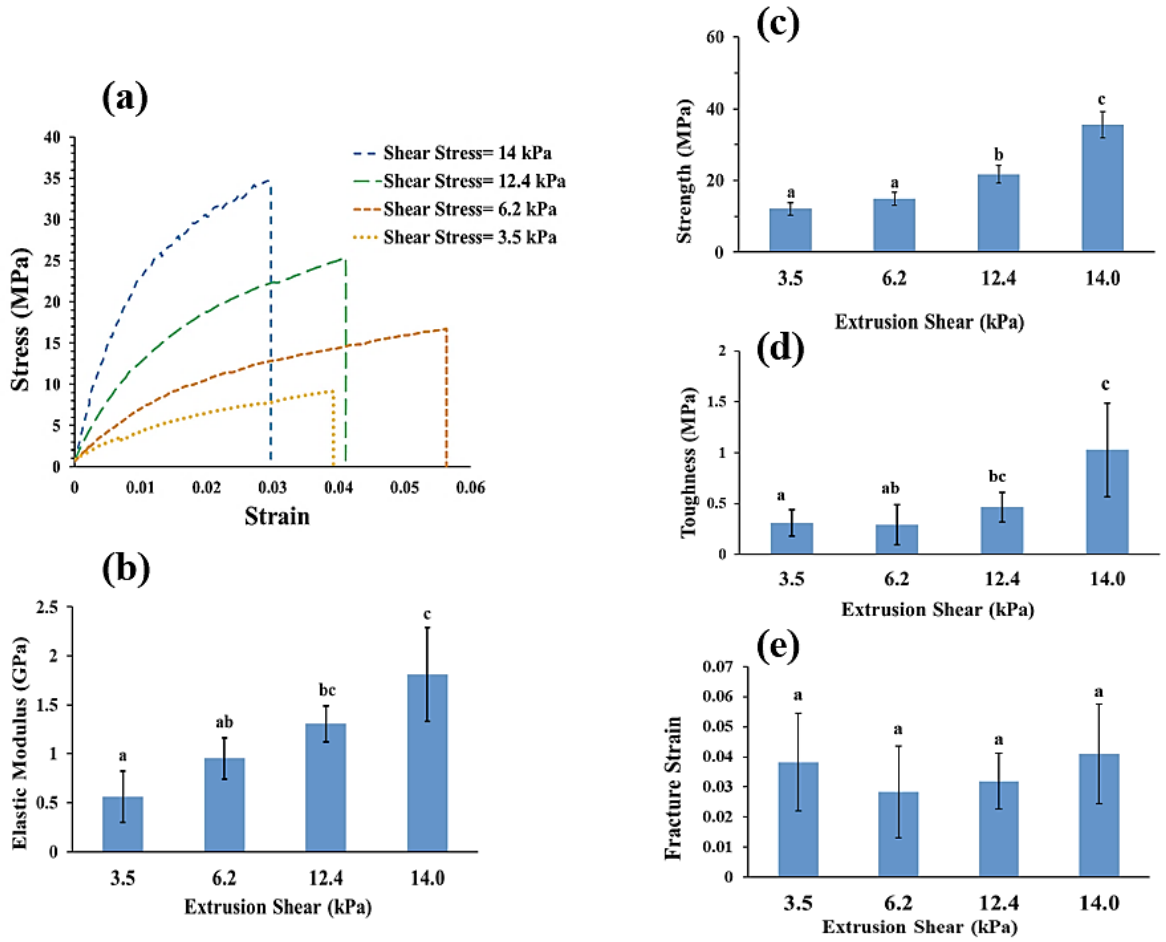


Fig. 4.13. a) Representative stress-strain curves, b) elastic modulus, c) strength, d) Toughness, e) fracture strain of the 3D printable nanocomposites extruded with different applied shear stresses (n=7 specimens of each case).

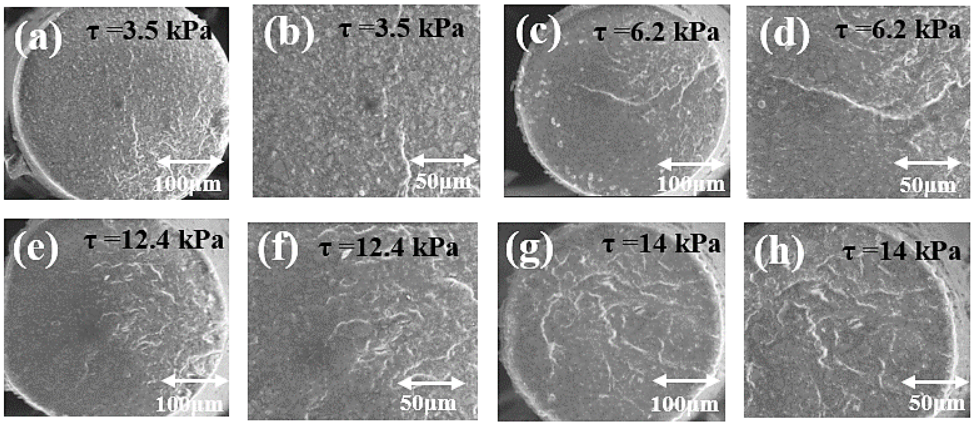


Fig. 4.14. Representative SEM images extruded filaments' fracture surfaces after tensile testing. a-h) Transverse cross-section of filaments extruded with 3.5 kPa, 6.2 kPa, 12.4 kPa and 14 kPa respectively at lower (250 x) and higher (500 x) magnifications.

4.3.4. DMA

The DMA results for the thin film extruded at 14 kPa and cast specimens are shown in Fig. 4.15. The glass transition temperature (Tg) was measured from the peaks of the tan δ curves. Comparing the glass transition temperatures of the cast and high-shear-stress thin film specimens, the Tg for the cast film was 55.8 °C and 58.4 °C for the extruded specimen, which indicates a slight increase and no significant effect of shear stress during extrusion on the glass transition temperature. The storage modulus of the extruded thin-film specimens at room temperature was approximately 2.1 GPa whereas that of the cast specimen was approximately 0.9 GPa. The loss modulus of the extruded thin film and cast specimens at room temperature was 341.6 MPa and 88.78 MPa respectively.

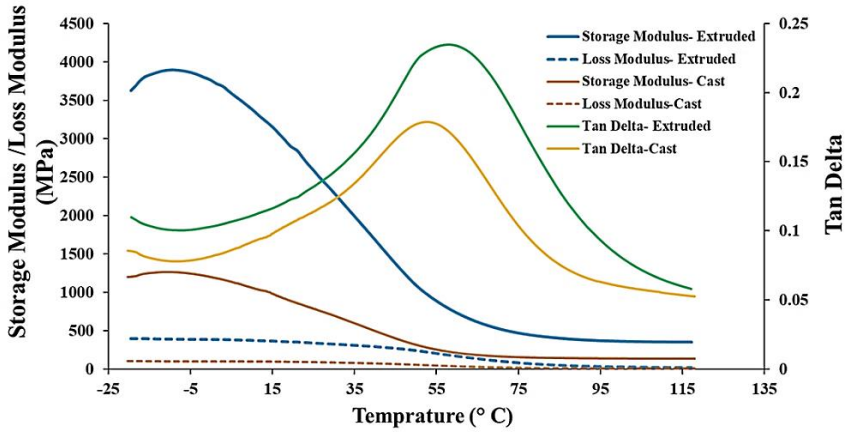


Fig. 4.15. Dynamic mechanical properties of an extruded thin film nanocomposite (14 kPa) compared to a cast nanocomposite thin film specimen.

4.4. Discussion

Biomaterials with nanocomposite structures comparable to those of bone that effectively combine the stiffness and biocompatibility of the inorganic phase with the toughness and resorbability of the organic phase are advantageous in bone reconstruction applications [297,298]. Hydroxyapatite (HA) is a bioceramic widely used in the repair and regeneration of bone defects. Rod- or fiber-shaped nHA particles have been shown to improve composite biomaterial scaffolds' mechanical properties and cell-material interactions. nHA, which mimics the inorganic component of bone minerals, has been investigated *in vitro* and *in vivo* studies [299–302].

In this study, 30% volume fraction of nHA nanocomposite ink was produced by mixing nHA with AESO and PEGDA to mimic the organic phase of the bone composition. UV-initiated photopolymerization was used to cure nanocomposites immediately after extrusion. UV-curable monomers can undergo free-radical polymerization in the presence of adequate UV light and a photoinitiator, resulting in crosslinked thermoset polymers [63]. Effective curing is necessary in biomaterial nanocomposites to achieve superior mechanical properties, controlled degradation behaviour, and optimum cell-material interactions since partial curing occurs when unreacted monomers are present in the matrices [63]. Based on the cure depth analyses conducted on SP30 ink [20], the nanocomposite filaments were exposed to UV for a longer period of time than was necessary for full curing. The absence of a C=C associated peak in the FTIR spectrum confirmed effective and efficient curing. The prompt, consistent, and adjustable response of pneumatic pressure (SkelePrint system) allows better flow control and shear adjustment during extrusion than the mechanical piston-assisted extrusion system [295]. By adjusting and increasing the shear stress during extrusion by means of the developed custom-designed 3D printer, the modulus, ultimate strength, and toughness of 3D printed nanocomposite filaments were enhanced by more than three times without changing the ink composition. The novel 3D printer demonstrated the feasibility of 3D printing of multilayer tubular structures; therefore, the effect of increased extrusion shear stress on the macromechanical properties of 3D printed structures, as well as its effect on the interlayer bonding of printed structures, will be further investigated.

The fundamental requirement for proper DIW is the composition of inks with an optimum rheological behavior [284]. The rheology of the developed ink exhibited appropriate viscosity and shear yield stress, enabling the ink to maintain its shape upon extrusion before UV curing, and preventing deformation and flow of the deposited material when extrusion ceased. The current nanocomposite ink composition demonstrated shape-holding for single filaments extruded at different shear stresses, whereas the challenge of ink dispersion persists when deposited on the mandrel print bed for developing multilayer structures. Hence, the print quality of multilayered structures (Fig. 4.7) is largely controlled by the UV spotlight arrangement. It is possible to further enhance print quality by improving the ability to hold shape of the ink composition.

In DIW, similar to any extrusion process, there is a prominent driving force for leading polymer chain alignment in the flow [97,303–305]. The shear stresses that caused alignment were more

pronounced close to the nozzle wall. Extrusion-based additive manufacturing of resins has been reported to promote shear-induced crystallinity [306,307]. The formation of nanophase crystals in nanostructured thermosets in confined environments has been reported [116,117,285]. According to the DSC results, increasing the shear stress during extrusion through a needle, which can be considered a confined environment, significantly increased the enthalpy of melting (a measure of crystallinity). The relative degree of crystallinity analysis, as well as POM micrographs, showed that by applying a higher shear during extrusion, the crystallinity sites and spherulites increased in the extruded nanocomposite filaments. Presumably, these increases were due to the increased crystallites' formation in the AESO/PEGDA biopolymer matrix as a result of polymer molecular orientation during high-shear extrusion. Crystallite regions in composite nanostructures improve stiffness and strength by limiting the polymer chain mobility [97], [305]. Because no parameter other than shear stress has been altered during extrusion, increasing shear during extrusion leads to increased crystallite formation and, thus, improved mechanical properties without changing the chemical composition [308]. The fracture surfaces of the filaments after the tensile test showed an increased rough morphology with increasing shear stress during extrusion, which is presumably a result of the crystallites formed during higher shear extrusion.

In crosslinked systems such as thermoset polymers, glass transition is highly dependent on the degree of crosslinking [309–312]. According to the DMA data, Tg did not vary significantly because of high-shear extrusion, which is attributed to the same amount of cross-linking in the cast and extruded specimens because of the same chemical composition. For a greater crystallinity degree, the glass transition temperature was shown to increase [313]. Although a slight increase in Tg was observed for the extruded film specimens, presumably, the degree of crystallite formation during the high-shear case was not dominant compared to the degree of crosslinking to alter the Tg significantly. The storage and loss moduli of both the specimens decreased as the temperature increased. At room temperature, the storage modulus of the high-shear extruded specimen was greater than that of the thin-film cast specimen, whereas the loss modulus of the extruded thin-film specimen increased slightly.

In nanocomposites, owing to the high surface-area-to-volume ratio of nano-scale inclusions, the dispersion of nanoparticles is a significant factor affecting their strength [63,314]. In this study, the nanoparticles were added gradually with sufficient ultrasonic homogenization for the

homogenous nHA particles' dispersion in the polymer matrices, with some inevitable micron-scale agglomerations detected.

It should be noted that because of the DMA test setup specifications, the higher-shear extruded specimen was a thin film fabricated by depositing continuous filaments next to each other. Investigation of the specimen under optical microscopy revealed some microscale gaps between the extruded filaments. These defects may have caused some early-stage failure of extruded thin films and may have affected the dynamic mechanical properties of the extruded thin film.

Higher magnification SEM images showed no evidence of particle alignment in the center or at the edges of filaments where the shear was greatest. This is most likely owing to a limitation in the air pressure used during extrusion, which leads to a lack of induced shear stress during extrusion to align the particles along the extrusion axis [96,109]. The increased aspect ratio of nanoparticles may also increase the percentage of aligned particles. Consequently, increasing the shear stress during extrusion and increasing the particle length may result in particle alignment, particularly near the edges of the filaments, which can further improve the mechanical properties.

4.5. Conclusions

This study's findings showed that increasing the shear stress applied during extrusion (from 3.5 to 14 kPa) using our custom-designed SkelePrint increased the ultimate tensile strength and elastic modulus of the extruded AESO/PEGDA/nHA nanocomposite filaments by approximately three times. This may be attributed to the higher degree of crystallinity generated during higher shear stress extrusion, which is consistent with the DSC data and POM micrographs of the high-shear extruded filaments. As a result, by enhancing the manufacturing aspects, such as increasing the shear stress during extrusion in this work, the mechanical properties of the nanocomposites can be improved without modifying the chemical composition. This finding may pave the way for the fabrication of more mechanically competent hierarchal bone-mimetic extrusion 3D printed nanocomposite grafts and scaffolds for use as bone substitutes.

Chapter 5

Effects of Biopolymer Functionalization and Nanohydroxyapatite Heat Treatment on the Tensile and Thermomechanical Properties of Bone-Inspired 3D Printable Nanocomposite Biomaterials

5.1. Introduction

As a biological tissue, bone has the ability to remodel and heal itself. This ability to heal itself depends on the size of the defect. When a defect is too large, such as critically sized segmental bone defects in human long bones where gaps are >2.5 cm in length [9], the bone does not heal effectively and often results in fibrous non-union. These large gaps can be caused by traumatic injury, surgical treatment of infections or tumours. Every year over 2.2 million people in the world receive bone grafting surgeries to repair large bone defects [315] [10]. Conventional bone grafts such as bone allografts or metal mega-prostheses have disadvantages, such as the need for at least two or three revision surgeries, mechanical failures, stress shielding, immune rejection, and disease transmission, all of which may cause complications, poor outcomes and poor quality of life for the patient [13,14,257,316,317]. Hence, there is increasing demand for new technologies for fabricating long-lasting, biocompatible, bioresorbable and customized bone substitutes [15]. Bone-inspired nanocomposite grafts with their osteoconductive and biocompatible features are an alternative to conventional bone substitutes [14]. The selection of an appropriate material composition and manufacturing procedure that can generate a robust structure are challenges in the development of synthetic bone-inspired grafts and solutions may be inspired by bone tissue itself. Indeed, bone is a natural nanocomposite and its distinctive feature is its hierarchical structure - all the way down to the nano-scale - which provides excellent mechanical properties [318–321]. A primary concern in designing bone-inspired biopolymer nanocomposites is the selection of the constituent phases. These biocompatible nanocomposites should provide adequate structure and mechanical properties to withstand physiological loads in the body. They should provide both functionality and load-bearing capability with adequate strength and modulus to be used as bone substitutes in critically sized segmental bone defects, for example [18].

Multi-scale structure can play a key role in enhancing mechanical properties without changing the chemical composition of the composite materials. To develop a bone-inspired nanostructure, the fabrication procedure might control the arrangement of nano-scale inclusions as well as the layers of the structure at larger length scales [19]. Three-dimensional (3D) printing is an additive manufacturing method that has advanced in the field of tissue engineering for the repair and regeneration of injured bone tissue in order to produce bone substitutes as a potential replacement for existing transplant tissues [322,323]. Direct Ink Writing (DIW), which is an extrusion-based 3D printing method, can be an appropriate manufacturing method for printing bone-inspired nanocomposites due to its control of the microstructure, effective spatial resolution, low operation cost, adaptable set-up and high printing speeds [324]. The advantage of DIW compared to other fabrication techniques is that custom-designed materials with precise complex hierarchical structures may be achieved by controlling the extrusion parameters such as feed rate, needle size as well as ink rheological behaviour [19]. DIW has been used to print polymer-based inks such as polycaprolactone (PCL) and poly (lactic-co-glycolic acid) (PLGA) or photo-cross-linkable monomers such as hydroxyethyl methacrylate (HEMA), which demonstrated good printability and biocompatibility in bone scaffold fabrication but lacked adequate mechanical properties for bone repairs [325–330]. Biopolymer-based inks, as well as other photo-cross-linkable hydrogel inks like methacrylated alginate [18], gelatin methacrylate (GelMA) [16,17], methacrylated hyaluronic acid [13] and poly(ethylene glycol) dimethacrylates (PEGDMA), have also been used in this technique for preparing bone substitutes, but they also exhibit inadequate mechanical properties for bone repairs. Various scaffold design methodologies, materials and cells have been studied in recent years in an attempt to enhance a successful interaction with native bone [331,332]. Studies show that polymer nanocomposites provide better biocompatibility and mechanical properties compared to conventional polymeric biomaterials because of their nano-scale reinforcement, such as with nHA, the interaction between matrices and mineral phases, large surface-to-volume ratio and surface chemistry [333–341]. Developing 3D printable nanocomposite inks with enhanced mechanical properties can lead to the construction of long-lasting robust scaffolds produced by layer-by-layer deposition of extrusion-based 3D printed nanocomposite filaments [276]. Therefore, integrating 3D printing techniques with nanocomposite biomaterials can facilitate the fabrication of bone substitutes with improved physicochemical and mechanical properties [342,343]. The challenges found in the processing of nanocomposite materials are usually larger

than those encountered in the processing of neat polymer [344]. The process and design parameters are reported to have a crucial influence in determining the final properties of additively manufactured bone substitutes [344]. In this regard, the influence of the process parameters such as porosity, spatial distribution and pore size have been investigated on the mechanical and morphological properties of 3D extruded PCL (poly (ε-caprolactone), aliphatic polyester) scaffolds [345]. Also, different optimized design strategies of the extrusion/injection process have been employed for fabricating customized additively manufactured PCL/HA nanocomposite scaffolds for hard tissue regeneration. The reported design strategy additionally emphasized the possibility of tailoring the performances of 3D additive manufactured scaffolds via a suitable material-design combination [344]. It has been reported that extrusion-based additive manufacturing provides a higher degree of control on the structural properties of 3D printed scaffolds and more feasible manipulation of mentioned processing parameters [344].

Thermoset polymer resins can make excellent composite matrices as they provide good physical and mechanical properties, thermal and chemical resistance, and processability [161]. Acrylated epoxidized soybean oil (AESO), a functionalized triglyceride, which is a plant-based biopolymer and obtained from renewable resources, is prepared by adding acrylate groups to epoxidized soybean oil and is a great candidate for photopolymerization-based biomedical 3D printing [154,155,219,346]. This multifunctional, inexpensive and commercially available functionalized triglyceride has been utilized as a monomer for the synthesis of various thermoset polymers [157,159]. Miao et.al [64] synthesized soybean oil-based polyol by ring-opening reaction of epoxidized monoglyceride (EMG) with lactic acid. They were able to alter the tensile strength from 9.30 MPa to 27.1 MPa by adjusting the molar ratio of hydroxyl to isocyanate group and the chain extender content. They revealed that the soybean oil-based polyurethanes' good mechanical properties and biocompatibility make them a promising candidate for a broad range of biomedical applications. Liu et al demonstrated increased degree of cross-linking and hence stiffness as a result of further modification of AESO with methacrylate anhydride (MAA), replacing the hydroxyl groups of AESO with methacrylate groups [18]. One of the major challenges in the production of polymer nanocomposites is the agglomeration of nanoparticles at micron length scales which cause clogging issues during printing [323] and may function as stress concentrators for the matrix [347]. They hinder the potential of high-performance nanocomposites with enhanced mechanical properties [347,348]. Therefore, designing a 3D printable bone-mimetic polymer

nanocomposite biomaterial with sufficient printability and mechanical properties could open the way for the fabrication of long-lasting 3D printable bone grafts that eventually become suitable for clinical translation. Hydroxyapatite is a biocompatible and osteoconductive bioceramic that has been widely used for bone defect repair and regeneration [297,349–352]. The nanohydroxyapatite (nHA) particles are hydrophilic [353] while the AESO biopolymer matrix is hydrophobic [353]. Due to the incompatibility of these two phases, any moisture absorbed by nHA particles attracts other nHA particles, resulting in agglomerations trapped in the hydrophobic AESO biopolymer during the production of biopolymer nanocomposite inks. It has been reported that heating nHA before adding it to the nanocomposite ink helps to remove absorbed moisture [18,354]. However, how this impacts the nHA dispersion as well as mechanical properties has not been investigated.

In the current study, a set of novel 3D printable bone-inspired nanocomposite biomaterials with in vitro bone cell compatibility [20,63,84] were produced with the goal of achieving improved mechanical properties and towards the eventual application in bone reconstruction technologies. These inks have been made by combining distinct AESO-based biopolymer resins (functionalized and non-functionalized) with and without heat-treated nHA particles in a constant volume fraction of nHA. One of the important factors in designing 3D printed grafts is reaching superior mechanical properties that are adequate to be used as bone substitutes. We hypothesized that additional functionalization of the biopolymer matrix of our nanocomposites, while maintaining a constant nHA volume fraction, would give rise to an increase in the degree of cross-linking and therefore enhanced tensile and thermo-mechanical properties. Good dispersion of nanoparticles is crucial for getting the most out of nanoscale fillers in polymer nanocomposites, which contributes to improved mechanical behaviour [355]. As aggregated particles limit nanocomposite strength, we hypothesized that heat treatment of the nanohydroxyapatite particles, driving off water molecules, would lead to better dispersion of the nanoparticles and improved mechanical properties.

5.2. Materials and Method

5.2.1. Ink Composition

Rod-shaped hydroxyapatite nanoparticles (nHA) with 120nm length, 30–40 nm diameter, and a calcium-to-phosphorous ratio of 1.52 (MKNano, M K Impex Corp., Mississauga, Canada) were employed in the nanocomposite inks developed herein. The nanoparticles have a specific gravity of 2.92 and a crystallinity index of 0.52–0.54 on average [20].

All reagents were purchased from Sigma Aldrich Co. USA. The biopolymer matrix in two groups of inks was a mixture of AESO (as purchased) and PEGDA (250 MW). This material can be polymerized using UV light by adding Phenylbis (2, 4, 6-trimethyl benzoyl) Irgacure 819 phosphine oxide photoinitiator. For the other two groups of nanocomposite inks, the biopolymer matrix was a mixture of AESO functionalized with additional methacrylate groups and PEGDA.

5.2.2. Ink Preparation

5.2.2.1. Preparation of mAESO

Before preparing the inks, AESO was additionally functionalized with methacrylate groups. To do this, 39.7 ml methacrylic anhydride (MAA) was mixed with 0.51 g of 4-(Dimethyl Amino) pyridine (DMAP) (0.004 mol) on a stir plate at 500 rpm for 15 min until the DMAP dissolved completely in MAA. Then this mixture was added to 50 g of AESO (AESO: MAA molar ratio of 1:6) and the DMAP, MAA and AESO mixture was placed in a water bath at 60°C with continuous stirring at 500 rpm for 24 hours. During the functionalization process, hydroxyl groups on the AESO were replaced by methacrylate groups, resulting in a new biopolymer known as mAESO (Fig. 5.1(a)). After the functionalization procedure, the reaction products were washed with NaOH solution (100 mol of 0.5 M) and deionized water and then held under reduced pressure in the desiccator until it was dried. To ensure this, the weight change of the mixture was recorded daily until obtaining a constant weight.

5.2.2.2. Heat Treatment of nHA Particles

To eliminate the absorbed water from the nHA particles, they were heated in an oven at 120 °C for one hour. Then kept in a fume hood while covering the lid of the container with aluminum foil to reach room temperature before adding to the biopolymer matrix mixture.

5.2.2.3. Mixing the biopolymer matrix and nHA particles

A set of novel 3D printable bone-inspired nanocomposite inks was produced by mixing (30%vol. nHA) (Heat-treated vs. non-heat-treated) with (49%AESO) (Functionalized/non functionalized) and (21%PEGDA). The compositions of these inks are summarized in Table 5.1. First, the desired amounts of AESO (or mAESO referred to as functionalized AESO) and PEGDA were combined and homogenized using an ultrasonic homogenizer (Branson Sonifier 450, Emerson Inc., USA). Next, the Irgacure 819 (photoinitiator, 1 vol% of total ink) was dissolved in the resin and further homogenized. Finally, nHA particles (as-purchased or heat-treated) were added gradually (1 - 2 scoops at a time) to the mixture. To drive the dispersion of nHA particles in the mixture, an ultrasonic homogenizer was applied for 30 min until the desired amount of nHA particles was reached (Fig. 5.1(b-c)). The four different compositions will hereafter be referred to as SP30, SP30h, mSP30 and mSP30h according to Table 5.1.

Table 5.1. Nomenclature of the four 3D printable nanocomposites according to their constituents.

	As Purchased nHA	Heat-Treated nHA
As Purchased AESO	**SP30**	**SP30h**
Functionalized AESO	**mSP30**	**mSP30h**

*Constant Percentage Composition for all Four Groups: 49 vol% AESO, 21 vol% PEGDA, 30 vol% nHA

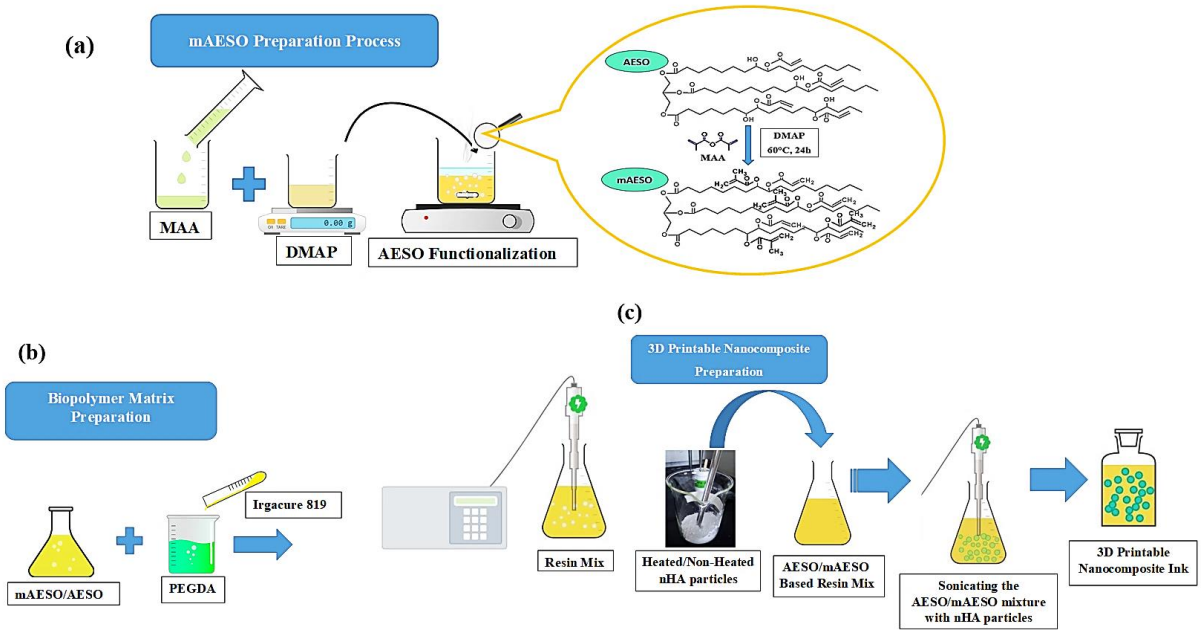


Fig. 5.1. 3D printable nanocomposite ink preparation: (a) Functionalizing AESO for preparation of mAESO, (b) biopolymer matrix preparation by mixing AESO (mAESO) with PEGDA and photoinitiator, (c) Adding nHA to biopolymer matrix mixture

5.2.3. Preparation of 3D printed nanocomposite filaments

After preparing the inks, nanocomposite filaments were extruded using a custom-built extrusion-based 3D Printer referred to as SkelePrint. In contrast to commercially available flatbed 3D printing systems, the SkelePrint system [356] is designed to 3D print objects by depositing extruded nanocomposite filaments in concentric layers on the mandrel bed. The drive assemblies of this custom-designed 3D printer consist of a linear motion in the radial and axial direction and a rotary motion about the axis of the mandrel. SkelePrint has an adjustable mounting configuration for the UV lamps (385 nm, at 175 mW/cm2 intensity, BlueWave® QX4® LED Spot-Curing System, Dymax Corp., USA). UV light position can be manually adjusted circumferentially around the mandrel print bed axis [356], linearly along the length of the print bed axis, and normally towards the print bed axis using the UV lamp mount. The mounting UV system cures and bonds extruded filaments to previously extruded filaments. These mounting systems allow regulated UV light exposure on the extruded photosensitive nanocomposite material while 3D printing complicated microstructural layups. A pressure regulator was installed to control the pressure during the extrusion of nanocomposite filaments. To begin printing filaments, the compressed air pressure was first set to the required value using the regulator and pressure gauge,

and then the valve opened using the 3D printer's control software. Due to the effect of applied shear during extrusion on the final mechanical properties of extruded nanocomposite filaments [356], all four sets of nanocomposite inks were printed with a constant compressed air pressure of 592 kPa through a 6.35-mm long stainless steel 20-gauge (0.6 mm internal diameter, Precision stainless steel tips, Nordson, EFD, USA). To demonstrate the developed inks' further printability and shape-holding ability for printing complicated objects, two 3D printed samples with both heated non-functionalized and heated functionalized nanocomposite inks (SP30h and mSP30h) were manufactured (Fig. 5.2 (a-b)) using the Skeleprint system.

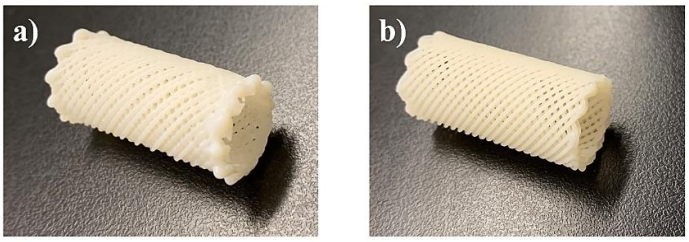


Fig. 5.2. 3D printed samples with developed nanocomposite inks: (a) 3D Printed sample with SP30h nanocomposite ink b) 3D Printed sample with mSP30h nanocomposite ink

5.2.4. Characterization of Nanocomposites

5.2.4.1. Rheology of the nanocomposite inks

To investigate the effect of AESO functionalization and nHA heat treatment on the rheology of the inks and determine if all the inks had the appropriate rheological behaviour for extrusion-based 3D printing, a Bohlin CS Rheometer equipped with a cone and plate arrangement (CP 4/40, with 150 μm gap) was used to obtain the viscosity and shear yield strength of each ink by testing three specimens per group (n=3). The tests were conducted at room temperature under shear rates from 0.01 s^{-1} and 100 s^{-1}. The viscosity was recorded at 10s intervals for each shear rate.

5.2.4.2. Cure Depth Analysis

Cure-depth analysis was used to determine the UV dosage necessary for the curing of extruded nanocomposite filaments. Cylindrical PTFE molds were filled with nanocomposite inks and exposed to known UV doses using a Dymax UV device (BlueWave® QX4® LED Spot-Curing System, Dymax Corp., USA) at the top end of the cylindrical hole. After curing, the solid layers

were rinsed with ethanol and the thickness of the cured layer was measured using digital calipers with a precision of ±0.01 mm (n=3). Jacob's standard cure-depth equation (Equation 5.1) [118] was fitted to the experimental data using a Genetic-algorithm optimization [357] method to find the cure-depth material constants for each nanocomposite system.

$$Z_c = D_p \ln\left(\frac{E}{E_c}\right) \tag{5.1}$$

where, Z_c is the cure depth, D_p and E_c are the depth of penetration and critical dosages respectively. Next, the required UV dosages and durations for each nanocomposite system were calculated from this equation using the obtained constants and a known UV intensity measured with a radiometer (ACCU CAL 50V, Dymax Corp., USA).

5.2.4.3. Fourier-Transform Infrared Spectroscopy (FTIR)

To assess the chemical composition, curing and conversion efficiencies, Fourier Transform Infrared Spectroscopy (FTIR) was conducted on the surfaces of cured nanocomposite samples (n=3). A Nicolet 6700 FT-IR Spectrometer (Thermo Scientific, USA) having a resolution of 4 cm^{-1} and a sample scan of 32 was used to obtain the FTIR spectra. All spectra were analyzed using OMNIC series software.

5.2.4.4. Thermo-Gravimetric Analysis (TGA)

Thermo-Gravimetric Analysis (TGA) analysis was used to determine the organic-inorganic ratios and thermal degradation of the 3D printed nanocomposites. Approximately 10-15 mg of each 3D printed nanocomposite specimen (n = 3) was heated and burned using a TA Q500 (TA Instruments Inc., New Castle, DE). The samples were heated to 800 °C in an air environment at a rate of 10 °C/min. Before heating, the samples were equilibrated at 40°C for 5 minutes. The organic-inorganic ratio of the nanocomposites was calculated using the remaining measured mass at 800 °C. The organic-inorganic volume fraction of each nanocomposite specimen was calculated by taking the remaining mass (inorganic) with the density of the nHA ($\rho_{nHA} = 2.92\,\frac{g}{cc}$) and the initial mass of the nanocomposite sample with the density of the nanocomposite ink ($\rho_{Ink} = 1.628\,\frac{g}{cc}$).

5.2.5. Mechanical Testing and Strain Measurements of Nanocomposite Filaments

Once single filaments were extruded (Fig. 5.3(a)), they were tensile tested to obtain their mechanical properties. To hold the filaments in the tensile grips of the testing machine, trapezoidal tabs were designed with a cylindrically shaped indent (Fig. 5.3(b)) to conform to the shape of the filament cross-section and were 3D-printed using a masked stereolithography (mSLA) 3D printer [219] (Fig. 5.3(c)). Filaments were cut consistently to 20 mm lengths. Epoxy adhesive (West System 105 resin, West System 205 hardener) was used to adhere the trapezoidal tabs (7 mm long) to both ends of each filament. The gauge length between the tabs was kept constant at 6 mm for all filaments (n=7). To make the specimens stable and to prevent the filaments from pulling out of the tabs during the tensile test, another trapezoidal part was glued to the other side of each filament head (Fig. 5.3(c)). After preparation, tensile testing was conducted on specimens of each group (Fig. 5.3(d)). All tests were conducted using a Psylotech μTS mechanical testing frame (1.6 kN load cell capacity, Psylotech Inc., Evanston, IL, USA), which is mounted on a vibration isolation table (Vision Isostation, Newport Corp., California, USA) (Fig. 5.3(d)). Strain measurements were conducted during the test via microscope-enabled Digital Image Correlation (DIC; Vic 2D 6, Correlated Solutions Inc., USA). A microscope (BXFM, Olympus Corp., Center Valley, PA, USA) with a mounted digital camera (Point Grey, 5 MP, 2/3" detector) captured magnified images of the gauge length during the test (Fig. 5.3(d)). Tests were conducted in displacement control at a rate of 16 μm/s, resulting in an average strain rate of 0.0024 s^{-1}. Data were collected at a rate of 5 Hz, and all experiments were carried out at room temperature. Before testing, specimens were sprayed using an atomizer jar filled with high-resolution toner powder (Xerox Phaser 6000 laser toner cartridge) to add a speckle pattern to enable DIC analysis. These toner particles are approximately 4–5 μm in diameter, which is suitable for 2D DIC using a 5x objective.

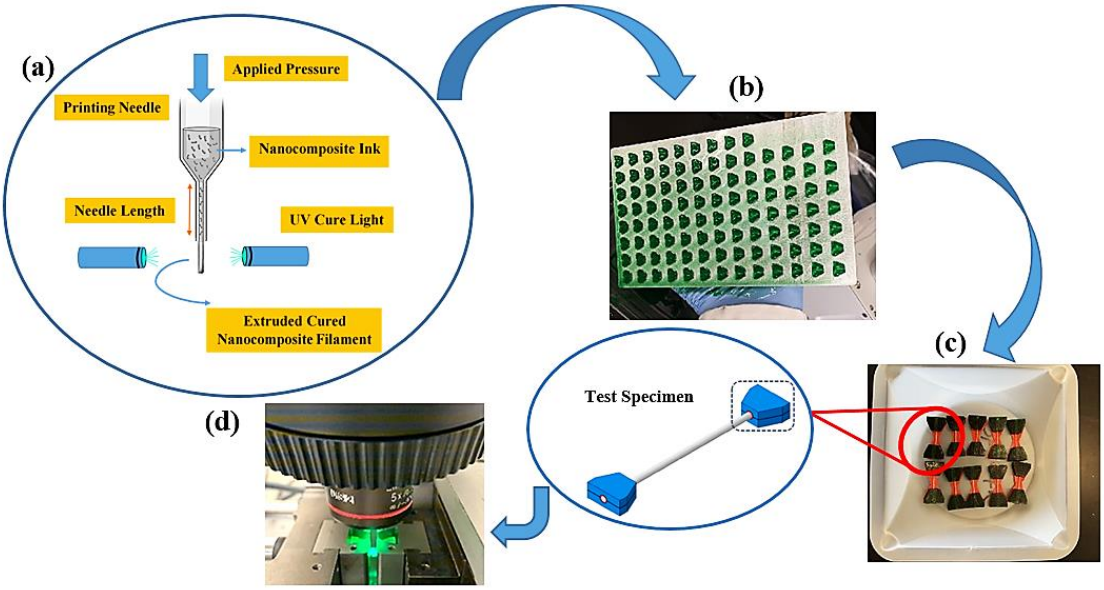


Fig. 5.3. Nanocomposite filament extrusion, sample preparation process and tensile test configuration. a) Extrusion of single nanocomposite filaments b) Trapezoidal tabs printed with mSLA printer. c) Schematic [219] and final filament test specimens. d) Psylotech mechanical testing machine and filament specimen in the test frame.

Strain measurement was conducted by feeding the captured images during the tensile test to the DIC software (Vic 2D). An Area of Interest (AOI, 4.03 mm length, 0.4-0.5 mm width) was selected on the reference image. The subset window and step size were set to 150 and 7 pixels, respectively, for all the tests (1 micron=1.373 pixel). To be consistent for strain measurement in all specimens, average engineering strain values were measured from DIC by using the extensometer tool over the length of AOI in each sample. Engineering stress values were derived by dividing the force by the initial cross-sectional area of the filaments. The ultimate stress and the slope of the first linear elastic parts of the stress-strain curves were used to calculate the tensile strength and elastic modulus, respectively.

5.2.6. Imaging of nHA dispersion and filament fracture surfaces

Sectioned filaments were mounted in a cylindrical mold with epoxy resin (West System 105 resin, West System 205 hardener) to image the longitude and transverse cross-sections of the filaments, respectively. After 24 hours, the resin-embedded filament was polished sequentially with 6μm, 0.05 μm and 0.01 μm sized polycrystalline diamond suspension (MetaDi Supreme, Buehler, IL, USA). After polishing, the embedded filaments were imaged by scanning electron microscopy (SEM) and Back-Scattered Electron microscopy using a Quanta FEG 250 (ThermoFisher

Scientific, USA) in low vacuum mode. The fracture surfaces resulting from tensile testing of the filaments were mounted on SEM stubs without any treatment to obtain SEM images of fracture surfaces for each nanocomposite system.

5.2.6.1. Image analysis of nHA dispersion

In order to investigate the effect of heat-treated nHA vs as-purchased nHA on the dispersion of nanoparticles in the resin using quantitive methods, counting was performed using image processing techniques through ImageJ software [358]. SEM images of the extruded filaments' longitudinal sections for all the four studied nanocomposite groups were imported (n= 3). Initially, the image was converted to an 8-bit greyscale image. Then the image was calibrated [359,360]. To be consistent, a constant area of 240 μm by 400 μm was selected in all images as the Region of Interest (ROI). *Image pre-processing* was conducted on the ROI by selecting the appropriate filters [361]. After calibration, the image was pre-processed using a Band-pass filter which eliminates both high and low spatial frequencies [362]. *Image segmentation* was implemented by binarizing the image using the threshold function (default threshold (102,255)) [360]. Finally, after the image segmentation process, the microscale agglomerations of nanoparticles were counted using the *analyze particles* function by setting the size (1 μm - inf), and circularity (0-1) to capture the micro-scale agglomerations.

5.2.7. Differential scanning calorimetry (DSC)

Material characteristics including crystallisation temperature, crystallinity, melting temperature, and glass transition temperature can be determined using differential scanning calorimetry (DSC). This study employed DSC to measure the degree of crystallinity that resulted from the extrusion of each set of nanocomposites (n=3) by evaluating the enthalpy of melting [287]. Before sealing the prepared nanocomposite filaments in Tzero Aluminum Hermetic pans, they were weighed (7±1 mg) on an analytical balance (Kern, ABT 120-5DM, Germany, ±0.01 mg precision). Then the prepared pans were placed on the sample platforms to run the DSC. The samples were heated to 25 °C at 10 °C/min and equilibrated for 5 min. Then the specimens were cooled down to -25 °C at 10°C/min followed by heating up to 350 °C at 5 °C/min. The maximum temperature of the DSC experiment is chosen based on the decomposition temperature observed in the TGA experiments.

Enthalpy of melting was obtained by measuring the area beneath the melting endotherm zone of heat flow vs temperature graphs normalized to sample mass.

5.2.8. Dynamic Mechanical Analysis (DMA)

Dynamic mechanical analysis (DMA) was performed using a DMA Q800 from TA Instruments (USA) in three-point bending mode using dual cantilever clamps at an oscillatory frequency of 1 Hz, under a 0.02% strain amplitude, for a temperature range from -20 $^{\circ}$ C to 120 $^{\circ}$ C and at a heating rate of 3 $^{\circ}$ C /min. Test specimens with 120 mm in length, a width of 12 mm and a thickness of 3mm, were cast using a machined Teflon mold. To minimize trapped air bubbles during casting, all inks were put under a vacuum for 20 min before preparing the samples. For consistency, all the cast samples were cured for 20 min (10 min for each side) in the UV oven.

5.2.9. Statistical Analyses

The data are represented using mean and standard deviation (SD). Data were analysed using SigmaStat (Version 4.0, Systat Software Inc., CA, USA). To compare means, a Two-way analysis of variance (ANOVA) was utilized, followed by Tukey's multiple comparison test. At $p<0.05$, the differences in means were declared statistically different.

5.3. Results

5.3.1. Characterization of nanocomposite

The rheological properties of our 3D printable nanocomposite inks define the shape-holding ability of the filaments before curing, as well as the flow during extrusion-based 3D printing. Fig. 5.4(a, b) demonstrates the representative shear stress and viscosity vs. shear rate plots, respectively. The rheology properties are reported in Table 5.2. The mSP30 nanocomposite ink had a higher shear yield strength than the rheometer's stress limit.

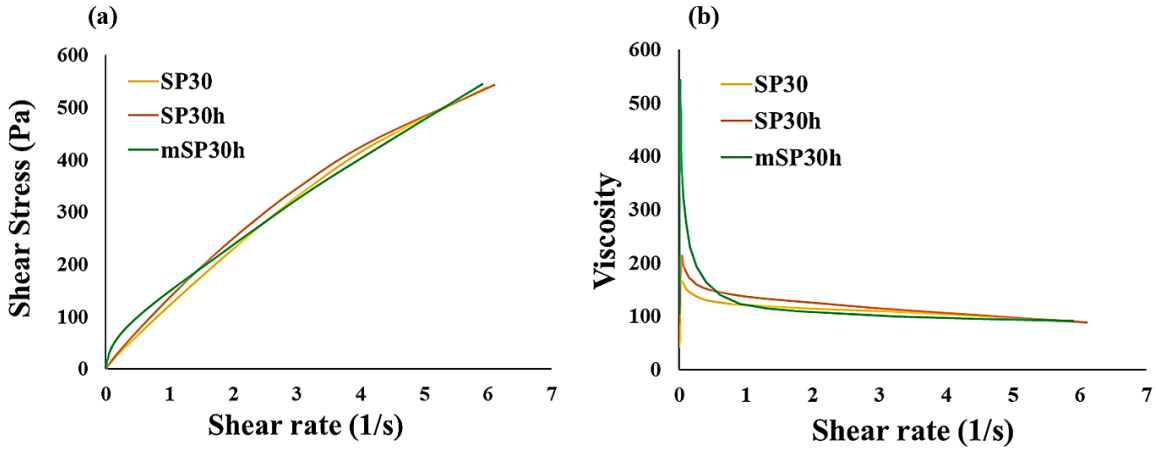


Fig. 5.4. Rheological data of the three nanocomposite inks over a variety of shear strain rates. a) Representative shear stress vs shear strain rate curves b) Representative viscosity vs shear strain rate curves.

Table 5.2. Viscosity and shear yield strength results of as-prepared nanocomposite inks (n = 3; data are presented as mean ± SD) Different lower-case letters indicate statistically significant differences (p <0.05).

	Shear Yield Strength (Pa)	**Viscosity (Pa.s)**
SP30	9.77±1.42[a]	83.36±13.94[a]
SP30h	16.07±1.02[a,b]	94.51±10.12[a]
mSP30h	21.76±3.37[b]	91.15±3.92[a]

As indicated in Table 5.2, no statistically significant differences were detected in the viscosity data for the studied inks. Functionalization and heat treatment of nHA particles simultaneously increased the shear yield strength from 9.77±1.42 Pa to 21.76±3.37 Pa which provides a better shape holding ability for the ink during the DIW printing.

By constructing standard cure depth curves, the UV doses necessary for successful curing of various layer thicknesses were calculated. Fig. 5.5(a) shows plots of cure depths in response to varied UV doses for the SP30, SP30h, mSP30 and mSP30h nanocomposite inks. The functionalization reduced the cure depth throughout the same dosage range. In propagating the end group in radical polymerization, acrylate groups (AESO based groups) produce secondary radicals, whereas methacrylate groups (mAESO based groups) produce tertiary radicals (which are more stable than a secondary radical). The tertiary radical's stability is assumed to reduce the reactivity of the propagating end for further polymerization [363]. The material constants fitted to the cure depth curves are reported in Table 5.3. The depth of penetration (D_p) value was almost the same in all groups but the critical dosages (E_C) had greater values for the mSP30 and mSP30h groups.

Table 5.3. Cure depth material constants for the nanocomposite inks.

Material Constants	D_P	E_C	R^2
SP30	0.244	5.3885	0.9655
SP30h	0.268	14.47	0.973
mSP30	0.249	16.807	0.952
mSP30h	0.250	16.541	0.9516

The FTIR spectra analysis of all cured SP30, SP30h, mSP30 and mSP30h nanocomposite 3D printable inks are shown in Fig. 5.5(b). No peak associated with the strong alkene stretching vibration for C=C at 1646 cm^{-1} was detected, indicating the lack of vinyl groups in all spectra obtained for four studied groups of nanocomposites. A very small peak at 806 cm^{-1} related to asymmetric vibration of out-of-plane vinyl groups was observed which suggests the presence of a very small amount of unreacted monomers in the resin. Peaks at 1018 cm^{-1} are attributable to the PO_4 from nanohydroxyapetite in all spectra. Thermograms from TGA analysis of SP30, SP30h, mSP30 and mSP30h are shown in Fig. 5.5(c-d). The final residual mass in all four groups of inks corresponds to the final nHA particles in the nanocomposite. The nHA volume fraction after burnout samples for each of SP30, SP30h, mSP30 and mSP30h was calculated to be 29.61± 0.67 % (n=3) which was close to the target volume fraction of 30%. The peak temperature for all four groups of inks was in the 300-500 °C range. To compare the decomposition behaviour of each nanocomposite in different temperature ranges the peak points of the derivative loss weight curves for each nanocomposite have been captured accordingly in Table 5.4. As indicated in Table 5.4, the decomposition temperatures are significantly different between functionalized and non-functionalized groups and the decomposition of functionalized groups is initiated at a higher temperature than in non-functionalized.

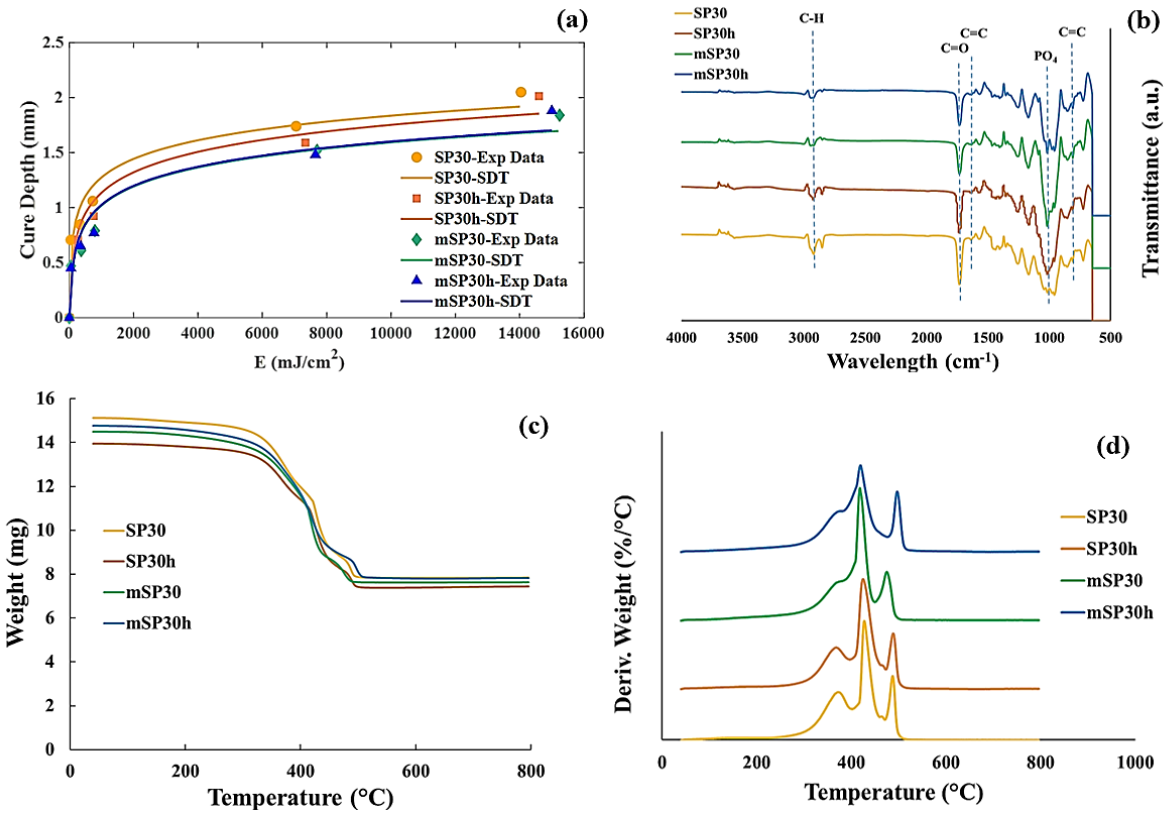


Fig. 5.5. (a) Cure depth vs. UV energy dosage for SP30, SP30h, mSP30 and mSP30h nanocomposites. Data are mean ± SD. b) FTIR spectra of cured nanocomposites c) Representative DTG thermograms of cured nanocomposites. d) Representative TGA thermograms of cured nanocomposites.

This is presumably due to the greater cross-linking in mSP30 and mSP30h which provokes a higher temperature required to start the decomposition compared to the SP30 and SP30h.

Table 5.4. Peak temperatures of derivative loss weight vs temperature curves for studied nanocomposites obtained from TGA (n = 3; data are presented as mean ± SD), Different lower-case letters indicate statistically significant differences (p <0.05).

	1st derivative peak temperature (°C)	*2nd derivative peak temperature (°C)*	*3rd derivative peak temperature (°C)*
SP30	366.88 ± 3.06[a]	424.4 ± 3.03[a]	486.93 ± 2.81[a]
SP30h	373.41 ± 1.91[a]	426.83 ± 1.56[a]	489.01 ± 0.87[a]
mSP30	418.04 ± 1.04[b]	486.14 ± 9.18[b]	-
mSP30h	418.04 ± 0.13[b]	493.63 ± 4.18[b]	-

5.3.2. DSC analysis

Representative DSC thermograms of extruded filaments, from four groups of nanocomposites, are shown in Fig. 5.6(a). which represents the heat flow versus temperature. In all four groups of extruded filaments, there are two visible endothermic peaks. The first peak in all groups occurred at around 190°C and the second peak occurred in the range of 280-300 °C.

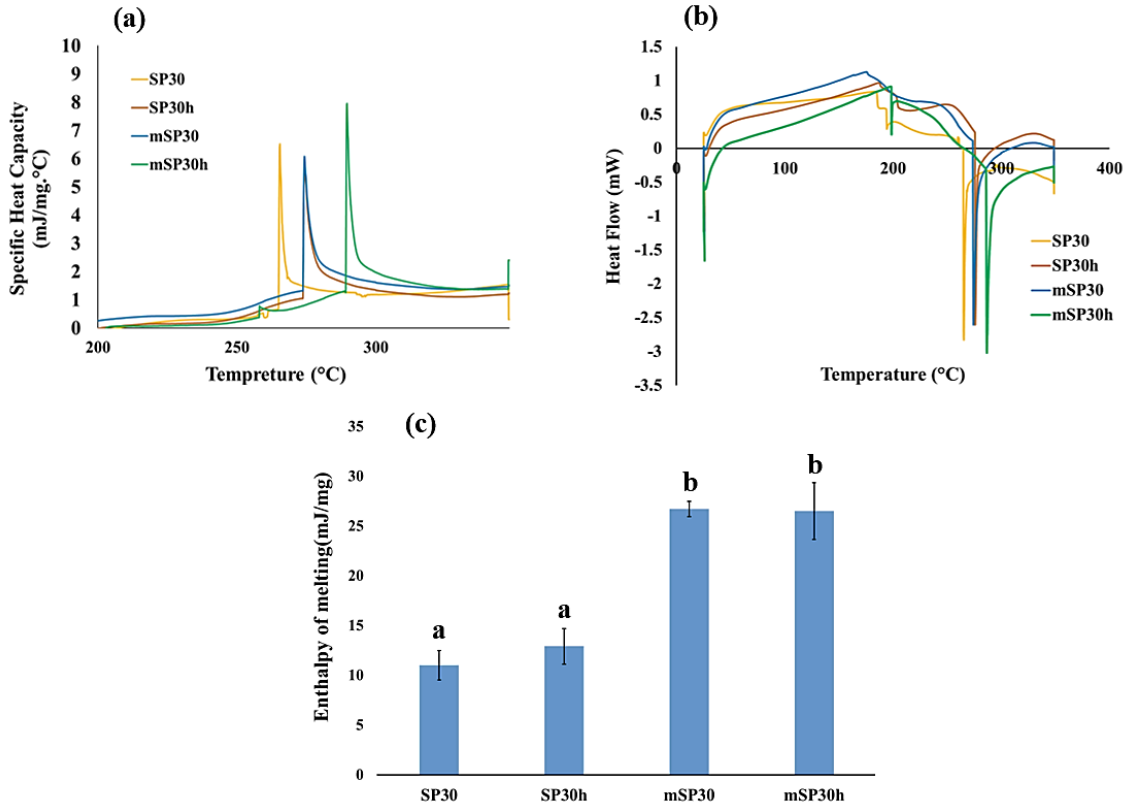


Fig. 5.6. DSC data. a) Representative DSC thermograms b) Representative specific heat capacity versus temperature c) Melting enthalpies of the four nanocomposite systems.

Fig. 5.6(b). shows the representative specific heat capacity (mJ. mg^{-1}. $°C^{-1)}$ curves of four groups of extruded nanocomposite filaments. The melting temperatures increased due to the extra functionalization in the mAESO inks and heat treatment of nHA particles. Fig. 5.6(c) shows the average values of enthalpy of melting for four groups of extruded filaments calculated from the area under the heat capacity vs temperature curves in the same temperature range. The enthalpy of melting of the mAESO-based nanocomposites was more than two times higher compared to those of the AESO-based nanocomposites.

5.3.3. Dispersion of nHA in the nanocomposites

SEM images of the longitudinal sections of the extruded filaments for studied groups of nanocomposites, as well as transverse sections of fracture surfaces for four groups (Fig. 5.7(a-e)), reveal the dispersion of nHA particles in micron scales with some agglomerations observed in longitudinal sections images.

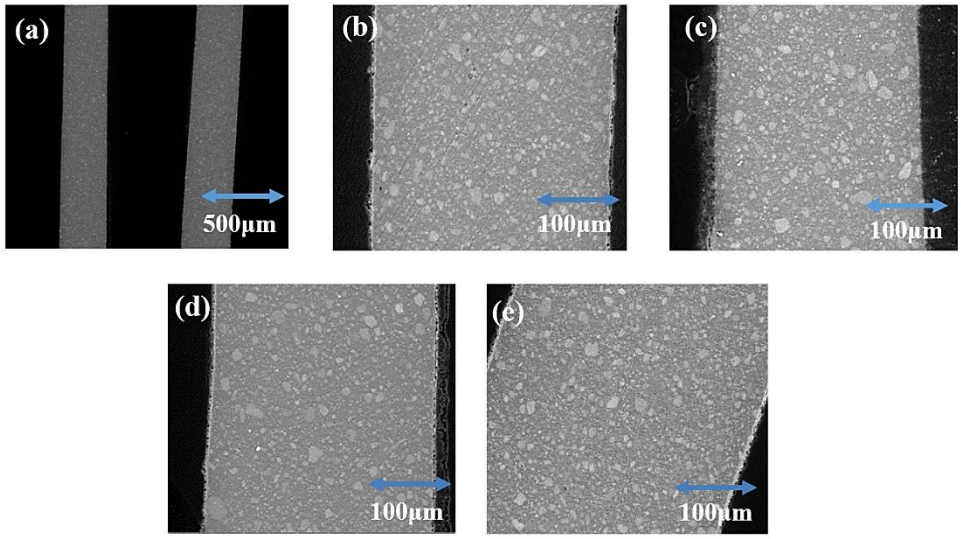


Fig. 5.7. Representative SEM images of longitudinal sections of extruded filaments. a) Longitudinal cross-sections b-e) Longitudinal cross-sections of SP30, SP30h, mSP30, mSP30h in higher magnifications (250 x).

No significant differences were observed regarding the dispersion of nHA particles treated with heat compared to the other groups. The distributions presented in Fig. 5.8. are the result of a quantitative evaluation of the particle agglomerations using the ImageJ data.

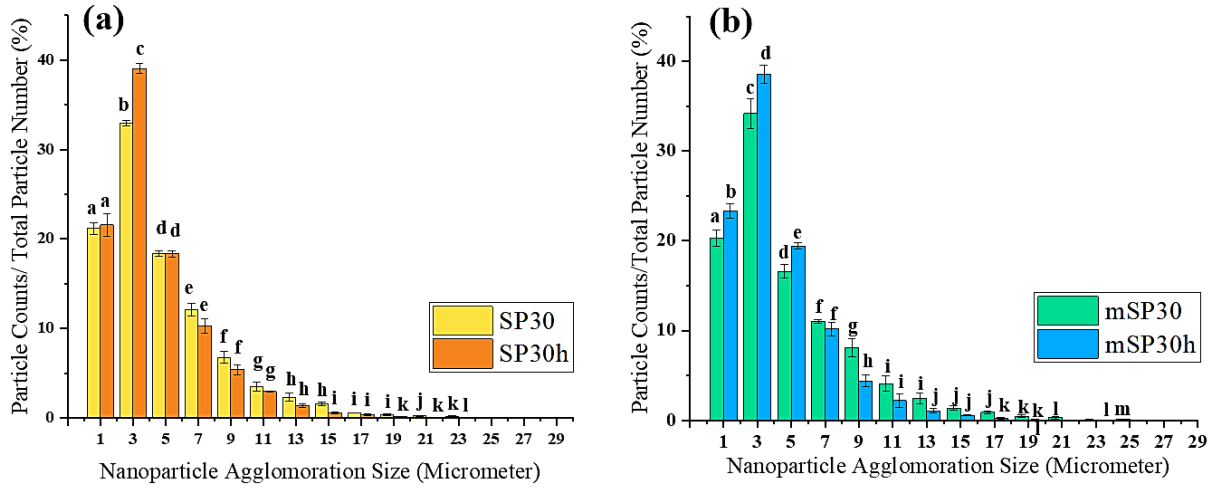


Fig. 5.8. Distribution of nanoparticle agglomerations for D>1 μm a) Distribution of nanoparticle agglomerations in SP30 and SP30h nanocomposite systems b) Distribution of nanoparticle agglomerations in mSP30 and mSP30h nanocomposite systems Dissimilar letters indicate statistically detectable differences in the means ($p<0.05$). (n=3 for each group of extruded nanocomposite filaments)

The peak of distribution for aggregation size, in all four groups of nanocomposites, was in the range of 2.95 ±0.3 μm. As shown in Fig. 5.8(a) and Fig. 5.8(b), the frequency of agglomerations with sizes ranging from 1 μm to 7μm is higher in heated nHA nanocomposites (SP30h and mSP30h) compared to non-heat-treated nanocomposites (SP30, mSP30). While the frequency of agglomerations larger than 7μm was significantly lower in the heated-functionalized nanocomposites (mSP30h) compared to non-heated functionalized nanocomposites (mSP30). No statistically detectable differences were observed in the distribution of agglomerations larger than 7μm in heated-non-functionalized (SP30) compared to non-heated-non-functionalized (SP30h) nanocomposites. Furthermore, as demonstrated in both functionalized and non-functionalized groups, heating reduced the size of the largest agglomeration observed in heated nanocomposites compared to the non-heated nanocomposites. This is most likely due to the fact that heating nHA particles before adding them to inks help to dry the hydrophilic nHA particles by eliminating interfering moisture. As a result, in heated nanocomposite systems, large agglomeration caused by hydrogen bonding between particles is less likely to occur.

5.3.4. Tensile Testing of Nanocomposite Filaments

Representative stress-strain curves and column plots of strength, elastic modulus and fracture strain for the four nanocomposite filaments groups are shown in Fig. 5.9(a-d).

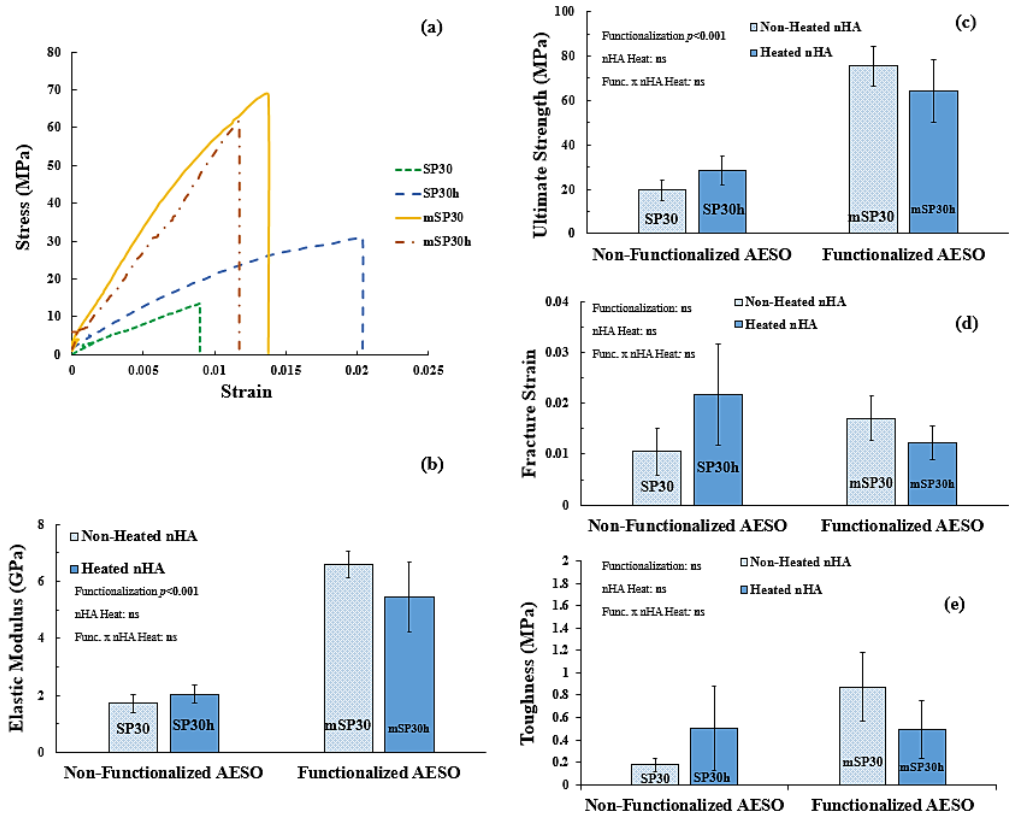


Fig. 5.9. (a) Representative stress-strain curves, (b) elastic modulus, (c) strength, (d) fracture strain of the four novel,(e) Toughness 3D printable nanocomposites in this study (For plots b-d, data are means ± SD (n =7 specimens of each composition). Two-way ANOVA followed by Tukey's multiple comparison tests were used for statistical analysis)

As shown in the plots in Fig. 5.9, the additional functionalization of AESO enhanced both the elastic modulus (Fig. 5.9(b)) and the ultimate tensile strength (Fig. 5.9(c)) more than threefold in a constant volume fraction of nHA. This is due to the increased degree of cross-linking in the mSP30 and mSP30h nanocomposite systems in which OH groups are replaced with methacrylate groups through functionalization. Two-way ANOVA was performed on the data collected for strength, elastic modulus, and fracture strain (n=7). Functionalized and non-functionalized strength and elastic modulus values show statistically significant differences while no significant differences were detected between non-heated and heated data. For fracture strain data (Fig. 5.9(d),

and toughness (Fig. 5.9(e) no statistically significant changes were observed across groups. Considering all data, no significant interactions between heating and functionalization were detected according to the Two-Way ANOVA analysis.

Fig. 5.10(a-h) shows the fracture surfaces of filaments from the SP30, SP30h, mSP30 and mSP30h groups after tensile test. The lower magnification images of fracture surfaces of mSP30 and mSP30h are smoother compared to SP30 and SP30h which suggests more brittle failure.

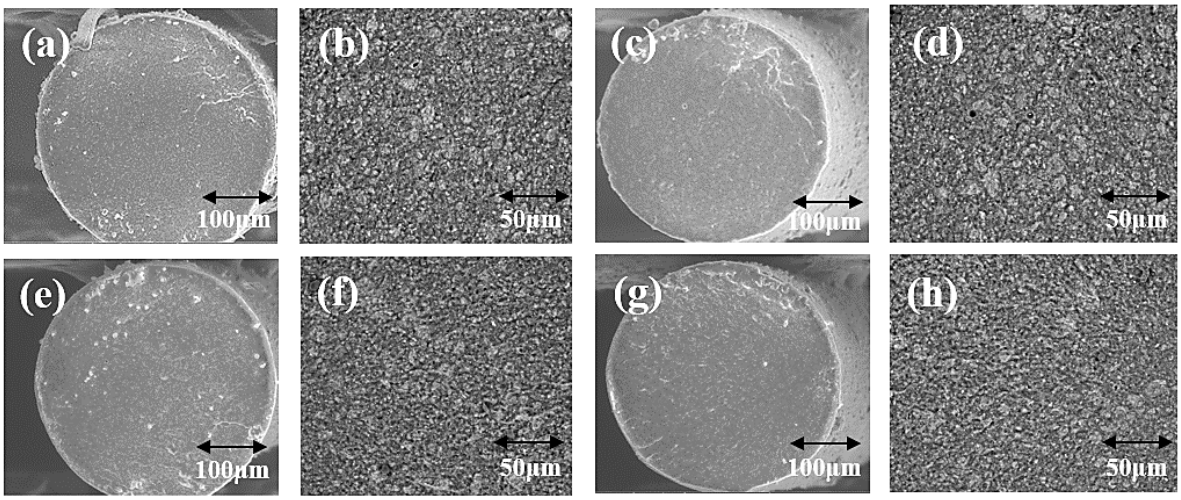


Fig. 5.10. Representative SEM images of fracture surfaces of extruded filaments after tensile tests. a-h) Transverse cross-section of SP30, SP30h, mSP30 and mSP30h respectively in 250x and 500x magnifications

5.3.5. DMA Results

The DMA results for the nanocomposites and their neat resins are shown in Fig. 5.11(a-c). The storage modulus versus temperature is shown in Fig. 5.11(a). At room temperature, the storage modulus (E') of neat AESO resin increased from 0.8 GPa to 4.2 GPa (increased more than four times) by extra functionalizing of AESO. Moreover, the addition of 30% volume nHA particles to this resin increased the storage modulus from 0.8 GPa to 5.9 GPa. Heat-treated SP30h nanocomposite resulted in a similar storage modulus at room temperature compared to non-heated SP30 nanocomposite whereas heat treatment of mAESO-based nanocomposite at room temperature resulted in a minor drop in modulus, which is consistent with the static modulus trend. Adding 30% volume nHA to the functionalized pure resin at room temperature increased the storage modulus from 4.1 GPa to 10.8 GPa. Finally, comparing the functionalized nanocomposite

mSP30 with the non-functionalized SP30 nanocomposite system, the storage modulus increased from 5.9 GPa to 10.8 GPa.

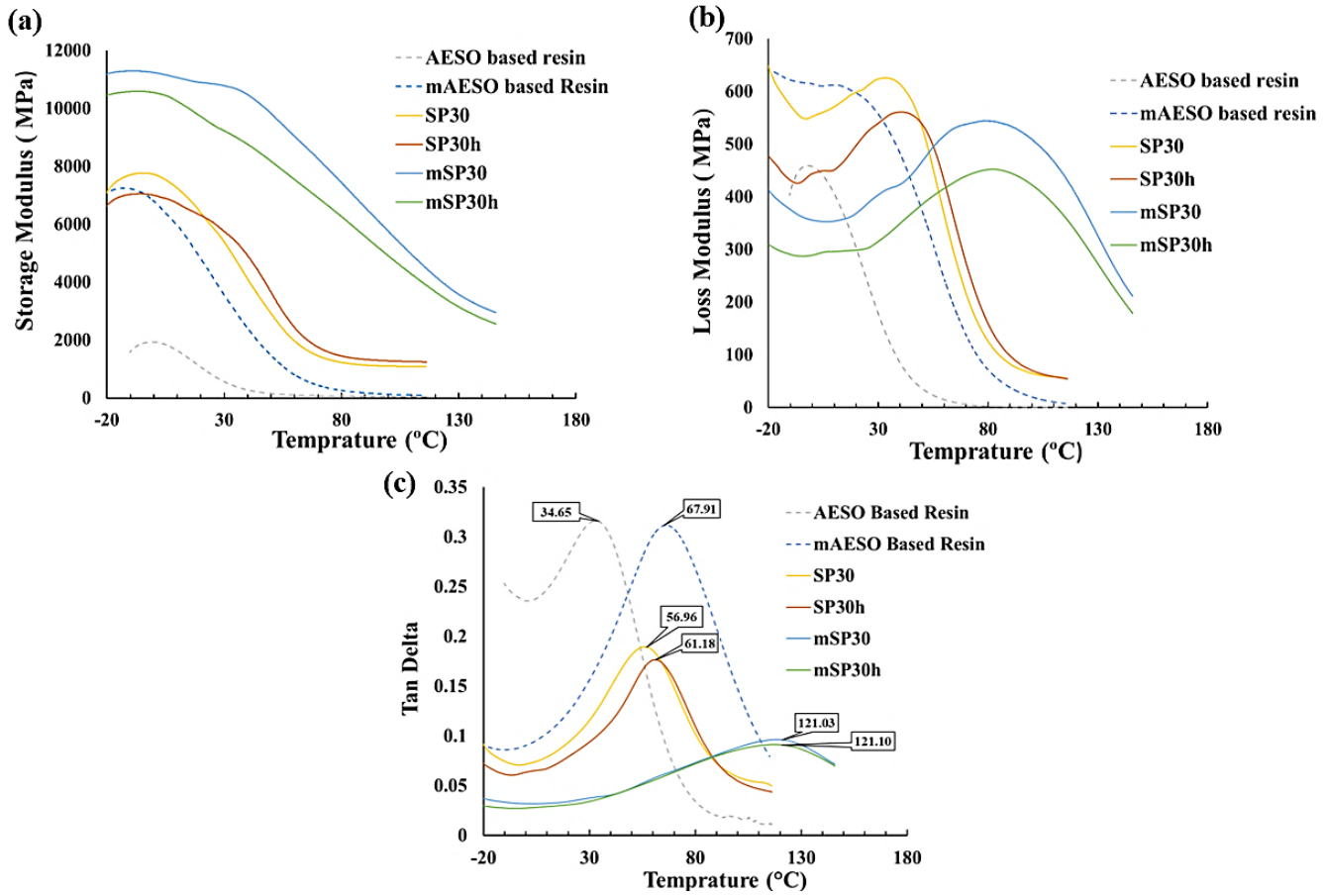


Fig. 5.11. DMA results of AESO and mAESO based neat resins and SP30, SP30h, mSP30 and mSP30h nanocomposites a) Storage modulus vs Temperature b) Loss Modulus vs Temperature c) Tan δ vs Temperature

The loss modulus plots are presented in Fig. 5.11(b) for the neat resins as well as four nanocomposites. The loss modulus (E") of functionalized pure resin at room temperature, increased about three times compared to the non-functionalized pure resin. While the loss modulus of functionalized nanocomposite (mSP30) at room temperature compared to SP30 has decreased from 0.61 GPa to 0.38 GPa. This suggests that at room temperature, the loss modulus of non-functionalized nanocomposites is higher than functionalized nanocomposite groups. Moreover, adding nHA particles to the functionalized resin lowers the loss modulus whereas adding nHA particles to the non-functionalized resin raises the loss modulus. Heat treatment in both functionalized and non-functionalized nanocomposites (SP30 vs SP30h and mSP30 vs mSP30h) lowered the loss modulus at room temperature.

The loss tangent plots are shown in Fig. 5.11(c). The peak of the tan δ curves can be used to determine the glass transition temperature, Tg. Tg increased from 34.65 °C in AESO-based neat resin to 67.9 °C in functionalized neat resin. The introduction of nHA particles to both functionalized and non-functionalized resin systems enhanced the Tg as expected. The glass transition temperature also increased dramatically in mSP30 and mSP30h compared to SP30 and SP30h, reaching from 60 °C to 120 °C. In the non-functionalized resin system, heat treatment of nHA particles enhanced the Tg only slightly. In the functionalized system, there was no detectable change in Tg due to heat treatment of nHA particles.

5.4. Discussion

It has been demonstrated that by manipulating the structure of nanocomposites opportunities will be opened to develop new bone-inspired material systems [2,3,321]. The implementation of appropriate material composition and manufacturing methods that can mimic the mechanical and physiological features of bone composite will pave the way for emerging mechanically competent bone-inspired nanocomposite grafts.

In this study, four groups of 3D printable nanocomposite inks were developed using nHA as inclusions and AESO combined with PEGDA as the matrix. Liu et al demonstrated that additional functionalization of AESO increased the cross-linking density and the levels of C=C bonds in the resin [161], so in two groups of our nanocomposite inks, the AESO-based biopolymer matrix was further functionalized to test the effect of functionalization on the final mechanical properties of printed nanocomposite filaments. [63]. The tensile test results demonstrated that the mean ultimate strength and elastic modulus of our mAESO/PEGDA/nHA nanocomposites reached 75.5 MPa and 6.6 GPa respectively. While AESO is a promising candidate for a variety of biomedical applications including biopolymer matrix of nanocomposite biomaterials [64,84,219], we demonstrated that additional functionalization of the AESO boosts the strength and elastic modulus of our nanocomposites more than threefold, making it more suitable for fabricating bone-mimetic 3D printed grafts. Cortical bone experiences a maximum in vivo stress of approximately 45 MPa under normal physiological circumstances [364]. By the current mechanical properties obtained for our functionalized 3D printable nanocomposites, we achieved a strength safety factor of 1.5 without altering the nHA volume fraction or changing the composition of ink and just by further functionalizing our AESO-based biopolymer resin. The functionalized nanocomposite

group surpasses the minimum needed standard mechanical properties for bone cement according to ISO standard 5833 standards (Tensile strength ⩾50 MPa) [365]. A crucial need for creating stronger nanocomposites is the homogeneous dispersion of nanoparticles in the polymer matrix [366]. Using an ultrasonic homogenizer, we dispersed the nHA particles in the resin in different steps for all nanocomposite inks in this work. To investigate the effect of heat treatment on nHA particle dispersion, we added the nHA particles to the resin after heating at 120 °C to minimize the probability of hydrophilic nHA particle agglomeration [354] trapped in the hydrophobic AESO biopolymer matrix [353]. Further image processing analysis of SEM images revealed that the combination of heat-treatment and functionalization reduced the frequency of agglomerations larger than 7μm compared to the non-heated functionalized group (mSP30) while there were no significant differences in the frequency of larger agglomerations in the non-functionalized-heated nanocomposite systems. Drying the nano-hydroxyapatite at 120 ° C removes surface-absorbed water and increases its reactivity towards organic functional groups [354]. This is the most likely explanation for the observed reduction in nano-hydroxyapatite agglomeration sizes in the functionalized nanocomposites, however, it did not detectably improve the mechanical properties. There were still micron-sized agglomerations detected in the SEM images of all of the nanocomposites. They can cause the particles to not be wetted by the matrix sufficiently resulting in a reduced interfacial area [347,367] and also may act as stress concentrators for the matrix which all effects the final mechanical properties [81]. Optimal rheological behaviour is the primary requirement for successful direct ink writing. The developed inks' rheology displayed proper viscosity and shear yield strength for DIW, allowing the ink to retain its shape for single filament extrusion prior to UV curing. The shear yield stress in functionalized nanocomposite inks has enhanced, resulting in improved shape holding and less ink dispersion during printing multilayered structures, as seen in 3D printed samples (Fig. 5.2(a-b)).

In the presence of sufficient UV light, UV-curable multifunctional monomers can undergo free radical polymerization, resulting in strongly cross-linked thermoset polymers [20]. Successful curing is required for good mechanical characteristics, controlled degradation behaviour, and favourable cell-material interactions in biomaterial nanocomposites, as partial curing results in the presence of unreacted monomers in the matrices [63]. By producing standard cure-depth curves, it is feasible to compute the minimal UV radiation necessary for curing a given nanocomposite thickness[20]. We discovered that over the same UV dosage, the cure depth for mSP0 and mSP30h

was less than for SP30 and SP30h groups. An additional methyl group is attached to the alpha carbon of the -C=C- double bond in methacrylates. This additional methyl group causes steric hindrance [363]. As a result, methacrylates have lower reactivity than equivalent acrylates. During extrusion, all of the nanocomposite filaments in this study were exposed to UV dose for longer than required based on the cure depth data to ensure efficient curing as demonstrated by the FTIR spectra for all extruded nanocomposite filaments proving successful and efficient curing after extrusion. The TGA results demonstrate a higher temperature required for decomposition initiation in the functionalized nanocomposite groups, presumably due to different interactions between nanoparticles, higher levels of C=C bonds and higher cross-linking density in the functionalized resin. The nHA volume fraction after burnout samples for all groups was calculated to be 29.61± 0.67 % (n=3) which was close to the target volume fraction of 30%.

Like any other extrusion process, DIW does have a significant driving force for inducing polymer chain alignment in the direction of flow [20,303–305]. The enthalpy of melting, which measures the degree of crystallinity in thermoset polymers [287], rises on functionalized extruded nanocomposite inks, according to the DSC data. Polymer properties such as rheology, crystallization and mechanical properties are influenced by a higher molecular weight [368–371]. It has been reported that high molecular weight chains stretch during shear flow [372,373] and promote the formation of the strong orientation of high molecular weight chains, resulting in enhanced shear-flow induced crystallization [371]. The presence of additional methacrylate groups in the functionalized mSP30 and mSP30h nanocomposite systems raise the molecular weight compared to the SP30 and SP30h systems, resulting in an increase in the enthalpy of melting of their extruded nanocomposite filaments, as evidenced by DSC data and consistent with mechanical properties results. No significant change was observed regarding the enthalpy of melting in the groups with heated nHA.

The SEM images of fracture surfaces of mSP30 and mSP30h are smooth and less featured compared to the SP30 and SP30h which is consistent with brittle behaviour for highly-cross linked thermoset polymers [309]. The absence of flaws and entrapped bubbles in SEM images of longitudinal and transversal cross-sections of extruded filaments indicates that the nanocomposite filaments were properly processed and printed.

The DMA results also demonstrated that additional functionalization in the mSP30 and mSP30h nanocomposites as well as in pure resins boosted the glass transition temperature by two-fold when compared to non-functionalized groups. This is a result of the higher degree of cross-linking in the functionalized groups. This indicates that by further functionalization of the biopolymer matrix, better thermal stability is obtained which is comparable to high-temperature expensive epoxy resins [374]. The storage modulus at the room temperature of functionalized nanocomposites and functionalized pure resins was also two times greater.

Finally, we demonstrated that the ultimate strength, elastic modulus and glass transition temperature were enhanced significantly by converting the non-functionalized AESO biopolymer to functionalized mAESO. These significant enhancements in both tensile and thermo-mechanical properties are attributed to the increased density of cross-linking in the mAESO-based nanocomposites. The heat treatment in the mAESO nanocomposites had smaller agglomerations sizes but this did not enhance the final mechanical properties. By further enhancing the dispersion of the nanohyroxyapatite particles within the mAESO matrix, it may be possible to achieve even greater mechanical properties than those observed in this study.

5.5. Conclusion

The novel nanocomposite inks developed in this study were successfully 3D printed using DIW technique. The extruded functionalized 3D printable nanocomposite inks had greatly improved tensile (ultimate strength and elastic modulus), rheological and thermo-mechanical properties. They displayed higher glass transition temperature and enthalpy of melting as a result of additional high molecular weight methacrylate groups in these nanocomposites implying good thermal stability and making them suitable candidates for a wide range of biomedical applications. The heat treatment of nHA decreased the frequency of larger agglomerations while no significant differences were observed in the mechanical properties across these groups. The findings of this work, as well as the innovative 3D printable nanocomposite inks, may be useful for 3D printing grafts and scaffolds for advanced bone reconstruction technologies to be used in clinical translations.

Chapter 6

Improved Dispersion and Interfacial Bonding of Nanoparticles in 3D Printable Nanocomposite Biomaterials via Innovative Surface Modification and Processing of Nanohydroxyapatite Particles

6.1. Introduction

Synthetic hydroxyapatite (HA) has both composition and structure that are almost identical to the natural HA found in human teeth and bones [375,376]. It is a ceramic that belongs to an important class of apatite minerals and is widely applied in the repair of bone defects due to its bioactivity, non-immunogenicity, biocompatibility, and bone conductivity [217,377–379]. Nanoscale hydroxyapatite (nHA) particles, in particular, which have physical and chemical properties similar to natural bone minerals, have been researched for decades due to their bioactivity and osteoconductivity *in vitro* and *in vivo* [301,302,380–382]. It has been demonstrated that the high surface area-to-volume ratio of the nanoscale hydroxyapatite leads to improved *in vitro* cell-biomaterial interaction [301,382] as well as enhanced mechanical properties [20,63,84]. As a result, incorporating nHA into composites can improve their chemical, mechanical, and biological performance when compared to conventional micro-scale composites [381].

Bone is a natural nanocomposite of collagen, other organic molecules, hydroxyapatite, and structural water. The mineral phase of natural bone is composed of plate-like crystals of nanometric size, which are dispersed throughout collagen fibrils [383–386]. To mimic natural features with synthetic materials, highly homogenous and stable nHA dispersions with intimate contact with the organic component are desired as intermediates, which may then be moulded into final structures that will function as bone substitutes. Therefore, reinforcing polymers with nHA can mimic natural bone by acting as the "*organic*" and "*mineral*" phases of the composite, respectively [84]. However, nHA is associated with some drawbacks, such as brittleness and aggregation due to their hydrophilic nature and weak interfacial adhesion with polymers, which can limit the dispersion of the nanoparticles and negatively impact the material properties and its applications in biomedical fields and bone tissue engineering [387,388]. The calcium-deficient sites in nHA can be occupied by different cations through a process called cation binding or

substitution. This allows for the introduction of desired ions into the nHA structure, which can alter its properties and functionalities [389]. Barium, being a divalent cation with a similar size and charge to calcium [390], can replace calcium ions within the crystal lattice. This substitution process allows for the introduction of barium ions into the nHA structure.

One of the main issues with creating nanocomposite inks, particularly for use in 3D printing is achieving homogeneous nanoscale dispersion of nanoparticles into the polymer matrix. Aggregation/agglomeration can occur during the manufacturing of nanoparticles or their incorporation into polymers [391]. Nanoparticles tend to form agglomerates owing to their surface chemistry, high surface area, and interparticle forces, which can result in poor mechanical properties, bulk degradation of nanocomposites and affect the ink rheology for 3D printing as well as biocompatibility. Nanoparticle aggregation/agglomeration reduces the potential enhancement of mechanical properties in nanocomposites due to the restriction of the interfacial area [347,348], affecting the final macroscopic properties and eliminating a wide range of potential material applications [392,393]. Nanocomposite properties are determined not only by the properties of their constituents but also by the extent of filler dispersion and agglomeration, where dispersion in composites with random particle distribution can be defined by the average inter-particle distance. The fabrication of nanocomposites may benefit from the formation of homogeneous dispersions, as the high surface-to-volume ratio is projected to result in higher interfacial particle-matrix interactions, which can improve the overall characteristics of the resultant material [394,395]. However, preparing homogeneous dispersions remains a significant challenge. There are several reasons why nHA particles may agglomerate in nanocomposites, including van der Waals forces, electrostatic interactions, and capillary forces. To address this problem, several approaches have been proposed to disperse nHA particles and prevent agglomeration. One approach is to modify the surface of the nHA particles by coating them with a surfactant or polymer. This can reduce the surface energy of the particles and increase their stability in the matrix material [396,397].

Another approach is to use a processing technique that can break up agglomerations and disperse the particles more evenly throughout the matrix material. For example, high-energy ball milling, sonication, or shear mixing can be used to mechanically break up agglomerates and improve the dispersion of the particles [126,127]. However, ball milling produces undesirable damage to the surface and structure of the ceramic particles due to the repetitive process of high-impact grinding.

In addition, the use of a coupling agent can enhance the compatibility between the nHA particles and the matrix material, which can reduce the tendency for agglomeration. Coupling agents can form chemical bonds between the nHA particles and the matrix material, improving the interfacial bonding and preventing the particles from clustering together.

A coupling agent can help increase dispersion by increasing miscibility and having two (or more) functional groups can help generate covalent or ionic connections to link the phases via interfacial bonding [398,399]. HA has been modified with a variety of coupling agents, monomers, and polymers to improve the cell-material interactions, mechanical properties, its physical, biological, and chemical properties and increase the effectiveness of nanoscale reinforcement in the nanocomposites [168,175,183,400,401]. However, achieving a uniform dispersion of nanoscale HA particles and preventing micron-scale agglomeration continues to pose a significant challenge in the field.

In the previous studies by the WCBS group, different approaches have been implied for improving the dispersion of nHA particles, such as using an ultrasonic homogenizer for dispersing nHA in developed inks with [20] and without solvent [63,84], heating nHA up to 120 ℃ before adding to ink [136] and silanization of nHA particles [402] before adding to ink. Although encouraging results were obtained regarding mechanical properties through these modifications, getting a nanoscale particle dispersion has not yet been achieved. The nHA agglomerations can also affect the efficacy of nHA particle surface functionalization. Since microscale aggregation provides a lower surface/area ratio, the functional material has fewer chances of interacting with the nHA surface.

In this paper, a novel approach for developing and obtaining a well-dispersed nHA-based bone-inspired nanocomposite system with enhanced interfacial bonding is introduced. We hypothesized that by separating the fine nHA through steps of centrifuging and surface functionalization of fine nHA, a nanocomposite with effective interfacial bonding and improved dispersion of nHA would be achieved. To do this, the nHA particles were refined, and the refined nHA were functionalized with sulfopropyl methacrylate (SPM) to enhance the interfacial bonding as well as help for further improvement of dispersion. The nHA dispersion, effectiveness of surface functionalization and interfacial bonding were assessed thoroughly in the developed nanocomposite system through different characterization experiments. The effect of dispersion and surface functionalization of

nHA on the tensile mechanical properties of nanocomposite inks and on their rheology for 3D printing was further assessed. Developing a well-dispersed nHA-based nanocomposite system with improved interfacial bonding will enhance the potential applications of these materials in the field of bone tissue engineering due to enhanced mechanical properties and/or improved cell interaction.

6.2. Materials and Method

6.2.1. Ink Composition

All reagents including acrylated epoxidized soybean oil (AESO, average molecular weight 1200), methacrylic anhydride (MAA), polyethylene glycol diacrylate (PEGDA; MW 250), 3-sulfopropyl methacrylate (SPM),sodium hydroxide (NaOH), and phenylbis(2,4,6-trimethylbenzoyl)phosphine oxide (Irgacure 819) were purchased from Sigma Aldrich Co. The nanocomposite ink developed herein used rod-shaped hydroxyapatite nanoparticles (nHA) with 120nm length, 30-40 nm diameter, and a calcium-to-phosphorous ratio of 1.52 (MKNano, M K Impex Corp., Mississauga, Canada). On average, the nanoparticles had a specific gravity of 2.92 and a crystallinity index of 0.52-0.54 [20].

6.2.2. Ink Preparation

6.2.2.1. nHA Purification

To eliminate nHA particle agglomeration, the as purchased raw nHA powder was first purified to obtain fine nHA particles (Fig. 6.1-a). To do this, 60 g of nHA was measured in a 500 ml glass beaker. Then the nHA particles were heat treated at 120 °C for 1 hour to remove absorbed moisture [6]. The beaker was covered with aluminum foil and placed back inside the fume hood. Then 600 ml of ethanol was added to a 1000 ml beaker, and the nHA powder was added to the ethanol gradually using a spatula. The nHA and ethanol were mixed for 5 minutes with a mechanical homogenizer and further dispersed for 20 minutes using an ultrasonic homogenizer. The beaker with the covered lid was mixed on the stirrer plate at 300 rpm for 24 hours. After 24 hours, 35 ml of the emulsion was added to 50 ml conical centrifuge tubes. Tubes were centrifuged at 500 RCF for 10 minutes at room temperature. The tubes were then gently taken, and the top emulsion was carefully collected in a container. This supernatant contained refined nHA. The remaining nHA

pellets on the bottom of the centrifuge tubes were mixed with ethanol, and these steps were repeated until the entire fine particles were collected from the nHA-ethanol emulsion.

6.2.2.2. Surface Functionalization of nHA

The measured refined nHA from the purification process was further functionalized using sulfopropyl methacrylate (Fig. 6.1.b). First, 13.86 g of barium chloride was dissolved in 500 ml deionized H_2O (1mol nHA:1 mol $BaCl_2$) and then added to the fine nHA-ethanol emulsion obtained from section 2.2.1 and homogenized using an ultrasonic homogenizer. Then the mixture was stirred at 300 rpm for 24 h in an uncovered beaker inside the fume hood at ambient temperature to evaporate the ethanol.

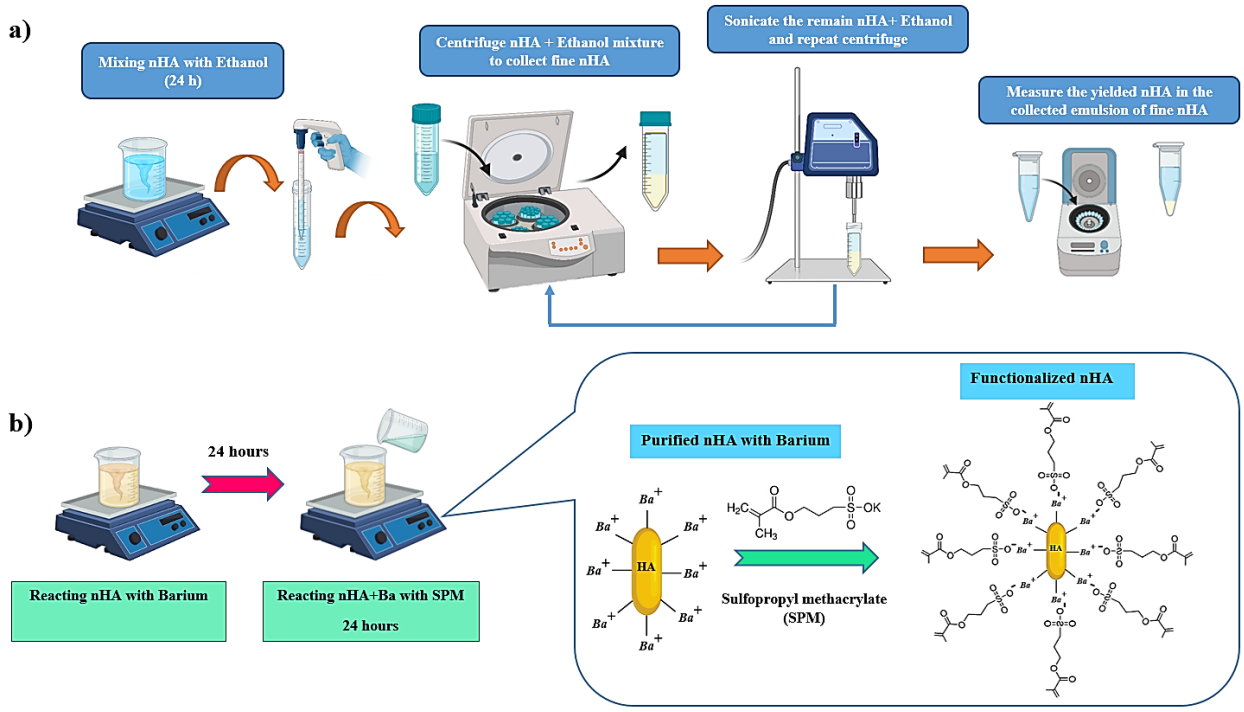


Fig. 6.1. nHA purification procedure and functionalization process. a) several steps of centrifuging until obtaining the fine nHA b) Functionalization of nHA particles with 3-sulfopropyl methacrylate by several phases of reaction with Ba and SPM.

After 24 hours, 14.07g of sulfopropyl methacrylate was dissolved in 100 ml deionized H_2O and then added to the nHA-Ba/water mixture. The mixture was stirred at 300 rpm for another 24 hours. After 24 hours of reaction, to separate the water from the mixture, 35 ml of the mixture was added to each 50 ml conical centrifuge tube and centrifuged at 1000 RCF for 5 minutes at room temperature. The supernatant water containing unreacted $BaCl_2$ and SPM was discarded, and then

30ml of acetone was added to each conical centrifuge tube. The functionalized nHA-acetone mixture was then homogenized and centrifuged twice to remove any remaining water. Finally, the functionalized nHA-acetone emulsion was added to the biopolymer mixture and kept in the fume hood at ambient temperature until dry. The mixture was sonicated twice daily for 10 min to maintain homogeneity. For consistency, the preparation of refined nanocomposite ink followed the same procedure except for the surface functionalization step.

6.2.2.3. Preparation of Functionalized Biopolymer Matrix

AESO was further functionalized with methacrylate groups prior to ink preparation using methacrylic anhydride (MAA) and 4-(Dimethyl Amino) pyridine (DMAP) as catalyst following the detailed steps described in reference [136]. During the functionalization process, the AESO's hydroxyl groups were replaced by methacrylate groups, resulting in methacrylated AESO (mAESO). After the functionalization process, the biopolymer matrix was produced by combining mAESO with PEGDA (in equal volume ratio) using an ultrasonic homogenizer.

6.2.2.4. Preparation of Nanocomposite Ink

The novel bone-inspired 3D printable nanocomposite inks developed in this study were composed of 5% vol. nHA with 47.5% of mAESO and 47.5% of PEGDA. Three groups of nanocomposite inks were prepared: with i) as purchased nHA (Raw), ii) purified and nanoscale nHA (Refined), and iii) nHA-Ba-SPM (Functionalized Refined).

6.2.2.5. Rheology

A Bohlin CS Rheometer with a cone and plate arrangement (CP 4/40, with 150 μm gap) was utilized to determine the viscosity and shear yield strength of various inks and to study the effect of nHA dispersion and functionalization on their rheology. The aim was to ascertain if the inks exhibited the appropriate rheological behavior for mSLA 3D printing. Three specimens per group (n=3) were tested, and measurements were taken at room temperature over a range of shear rates from 0.01 s^{-1} to 100 s^{-1}. The viscosity was recorded at 10s intervals for each shear rate.

6.2.3. 3D Printing of Nanocomposite Inks

Dogbone test specimens of pure biopolymer matrix as well as nanocomposite ink were 3D printed using Phrozen Sonic XL 4 K (Phrozen Technology, Taiwan) – an mSLA-based 3D printer. The

Phrozen slicer software was used to slice the 3D stereolithographic (.stl) files and build adequate support fixtures around the grip region to appropriately attach the dogbone samples to the print bed as well as avoid defects to the specimen during printing and facilitate the removal of samples from the print bed. To eliminate defects that might impair mechanical testing results, no supports or fixtures were added along the gauge length. All specimens were printed with 50 μm layer height. Except for the first six layers, which were cured for 15 seconds to ensure good build plate adhesion, each layer was exposed to UV for 6 seconds. After 3D printing was completed, the specimens were carefully taken from the print bed, the supports discarded carefully and the specimens wiped thoroughly to remove the residue-uncured ink. Then samples were exposed to further UV for 10 minutes on each side in a post-print curing chamber (CureZone MKII, Creative CADWORKS, Canada). Finally, samples were thoroughly washed and wiped with ethanol.

6.2.4. Mechanical Testing of Biopolymer Matrix and Nanocomposite Sample

The dogbone-shaped test specimens (Overall length: 30 mm; Gauge length: 10 mm long, 2.5 mm broad, and 2 mm thick; according to the ASTM D3039, 2017) were 3D printed with the mSLA 3D printer. Tensile testing was carried out using a Psylotech UTS mechanical testing system with a 1.6 kN load cell (Psylotech Inc., Evanston, IL, United States) (Fig. 6.2). Strain measurements were performed using a microscope-enabled Digital Image Correlation system (DIC; Vic 2D 6, Correlated Solutions Inc., USA). During the test, a microscope (BXFM, Olympus Corp., Center Valley, PA, USA) equipped with a 2.5x objective lens (Olympus Corp., Center Valley, PA, USA) with a mounted digital camera (Point Grey, 5 MP, 2/3" detector) took magnified images of the gauge length. Before testing, all specimens (n = 7 per group) were sprayed with high-resolution laser printer toner powder (4-5 μm in diameter, Xerox Phaser 6000) using an atomizer jar to generate speckle patterns that allowed DIC-based strain measurements. The specimens were initially preconditioned with a small load (5N) at room temperature for 100 cycles at 1 Hz. The extension was then conducted at a speed of 16 μm/s (average strain rate of 0.0016 s^{-1}). The load cell data was collected at 5 Hz. For the DIC in all experiments, the subset window and step size were set to 150 and 7 pixels, respectively (1 micron=2.75 pixels) while the filter size was 15 pixels. This lead to a VSG (Virtual Strain Gage) of 1050 pixels.

The extensometer tool (Fig.6.2. e) from the DIC was employed over the length of Area of Interest to calculate the average engineering strains. Using the following formula, the true strain (ε_t) was calculated accordingly.

$$\varepsilon_t = \ln\left(\frac{l}{l_0}\right) \tag{6.1}$$

The extensometer tool provided the current length (l) and the initial length (l_0). The extensometer tool was used to determine the transverse strain (y-axis), assuming that the z-axis strain also is the same as the transverse strain to obtain the true cross-sectional area for each point. The true stress was obtained by dividing the applied load by the true cross-sectional area.

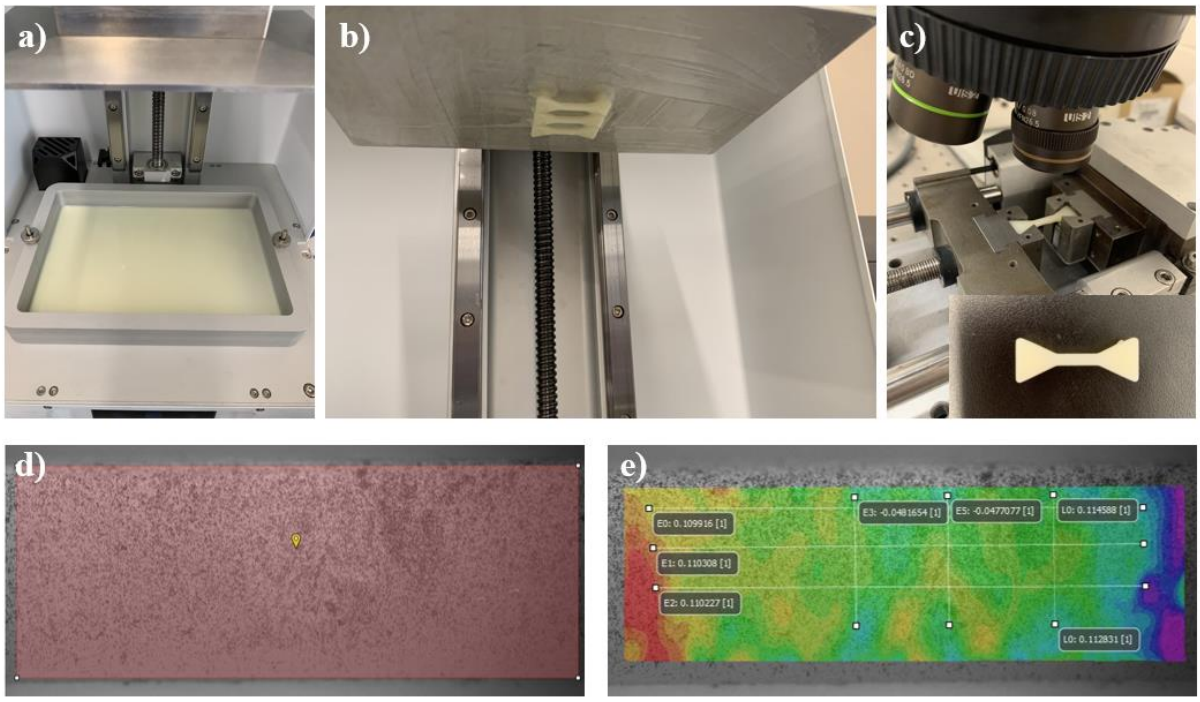


Fig. 6.2. Printing dogbone specimens and tensile testing. a) Ink in the resin reservoir of mSLA 3D printer, b) Printed dogbone specimens on the print bed. c) Tensile testing after postprocessing of the specimens. d) ROI selected on a speckle patterned specimen.e) DIC map and extensometers used for measuring strains.

The slope of the stress-strain curve's linear elastic region was used to calculate Young's modulus. Poisson's ratio (ν) was computed using the ASTM standard for tensile testing.

$$\nu = -\frac{\Delta\varepsilon_t}{\Delta\varepsilon_l} \tag{6.2}$$

Where ν represents the slope of the $\varepsilon_t - \varepsilon_l$.

6.2.5. Characterization of 3D printed Nanocomposite

6.2.5.1. Thermo-Gravimetric Analysis (TGA)

TGA analysis was utilized to assess the volume fraction as well as heat degradation of the 3D-printed nanocomposites. Samples were cut from different parts of the printed sample to make sure the obtained volume fraction was representative of the entire nanocomposite. A TA Q500 (TA Instruments Inc., New Castle, DE) was used to heat and burn about 10-15 mg of each 3D-printed nanocomposite specimen (n = 3). The samples were heated to 800 °C at a rate of 10 °C/min in an air environment. The samples were equilibrated at 40°C for 5 minutes before heating. Using the residual measured mass at 800 °C, the organic-inorganic ratio of the nanocomposites was estimated. Each nanocomposite specimen's organic-inorganic volume fraction was calculated by dividing the residual mass (inorganic) by the density of the nHA (nHA=2.92 g/cc) and the starting mass of the nanocomposite sample by the density of the nanocomposite ink (Ink=1.628 g/cc).

6.2.5.2. Fourier Transform Infrared Spectroscopy (FTIR)

Fourier Transform Infrared Spectroscopy (FTIR) was performed on the surfaces of raw and functionalized nHA pallets (n=3) to examine the chemical composition and bonding associated with the functionalized SPM-nHA particles. The FTIR spectra were obtained using a Nicolet 6700 FT-IR Spectrometer (Thermo Scientific, USA) with a resolution of 4 cm^{-1} and a sample scan of 32. The OMNIC series software was used to analyze all spectra.

6.2.5.3. Scanning Electron Microscopy (SEM)

Scanning electron microscopy (SEM) was employed to observe the nanoparticle dispersion within the cured biopolymer matrix. 3D printed nanocomposite samples were polished progressively with polycrystalline diamond suspensions of sizes 6 μm, 0.05 μm and 0.01 μm. After polishing, the

samples were imaged using a Quanta FEG 250 (ThermoFisher Scientific, USA) in low vacuum mode for scanning electron microscopy (SEM) and back-scattered electron microscopy (BSEM). The fracture surfaces resulting from tensile testing were mounted on SEM stubs without any treatment to obtain SEM images of fracture surfaces for each nanocomposite system.

6.2.5.4. EDX

Energy-Dispersive X-ray spectroscopy (EDX) was used to analyze the elemental composition of functionalized SPM-nHA and the efficiency of the functionalization procedure. EDX was performed using a Quanta FEG 250 (ThermoFisher Scientific, USA) fitted with an EDX detector on the as-purchased and functionalized nHA powders.

6.2.6. TEM Characterization

Sections were taken from the printed nanocomposite specimens using a microtome to examine the coverage of hydroxyapatite nanoparticles and corresponding particle aggregation using transmission electron microscopy (TEM). Sections were attached to a copper mesh TEM grid and sputtered with carbon before conducting scanning transmission electron microscopy (STEM) with a high-angle annular dark field (HAADF) detector. HAADF-STEM imaging was conducted using a Talos 200X microscope (Thermofisher Scientific) at 200 kV with a dwell time of 5 μs. Energy-dispersive X-ray spectroscopy (EDX) was also used to co-localize barium and sulfur from the functionalization process to individual hydroxyapatite nanoparticles in the energy range of 0-20 keV using a dwell time of 20 μs and drift correction during acquisition. Postprocessing of elemental maps was conducted in Velox (ThermoFisher Scientific) using recommended average filters (< 11 px) in both pre-filtering and post-filtering stages.

6.3. Results

6.3.1. TGA

After the preparation of the nanocomposite inks and prior to conducting any experiments, TGA analysis was performed on three groups of nanocomposites to validate the targeted volume fractions and ensure that the desired volume fractions of nanoparticles were achieved. By comparing the remaining mass to the initial mass of the samples after TGA experiments, the achievement of the targeted volume fractions was confirmed, as reported in Table 6.1.

Table 6.1. TGA analysis results, volume fraction calculated for each nanocomposite system (n=3)

Nanocomposite ink	Calculated Volume Fraction
Raw-nHA	4.8±0.1
Refined nHA	5.0±0.2
Refined-SPM Functionalized nHA	4.9±0.1

6.3.2. Surface Functionalization and Interfacial Bonding Assessment

The EDX results (n=4) demonstrated (Fig. 6.3) the sulfur and Barium elements with the reported atomic percentage (Table 6.2) on the functionalized SPM-nHA samples. In a full crystalline nHA ($Ca_{10}(PO_4)_6(OH)_2$), the proportion of Ca to P is 10/6=1.67. As the currently studied nHA particles are calcium deficient, the proportion of Ca/P in raw nHA is 1.55. In the functionalized nHA specimens, the atomic percentage associated with Ba (Ba/P=0.04) indicates that the Ba atoms bonded with $(PO_4)^-$. So according to the (Ca+Ba)/P ratio (1.55+0.04=1.59), Ba has filled part of the calcium deficiencies in the functionalized nHA specimens and bonded nHA surface. The increased S atomic percentage also indicates the presence of S on the functionalized nHA surface, which is representative of sulfopropyl methacrylate. The percentage of S/P is lower than the percentage of Ba/P, indicating that part of Ba reacted with S and part with Cl. The sum of Cl+S element almost equals Ba percentages which indicates that the washing procedure was successful and almost no unbond agent remained after multiple steps of washing.

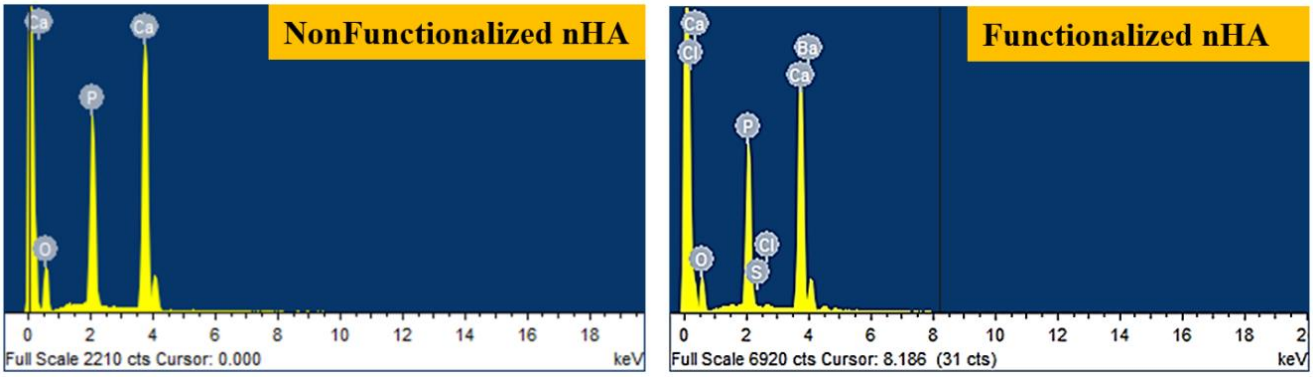


Fig. 6.3. SEM EDX results of non-functionalized and functionalized nHA

Table 6.2. EDX-SEM Atomic percentage of non-functionalized raw nHA and SPM functionalized nHA

Element	Atomic% NonFunctionalized nHA	Atomic% Functionalized nHA
O	68.48±0.79	66.31±1.47
P	12.82±0.71	12.80±0.53
Ca	19.90±1.35	19.92±1.21
S	-	0.16±0.02
Ba	-	0.50±0.04
Cl	-	0.30±0.05

6.3.3. TEM Surface Characterization of Functionalized and NonFunctionalized nHA Nanorods

Imaging microtomed sections of the nHA-biopolymer nanocomposites using HAADF-STEM-EDX showed a change in surface composition associated with the sulfopropyl methacrylate functionalization. In the functionalized nanoparticles (Fig. 6.4), the bulk of the nanoparticle consists of Ca, P, and O with a dominant C background characteristic of the biopolymer matrix. Examination of unique elements characteristic of the functionalization method (namely S and Ba) shows a minor degree of localization to the nanoparticle surface, with intensity above that of the background signal.

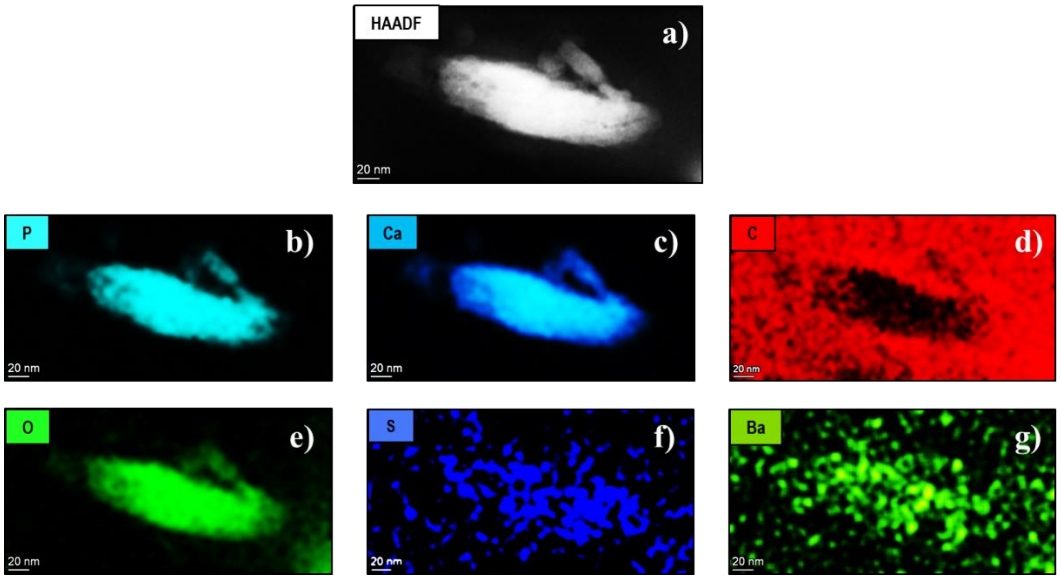


Fig. 6.4. a) HAADF-STEM images and (b-g) EDX mapping of a hydroxyapatite nanorod grafted with sulfopropyl methacrylate. Strong Ca, P, and O signals are associated with the nanoparticle, while C is mostly characteristic of the resin. A faint signal from both S Kα X-ray energy and Ba Lα X-ray energy appears co-localized to regions of elevated Ca, P, and O as a result of SPM functionalization.

As a control, in Fig. 6.5, the elemental analysis of single raw nHA nanoparticles without sulfopropyl methacrylate functionalization reveals the presence of the same core elements in the nHA (Ca, P, O), along with carbon (C) from the biopolymer matrix. However, levels of S and Ba are indistinguishable from the background signal due to the absence of sulphopropyl methacrylate functionalization.

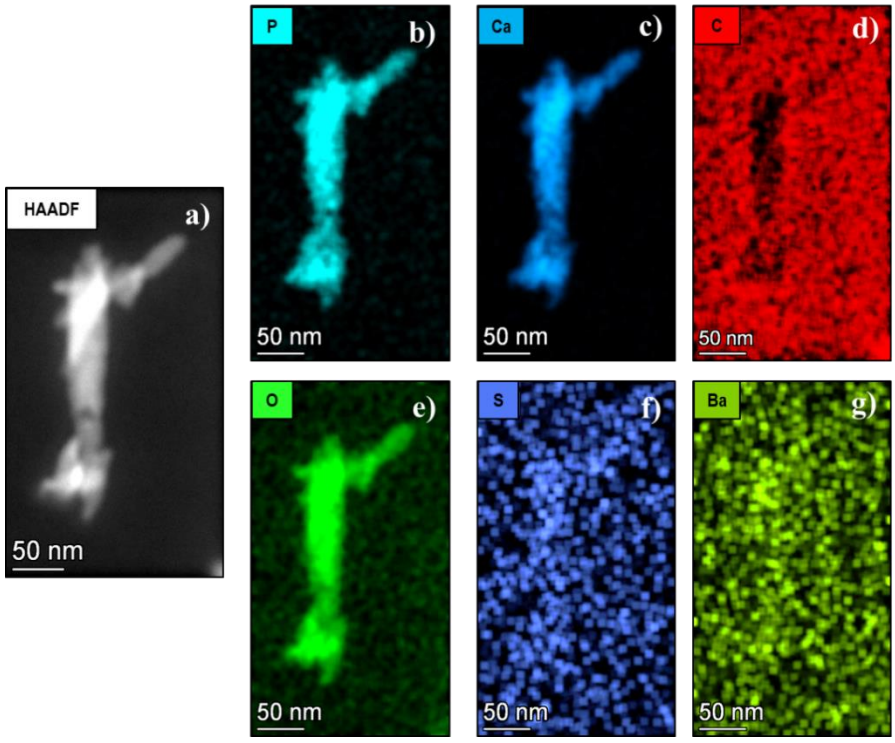


Fig. 6.5. a) HAADF-STEM images and (b-g) EDX mapping of a hydroxyapatite nanorod (as purchased, without sulfopropyl methacrylate functionalization). Strong Ca, P, and O signal is associated with the nanoparticle, while C is mostly characteristic of the resin. There does not appear to be significant localization of either Ba or S on the nanoparticle surface.

EDX line scans across the major and minor nanoparticle axes validate the trace elemental localization attributed to the sulfopropyl methacrylate functionalization (Fig. 6.6), where an increase in Ba and S X-ray generation correspond to the same spatial domain as increases in Ca, P, and O (characteristic of the particle itself). Variations in Ba and S intensity and associated peeks greater than the background noise across the nanoparticle may indicate slight variations in coverage of the sulfopropyl methacrylate across the functionalized particle. Ultimately, the increase in residual Ba and S content on the processed functionalized nHA demonstrates the effectiveness of the functionalization method and grafted nHA in the SPM.

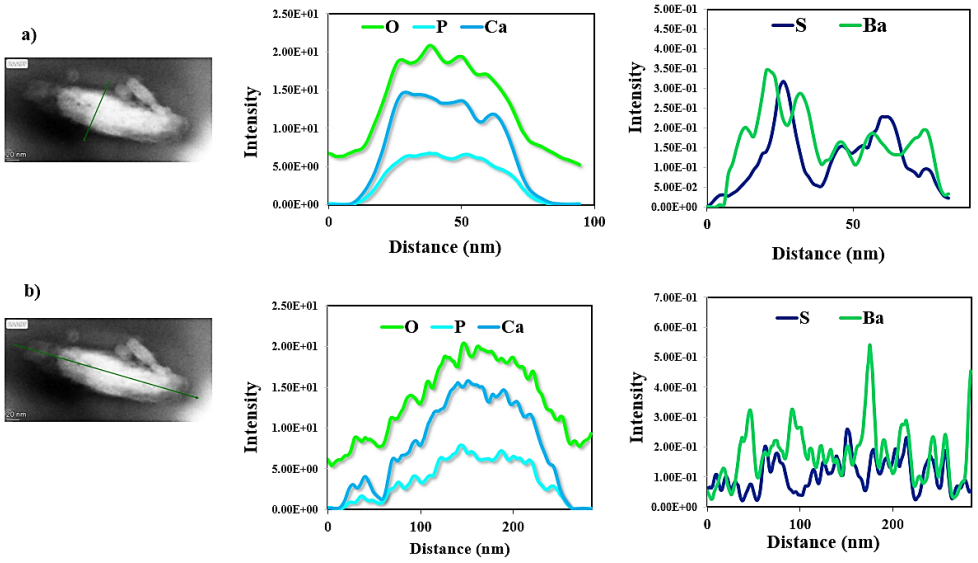


Fig. 6.6. EDS line scans across the (a) minor and (b) major axes of a functionalized nanoparticle. Slightly elevated Ba and S correspond to trace elements present following functionalization.

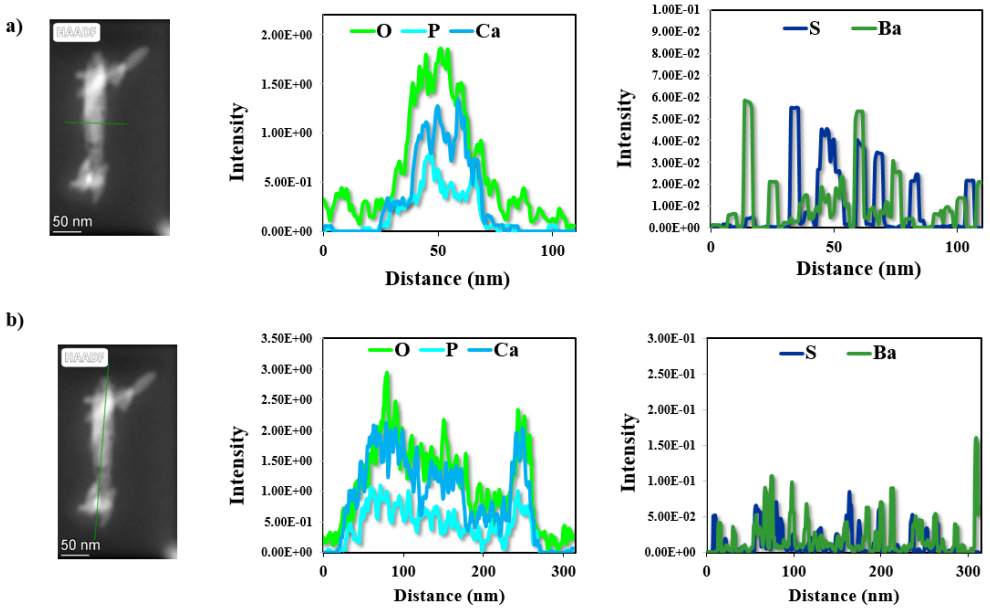


Fig. 6.7. EDS line scans across the (a) minor and (b) major axes of a nanoparticle without functionalization. Ba and S signals are equivalent to that of background noise.

Similar to the EDX maps, the EDS line scans across the major and minor nanoparticle axes in the absence of functionalization as a control (Fig. 6.7) definitively show the presence of Ca, P, and O with intensity peeks associated in the range of their major and minor axes lengths. The different

range of intensity for Ca, P, and O compared to the functionalized sample is due to randomness of choosing nHA particle. There are no detectable signals for barium (Ba) and sulfur (S) within the major and minor axes of nHA, and the observed multiple intensity peaks are mostly regarded as background noise. This affirms the EDX maps of S and Ba in the non-functionalized nHA which almost no brighter regions rather than signal background noises observed for these elements (Fig.6.5. f – Fig.6.5.g).

6.3.4. FTIR Results

The FTIR spectra of functionalized and nonfunctionalized nHA are shown in Fig. 6.8. According to the atomic structure of nHA, the OH, CO3, and PO4 bonds are related to the hydroxyapatite structure. The FTIR spectra for both functionalized and non-functionalized nHA samples exhibited peaks associated with these bonds. (Fig. 6.8(a-c)).

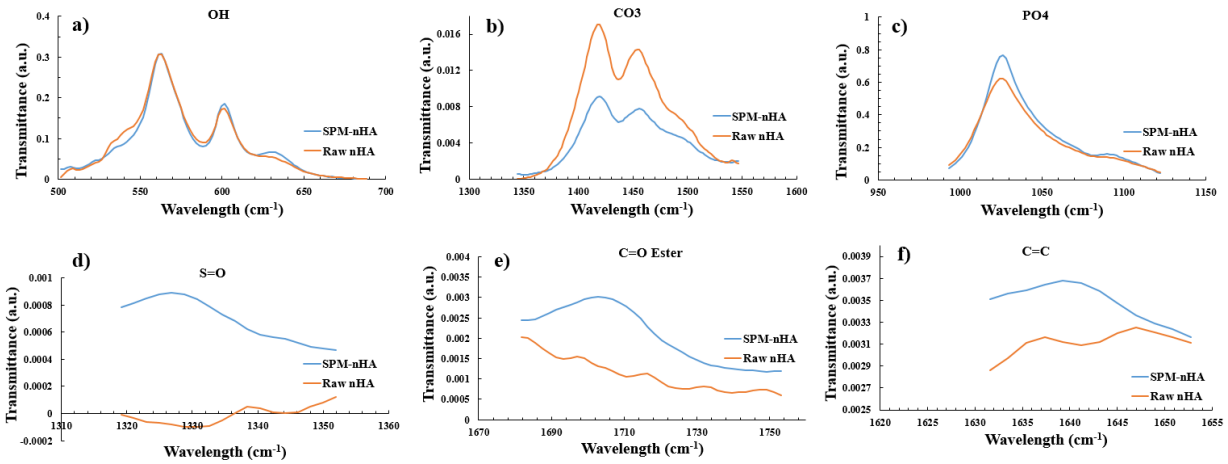


Fig. 6.8. FTIR Spectra for non-functionalized and functionalized SPM-nHA (a,b,c) Peaks associated with the bonds in the hydroxyapatite structure (d-f) The efficiency of surface functionalization and the investigation of peaks associated with sulfopropyl methacrylate

According to the atomic structure (Fig. 6.1) of SPM-nHA, the S=O, C=O Ester, and C=C are the bonds associated with SPM functional groups, which the functionalized SPM-nHA's FTIR spectra demonstrate peaks associated with these bonds in the functionalized SPM-nHA samples (Fig. 6.8(d-f)). These peaks are prominent in functionalized nHA samples, while no peaks associated with these bonds are demonstrated in the non-functionalized nHA control samples, confirming the

efficiency of functionalization and associated interfacial bondings in surface functionalized nHA nanocomposite samples.

6.3.5. nHA Dispersion in Developed Nanocomposite Systems

Imaging of the nHA dispersion using STEM and SEM imaging shows that, in the raw nHA nanocomposite system, a multiscale range of ceramic aggregates appears throughout the biopolymer matrix.

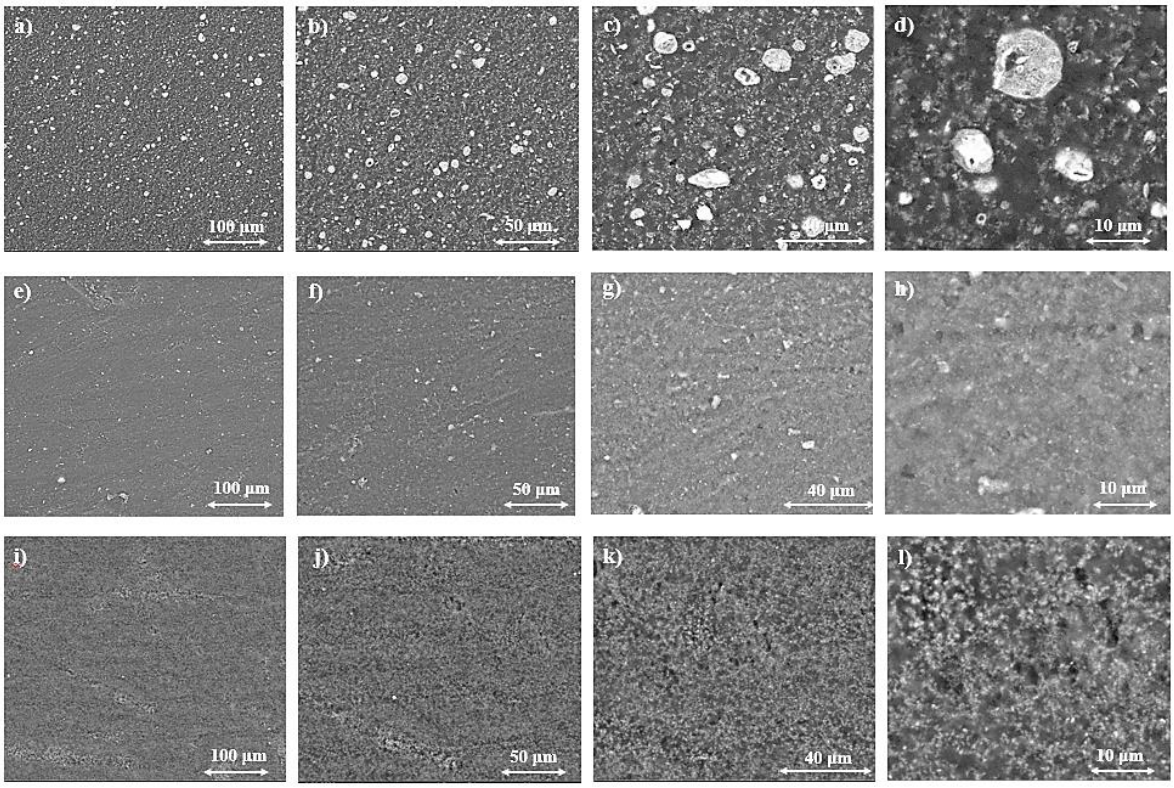


Fig. 6.9. SEM images of different processed nanocomposite systems (a-d) Raw nHA nanocomposite system (d-c) refined nHA nanocomposite system and (d-e) refined-functionalized nHA nanocomposite system. Refining nHA and SPM functionalization greatly improves nanoparticle dispersion into the nanoscale.

SEM images of raw nHA (Fig. 6.9(a-d)) demonstrate that these globular, quasi-spherical nHA agglomerations can be as large as 10-15 µm in diameter. Fig. 6.9(e-h) demonstrates SEM images of centrifuged refined-nHA nanocomposite system. While centrifuging significantly improved the dispersion of nHA in the biopolymer matrix, we still observed random 1-2 µm dense agglomerations. The SEM images of the refined-functionalized nanocomposite system are shown in Fig. 6.9(i-l), which demonstrates drastic improvement in the dispersion of nHA with almost no

dense agglomeration occurring in this nanocomposite system and that nHA particles dispersed more homogenously with almost no micron-scale agglomerations observed.

STEM imaging of the raw nHA system (Fig. 6.10(a-c)) shows globular agglomerations of the nHA, most commonly appearing at the microscale. The refined-nHA nanocomposite system (Fig. 6.10(d-f)) demonstrates a greatly improve in the dispersion of nHA, while the high magnification TEM images of this system demonstrate some agglomerations at the lower end of the microscale.

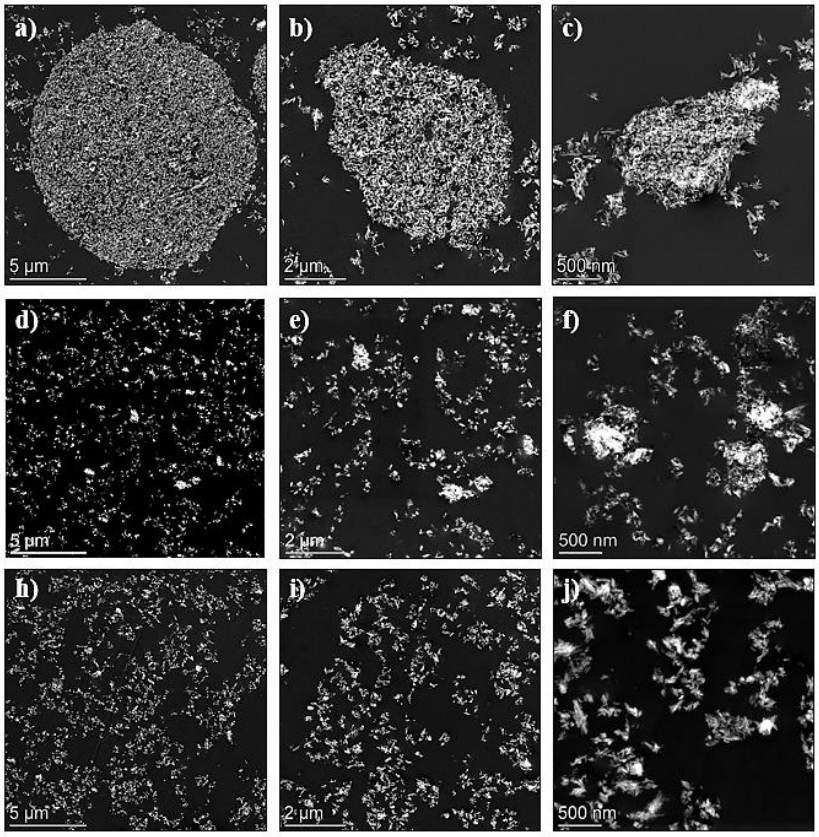


Fig. 6.10. HAADF-STEM images of hydroxyapatite nanorod aggregation (a-c) Raw nHA nanocomposite system without sulfopropyl methacrylate functionalization or centrifuging, (d-f) refined nHA system with centrifuging, and (h-j) SPM-refined functionalized and centrifuged system. Centrifuge refining greatly improves nanoparticle dispersion into the nanoscale, with SPM functionalization dispersing remaining micron-scale aggregates.

In the refined-functionalized nanocomposite system (Fig. 6.10(e-h)), nHA dispersion enhanced greatly and became much more homogenous and predictable – with no clear agglomerations in the microscale. High-magnification STEM images demonstrate small nanoscale agglomerations (clusters on the order of 100-250 nm in diameter) in the refined-functionalized nHA nanocomposite system.

6.3.5.1. Quantitative Comparison of nHA Dispersion

The distributions depicted in Fig. 6.11 are the result of an ImageJ-based quantitative analysis of nHA particle agglomerations on three developed nanocomposite systems. The histogram shows that by following the nHA refining procedure, the frequency and size of agglomerations decreased greatly, with some lower micron scale agglomerations remaining. While the SPM surface functionalization, in combination with the refinement procedure, assisted in avoiding any micron-scale nHA particle agglomerations, with only a few nanoscale agglomerations being observed.

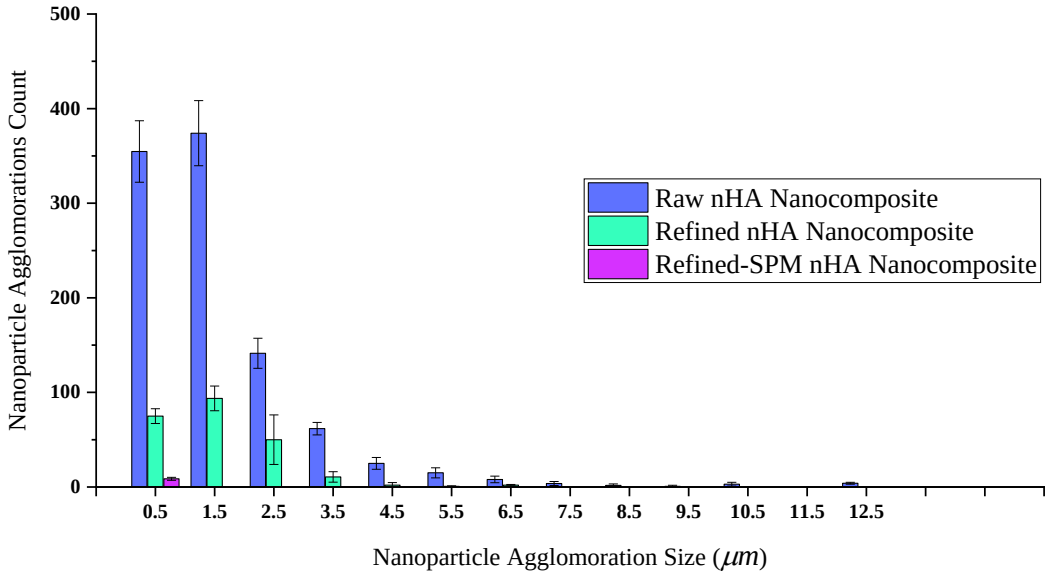


Fig. 6.11. Distribution of nanoparticle agglomerations for the three nanocomposite systems. (n = 3 for each group of extruded nanocomposite filaments).

6.3.6. Effect of nHA dispersion on Ink rheology

The rheology results for three nanocomposite inks are demonstrated accordingly in Fig. 6.12. The nanocomposite inks behaved non-newtonian with low shear yield strength. While in all these three groups of inks, the volume fractions of components are consistent, the dispersion of nHA is affecting the ink viscosity. By improving the dispersion in the refined-functionalized nHA nanocomposite system, the viscosity has increased from 150 mPa.s to 236 mPa.s, and the shear yield strength increased from 0.803 Pa to 2.94 Pa as a result of improved dispersion (Table 6.3). While the ink viscosity didn't change significantly in the refined-functionalized system compared to the refined system, the shear yield strength increased from 1.25 Pa to 2.94 Pa.

Table 6.3. Viscosity and shear yield strength results of nanocomposite inks (n = 3; data are presented as mean ± SD). Different lower-case letters indicate statistically significant differences (p <0.05).

	Shear Yield Strength (Pa)	Viscosity (Pa.s)
Raw nHA	0.81±0.14[a]	0.15±0.01[a]
Refine nHA	1.25±0.02[a,b]	0.23±0.00[b]
Refine-SPM nHA	2.94±0.37[c]	0.24±0.01[b]

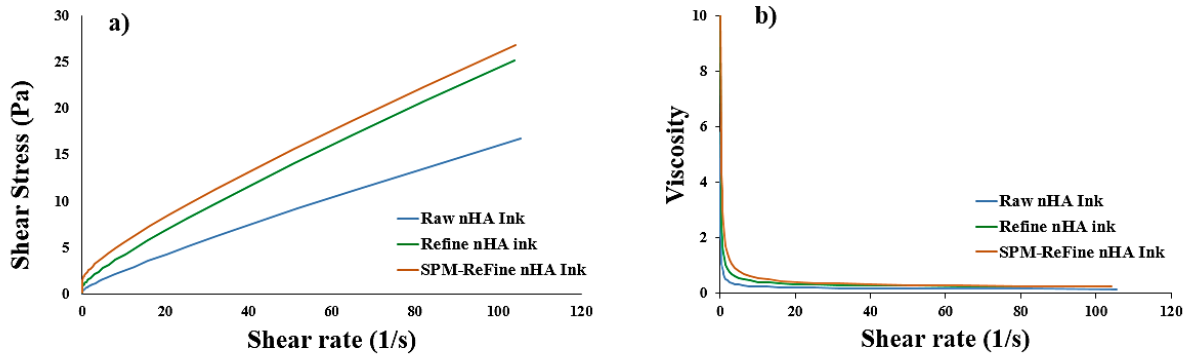


Fig. 6.12. Rheological data of three developed nanocomposite inks at different shear strain rates. a) Shear stress versus shear strain rate curves. b) Representative viscosity vs. shear strain rate curves

6.3.7. Tensile Testing of 3D-Printed Nanocompsoite Inks

The tensile test results of three developed nanocomposite inks are demonstrated in Fig. 6.13. As seen by improving the dispersion and addition of SPM functional groups, the fracture strength (Fig. 6.13. (d)), fracture strain (Fig. 6.13. (e)) and toughness (Fig. 6.13. (f)) increased significantly while the elastic modulus (Fig. 6.13. (b)) and yield strength (Fig. 6.13. (c)) properties remained unchanged. Through the combination of nHA refinement and SPM surface functionalization, the fracture strength and fracture strain increased from 33.9 MPa to 46.4 MPa (37% increase) and from 0.02 to 0.08 (75% increase), respectively, in a constant volume fraction of nHA and ink composition and due to enhanced dispersion of nHA as well as improved interfacial bonding. In calculating the area under the stress-strain curves, we see that the toughness increased by more than three times from 1.2 MPa to 4.2 MPa,

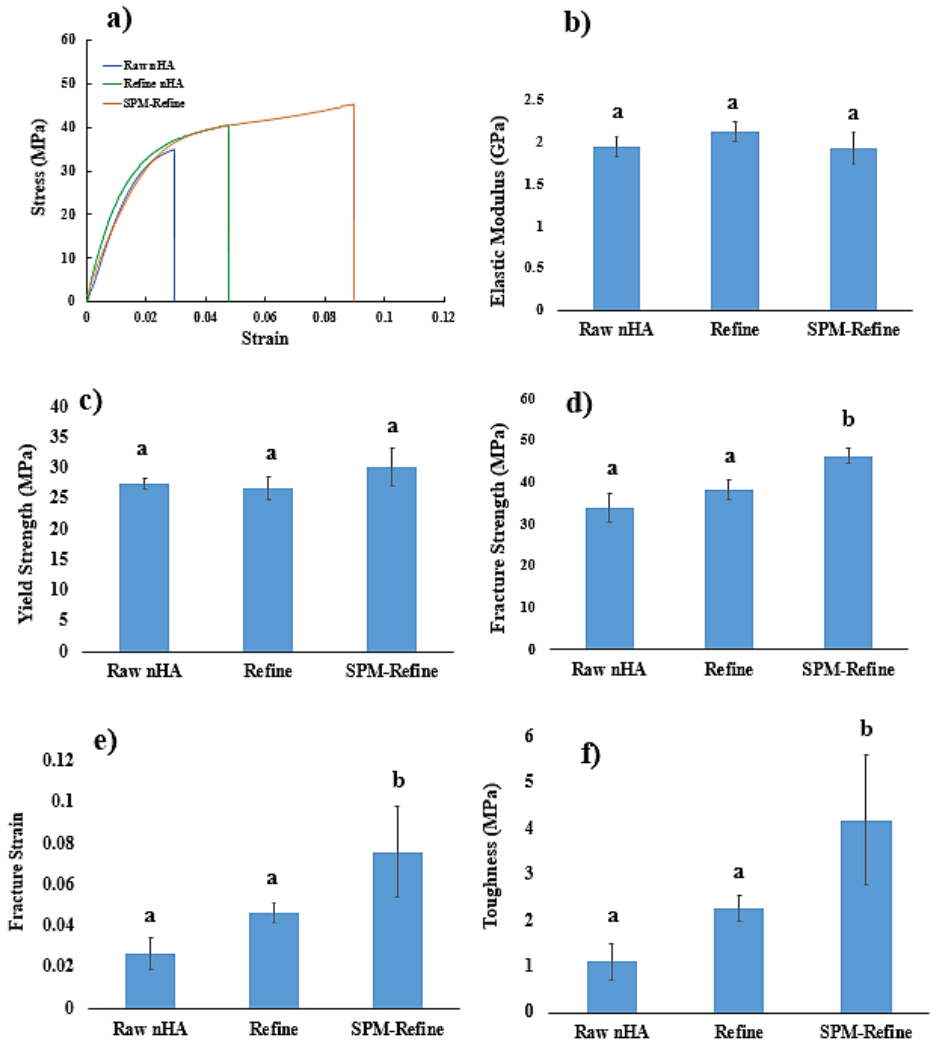


Fig. 6.13. a) Representative stress–strain curves, b) Elastic modulus, c) Yield strength, d) Fracture strength, e) Fracture strain, f) Toughness of the three 3D printable nanocomposites in this study. (For plots b-f, data are means ± SD (n = 5 specimens of each composition). One-way ANOVA followed by Tukey's multiple comparison tests were used for statistical analysis)

6.3.8. Fracture Surfaces

SEM was used to observe the fracture surfaces (Fig. 6.14) of all nanocomposites after they underwent tensile testing. The excellent processing and printing of these nanocomposites are indicated by the absence of voids or entrapped bubbles in the demonstrated crosssections. The fracture surfaces of raw nHA nanocomposite samples are smoother compared to refined nHA and refined-functionalized nHA nanocomposite systems, which suggests more brittle failure compared to the other two groups.

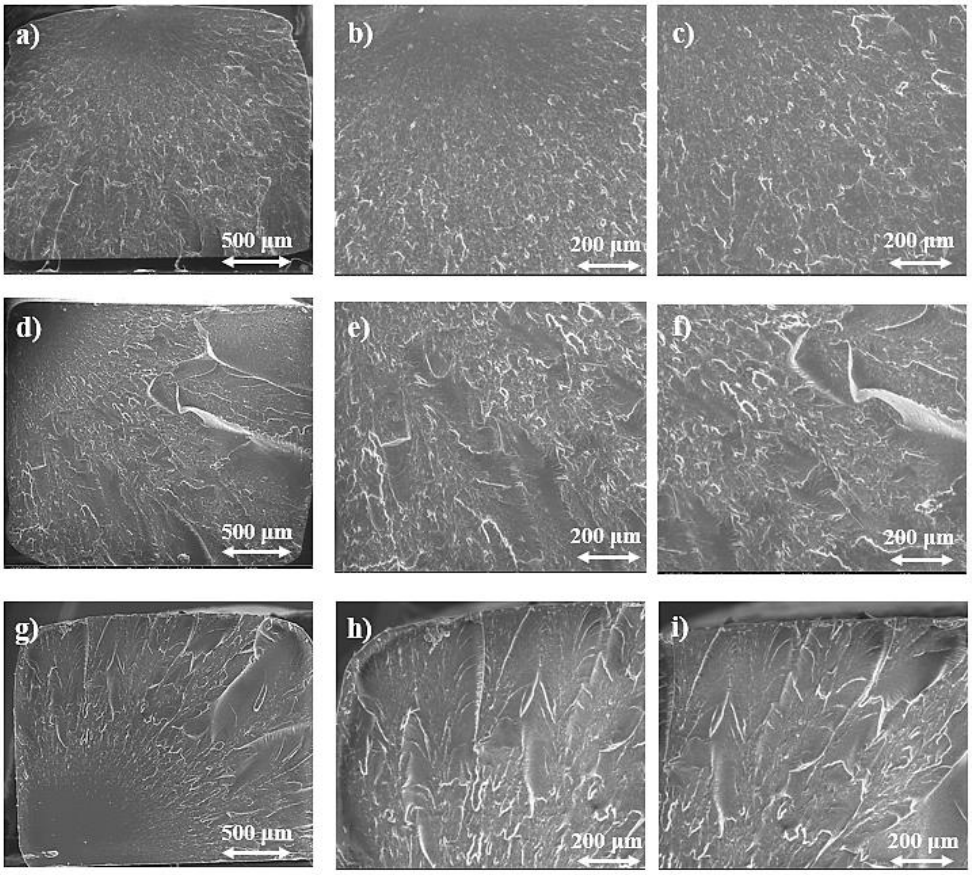


Fig. 6.14. SEM images of fracture surfaces of tensile tested nanocomposite samples for (a-c) Raw nHA nanocomposite system, (d-f) Refined nHA with centrifuging nanocomposite system, and (g-h) SPM-refined nHA nanocomposite system.

6.4. Discussion

In this study, a series of novel 3D printable nanocomposite inks were synthesized and prepared using various processing techniques for nHA particles. An innovative method is presented to create a highly dispersed nanohydroxyapatite (nHA)-based nanocomposite system inspired by bone. This approach involves two key steps: centrifuging and sulfopropyl methacrylate (SPM) surface functionalization of refined nHA particles. The centrifuging process is carried out on raw nHA in multiple steps to separate fine nHA particles from larger aggregates. Following centrifugation, the refined nHA particles underwent surface functionalization using sulfopropyl methacrylate (SPM). This treatment modified the surface properties of the nHA particles, making them more compatible with the matrix material. As a result, the interfacial bonding between the nHA and the matrix is strengthened, enhancing the overall performance and mechanical properties of the nanocomposite

system. The refining process, along with SPM functionalization, resulted in great improvement in the dispersion of nHA in the matrix, with no micro-scale agglomerations being observed. When particle sizes are around 100 nm or lower, intermolecular van der Waals interactions between them dominate, causing agglomeration or clustering [403,404]. The addition of functional groups to nanoparticle surfaces may be advantageous in the production of nanocomposites with strong interfacial interaction between polymer matrices and nanoparticles [398,405–407], which contributes to improved dispersion of nanoparticles into matrix due to miscibility [398,407] as well as resultant material properties [398,406,408]. The bonding might be weak (van der Waals, hydrogen bonding) or strong (covalent, ionic) depending on the chemical composition of these functional groups. The addition of functional groups to nanoparticles can improve the interfacial interactions among the phases and affect the dispersion of nHA, which can lead to further mechanical properties as well as cell interaction.

The raw nHA was purified and refined following several stages of centrifugation to sediment the micron-size agglomerations and acquire more of the nanoscale particles as the initial phase of nanocomposite ink preparation to improve the dispersion and boost the efficiency of surface functionalization on nHA particles. Washing the functionalized nHA with water to discard the unreacted parts can lead to the increased tendency of nHA particles for agglomerations, and secondary agglomerations appear in the functionalized nHA, which limits the effectiveness of functionalization [160]. In addition, functionalizing nHA without the purification step will reduce its effectiveness and lead to particles with more amphiphilic nature. In this study, three steps from the prior studied silanization surface functionalization procedure were modified [160] to increase the effectiveness of surface functionalization and its effect on the nHA particle dispersion. To minimize secondary agglomeration of functionalized particles during the drying operation, we first purified the nHA, then applied surface functionalization to the purified nHA, and lastly added the reacted nHA directly to the ink after complete washing with acetone. The functionalization of nHA with SPMA can enhance its dispersibility in aqueous solutions, improve its compatibility with polymer matrices, and promote interactions with biomolecules or cells. Methacrylate groups can assist in the covalent cross-linking of inorganic and organic phases within a composite, which can be particularly useful in the manufacturing and use of nanocomposites in a variety of applications. To enhance the efficacy of functionalization and successful grafting of nHAwith SPM, nHA particles were reacted with BaCl for 24 hours. When a calcium-deficient nHA surface is exposed

to a solution containing barium ions, the barium ions can occupy the vacant calcium ion sites within the nHA crystal lattice. This substitution occurs due to the similarities in ionic size and charge between calcium and barium ions. Following the introduction of barium ions, they serve as bridges or connection points to facilitate the grafting process between nHA and SPM. This step allows for the successful functionalization of the nHA surface with sulfopropyl methacrylate.

The presence of effective coupling agents on the surfaces of nanoparticles results in significant interfacial bonding between the fillers and the resin matrices. Several research on the surface modification of nHA has been conducted [409–412]. Functionalized nanoparticles such as TiO_2 [413], ZrO_2 [414], or dicalcium phosphate [415] lowered the viscosity and enhanced the dispersion among the polymer matrices. Yadav et al. reported dental composites with nHA filler treated with various silane coupling agents improved the mechanical properties regardless of the presence of large lumps or agglomerates [412]. Alosaimi et. al fabricated sulfonated polyethersulfone composite membranes coated with the 3-sulfopropyl methacrylate functionalized SBA-15 silica nanoparticles. They investigated that functionalization of SBA nanoparticles with SPM functionalization, enhanced the interaction of particles with polymer and prevented the nanofiller agglomeration which resulted in high permeability of the membrane [416].

The SEM-EDX results in this work demonstrated S and Ba elements along with the Ca, O and P elements in the spectrum of refined-functionalized nHA. The (Ba+ Ca)/P atomic ratio compared to the Ca/P in the raw nHA demonstrated an increase from 1.55 to 1.59, which confirms the hypothesis of Ba replacing the calcium deficiency of nHA. Moreover, as the Ba^{2+} attached to the nHA surface are either bonded with $-OSO_2^-$ (from SPM) or Cl^-, the S+Cl =0.46 atomic ratio compared to the Ba =0.5 atomic percentage in the functionalized nHA indicates a thorough washing of unreacted reagents. It is more likely that Ba^+ bonds with Cl^- rather than bonding with SPM due to the higher steric hindrance in the SPM functional group, so it is not feasible to bond all the Ba^+ with SPM while the atomic percentage of S/P in the functionalized nHA specimens indicates a successful surface functionalization of nHA with SPM. To further investigate the interfacial bonding, a thorough FTIR analysis was conducted on the functionalized nHA samples and raw nHA samples as control. The FTIR spectra for the refined-functionalized nHA samples demonstrated a dominant peak for the S=O, C=O ester, and C=C bonds which are associated with the SPM molecule structure and suggest the effectiveness of nHA graft in SPM.

TEM images of high-resolution images of individual particles for both functionalized and non-functionalized nHA groups were captured. TEM analysis aimed to discern and quantify the structural details and surface features, thereby identifying the distinct elements present in the particles and determining their relative abundance. This information was used to create elemental distributional maps, which showed the spatial distribution of different elements within the functionalized and non-functionalized nHA particles. Ca, P, and O compose the majority of the nanoparticle, with a dominant C background characteristic of the biopolymer matrix. Examining the unique elements of the functionalization method (namely S and Ba) demonstrates a minor degree of localization to the nanoparticle surface, with intensity above that of the background signal. Due to the small diameter of a single nHA particle, it is possible that the entire or majority of a nanorod's circumference lies within the TEM section, depending on the axis vector of the particle for the sectioning orientation. As X-rays are generated throughout the entire thickness of the TEM section, the appearance of S and B signals throughout the core of the nanoparticle may not necessarily indicate that these elements are incorporated in the nanoparticle interior but instead may line the nHA exterior through the thickness of the section. In single nanoparticles without the sulfopropyl methacrylate functionalization, levels of S and Ba are indistinguishable from the background signal. EDS line scans across the minor and major axes of nanoparticle increase in Ba and S X-ray generation correspond to the same spatial domain as increases in Ca, P, and O (characteristic of the particle itself). Variations in Ba and S intensity across the nanoparticle may indicate slight variations in coverage of the sulfopropyl methacrylate across the particle. Ultimately, the increase in residual Ba and S content on the functionalized nHA shows that the functionalization method is effective. SEM and TEM images of raw nHA nanocomposite and refined-functionalized nHA nanocomposite demonstrate a significant difference regarding nanoparticle dispersion. TEM and SEM imaging of nanocomposites on raw nHA nanocomposite systems demonstrate multiple globular, quasi-spherical nHA agglomerations on the microscale that can be as large as 10-15 μm in diameter. Where the aim of nHA strengthening is to provide a dispersed network of the bioceramic phase for a homogenous and predictable mechanical response. This form of agglomeration is detrimental to the micromechanical stress distribution and macroscopic mechanical performance of the nanocomposite materials [417–420]. As these microscale agglomerations serve as stress concentrators [421–423] within the material, the addition of nonprocessed nHA without functionalization, which resulted in microscale

agglomerations, may actually restrict the scope to which the nanocomposite can be used for biomaterial design and further multiscale simulations as a design tool. The SEM S-TEM images of the refined nHA nanocomposite system demonstrated a great improvement in the dispersion of nHA particles, while a few lower micron scale agglomerations were observed. Further functionalization of refined nHA samples reduced the remaining microscale agglomerations and demonstrated a homogenous dispersion of nHA particles with no clear agglomerations in the microscale with few small agglomerations around 100-200 nm. While in the previous studies, the silanization surface functionalization of nHA reduced the dispersion of nHA due to post-agglomerations created during the drying step, here in this study, the SPM functionalization in combination with nHA refinement improved the nHA dispersion significantly. The fracture strain and fracture strength increased by 75% and 37%, respectively, due to additional SPM functionalization and nHA refinement, while no significant difference was observed in the elastic modulus properties. This suggests an improvement in the ductility of SPM nanocomposite system, which requires further investigation. The increase in mechanical properties is associated with improved interfacial bonding due to the nanoscale dispersion of particles as well as the surface functionalization of nHA particles. The rheology results demonstrated that by improving the nHA dispersion, the ink viscosity and shear yield strength increased while still low enough for 3D printing on mSLA 3D printer, and they were successfully 3D printed. The increased viscosity and shear yield stress could be one of the drawbacks of improved dispersion in these nanocomposite inks, especially when designing higher volume fraction ink compositions if they are aimed to be printed using mSLA 3D printing techniques otherwise it will require further optimize and dilution of matrix. This should be considered carefully in designing inks, or DIW-based techniques can be used instead, which require higher viscosity and shear yield stress ink compositions.It should be noted that the lower intensity signals attributed for Ba and S elements on EDX and EDS results of SPM-refined nanocomposites in this study, could be due to the low percentage of nHA (5%) in the developed nanocomposite system and can be further optimized by increasing the volume fraction of nHA in the ink. Also, the mechanical properties will further demonstrate an improvement by increasing the volume fraction of SPM-refined nanocomposite system.

6.5. Conclusion

A novel technique and surface functionalization has been introduced in this study for improving the dispersion and interfacial bonding of nHA particles in a functionalized biopolymer matrix. The centrifuging steps of nHA in combination with SPM surface functionalization improved the dispersion of nHA particles in nanocomposite drastically, with almost no agglomeration observed in the microscale. Moreover, SPM functionalization of refined nHA particles improved interfacial bonding, resulting in 75% and 37% increases in fracture strain and fracture strength, respectively. The findings of this work, as well as the novel techniques introduced, will assist in the development and optimization of more mechanically competent 3D-printed nanocomposite grafts for application in bone reconstruction technologies.

Chapter 7

Micromechanical Elastoplastic Modeling and Characterization of 3D Printable Biopolymer Nanocomposites Using Realistic RVEs

7.1. Introduction

Polymer nanocomposites are a class of advanced materials that consist of a polymer matrix reinforced with nanoscale particles. The addition of nanoparticles to a polymer matrix can significantly enhance the mechanical, thermal, and electrical properties of the resulting composite material [140,424–428]. One of the key advantages of polymer nanocomposites is their ability to combine the desirable properties of both the polymer matrix and the nanoparticles. For example, the polymer matrix may provide elasticity and ductility, while the nanoparticles can provide increased stiffness, strength, and thermal stability. As a result, polymer nanocomposites have found applications in a wide range of industries, including aerospace, automotive, electronics, and biomedical engineering [429–431]. Advanced fabrication methods offer a promising way to tailor the microstructural characteristics of materials locally. However, the local control of dispersion is hindered by the inconsistencies in shape, size, and orientation of nanoparticles, as well as the presence of agglomerations. Therefore, the complex nature of these materials, including the heterogeneous distribution of nanoparticles within the polymer matrix, makes it challenging to predict their mechanical performance accurately [96,188,432–437].

Experimental testing and analytical models have been used to investigate the mechanical properties of polymer nanocomposites [438–441]. However, conducting experiments at the nanoscale is costly, and determining the correlation between process, microstructure, and property for these materials is challenging and infeasible for early design purposes. On the other hand, formulating analytical models can be challenging, and solving them can be overly complex. Furthermore, analytical models have limitations in accurately describing the complex microstructure of nanocomposites, capturing their nonlinear material behavior, and assessing local failures within these systems. These models often struggle to account for the complexity of nanocomposites' structures [187,188].

Numerical modelling is a useful tool for studying the behavior of polymer nanocomposites at different length scales. These models can provide insight into the mechanical and thermal properties of nanocomposites, as well as their electronic and optical properties[187–189]. By simulating the behavior of nanocomposites under different conditions, numerical modelling can help engineers and scientists optimize the design and performance of these materials for specific applications while ideally saving on resources. One approach to nanocomposite numerical modelling involves molecular dynamics simulations [442]. These simulations use classical mechanics to model the behavior of individual atoms and molecules in a nanocomposite. By simulating the interactions between these particles, molecular dynamics can provide information on the mechanical properties of a nanocomposite system, such as its strength and elasticity [187]. Another approach to nanocomposite numerical modelling involves finite element analysis. This method uses a mesh-based approach to model the behavior of a nanocomposite at the microscopic level. FEM micromechanical modelling can be used to simulate the behavior of a nanocomposite under different loading conditions. This information can be used to optimize the design of nanocomposites for specific applications. Instead of modelling entire objects, which is not feasible computationally, a representative volume element (RVE) can be used to represent the material microstructure, where complex microstructures of composites may be reproduced [443]. Hill defined an RVE as a sample that, on average, is structurally and completely representative of the total mixture and has enough inclusions to account for the apparent overall moduli [444]. As a result, each RVE needs to be suitably big and statistically representative of the heterogeneous material's overall characteristics [445]. On the other hand, the RVE size should be as small as feasible to allow for roughly homogenous stress and strain levels over the whole RVE and to be feasible considering the computational cost of simulating the deformation. Utilizing the RVE approach for micromechanical modelling has the benefit of providing a description of the stress and strain distributions through the developed microstructure [445]. Although micromechanical and RVE methods have been used to predict the mechanical properties of nanocomposites, especially those based on CNT [203–209], the complexity of their microstructure and inconsistency in the inclusion dispersion, shape, aspect ratios, and clusters have resulted in the use of simplifying assumptions. As a result, there has been less attention given to the micromechanical modelling of realistic RVEs generated based on the actual microstructure of a nanocomposite system. Furthermore, most multiscale and micromechanical simulations of nanocomposites have

focused more on predicting elasticity and less focused on investigating the elastoplastic properties of these materials [211,212,214,446]. While few studies have investigated the experimental aspects of mechanical properties of nHA-based polymer nanocomposites, which are a new generation of nanocomposites with an intended application in orthopedics [5,77,160,216,217], there is a noticeable scarcity of research focusing on computational modelling of nHA-based polymer nanocomposites systems [218,219]. Experimental determination of the relationships between the process, microstructure, and properties of these nanocomposites is a challenging and costly task, making it generally impractical for preliminary design purposes. However, the advancement of general design guidelines is crucial to promote the widespread adoption of these nanocomposite material systems and help engineers designing these materials. The development of an elastoplastic micromechanical model based on realistic RVEs derived from image processing analysis of actual microstructures may offer a novel approach for the early design of nanocomposite systems. Such a model enables the prediction of performance of the nanocomposite systems and local failure behavior, ideally reducing the need for extensive experimental tests. These models would also benefit researchers studying these materials by providing insight into how different nHA distribution and arrangement will affect the elastoplastic behavior of the material and facilitate further investigation into the local failure of these materials and interfacial deboning. To accurately model the elastic-plastic behavior of a polymer nanocomposite system, in addition to the generation of RVEs, which follows the actual microstructure of studied system, it is important to assign appropriate constitutive material models to the constituents. Polymers display different levels of yield strength when subjected to compression, tension, and shear, and they also exhibit pressure-sensitive yielding behavior. Extensive research has been conducted to explore the impact of hydrostatic pressure on the yield behavior of polymers, as documented in a number of comprehensive investigations [226–232]. The Drucker-Prager model, is extensively used to characterize the elastoplastic behavior of polymers [236–242]. It is specifically suitable for materials that demonstrate plasticity dependent on pressure. The Drucker-Prager model was developed by smoothing the surface defined by the Mohr-Coulomb yield criterion and introducing adjustments to the Von Mises yield criterion, as detailed in various studies [243–245].

In this study, a computational tool was developed to predict the elastoplastic micromechanical behaviour of a novel biopolymer nanocomposite system [447]. First, realistic RVEs were generated according to the actual microstructure of the novel nanocomposite, considering nHA

particle dispersion through the biopolymer matrix, inclusion aspect ratio, and nHA length distribution. To predict the elastoplastic properties of the novel nanocomposite system properly, the constitutive model was calibrated, verified and validated by conducting tensile, compression and shear tests on 3D printed functionalized biopolymer matrix. By employing the constitutive model in realistic RVEs, the effects of nanoparticle dispersion and arrangement on the elastoplastic properties of the novel nanocomposite system was further investigated. The findings in this study can be used as design guidelines for developing mechanically competent 3D printable nanocomposite materials.

7.2. Materials and Method

In order to simulate the elastoplastic micromechanical properties of the novel nanocomposite system [447], the appropriate constitutive model should be used for both constituents. Here in this study, the nHA inclusions were modelled as elastic isotropic [448] and the biopolymer matrix modelled using the Drucker-Prager elastoplastic constitutive model [236,449]. The elastoplastic constitutive material model requires calibration, verification and validation [249]. Tensile and compression tests were performed in this work, to calibrate and verify the Drucker-Prager constitutive model, and the shear test was used as an independent test to validate the derived material constants [256].

7.2.1. Preparation of Functionalized Biopolymer Matrix

Acrylated epoxidized soybean oil (AESO) was functionalized with additional methacrylate groups using methacrylic anhydride (MAA) and 4-(Dimethyl Amino) pyridine (DMAP) following a detailed protocol [136,160]. During the functionalization process, the AESO's hydroxyl groups were replaced by methacrylate groups, resulting in mAESO, a new stronger biopolymer with additional functional groups for crossliking [136]. After the functionalization of the AESO was completed, the biopolymer matrix was produced by combining 50% mAESO with 50% polyethylene glycol diacrylate (PEGDA) using an ultrasonic homogenizer.

7.2.2. 3D Printing of the Functionalized Biopolymer Matrix

7.2.2.1. Tensile Test Specimens

The dogbone-shaped test specimens (Overall length: 30 mm; Gauge length: 10 mm long, 2.5 mm wide, and 2 mm thick; according to the ASTM D3039, 2017) were 3D printed using a Phrozen

Sonic XL 4 K mSLA-type 3D printer (Phrozen Technology, Taiwan). 3D stereolithographic (.stl) files were sliced using the Phrozen slicer software. The software was utilized to create suitable support fixtures around the grip area, ensuring the proper attachment of the specimens to the print bed during printing. Additionally, this helped prevent any defects in the specimen during the printing process and facilitated easy removal of the samples from the print bed. To eliminate defects that might impair mechanical testing results, no supports or fixtures were added along the gauge length. All specimens were printed with 50 μm layer height. Except for the first six layers, which were cured for 15 seconds to ensure good build plate adhesion, each layer was exposed to UV for 7.5 seconds. After 3D printing was complete, the specimens were carefully removed from the print bed, the supports removed carefully, and the specimens wiped thoroughly to remove the residue-uncured resin. Next, the specimens were exposed to further UV for 10 minutes on each side in a post-print curing chamber (CureZone MKII, Creative CADWORKS, Canada).

7.2.2.2. Compression Test Specimens

Guidelines provided by ASTM international testing standard ASTM - D695 for determining the compression properties of plastics under quasi-static stress were followed for measuring the behaviour of the functionalized biopolymer matrix under compression and for calibrating the constitutive model. Several enhancements were made to address the issues of specimen buckling and barreling and also to respect the capacity of the load cell (1.6 kN) in order to obtain the yield strength of the biopolymer matrix. According to ASTM-D695, a right cylinder or prism specimen with a length, twice the major width or diameter is recommended for compression tests. After some trial designs, the right cylinder specimen with 2.5 mm in diameter and 5 mm in length was selected. The cylindrical samples were printed on the mSLA printer without any fixtures and right on the bed of the 3D printer. In order to have consistency in the diameter of the specimen through the length, all specimens were printed with 50 μm layer height and exposed for 7.5 seconds to UV. After printing, the specimens were cured the same way as the tensile specimens in the UV chamber for 10 minutes.

7.2.2.3. Uniaxial Shear Test Specimens

There are no uniaxial testing standards for characterizing the shear properties of plastics. Consequently, the uniaxial shear specimen geometry was adapted from a unique specimen

geometry initially proposed for shear testing of metallic alloys under static and dynamic stress [450,451]. Although the mini-shear sample geometry had some complications related to fabrication, it has the advantage of enabling the shear test using a uniaxial test frame [452]. To keep the gaps in the top and bottom of the sample symmetrical and aligned during printing and after curing and to enable successful printing of the specimen, several beam support designs were implemented between the gaps on the top and bottom of the shear sample as well as base supports (Fig. 7.1). Specimens with different support designs were tested, and the Levy Mises equations [453] were checked in the center of the sample for the shear stress state by comparing the Hencky principal stresses ratio obtained from DIC (Appendix) to further evaluate the shear stress state in the centre of the mini-shear sample. Finally, the shown support design in Fig. 7.1 provided the optimum results. Specimens were printed with 50 μm layer height. Each layer was exposed to UV for 7.5 seconds, except for the first six layers, which were cured for 15 seconds to guarantee proper build plate adhesion.

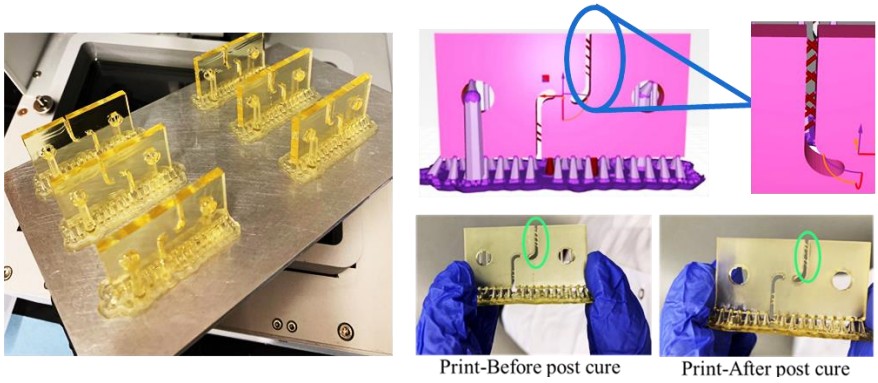


Fig. 7.1. 3D printed mini-shear samples with final beam support design

7.2.3. Mechanical Testing of the Biopolymer Matrix

7.2.3.1. Tensile testing of 3D Printed Biopolymer Matrix and Nanocomposite Specimens

Tensile testing (Fig. 7.2) was carried out using a Psylotech μTS mechanical testing system equipped with a 1.6 kN load cell (Psylotech Inc., Evanston, IL, United States). Strain measurements were performed using a microscope-enabled Digital Image Correlation system (DIC; Vic 2D 6, Correlated Solutions Inc., USA). During the test, a microscope (BXFM, Olympus Corp., Center Valley, PA, USA) equipped with a 2.5x objective lens (Olympus Corp., Center Valley, PA, USA) and a mounted digital camera (Point Grey, 5 MP, 2/3" detector) took magnified

images of the gauge length. Before testing, all specimens (n = 7 per group) were sprayed with high-resolution laser printer toner powder (4-5 μm in diameter, Xerox Phaser 6000) using an atomizer jar to generate speckle patterns that allowed DIC-based strain measurements. The specimens were initially preconditioned with a small load (5N) at room temperature for 100 cycles at 1 Hz. The extension was then conducted at a speed of 16 μm/s (average strain rate of 0.0016 s^{-1}). The load cell data was collected at 5 Hz. For the DIC in all experiments, the subset window and step size were set to 150 and 7 pixels, respectively (1 micron=2.77 pixels).

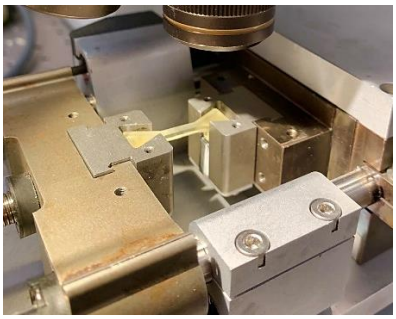


Fig. 7.2. Biopolymer matrix Dogbone tensile test set-up

The extensometer tool from the DIC was employed over the length of the Area of Interest to calculate the average engineering strains. The slope of the stress-strain curve's linear elastic region was used to calculate Young's modulus. Poisson's ratio (ν) was computed using the ASTM standard for tensile testing:

$$\nu = -\frac{D\varepsilon_t}{D\varepsilon_l} \tag{7.1}$$

Where ν represents the slope of a $\varepsilon_t - \varepsilon_l$ plot. To define the yield strength a 0.2% offset of the elastic modulus slope line was reported which is commonly accepted in the polymer technical community [249].

7.2.3.2. Compression Testing

The quasi-static compression tests were performed on a Psylotech TS mechanical testing system with a 1.6 kN load cell (Psylotech Inc., Evanston, IL, United States) using compression platens fixtures (Fig. 7.3). To minimize specimen barreling during compression testing and grease was applied to the platens.



Fig. 7.3. Biopolymer matrix compression test set-up

The strain was calculated using the local displacement sensor directly connected to the moving crosshead after calibration due to the limitation of using a 2D DIC setup for analyzing the cylindrical specimen surface. Using the force-displacement data, the compression stress-strain curves were obtained accordingly for the biopolymer matrix, and the compression yield strength value was defined to use for calibrating the Drucker-Prager constitutive model [249].

7.2.3.3. Uniaxial Shear Testing

The same test frame, fixtures, microscopy and camera system used for the uniaxial tension testing were used for the uniaxial shear tests (Fig.7.3). The same DIC method was employed to analyze the sample deformation. In order to use the tensile test fixtures for the shear samples, pin inserts were designed and fabricated from steel in the University of Waterloo's tool shop to hold the shear sample during the testing.

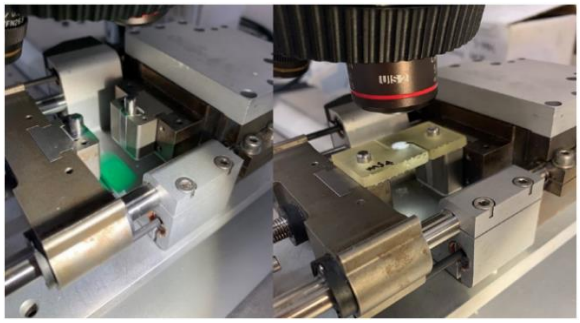


Fig. 7.4. Uniaxial shear test setup

To evaluate the simple shear state in the center of the shear sample, the Hencky (logarithmic) strains were calculated during DIC analysis and the principal logarithmic shear strains were obtained and compared to investigate the simple shear stress state in the middle of the mini-shear samples (Appendix) [453].

7.2.4. Material models

7.2.4.1. Drucker-Prager Elastoplastic Constitutive Model for the Biopolymer Matrix

The Drucker-Prager model is a widely used elastoplastic model for polymers which takes into account the influence of hydrostatic pressure on the plastic behavior of these materials. As the hydrostatic pressure increases, the yield surface expands and moves outward. The Drucker-Prager criterion (Fig.7.5) incorporates the influence of hydrostatic pressure on the resistance of a material to shearing [243,454].

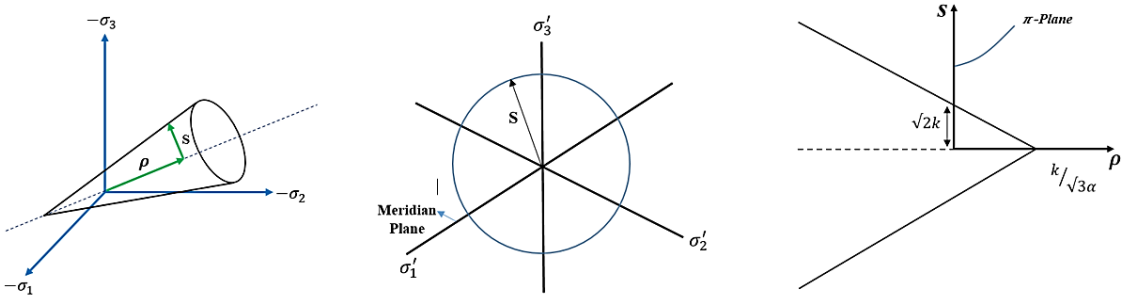


Fig. 7.5. Drucker-Prager yield criterion in principal stresses, π-plane and meridian plane

And the yield criterion is expressed by [455]:

$$f(I_1, J_2) = \sqrt{J_2} + \alpha I_1 - k = 0 \tag{7.2}$$

Where α and k are defined as the positive constants at each point of the material and are known as Drucker-Prager parameters. I_1 and J_2 are defined as the first invariants of Cauchy stresses and the second invariant of the deviatoric part of the Cauchy stresses, respectively. For uniaxial tension and compression, the α and k are obtained as follows:

$$\alpha = \frac{1}{\sqrt{3}}\left(\frac{\sigma_t - \sigma_c}{\sigma_c + \sigma_t}\right), \qquad k = \frac{2}{\sqrt{3}}\left(\frac{\sigma_c \sigma_t}{\sigma_c + \sigma_t}\right) \tag{7.3}$$

Where σ_t and σ_c are yield strength under tension and compression (Table 7.1). The cohesion and internal friction angles, which are denoted as c and ϕ respectively, are obtained using the following equation:

$$\alpha = \frac{2\sin\emptyset}{\sqrt{3}(3+\sin\emptyset)}, \qquad k = \frac{6c\cos\emptyset}{\sqrt{3}(3+\sin\emptyset)} \tag{7.4}$$

Using the yield strength values obtained from experiments, the material constants were obtained accordingly for the biopolymer matrix.

7.2.4.2. Hardening Properties

Once the yield criterion for the elastoplastic simulations has been calibrated and verified, it is essential to accurately define and capture the hardening properties of the biopolymer matrix using the available hardening models in Digimat FE. The hardening properties of the biopolymer matrix were determined by fitting the experimental data to an isotropic exponential hardening model defined as follows. The fitting was performed using a developed genetic optimization algorithm [357] by comparing the theory and experiment plastic stress-strain values. Isotropic exponential hardening model described as follow:

$$R(\epsilon_p) = R[1 - \exp(-b\epsilon_p)] \tag{7.5}$$

Where *R* and *b* are the hardening constants (hardening modulus and hardening exponents) obtained accordingly and presented in Table 7.2.

7.2.5. Realistic RVE Generation

The goal of micromechanical modelling is to capture the interactions and behavior of individual components within the material's microstructure/nanostructure and to determine the effect of the microstructure on the macroscopic (or effective) response. Solving the entire mechanical problem at the microscale would be computationally prohibitive. As a result, we distinguish two scales: the microscopic (that of heterogeneities) and the macroscopic (that of the solid being locally homogeneous). The concept of representative volume element (RVE) serves as a mesoscale bridge between the two previously mentioned scales.

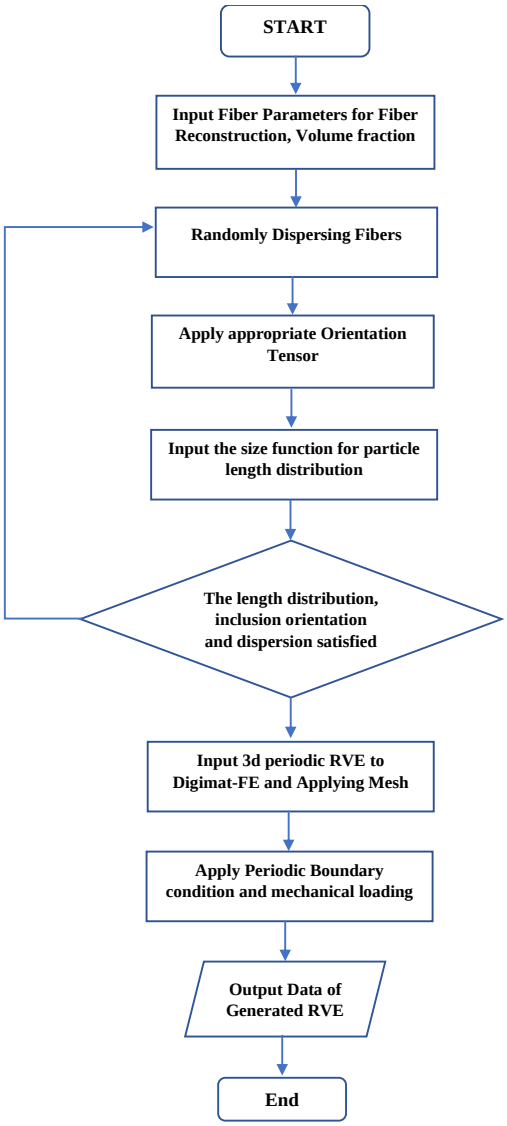


Fig. 7.6. RVE generation algorithm using Digimt-FE

Digimat-FE, a commercial finite element-based homogenization software produced by e-Xstream Engineering S.A.(MSc Software), was used in this study to generate realistic three-dimensional periodic RVEs based on the measured microstructure of our novel 3D printed nanocomposite system [447]. Each RVE was generated following the algorithm demonstrated in Fig. 7.6. After generating the RVEs, they were exported to the Digimat-FE solver to run the simulations. After mesh sensitivity analysis (Appendix), RVEs meshed with 500,885 integration three-dimensional tetrahedral quadratic elements with an average element size of 10 nm. The particles and matrix were assumed to be perfectly bonded. In the model nanocomposite system, the nHA particles were further functionalized to improve interfacial bonding as well as to partially address the assumption

of perfect bonding in the computational model. Periodic boundary conditions (PBCs) were applied to the RVEs as they are widely used when determining the effective properties of composites with periodic microstructures [456]. Microscale homogenization through Digimat-FE was performed to predict the effective stress–strain response. Uniaxial tensile displacements were imposed on the surfaces of the RVEs to capture effective elastic modulus and other orthotropic elastic constants using the FE method.

7.2.5.1. RVE Size Definition

The first step in the micromechanical modelling is to determine an appropriate RVE size for a sufficient approximation of heterogeneous material systems and for estimating the overall properties of polymer nanocomposite systems [443]. The computational costs (time, memory, number of elements, etc.) depend on the RVE size. In general, the size of RVE should be determined to properly capture the average local material displacement and strain fields while also balancing the computational effort. So as the first step in RVE micromechanical modelling, the optimum RVE size was obtained according to the size sensitivity analysis.

7.2.5.2. Orientation Tensors

Since the rod-shaped nHA particles are not aligned in our nanocomposite system, in order to generate realistic RVEs according to the real microstructure, nanorods are randomly dispersed and oriented through the RVE. The inclusions must not only be non-uniformly dispersed but also randomly oriented in the RVEs to follow the real microstructure. This requires introducing additional orientation tensors to individual nanorods. Each individual inclusion's orientation is described by a unit vector P along its axis of revolution, which can be determined in 3D configuration with two spherical angles θ and ϕ (Fig. 7.7).

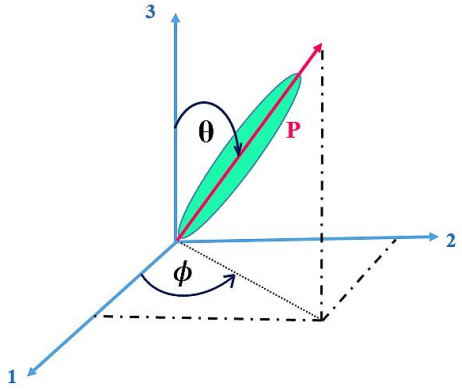


Fig. 7.7. Nanoparticle oriented in 3D with unit vector p along its axis of a revolution described with two spherical angles θ and ϕ.

The axis vector p differs between inclusions within the same RVE, so the concept of orientation distribution function (ODF) (p) was used. (p)dp is the probability of finding fibres within [p, p + dp] solid angles. The fourth-order orientation tensor is defined as [457,458]:

$$a_4 = \int P \otimes P \otimes P \otimes P \, \psi(P) dP \tag{7.6}$$

Where P is the unit vector aligned in the fiber axis direction, " $\otimes$ " indicates the tensor product and $\psi(P)$ is the orientation distribution function which should satisfy the normality condition ($\int \psi(P) dP = 1$) imposing that the sum of probabilities equals one and also two opposite axis vectors determining distinct particles ($\psi_i(P) = \psi_i(-P)$). The second and fourth-order orientation tensors a_2, a_4 are defined also as the following orientation averages:

$$a_2 = \langle P \otimes P \rangle_\psi \qquad a_4 = \langle P \otimes P \otimes P \otimes P \rangle_\psi \tag{7.7}$$

These tensors are required to satisfy the following condition:

$$\begin{aligned} &a_{ij} = a_{ji} \\ &a_{11}, a_{22}, a_{33} \geqslant 0, a_{ii} = 1 \\ &A_{ijij} \geqslant 0, A_{ijll} = a_{ij} \end{aligned} \tag{7.8}$$

In practice, only the second-rank orientation tensor, not the ODF, is typically provided for a composite with misaligned inclusions. However, in some cases, both the second and fourth-rank orientation tensors are required for homogenization. To compute the fourth-rank orientation tensor from the second-rank orientation tensor, the following closure problem or exact solution was implemented [457,458]:

$$\begin{aligned} &A^I(a) = \alpha_1 1 \otimes 1 + 2(\alpha_1 - \beta_1) I^s + \beta_1 (1 \otimes a + a \otimes 1) + 2\beta_1 [\mathrm{I(a+1)\text{-}I(a)}] \\ &\alpha_1 = -\frac{1}{35} and \; \beta_1 = 1/7 \end{aligned} \tag{7.9}$$

The average orientation tensor for randomly orienting inclusions in three dimensions is defined as a second-order tensor with all diagonal components equal to 1/3 and all off-diagonal components being null. This tensor is applied to particles to randomly align them in the RVE and assign each individual particle random θ and φ, which define the orientation of each individual particle. The global error, which computes the difference between the actual reference orientation tensor of RVE and the reference orientation tensor, is computed as follows:

$$Global\ Eror = \sqrt{\sum_{ii}(a_{ii}^{actual} - a_{ii}^{ref})^2 + 2.0 * \sum_{ij}\sum_{ii}(a_{ij}^{actual} - a_{ij}^{ref})^2} \quad (7.10)$$

7.2.5.3. Length Distribution

The rod-shaped nanoparticles in the biopolymer matrix are not all the same length in practice, and their length varies according to high-resolution SEM and TEM images [447] and ImageJ measurements. According to ImageJ measurements, the length of nanohydroxyapatite ranges from 80 nm to 160 nm, with the majority of the particles falling between 100 nm and 120 nm. To impose the length distribution on the nanorods, a normal Gaussian distribution function with the following distribution parameters was applied (Fig.7.8) as the nanorod size function in Digimat-FE. The effective size distribution in RVEs was compared to the applied size distribution to check for discrepancies between the two.

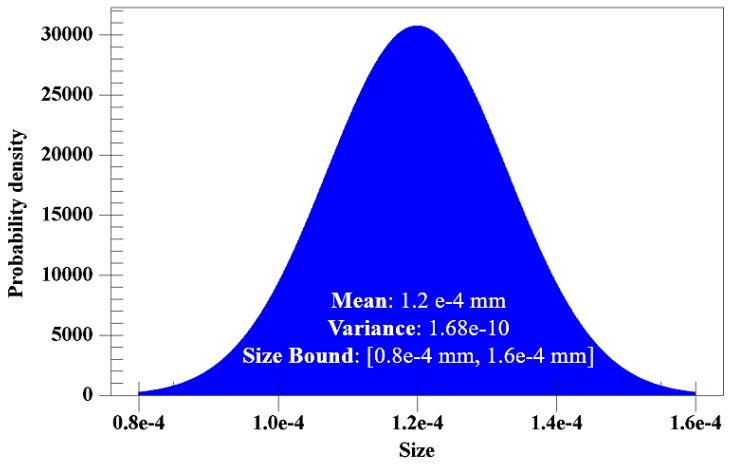


Fig. 7.8. Gaussian probability distribution vs size of rod-shaped nanoparticle in the matrix.

7.2.5.4. Agglomerations

Despite the fact that dispersion improved significantly in the new 3D printable nanocomposite system and no micron-scale agglomerations were observed, high-resolution TEM and SEM images revealed small nanoscale agglomerations. In order to generate RVEs with realistic features, we introduced small agglomerations with varying volume fractions and randomly dispersed them in the generated RVEs. While these small nanoscale agglomerations may not affect the elastic properties of RVEs in the elastic region significantly, they may act as stress concentrators in the microstructure, influencing local stress values and the onset of local failure. As a result, introducing these clusters aids in obtaining more realistic RVEs for further micromechanical assessments. By keeping the total volume fraction of the RVEs constant at 5% according to the volume fraction of the new nanocomposite system, the agglomeration volume fraction ranged from 0.25% to 1.5% by changing their number and individual volume fractions through the RVE.

7.2.6. Application of Periodic Boundary Condition on 3D Periodic RVEs

According to the literature, obtaining the effective mechanical properties in composite structures by imposing periodic boundary conditions (PBC) has led to better approximations compared to other boundary conditions [459–462]. Before employing computational homogenization, periodic boundary conditions were applied to our microscale 3D periodic RVEs (Fig. 7.9).

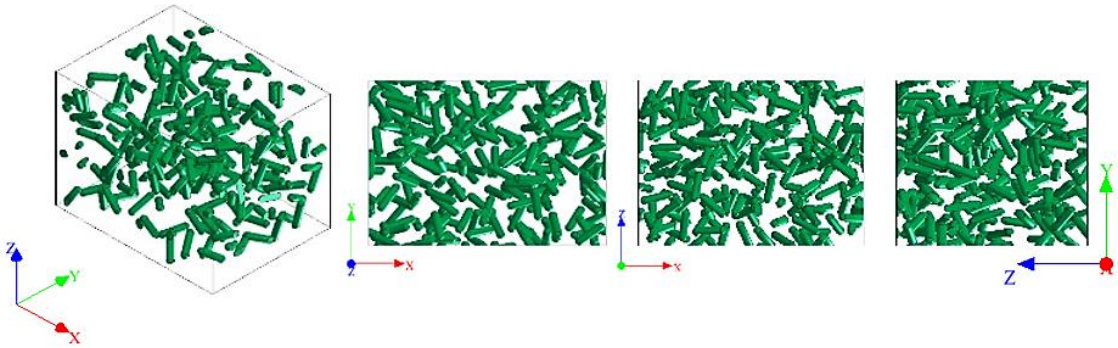


Fig. 7.9. 3D periodic RVEs; sample RVE cross-section views demonstrate periodic geometry in all three directions

Periodic boundary conditions ensure that the flux of the field variable (displacement, temperature, electric potential) is periodic with respect to the faces of the volume element. This is imposed by a large set of equations that, on a two-by-two basis, associate the degrees of freedom of the nodes on one face to those of the corresponding nodes on the opposite face. Node duplication is used to

avoid problems caused by non-periodic meshes. The displacement field u for the periodic RVE of composites under macroscopic strain u is given by [463]:

$$u_i(x_1, x_2, x_3) = u_i^0 + u_i^*(x_1, x_2, x_3) \;\; with \;\; u_i^0 = \varepsilon_{ij}^0 x_j \tag{7.11}$$

In the above equation, $u_i^0 = \varepsilon_{ij}^0 x_j$ defines the displacement field in the periodic composite while $u_i^*(x_1, x_2, x_3)$ is the periodic part of the displacement field on the boundary surfaces which generally is unknown and can not be directly applied to the RVE's boundaries. In a periodic RVE, boundary surfaces appear in parallel pairs, and displacements on two parallel opposite boundary surfaces can be expressed as follow:

$$u_i^{k+} = \varepsilon_{ij}^0 x_j^{k+} + u_i^* \;\; and \;\; u_i^{k-} = \varepsilon_{ij}^0 x_j^{k-} + u_i^* \tag{7.12}$$

where k+ and k- denote the kth pair of two opposite parallel boundary surfaces of an RVE. Because of the periodicity, u_i^* is identical at the two parallel boundaries.

$$u_i^{k+} - u_i^{k-} = \varepsilon_{ij}^0 (x_j^{k+} - x_j^{k-}) = \varepsilon_{ij}^0 D x_j^k \tag{7.13}$$

With a specified macroscopic strain ε_{ij}^0, $x_j^+ - x_j^-$ becomes constant for each pair of nodes located on the parallel boundary surfaces, edges, and corner vertices in the RVE of composites, and the right-hand side of Eq. (13) becomes constant, allowing the equations to be easily implemented in finite element analysis as a nodal displacement constraint. In addition to displacement continuity, periodic boundary conditions should satisfy the traction continuity as well. As a result, the periodic boundary condition on the boundary of an RVE for composites is given below:

$$\begin{aligned} &u_i^+ - u_i^- = \varepsilon_{ij}^0 \left(x_j^+ - x_j^-\right) = D u_i \\ &t_i^+ = -t_j^- \,, t_i = s_{ij}^0 n_j \end{aligned} \tag{7.14}$$

7.2.7. Homogenization and Mesh Sensitivity Analysis

Homogenization, as a critical step in micromechanical modelling with the RVE technique, was employed in the RVEs to obtain the required bulk mechanical properties of the RVE [218,464,465]. Homogenization assumes that the material is sufficiently homogeneous at the macroscale but heterogeneous at the microscale due to the presence of inclusions, grains, clusters,

etc. [220]. Fig. 7.10 demonstrates a heterogeneous periodic microstructure which comprises at least two constituents. The body has two length scales, a global length scale, D, that represents the order of the size of the body, and a local length scale, d, that is proportional to the wavelength of the variation of the microstructure [465].

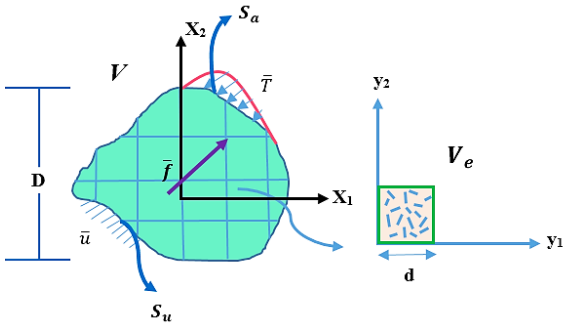


Fig. 7.10. a) Heterogeneous periodic microstructure (V) b) RVE of the composite structure (V_e) with matrix and inclusions.

$$\delta = \frac{d}{D} \ll 1 \tag{7.15}$$

In general, the equilibrium equations, strain-displacement relations, and constitutive law for a heterogeneous material are defined as follows:

$$\begin{aligned} &\sigma_{ij,j} + \overline{f_i} = 0 \quad in \quad V \\ &\sigma_{ij} = C_{ijkl}(\frac{x}{\delta}, \varepsilon)\varepsilon_{kl} \\ &\varepsilon_{kl} = \frac{1}{2}(u_{k,l} + u_{l,k}) \\ &\sigma_{ij} n_j = \overline{T}_i \quad on \quad S_a \\ &u_i = \overline{u}_i \quad on \quad S_u \end{aligned} \tag{7.16}$$

Where V, $\sigma_{ij,j}$ and $\overline{f_i}$ represents the whole volume, the derivatives of stress components with respect to j and body forces, respectively. ε_{ij} and C_{ijkl} are the strain components in equilibrium equations and elastic stiffness matrix, respectively. $\overline{T}_i$ and u_i demonstrate the prescribed external force and displacement per unit area on the boundaries S_a and S_u respectively.

The coupling of macroscopic and microscopic deformation and stress in first-order homogenization is achieved through the use of integral averaging theorems [218]. If the RVE is

subjected to a macroscopically homogeneous stress or displacement field on its surface without anybody forces, then the volume-averaged stresses, $\bar{\sigma}$, and strains, $\bar{\varepsilon}$, are defined as follow:

$$\langle \overline{\sigma}_{ij} \rangle = \frac{1}{V_e} \int_{V_e} \sigma_{ij} \, dV_e$$
$$\langle \overline{\varepsilon}_{ij} \rangle = \frac{1}{V_e} \int_{V_e} \varepsilon_{ij} \, dV_e \tag{7.17}$$

Which $\overline{\sigma}_{ij}$ is the volume-averaged stress, σ_{ij} is the local stress or micro stress, $\overline{\varepsilon}_{ij}$ is the volume-averaged strain, and ε_{ij} are the local strain components. To calculate the effective stiffness (Compliance) tensor, the averaged stress (strains) should be determined, hence to get this the local stresses (strains) within the RVE should be defined. The equivalent homogenized stiffness matrix of $\overline{C_{\iota jkl}}$ for three-dimensional RVEs are calculated using six independent unit macro strains and PBCs for six independent cases and could be computed using the evaluated volume averaged stresses and strains according to the following equation:

$$\langle \overline{\sigma}_{ij} \rangle = \overline{C_{\iota jkl}} \langle \overline{\varepsilon}_{ij} \rangle \tag{7.18}$$

7.3. Results and Discussion

7.3.1. Material Model Calibration and Verification

The experimental tensile, compression and shear test results are presented in Fig. 7.11 to Fig. 7.13. The obtained tensile and compression yield strengthes of biopolymer matrix were used to calibrate the elastoplastic constitutive model and derive the material constants for the functionalized biopolymer matrix.

Table 7.1. The assumed elastic properties of nHA [466] and measured biopolymer matrix properties.

	Young Modulus (MPa) *E*	**Poisson Ratio (*v*)**	**Tensile Yield Strength (MPa)**	**Compression Yield Strength (MPa)**
Nanohydroxyapetite	114000	0.29	-	-
Biopolymer matrix	1690	0.39	21	35

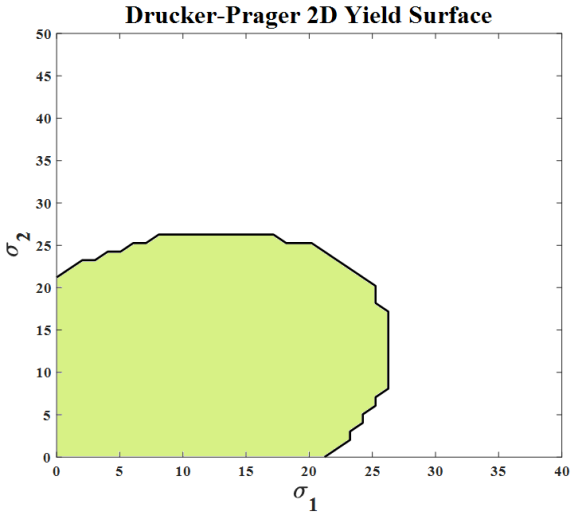


Fig. 7.11. Drucker-Prager 2D yield surface for the biopolymer matrix.

Using the experimental data (Table.7.1) and implementing Eq.7.2 to Eq.7.4, the Drucker-Prager yield surface was obtained for the biopolymer matrix. See Fig.7.11. Single element uniaxial tension, compression and shear tests were performed to verify the suitability of the Drucker Prager model to capture the experimentally measured response of the matrix material at quasi-static strain rates. This was achieved by implementing the appropriate boundry conditions for each case. A 3D hexahedral element measuring $1 \times 1 \times 1$ mm^3 was employed, along with the boundary conditions illustrated in Fig. 7.12- Fig. 7.14.

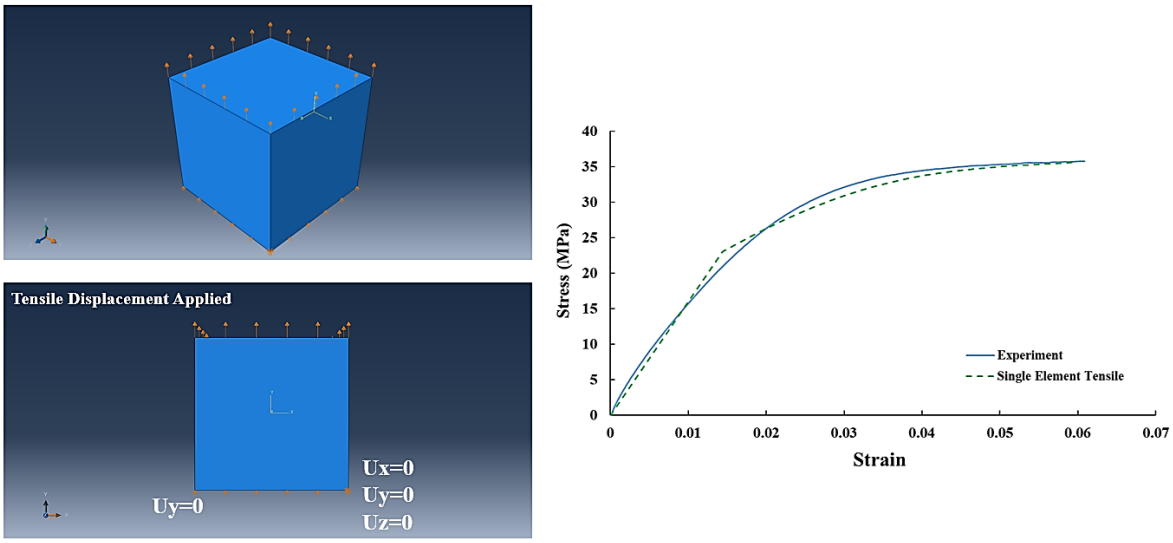


Fig. 7.12. Single element verification test models for the biopolymer matrix under tension.

(Ux, Uy, and Uz represent the displacement in the x, y and z directions, respectively).

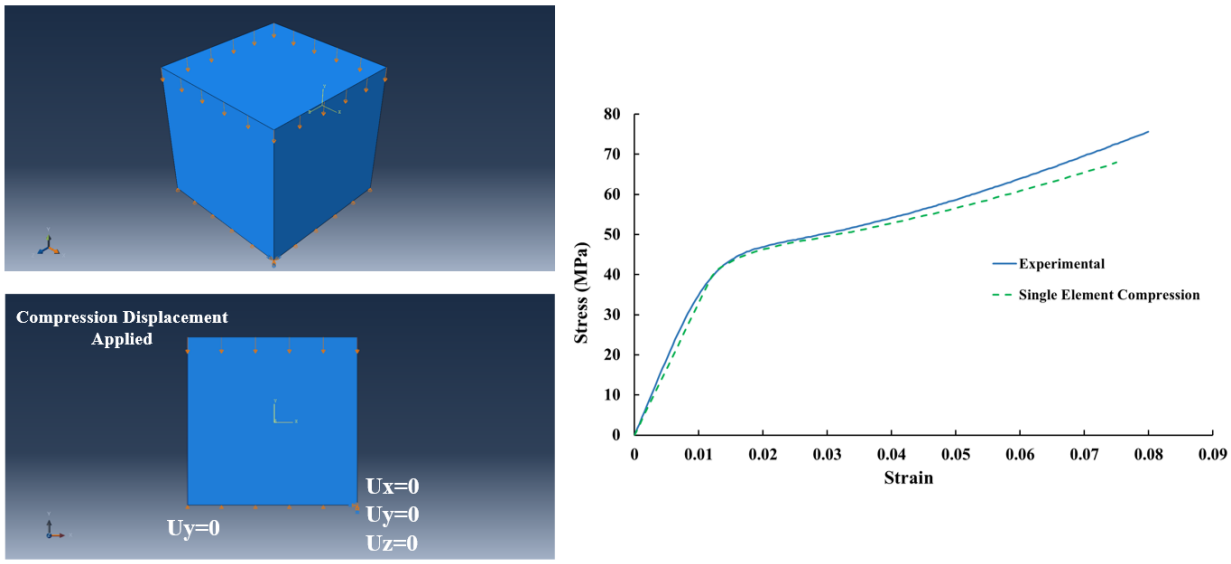


Fig. 7.13. Single element verification test models for the biopolymer matrix under compression.

(Ux, Uy, and Uz represent the displacement in the x, y and z directions, respectively).

The tensile hardening values and obtained material constants were input into the material model to verify the response of the model against independent shear test data. The material properties utilized were obtained from Table 7.1. The single-element predictions compared well with the experimentally measured results for the quasi-static strain rates and the stress–strain response are in good agreement with the experimental results.

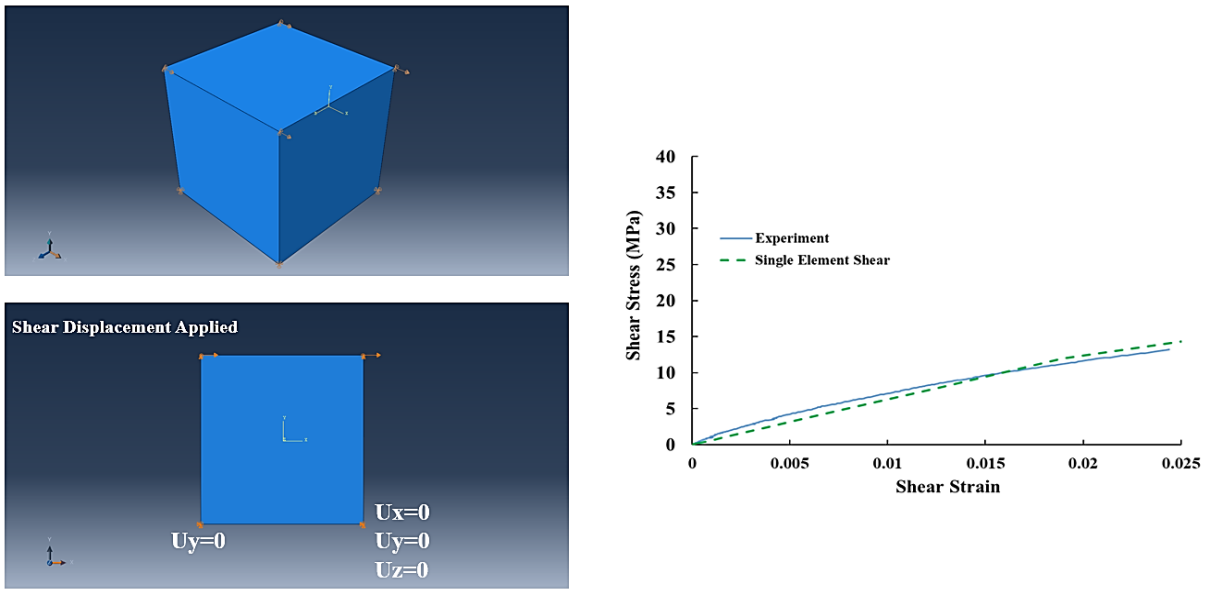


Fig. 7.14. Experimental and single-element quasi-static test results for the biopolymer matrix tested in shear.

(Ux, Uy, and Uz represent the displacement in the x, y and z directions, respectively).

7.3.1.1. Hardening Properties

Using the derived yield parameters as well as obtained optimized hardening parameters (Table 7.2) for the biopolymer matrix, a single element test conducted in Digimat-FE to examine the obtained material constants suitability for capturing the elastoplastic properties studied biopolymer matrix (Fig. 7.15).

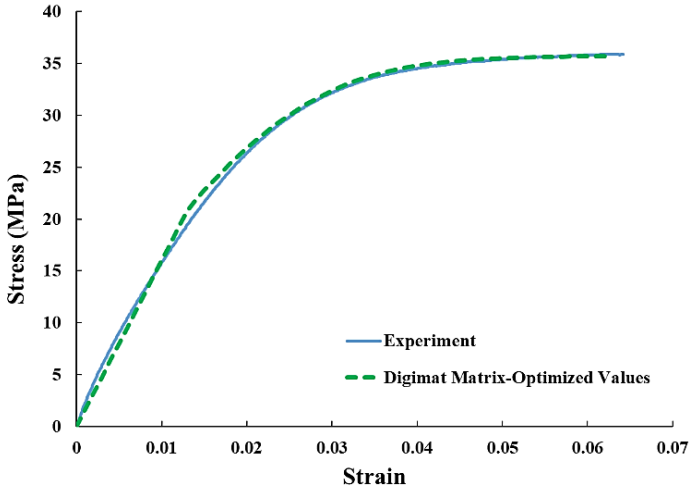


Fig. 7.15. Comparison the Digimat-FE tensile single-element and averaged experimental quasi-static test results for the biopolymer matrix using derived material and hardening properties.

Table 7.2. Calibrated hardening parameters

	R	b
Biopolymer matrix	150	14.5

7.3.2. Micromechanical Simulations

When studying nanocomposites, it is important to determine an appropriate RVE size that captures the essential features of the material's microstructure while still being computationally feasible [220]. Finding the optimal RVE size involves a trade-off between computational feasibility and accuracy. Through different iterative analyses, the RVE size sensitivity was evaluated by conducting micromechanical elastic modelling on several generated 3D periodic RVEs with different sizes to obtain the optimal RVE size while also balancing the computational cost.

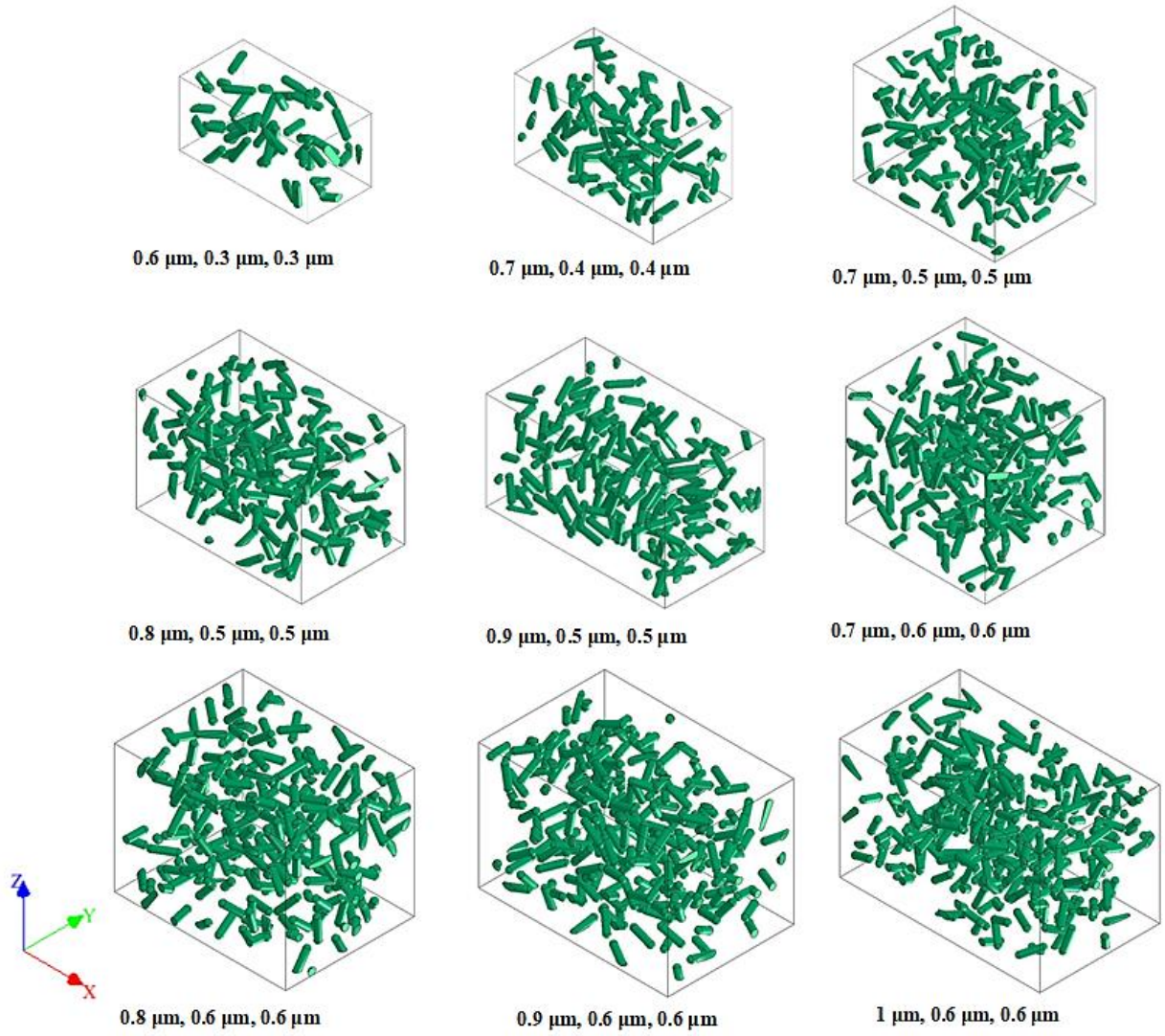


Fig. 7.16. RVE size sensitivity analysis. RVE size was increased in all three directions while keeping the volume fraction of particles constant at 5% in all RVEs.

Fig. 7.16 shows the generated RVEs with varying dimensions but a constant volume fraction of 5%. Due to the sphero-cylindrical shape of the nHA particles [447], particles have been modelled as sphero-cylindrical nanorods (120 nm, Average aspect ratio of 4). The inclusions were distributed randomly while random 3D orientation tensors were applied to the inclusions. By increasing the RVE size, which leads to an increased number of inclusions at a constant volume fraction, the required computational time increased. Referring to [208], an RVE size with five inclusions per length of RVE is an appropriate representative size for a nanocomposite system with rod shaped inclusions. Assuming an average length of inclusion of 120 nm, an RVE size of 0.6 µm is therefore appropriate for the studied nanocomposite system. According to Table 7.3 and

the RVE size sensitivity analysis (Fig. 7.16) and comparing with the experimental elastic modulus of 1926 MPa [447], the computed elastic modulus converges to an relatively consistent value by the RVE with 162 inclusion. By exceeding the inclusion number of 200 in the generated RVEs, the computation time with Digimat-FE increased significantly for only modelling the elastic properties. Therefore, considering the computational cost and balancing feasibility and accuracy and consistency in obtained elastic modulus, an RVE size of 0.8 μm, 0.6 μm, and 0.6 μm with 185 inclusions was chosen in this study as the optimum RVE size for running the micromechanical simulations.

Table 7.3. RVE size sensitivity analysis results.

RVE size (μm)	Number of Inclusions in RVE	Elastic Modulus (MPa)
0.6,0.3,0.3	34	1937.3
0.7,0.4,0.4	72	1938.3
0.7,0.5,0.5	112	1937.6
0.8,0.5,0.5	128	1936.7
0.9,0.5,0.5	144	1938.7
0.7,0.6,0.6	162	1945.3
0.8,0.6,0.6	185	1946.3
0.9,0.6,0.6	208	1947.0
1,0.6,0.6	231	1947.3

7.3.2.1. Nanorod Alignment Effect

In order to examine the impact of nanoparticle dispersion and alignment, a case study was conducted with the aim to investigate the influence of particle alignment on the elastic properties of the current nanocomposite system. Six RVEs were created (Fig.7.17), each having a fixed number of inclusions and identical inclusion properties (length of 120 nm and aspect ratio of 4) with a consistent volume fraction in order to investigate only the alignment effect on the final elastic properties. The percentage of aligned nanoparticles in the loading direction (x-axis) was incrementally varied from 0% to 100%. The elastic modulus (E_{11}) was computed and is reported in Table 7.4.

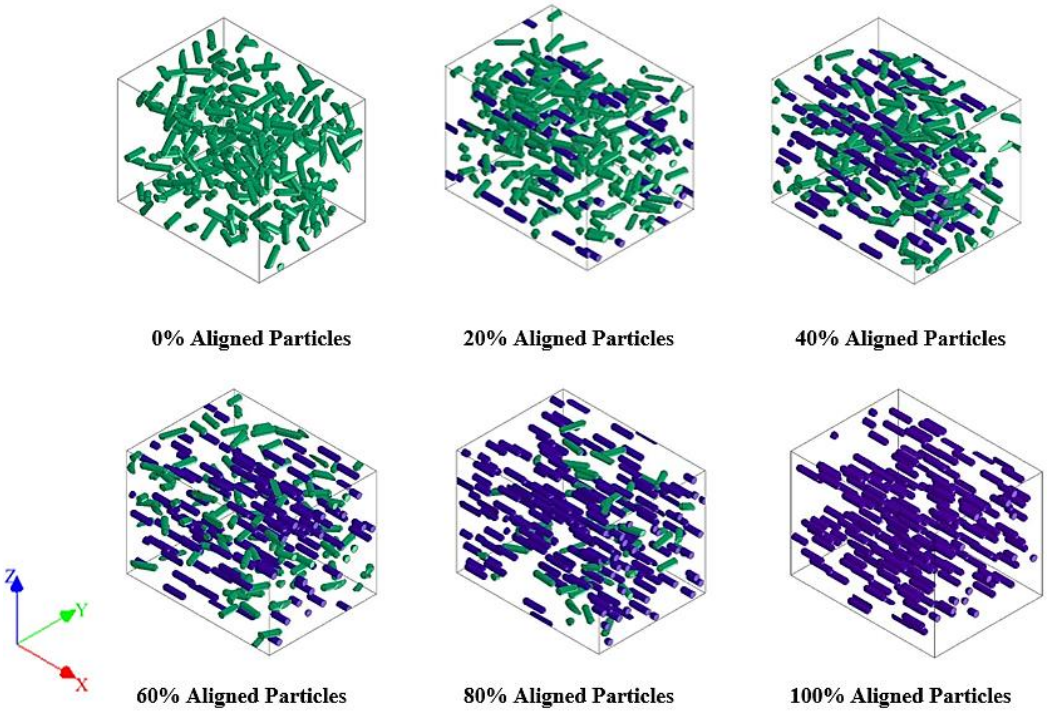


Fig. 7.17. Represented RVEs generated with different percentages of aligned particles at a constant volume fraction.

As seen from the results, the elastic modulus (E_{11}) increases by increasing the percentage of aligned particles in the x direction. When all the nHA particles are aligned in the x direction, the elastic modulus increases by 16% in a constant volume fraction, which has also been observed in the other nanocomposite systems [463].

Table 7.4. The elastic modulus of representative RVEs with increasing particle alignment in the uniaxial loading direction.

Aligned Particles Percentage	Elastic Modulus (MPa)
0%	1946.3
20%	2063.3
40%	2112.3
60%	2171
80%	2215
100%	2250

7.3.2.2. Nanorod Length and aspect ratio effect

In addition to inclusion dispersion, the aspect ratio and length effect on the elastic properties of developed nanocomposite systems was studied.

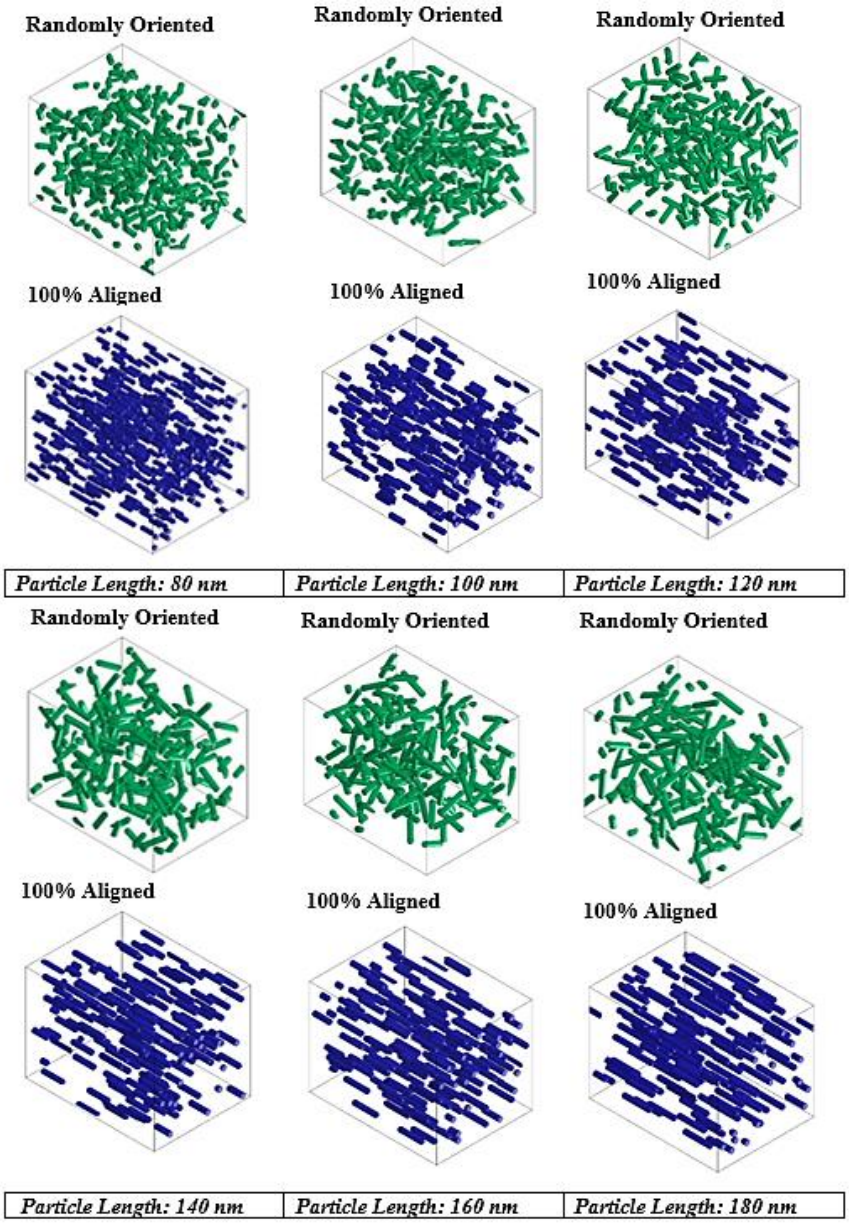


Fig. 7.18. Represented RVEs with different length scales of nHA particles with randomly dispersed randomly oriented and 100 % aligned particles.

To investigate the aspect ratio and inclusion length effect in the current nanocomposite system, twelve RVEs with a constant volume fraction were generated while increasing the aspect ratio and length of the inclusions (with constant diameter) in two systems: 1) randomly dispersed, randomly oriented inclusions and 2) in RVEs with randomly dispersed, all-aligned inclusions aligned in the loading direction. As seen in Fig. 7.18 by increasing length from 80 nm-180 nm while maintaining

a constant diameter of 30 nm (changing the aspect ratio from 2.7 to 6), the elastic modulus (E_{11}) in the randomly dispersed, randomly oriented nanocomposite systems increased by 6 % while in a randomly dispersed, all-aligned system, the elastic modulus increased by more than 20%. Comparing randomly oriented RVEs with nHA nanorods of 80 nm length and the all-aligned nanocomposite system with high aspect ratio nHA nanorods, it is seen that the elastic modulus has increased from 1913.3 MPa to 2547 MPa which is about 35% increase while keeping the volume fraction constant (5%). This demonstrates that in designing nanocomposite systems, in addition to the V_f of inclusions, the distribution, alignment and aspect ratio of inclusions play a crucial role.

Table 7.5. The elastic modulus (E_{11}) of represented RVEs with increased nHA aspect ratio in randomly oriented and 100% aligned inclusions in the loading direction.

Length of Particle (nm)	Aspect Ratio	Elastic Modulus (MPa) Randomly oriented	Elastic Modulus (MPa) Aligned
80	2.7	1913.3	2143
100	3.3	1934.6	2166.2
120	4	1946.3	2253.1
140	4.66	1946.7	2363.3
160	5.35	1985.3	2493.3
180	6	2024.3	2574.7

7.3.2.3. Nanorod length distribution

The high-resolution SEM images demonstrated that, while inclusion diameters are almost constant, inclusion lengths vary throughout the nanocomposite. According to ImageJ analysis, the length of inclusions changes from 80 nm to 160 nm. It is demonstrated how the inclusion length and aspect ratio affects the final elastic modulus, so in order to have realistic RVEs and more accurate micromechanical modelling, it is necessary to employ a similar length distribution of nHA in the developed RVEs as of the studied microstructure. The normal Gaussian distribution function with the mentioned properties was introduced to Digimat-FE to implement the length distribution in the generated RVEs. Fig. 7.19 illustrates a favorable agreement between the size distribution of inclusions in the generated RVE (Actual) and the size distribution of inclusions in the reference microstructure RVE (Reference) as inputted according to the image J analysis.

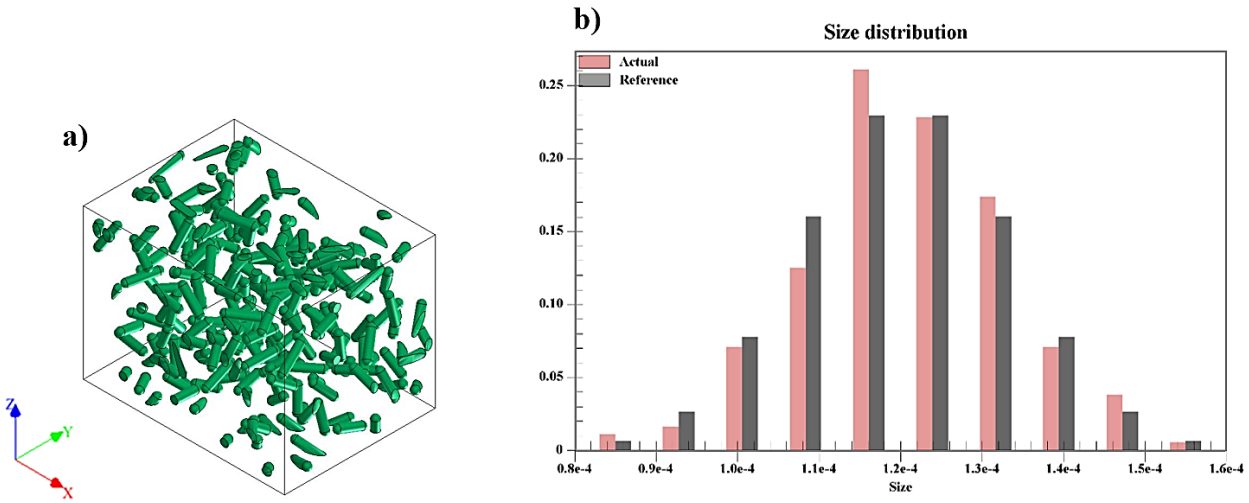


Fig. 7.19. Randomly dispersed, randomly oriented, length distributed RVE a) Representative generated RVE b) Comparison of the length distribution of generated RVE with inputted reference microstructure.

7.3.2.4. RVEs with length distribution and agglomerations

According to TEM images of our nanocomposite system, some small nanoscale agglomerations can still be seen in the well-dispersed microstructure. To model and predict more accurately the micromechanical properties of the current system, small nanoscale agglomerations were introduced in the RVEs accordingly to investigate the effect of different volume fraction agglomerations on elastic modulus. Later by running the elastoplastic simulations on these RVEs the effect of agglomeration on the onset of failure will be further investigated on the current nanocomposite system as suggested in literature to act as stress concentration regions [125]. In Fig. 7.20, nine RVEs with agglomeration volume fractions changing from 0.25%-1.5% were generated. As seen by introducing the agglomerations to the randomly dispersed randomly oriented length distributed RVEs, the elastic modulus decreased slightly. According to the results presented in Table 7.5, the elastic modulus shows a decline with an increase in the volume fraction of agglomerations. However, when comparing the same volume fraction of agglomerations, it is evident that the number of agglomerations has a more pronounced negative impact on the elastic modulus. By increasing the number of agglomerations, the changes in the elastic modulus are more significant.

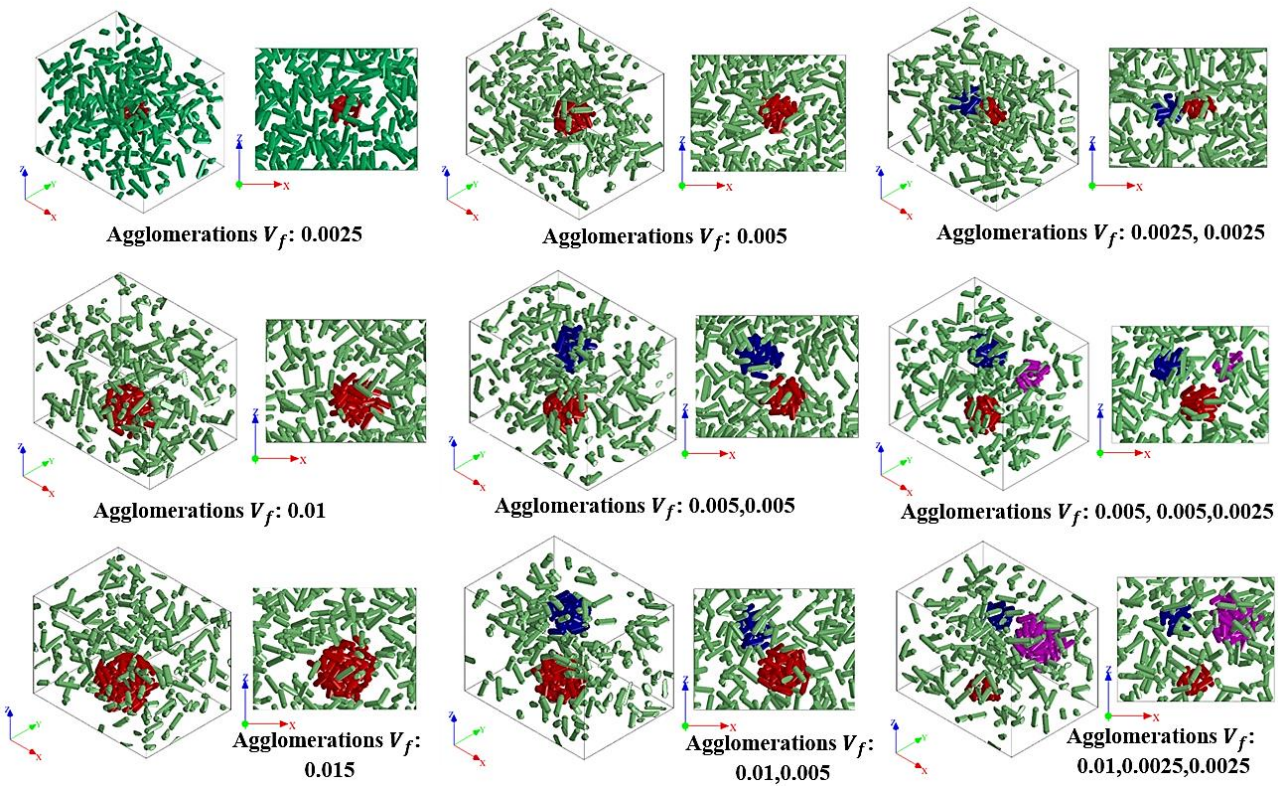


Fig. 7.20. Randomly dispersed, randomly oriented, length-distributed RVEs with nanoscale agglomerations.

Table 7.6. The elastic modulus (E_1) of represented RVEs with increased volume fraction of agglomerations in randomly oriented, randomly dispersed, length distributed RVEs (The elastic modulus of our model nanocomposite system was 1926 ±20 MPa [SPM paper]).

Total agglomeration v_f	**1st Agglomeration size (µm)**	**2nd Agglomeration size (µm)**	**3rd Agglomeration size (µm)**	**Elastic Modulus E_1 (MPa)**
	0	0	0	1944.3
0.0025	0.0025	0	0	1941.6
0.005	0.005	0	0	1941.1
0.005	0.0025	0.0025	0	1938.3
0.01	0.001	0	0	1937.7
0.01	0.005	0.005	0	1933.3
0.0125	0.005	0.005	0.0025	1930.1
0.015	0.015	0	0	1936.7
0.015	0.01	0.005	0	1932.3
0.015	0.01	0.0025	0.0025	1931.6

7.3.2.5. Orthotropic properties of generated RVEs

The orthotropic elastic properties were computed for different classes of generated RVEs by inputting the elastic properties of the matrix and nHA provided in Table 7.1. As presented in Table 7.6, the aligned high aspect ratio class of RVEs resulted in the highest E_{11} due to the enhanced load transfer efficiency between matrix and inclusion [467,468] and the applied load is effectively transferred and borne by the inclusions. In the first three classes of all aligned particle RVEs, the E_{11} is higher than the E_{22} and E_{33} due to the anisotropic microstructure of these RVEs. In randomly oriented RVEs, the random orientation of inclusions introduces statistical variations in the composite's mechanical properties. While some inclusions may align favourably to contribute to higher stiffness in certain directions, the overall effect of random alignment is a more isotropic distribution of elastic moduli, and as it is demonstrated in randomly dispersed and randomly aligned class of RVEs the value of elastic modulus in three directions are close.

Table 7.7. The orthotropic mechanical properties for five representative classes of generated RVEs; Aligned nanorods with a constant average length of 120 nm, aligned.

	E_1	E_2	E_3	ν_{12} (ν_{21})	ν_{13} (ν_{31})	ν_{23} (ν_{32})	G_{12}	G_{23}	G_{13}
Aligned constant	2260.61	1907.93	1908.87	0.38 (0.32)	0.38 (0.32)	0.42 (0.42)	681.07	669.43	681.57
Aligned High Aspect Ratio	2571.81	1937.47	1929.77	0.38 (0.29)	0.38 (0.29)	0.44 (0.44)	680.21	668.21	678.91
Aligned Length distributed	2257.22	1907.5	1906.8	0.38 (0.32)	0.38 (0.32)	0.42 (0.42)	681.56	670.433	681.03
Randomly dispersed & oriented, Length distributed	1944.52	1936. 47	1948.83	0.38 (0.38)	0.38 (0.38)	0.38 (0.38)	700.33	704.17	703.20
Randomly dispersed & oriented, Length distributed with three random clusters ($V_{f=0.00125}$)	1930.11	1928.11	1945.17	0.38 (0.38)	0.38 (0.38)	0.38 (0.38)	697.53	701.43	704.70

Fig. 7.21 illustrates stress contours within RVEs belonging to different categories: randomly dispersed aligned with average constant length, randomly dispersed aligned with high aspect ratio, randomly dispersed aligned with length distribution, randomly dispersed randomly oriented, and

randomly dispersed randomly oriented with clusters. The contours provide insights into the load transfer efficiency within these class of RVEs. The contours reveal that the aligned inclusions exhibit superior load transfer capabilities compared to randomly oriented inclusions.

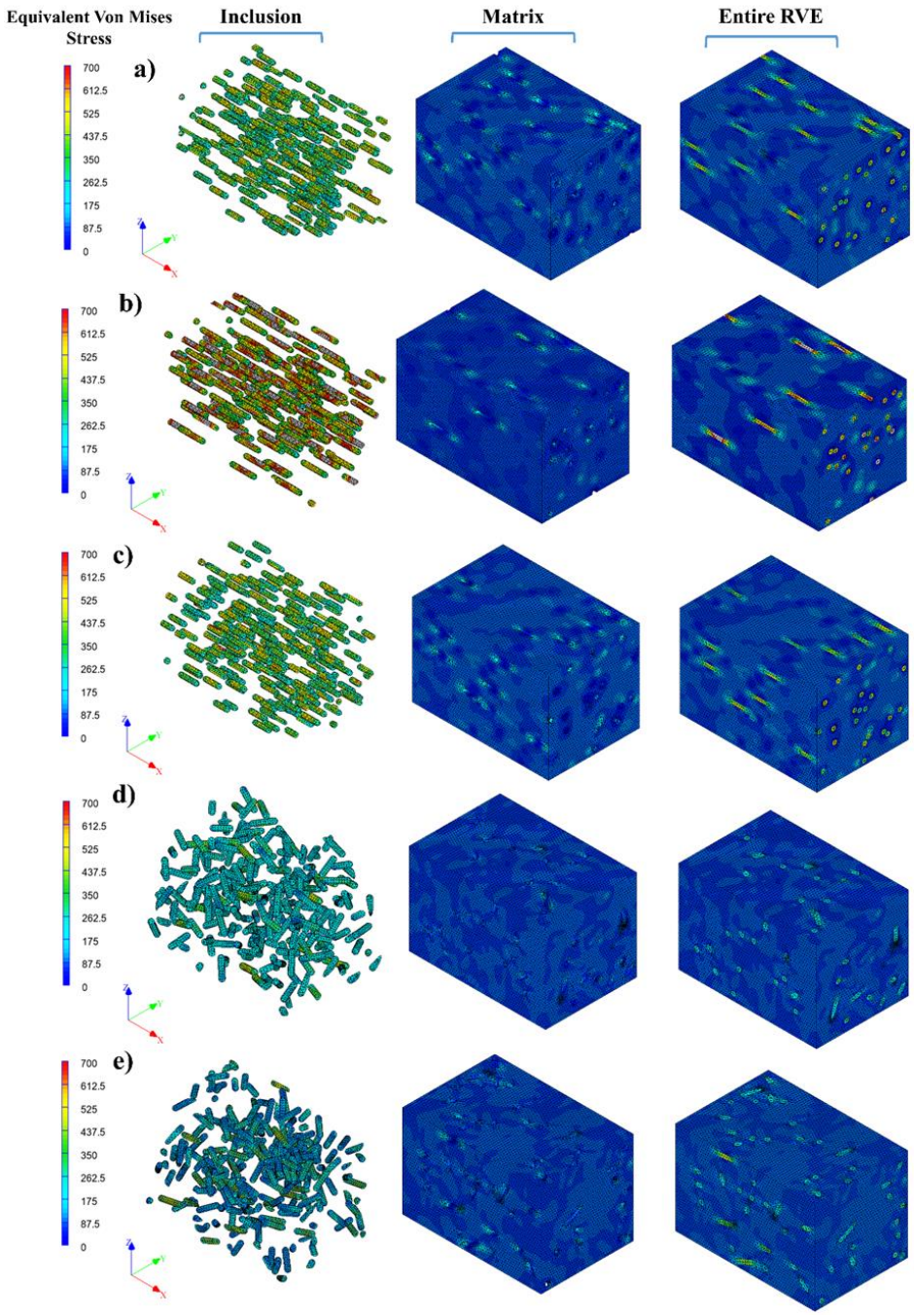


Fig. 7.21. Elastic stress contours (σ_{vm}) in the matrix and inclusion through five class of RVEs, a) Average constant length aligned inclusions, b) Aligned high aspect ratio inclusions, c) aligned length distributed inclusions, d) randomly oriented, e) randomly oriented with clusters (All inclusions are randomly dispersed).

Among the aligned RVEs, those with high aspect ratio (longer) inclusions demonstrated enhanced load transfer efficiency due to the increased interfacial area between the inclusions and the matrix [468]. This extended interface facilitates more effective distribution of load across the material. On the other hand, the randomly oriented inclusions, except for those that align favourably with the load direction, exhibit lower load transfer capabilities. This is primarily due to the absence of a well-defined alignment, which hampers efficient load transfer within the material. Agglomerations in nanocomposites disrupt the uniform dispersion and distribution of nanoparticles or reinforcements within the matrix, which hinders effective load transfer. This inefficient load transfer negatively impact the overall load-bearing capabilities and compromises the mechanical properties of the material. Consequently, the inclusions within the agglomerations experience lower stress levels and are unable to effectively reinforce the matrix material.

7.3.3. Elasto-Plastic Micromechanical Modeling of RVEs

The response of the generated class of RVEs was further examined for predicting the elasto-plastic behavior of the model nanocomposite system. By incorporating the elastoplastic properties of the biopolymer matrix and the elastic properties of the nHA inclusions, as outlined in Table 7.1, and implementing the periodic boundary condition, the predicted homogenized elastoplastic stress-strain response was obtained for the five representative classes of RVEs, as shown in Fig. 7.22.

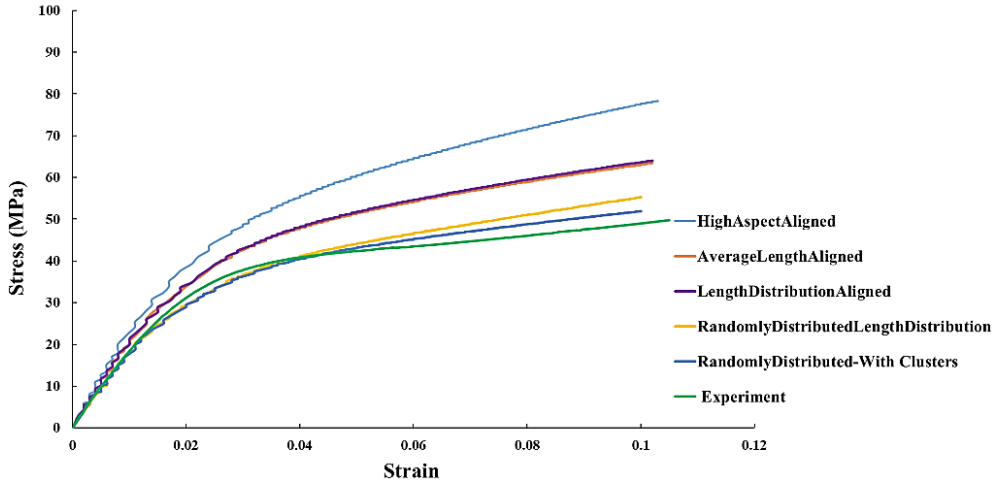


Fig. 7.22. Elasto-plastic stress-strain response of five classes of generated RVEs compared with the average experimental stress-strain response of our novel nanocomposite.

The RVEs generated with a constant volume fraction exhibit slight disparities in their elastic regions initially. However, noticeable differences emerge after the yield point, emphasizing the impact of particle dispersion and distribution on the elastoplastic properties of the material.

Notably, a more pronounced deviation is observed between the stress-strain curves of the aligned RVE classes compared to the randomly oriented RVE class and the experimental data after yielding. It is important to highlight that even with a constant volume fraction of inclusions, the dispersion and aspect ratio of the particles can have a substantial influence on the elastoplastic response of the nanocomposites. It becomes clear that optimizing the volume fraction alone is insufficient, and it is necessary to investigate the distribution of nanoparticles (nHA) within the matrix for obtaining higher elastoplastic mechanical properties due to its significant effect. This highlights the need to accurately capture realistic microstructures when generating RVEs to reliably predict the elastoplastic mechanical properties of developed nanocomposite systems. The stress-strain curves obtained from randomly oriented, length-distributed RVEs with nanoscale clusters show better agreement with the average experimental stress-strain curves of functionalized nanocomposite systems [447] with a slight deviation being observed in the after strain of 4%. Stress contour maps in RVEs for elastoplastic deformation of five classes of studied generated RVEs are presented in Fig. 7.23. For all classes, the stress contours at the interfaces between the inclusions and matrix reveal the effects of random and nonuniform dispersion. In all RVEs, the shear stress contour in the matrix (Fig. 7.23) demonstrates a distinctive shear lag response when subjected to a normal strain [469]. This response is characterized by higher shear stress in the matrix, especially near the ends of the fibers, particularly noticeable in the aligned class of RVEs and more significantly around the high aspect ratio aligned inclusions. The stress contour patterns at the interfaces between the inclusions and the matrix illustrate that the dispersion of inclusions is non-uniform in all cases. The stress contour plots within the matrix confirm the shear lag phenomenon in response to an applied normal strain. This characteristic shear lag behavior is evident by the presence of elevated shear stresses in the matrix, especially near the ends of the nanoparticles, as observed more dominantly in the aligned case of RVEs. These stress contours reveal the importance of considering the microstructure features and inclusions dispersion for accurate prediction of elastoplastic properties of studied nanocomposite. Under consistent loading conditions, the elastoplastic stress contours vary significantly in the different classes of RVEs while all having consistent inclusion shape and volume fraction. The normal stress contours in the

inclusions also shows how the alignment of inclusions in the loading direction improves the efficient load-bearing capability of inclusions [468] and how agglomerations hinder the efficient transfer of load between the matrix and the nanoparticles and comprised of the mechanical properties of nanocomposites [470].

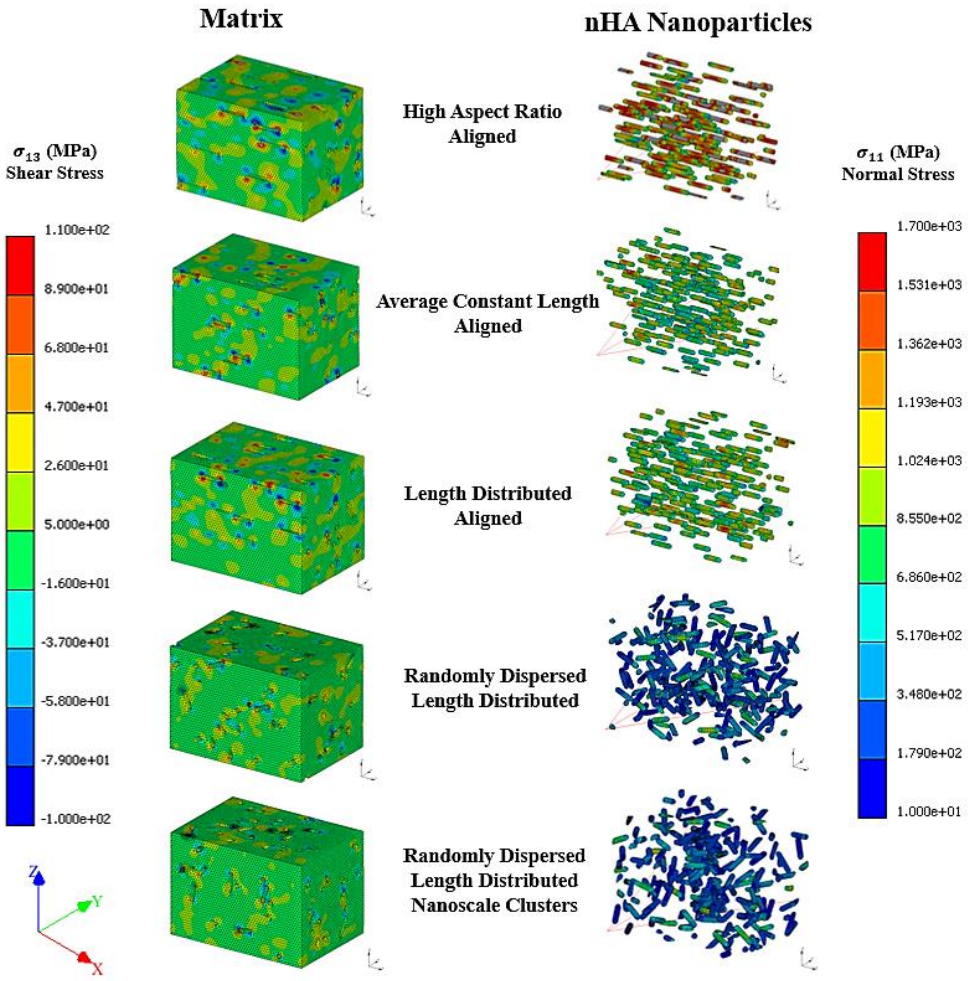


Fig. 7.23. Shear stress (σ_{13}) contour in the matrix and normal stress (σ_1) contour in the inclusion of five class of generated RVEs

To further investigate the effect of agglomerations on the local deformation of the matrix in the studied nanocomposite systems, planes were cut through the location of agglomerations. As seen in the contour plots (Fig.7.24), the agglomerations can act as stress concentrations within the nanocomposite material. The stress tends to concentrate around the agglomerations, putting excessive stress on the surrounding matrix material. This concentrated stress can exceed the material's strength, leading to local plastic failure or fracture of the matrix material. Moreover, the

matrix around agglomerations is confined and can restrict the movement of the surrounding matrix material. This confinement effect can hinder the plastic deformation and flow of the matrix around the agglomerates and the material may exhibit reduced ductility in these regions [449].

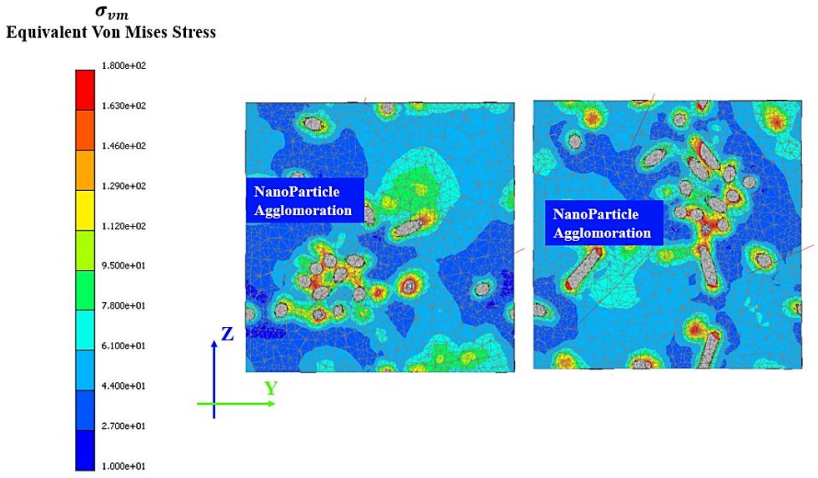


Fig. 7.24. Von mises stress contour in the regions of agglomerations; the matrix demonstrates higher stress levels and may act as stress concentration regions for the onset of local failure.

As presented, the stress-strain curves of randomly dispersed, randomly oriented, length-distributed inclusions with random clusters demonstrate a good agreement with the averaged experimental stress-stain response of our nanocomposite material except for slight deviations after 4% of strain. This deviation could arise due to the assumption of perfect bonding between the inclusions and the matrix in the micromechanical simulation. Although, in practice, through surface functionalization, enhanced interfacial bonding was sought, the EDX results demonstrated not all of the nHA particles were functionalized throughout the nanocomposite. The error between the experimental data and the output of the micromechanical model could be due to this issue. As shown in the contour plots of RVE at different increments of deformation (Fig.7.25), by increasing the load, the interfacial area around the inclusions demonstrates the highest stress through the matrix [390]. The developed elastoplastic micromechanical model, based on the perfect bonding assumption, does not account for debonding. However, in practical scenarios, damage can initiate from the interfacial regions of nanoparticles that have not been adequately functionalized. This limitation in the modelling approach can lead to a slight overestimation of results compared to experimental observations.

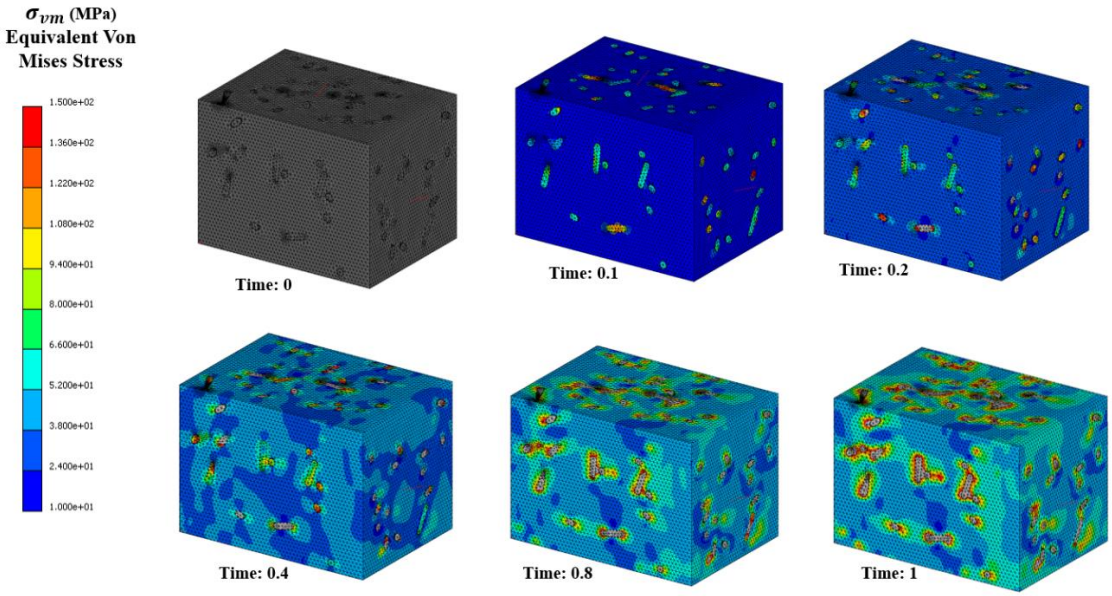


Fig. 7.25. Stress contours (σ_{vm}) in RVEs of randomly dispersed, randomly oriented, length-distributed inclusions with random clusters through different increments of deformation. Increases in interfacial stresses are observed. (The yield strength of matrix σ_{1y}=35 MPa)

7.4. Conclusion

This paper presents a computational tool for predicting the elastoplastic micromechanical properties of biopolymer nanocomposite systems. Realistic RVEs were generated based on the microstructure of the studied nanocomposite, and various case studies were conducted to further investigate the impact of nHA nanorod alignment, dispersion, length distribution, and aspect ratio on the elastoplastic properties of nanocomposite system. The findings reveal that nanoparticle alignment can significantly increase the elastic modulus, with an improvement of over 16%. Furthermore, increasing the aspect ratio of inclusions resulted in a remarkable increase of more than 35% in the properties in a constant volume fraction of nHA. The results highlighted that optimizing the volume fraction alone is insufficient for designing mechanically competent nHA based 3D printable nanocompsoites, and it is necessary to dedicate more investigation on the distribution and alignment of nanoparticles (nHA) within the matrix due to its significant effect on both elastic and more importantly on plastic properties. It should be noted that there are limitations for increasing the volume fraction of inclusions in nanocomposite systems due to challenges associated with increased viscosity, which can adversely affect 3D printability and processing.

Therefore, there is a point at which increasing the volume fraction of inclusions becomes limited. However, the results presented in this work highlight the potential for effectively enhancing the mechanical properties by focusing on increasing the aspect ratio and alignment of inclusions within a constant volume fraction. In addition, literature suggests that increasing the length of inclusions in 3D printable nanocomposite inks, particularly using extrusion-based 3D printing [91,96], can facilitate the alignment of nanoparticles in the direction of extrusion. While shorter particles may align less than longer particles during extrusion. Different classes of RVEs, with varying inclusion arrangements, showed distinct elastoplastic behaviour at a constant volume fraction of inclusions. Comparisons between experimental data and the different classes of generated RVEs indicated a good agreement between randomly dispersed, randomly oriented with cluster RVEs with our experimental data, with a slight deviation observed after 4% strain, likely due to the assumption of perfect bonding between inclusions and matrix. Although in the studied nanocomposite system, inclusions were functionalized to improve the interfacial bonding, characterization experiments revealed that not all nHA particles were effectively functionalized. The examination of equivalent stress contours emphasized the significance of strengthening the interfacial area for developing mechanically competent nanocomposite systems. Increasing load results in higher stress transfer through the matrix to the interfacial area. This observation underscores the importance of optimizing and strengthening the interfacial region to improve the overall mechanical performance of nanocomposites. This research contributed valuable insights into the impact of nHA distribution on the elastoplastic behavior of 3D printable nHA based polymer nanocomposites. It also offers guidance for further optimizing their microstructure to achieve desired mechanical properties.

Chapter 8

Conclusion

Bone-inspired 3D Printable nanocomposite grafts present a promising alternative to conventional bone substitutes due to their osteoconductivity, biocompatibility, biodegradability and customized patient-specific design. One critical requirement in the design of these grafts is ensuring sufficient mechanical properties. These grafts need to possess both functionality and load-bearing capabilities to withstand the physiological loading demands of bone and effectively serve as substitutes in critically-sized segmental bone defects. To achieve the desired mechanical properties, several considerations should be taken into account during the design and fabrication process. The mechanical properties of bone exhibit enhancement across various length scales, ranging from the nano to the macro scale. The nanohydroxyapatite (nHA) crystals are uniformly distributed and aligned within the collagen fibers, forming an engineered interface with non-collagenous proteins that are compatible with the collagen matrix. This unique arrangement contributes to the preservation of the bone's high mechanical properties and structural integrity at the microscale. The central objective of this thesis was to improve the mechanical properties of bone-inspired nanocomposite grafts by exploring micron and submicron features. This was achieved by optimizing fabrication techniques and refining material design to enhance the overall performance of the grafts. Additionally, a micromechanical computational tool was developed to further investigate the elastoplastic mechanical properties of the resulting nanocomposite system that as a design tool will provide valuable insights to researchers in the early stages of bone-inspired graft design. To enhance the mechanical competence of bone-inspired nanocomposites at the nano-to-micro scales, several strategies were implemented. One approach involved utilizing advanced processing techniques such as DIW 3D printing to align the nanohydroxyapatite (nHA) nanoparticles and/or polymer chains. This involved increasing shear during extrusion to enhance the mechanical properties due to the formation of polymer chain crystallites and/or nanoparticle alignment as well as trying to mimick the aligned organic/inorganic nanostructure found in natural bone tissue. Another strategy revolved around optimizing the composition of the matrix. This was achieved by further functionalizing the biopolymer matrix, resulting in improved mechanical properties. Finally the objective of enhancing interfacial bonding between nHA and the biopolymer matrix, as well as achieving homogeneous dispersion of nHA particles, was achieved

through new processing techniques and surface functionalization of nHA. All these measures were taken to facilitate the development of bone-inspired mechanically competent nanocomposites. In addition, the developed micromechanical computational model will help to further investigate the effect of nHA distribution and orientation on elastoplastic properties of studied nanocomposite systems in the future.

The main conclusions of this thesis are as follows:

- By increasing the shear stress during extrusion using a custom-designed DIW-based 3D printer to control the shear stress, the tensile mechanical properties including elastic modulus, fracture strength and toughness of the studied nanocomposite system were enhanced without modifications to the ink composition. Characterization experiments confirmed the shear-induced alignment of polymer chains and increased crystallinity of the thermoset biopolymer matrix as a result of higher shear during extrusion combined with the nano-confinement crystallinity in thermoset biopolymers.

- A new group of nanocomposite inks was developed by functionalizing the AESO-PEGDA biopolymer matrix and heat-treating the nHA particles. Functionalization of the AESO to mAESO increased the degree of cross-linking in the matrix and therefore improved the tensile and thermo-mechanical properties of the 3D printed nanocomposite filaments extruded under high shear significantly. The mAESO nanocomposite inks demonstrated better shape-holding properties making them more suitable for extrusion-based 3D printing. They demonstrated Young's modulus of 6.6 GPa and ultimate tensile strength of 75.5 MPa, providing a strength safety factor of approximately 1.5 against the minimum required standard mechanical properties for bone cement according to ISO standard 5833 (Tensile strength $\geqslant$50 MPa).

- A novel approach for obtaining a well-dispersed nHA-based bone-inspired nanocomposite system with enhanced interfacial bonding was introduced by refining the nHA through centrifugation and subsequent sulfopropyl methacrylate (SPM) surface functionalization of the refined nHA using barium as an interfacial agent. The nHA dispersion, effectiveness of surface functionalization and interfacial bonding were characterized thoroughly using

various state-of-the-art characterization experiments. SPM functionalization of the refined nHA particles greatly improved dispersion and interfacial bonding within the MAESO-PEGDA matrix with no microscale agglomerations detected. All three SPM-containing inks printed successfully using our mSLA 3D printer and tensile test results demonstrated increases of 75% and 37% in fracture strain and fracture strength, respectively.

- Realistic RVEs were generated based on the image processing analysis of the studied nanocomposite's microstructure and a computational design tool for predicting the elastoplastic micromechanical properties of the studied nanocomposite system developed and validated with experimental results. To precisely characterize the matrix material's yield criterion and hardening parameters, mSLA 3D printed functionalized biopolymer matrix samples were tested in tension, compression, and shear modes. Several case studies were carried out to examine the effects of nHA nanorod orientation, dispersion, length distribution, and aspect ratio on the elastoplastic properties of the nanocomposite systems and to investigate local failure initiation in critical regions and the elastoplastic response of model demonstrated a good agreement with the averaged experimental response of latest nanocomposite system. The findings of these studies may serve as valuable design guidelines for the development of mechanically robust 3D printable nanocomposite materials.

8.1. Ideas for Future Work

In closing, the following suggestions are provided for developing more mechanically-competent bone-inspired nanocomposite grafts:

- Likely due to the limitations on the amount of shear stress applied during extrusion, no significant nHA particle alignment was observed. By further optimizing the shear stress during extrusion using the custom-design Skeleprint, further particle alignment may be achieved in the direction of extrusion which may lead to additional improvements in mechanical properties.

- One limitation in achieving alignment during extrusion is related to the aspect ratio restrictions of the nanohydroxyapatite (nHA) particles utilized in this thesis. By fabricating

the nHA particles in the laboratory, it may be feasible to generate nanoparticles with higher aspect ratios. This capability opens up possibilities for improving alignment and optimizing the properties of the extruded nanocomposite material. As demonstrated in the micromechanical modelling case studies, increased aspect ratio of nanoparticles with constant diameters may significantly improve the elastoplastic properties of our nanocomposite systems.

- While matrix optimization and functionalization resulted in a significant increase in the strength of the nanocomposite system, it is suggested to put more investigation into toughening the matrix material by possibly adding more toughening agents to the matrix material.

- To improve the effectiveness of SPM surface functionalization, it is suggested to optimize the method by adjusting the quantity of Sulphopropyl Methacrylate. This optimization process will aim to assess the effects of varying the quantity on the enhanced incorporation of surface-functionalized nanoparticles within the nanocompsoite system. Furthermore, it may seek to further enhance the interfacial properties of the system.

- Given the interesting increase in ductility (fracture strain) of the SPM nanocomposites without loss of modulus or strength, we might test the hypothesis that this increased ductility would translate into increased fracture toughness. This would be advantageous toward the robustness of grafts printed from these nanocomposites.

- The fatigue properties of bone-inspired 3D printable nanocomposite grafts are vital for their longer term performance and durability, as they are subjected to repetitive loading and unloading cycles akin to natural bone. Therefore, investigating how the dispersion, alignment and modifications of the nHA influence the fatigue resistance of the nanocomposite systems will be essential for understanding the long-term performance of these grafts.

- The validated computational micromechanical model can be extended to predict the elastoplastic properties of bone-inspired nanocomposite under complex loading conditions that human bone experiences on daily activity basis, such as bending, torsion and compression or combined loading.
- While there is a good agreement between the micromechanical model's elastoplastic response and the experimental results when employing the current RVE size obtained through RVE sensitivity analysis in accordance with the literature, it is worthwhile to extend the RVE sensitivity analysis by comparing the yield strength obtained through various RVE sizes in order to further optimise the computational cost and accuracy of results.
- The new model can capture the cavitation failure in the polymer matrix by comparing the hydrostatic stress state of the biopolymer matrix in the RVEs to the triaxial stress value of the studied biopolymer matrix, which requires additional experimental characterization using the poker chip test to obtain this value for the polymer.

- The computational elastoplastic model can be extended and used for predicting damage evolution in these nanocomposite systems. Extending the computational model will require modifications to capture nanoparticle failure and the progressive fiber-matrix interphase debonding by implementing algorithms to track and quantify the evolution of damage throughout the nanocomposite system.

Letter of Copy Right Permissions

Fig .1.1.

Open Access.

Fig .1.2.

Open Access.

Fig .1.3.

Open Access.

Fig .2.1.

This Agreement between Mrs. SANAZ SAADATMAND HASHEMI ("You") and Springer Nature ("Springer Nature") consists of your license details and the terms and conditions provided by Springer Nature and Copyright Clearance Center.

License Number	5627481352292
License date	Sep 14, 2023
Licensed Content Publisher	Springer Nature
Licensed Content Publication	Nature Materials
Licensed Content Title	Bioinspired structural materials
Licensed Content Author	Ulrike G. K. Wegst et al
Licensed Content Date	Oct 26, 2014
Type of Use	Thesis/Dissertation
Requestor type	academic/university or research institute
Format	electronic
Portion	figures/tables/illustrations
Number of figures/tables/illustrations	1
Would you like a high resolution image with your order?	no
Will you be translating?	no
Circulation/distribution	100 - 199
Author of this Springer Nature content	no
Title	Experimental and Computational Micromechanical Investigations for Developing Mechanically Competent 3D Printable Nanocomposite Biomaterials
Institution name	university of Waterloo
Expected presentation date	Sep 2023
Portions	Fig.1

	Mrs.	SANAZ	SAADATMAND		HASHEMI
	UNIT	11	434	Hazel	Street
Requestor Location					
	Waterloo,		ON		N2L3P8
	Canada				
	Attn: SANAZ SAADATMAND HASHEMI				
Total	0.00 USD				

Fig .2.2.-Fig.2.3-Fig.2.4:

This Agreement between Mrs. SANAZ SAADATMAND HASHEMI ("You") and Elsevier ("Elsevier") consists of your license details and the terms and conditions provided by Elsevier and Copyright Clearance Center.

License Number	5627491225500
License date	Sep 14, 2023
Licensed Content Publisher	Elsevier
Licensed Content Publication	Elsevier Books
Licensed Content Title	Additive Manufacturing of Biopolymers
Licensed Content Author	Dibakar Mondal,Sanaz S. Hashemi,Elizabeth Diederichs,Haresh Patil,Thomas L. Willett
Licensed Content Date	Jan 1, 2023
Licensed Content Pages	32
Start Page	135
End Page	166
Type of Use	reuse in a thesis/dissertation
Portion	figures/tables/illustrations
Number of figures/tables/illustrations	3
Format	electronic
Are you the author of this Elsevier chapter?	Yes
How many pages did you author in this Elsevier book?	32
Will you be translating?	No
Title	Experimental and Computational Micromechanical Investigations for Developing Mechanically Competent 3D Printable Nanocomposite Biomaterials
Institution name	university of Waterloo
Expected presentation date	Sep 2023
Portions	Fig.6.3-6.4-6.5

	Mrs.	SANAZ	SAADATMAND		HASHEMI
	UNIT	11	434	Hazel	Street
Requestor Location					
	Waterloo,		ON		N2L3P8
	Canada				
	Attn: SANAZ SAADATMAND HASHEMI				
Publisher Tax ID	GB 494 6272 12				

Total	0.00 USD

Fig .2.5:

This Agreement between Mrs. SANAZ SAADATMAND HASHEMI ("You") and Elsevier ("Elsevier") consists of your license details and the terms and conditions provided by Elsevier and Copyright Clearance Center.

License Number	5627500471110
License date	Sep 14, 2023
Licensed Content Publisher	Elsevier
Licensed Content Publication	Elsevier Books
Licensed Content Title	Smart Multifunctional Nano-inks
Licensed Content Author	Dibakar Mondal,Thomas L. Willett
Licensed Content Date	Jan 1, 2023
Licensed Content Pages	16
Start Page	579
End Page	594
Type of Use	reuse in a thesis/dissertation
Portion	figures/tables/illustrations
Number of figures/tables/illustrations	1
Format	electronic
Are you the author of this Elsevier chapter?	No
Will you be translating?	No
Title	Experimental and Computational Micromechanical Investigations for Developing Mechanically Competent 3D Printable Nanocomposite Biomaterials
Institution name	university of Waterloo
Expected presentation date	Sep 2023
Portions	Fig.23.2
Requestor Location	Mrs. SANAZ SAADATMAND HASHEMI UNIT 11 434 Hazel Street Waterloo, ON N2L3P8 Canada Attn: SANAZ SAADATMAND HASHEMI
Publisher Tax ID	GB 494 6272 12
Total	0.00 USD

Fig .2.6:

License Number	5627501209745

License date	Sep 14, 2023
Licensed Content Publisher	Springer Nature
Licensed Content Publication	Springer eBook
Licensed Content Title	Introduction to Rheology
Licensed Content Author	John M. Dealy, Kurt F. Wissbrun
Licensed Content Date	Jan 1, 1999
Type of Use	Thesis/Dissertation
Requestor type	academic/university or research institute
Format	electronic
Portion	figures/tables/illustrations
Number of figures/tables/illustrations	1
Will you be translating?	no
Circulation/distribution	500 - 999
Author of this Springer Nature content	no
Title	Experimental and Computational Micromechanical Investigations for Developing Mechanically Competent 3D Printable Nanocomposite Biomaterials
Institution name	university of Waterloo
Expected presentation date	Sep 2023
Portions	Fig.3
Requestor Location	Mrs. SANAZ SAADATMAND HASHEMI UNIT 11 434 Hazel Street Waterloo, ON N2L3P8 Canada Attn: SANAZ SAADATMAND HASHEMI
Total	0.00 USD

Fig .2.7:

Open Access.

Fig .2.8:

Open Access.

Fig .2.11:

Order Number: 1396619
Order Date: 14 Sep 2023

Payment Information

SANAZ SAADATMAND HASHEMIssaadatm@uwaterloo.ca**Payment method:** Invoice
Billing Address: Mrs. SANAZ SAADATMAND HASHEMIUNIT 11 434 Hazel StreetWaterloo, ON N2L3P8Canada+1 (519) 778-2912ssaadatm@uwaterloo.ca
Customer Location: Mrs. SANAZ SAADATMAND HASHEMIUNIT 11 434 Hazel StreetWaterloo, ON N2L3P8Canada

Order Details

- 1. Chemical Society reviews

  Article: Additive manufacturing of biologically-inspired materials.

Order License ID

1396619-1

Order detail status

Completed

ISSN

1460-4744

Type of Use

Republish in a thesis/dissertation

Publisher

ROYAL SOCIETY OF CHEMISTRY

Portion

Image/photo/illustration

View Details

0.00 CAD

Republication Permission

Total Items: 1

Subtotal: 0.00 CAD
Order Total: 0.00 CAD

Fig .2.13:

This Agreement between Mrs. SANAZ SAADATMAND HASHEMI ("You") and Springer Nature ("Springer Nature") consists of your license details and the terms and conditions provided by Springer Nature and Copyright Clearance Center.

License Number	5627521192969
License date	Sep 14, 2023
Licensed Content Publisher	Springer Nature
Licensed Content Publication	Journal of Materials Science: Materials in Medicine
Licensed Content Title	Problem of hydroxyapatite dispersion in polymer matrices: a review
Licensed Content Author	Monika Šupová
Licensed Content Date	Feb 20, 2009
Type of Use	Thesis/Dissertation
Requestor type	academic/university or research institute
Format	electronic
Portion	figures/tables/illustrations
Number of figures/tables/illustrations	1
Will you be translating?	no
Circulation/distribution	500 - 999
Author of this Springer Nature content	no
Title	Experimental and Computational Micromechanical Investigations for Developing Mechanically Competent 3D Printable Nanocomposite Biomaterials
Institution name	university of Waterloo
Expected presentation date	Sep 2023
Portions	Fig.1
Requestor Location	Mrs. SANAZ SAADATMAND HASHEMI UNIT 11 434 Hazel Street Waterloo, ON N2L3P8 Canada Attn: SANAZ SAADATMAND HASHEMI
Total	0.00 USD

Fig .2.14:

This Agreement between Mrs. SANAZ SAADATMAND HASHEMI ("You") and Elsevier ("Elsevier") consists of your license details and the terms and conditions provided by Elsevier and Copyright Clearance Center.

License Number	5627530214989
License date	Sep 14, 2023
Licensed Content Publisher	Elsevier
Licensed Content Publication	Journal of the Mechanical Behavior of Biomedical Materials
Licensed Content Title	Effect of silanization of hydroxyapatite fillers on physical and mechanical properties of a bis-GMA based resin composite

Licensed Content Author	Christie Ying Kei Lung,Zenab Sarfraz,Amir Habib,Abdul Samad Khan,Jukka Pekka Matinlinna
Licensed Content Date	Feb 1, 2016
Licensed Content Volume	54
Licensed Content Issue	n/a
Licensed Content Pages	12
Start Page	283
End Page	294
Type of Use	reuse in a thesis/dissertation
Portion	figures/tables/illustrations
Number of figures/tables/illustrations	1
Format	electronic
Are you the author of this Elsevier article?	No
Will you be translating?	No
Title	Experimental and Computational Micromechanical Investigations for Developing Mechanically Competent 3D Printable Nanocomposite Biomaterials
Institution name	university of Waterloo
Expected presentation date	Sep 2023
Portions	fig.12
Requestor Location	Mrs. SANAZ SAADATMAND HASHEMI UNIT 11 434 Hazel Street Waterloo, ON N2L3P8 Canada Attn: SANAZ SAADATMAND HASHEMI
Publisher Tax ID	GB 494 6272 12
Total	0.00 USD

Fig .2.16:

Permission is not required for academic reuses.

https://s100.copyright.com/AppDispatchServlet#formTop

Fig .2.17:

This Agreement between Mrs. SANAZ SAADATMAND HASHEMI ("You") and Elsevier ("Elsevier") consists of your license details and the terms and conditions provided by Elsevier and Copyright Clearance Center.

License Number	5627650397919
License date	Sep 14, 2023
Licensed Content Publisher	Elsevier

Licensed Content Publication	Construction and Building Materials
Licensed Content Title	Experimental determination of Drucker-Prager yield criterion parameters for normal and high strength concretes under triaxial compression
Licensed Content Author	Ertekin Öztekin,Selim Pul,Metin Hüsem
Licensed Content Date	Jun 1, 2016
Licensed Content Volume	112
Licensed Content Issue	n/a
Licensed Content Pages	8
Start Page	725
End Page	732
Type of Use	reuse in a thesis/dissertation
Portion	figures/tables/illustrations
Number of figures/tables/illustrations	1
Format	electronic
Are you the author of this Elsevier article?	No
Will you be translating?	No
Title	Experimental and Computational Micromechanical Investigations for Developing Mechanically Competent 3D Printable Nanocomposite Biomaterials
Institution name	university of Waterloo
Expected presentation date	Sep 2023
Portions	Fig.1
Requestor Location	Mrs. SANAZ SAADATMAND HASHEMI UNIT 11 434 Hazel Street Waterloo, ON N2L3P8 Canada Attn: SANAZ SAADATMAND HASHEMI
Publisher Tax ID	GB 494 6272 12
Total	0.00 USD
Terms and Conditions	

Fig .2.19:

Open Access. https://libuwspaceprd02.uwaterloo.ca/handle/10012/16308

References

[1] U.G.K. Wegst, H. Bai, E. Saiz, A.P. Tomsia, R.O. Ritchie, Bioinspired structural materials, Nat. Mater. 14 (2015) 23–36. https://doi.org/10.1038/nmat4089.

[2] W. Murphy, D.M.-N. biotechnology, undefined 2002, Molecular-scale biomimicry, Nature.Com. (n.d.).

[3] T. Drobek, N.D. Spencer, Nanotribology of surface-grafted PEG layers in an aqueous environment, Langmuir. 24 (2008) 1484–1488. https://doi.org/10.1021/la702289n.

[4] H. Gao, B. Ji, I.L. Jä Ger §, E. Arzt, P. Fratzl, E. Schmid, Materials become insensitive to flaws at nanoscale: Lessons from nature, n.d.

[5] O. Bas, F. Hanßke, J. Lim, A. Ravichandran, E. Kemnitz, S.H. Teoh, D.W. Hutmacher, H.G. Börner, Tuning mechanical reinforcement and bioactivity of 3D printed ternary nanocomposites by interfacial peptide-polymer conjugates, Biofabrication. 11 (2019) 035028. https://doi.org/10.1088/1758-5090/aafec8.

[6] S. S. Hashemi, D. Mondal, J. Montesano, T.L. Willett, Effects of biopolymer functionalization and nanohydroxyapatite heat treatment on the tensile and thermomechanical properties of Bone-Inspired 3D printable nanocomposite biomaterials, Mater. Des. 225 (2023). https://doi.org/10.1016/j.matdes.2023.111587.

[7] O. Craciunescu, L. Moldov, Designing Bio-Inspired Composite Materials for Medical Applications, 2011. https://doi.org/10.5772/17363.

[8] K. Li, S.C. Tjong, Preparation and mechanical and tribological properties of high-density polyethylene/hydroxyapatite nanocomposites, J. Macromol. Sci. Part B Phys. 50 (2011) 1325–1337. https://doi.org/10.1080/00222348.2010.516154.

[9] E.H. Schemitsch, Size Matters: Defining Critical in Bone Defect Size!, J. Orthop. Trauma. 31 (2017) S20–S22. https://doi.org/10.1097/BOT.0000000000000978.

[10] M. a Javaid, M.T. Kaartinen, Mesenchymal Stem Cell-based Bone Tissue Engineering, Int Dent J Students Res. 1 (2013) 24–35.

[11] T.H. Lê Thua, D.N. Pham, W. Boeckx, A. De Mey, Vascularized fibular transfer in longstanding and infected large bone defects, Acta Orthop. Belg. 80 (2014) 50–55.

[12] T. Boyce, J. Edwards, N. Scarborough, The Influence of Processing on Safety and Performance, n.d.

[13] W.W. Tomford, H.J. Mankin, Bone banking: Update on methods and materials, Orthop. Clin. North Am. 30 (1999) 565–570. https://doi.org/10.1016/S0030-5898(05)70109-7.

[14] E.C. Shors, Coralline bone graft substitutes, Orthop. Clin. North Am. 30 (1999) 599–613. https://doi.org/10.1016/S0030-5898(05)70113-9.

[15] E. Mohseni, E. Zalnezhad, A.R. Bushroa, Comparative investigation on the adhesion of hydroxyapatite coating on Ti-6Al-4V implant: A review paper, Int. J. Adhes. Adhes. 48 (2014) 238–257. https://doi.org/10.1016/j.ijadhadh.2013.09.030.

[16] K.A. Hing, Bone repair in the twenty-first century: Biology, chemistry or engineering?, Philos. Trans. R. Soc. A Math. Phys. Eng. Sci. 362 (2004) 2821–2850. https://doi.org/10.1098/rsta.2004.1466.

[17] S. Weiner, W. Traub, Bone structure: from ångstroms to microns, FASEB J. 6 (1992) 879–885.

https://doi.org/10.1096/fasebj.6.3.1740237.

[18] S. Lu, M.A.P. McGough, B.R. Rogers, J.C. Wenke, D. Shimko, S.A. Guelcher, Resorbable nanocomposites with bone-like strength and enhanced cellular activity, J. Mater. Chem. B. 5 (2017) 4198–4206. https://doi.org/10.1039/c7tb00657h.

[19] A.R. Studart, Additive manufacturing of biologically-inspired materials, Chem. Soc. Rev. 45 (2016) 359–376. https://doi.org/10.1039/c5cs00836k.

[20] D. Mondal, T.L. Willett, Mechanical properties of nanocomposite biomaterials improved by extrusion during direct ink writing, J. Mech. Behav. Biomed. Mater. 104 (2020). https://doi.org/10.1016/j.jmbbm.2020.103653.

[21] C.L. Pai, M.C. Boyce, G.C. Rutledge, Mechanical properties of individual electrospun PA 6(3)T fibers and their variation with fiber diameter, Polymer (Guildf). 52 (2011) 2295–2301. https://doi.org/10.1016/j.polymer.2011.03.041.

[22] J.F.V. Vincent, Biomimetic materials, J. Mater. Res. 23 (2008) 3140–3147. https://doi.org/10.1557/jmr.2008.0380.

[23] S. Gorb, T. Speck, Biological and biomimetic materials and surfaces, Beilstein J. Nanotechnol. 8 (2017) 403–407. https://doi.org/10.3762/bjnano.8.42.

[24] U.G.K. Wegst, M.F. Ashby, Philosophical Magazine The mechanical efficiency of natural materials, Taylor Fr. 84 (2007) 2167–2186. https://doi.org/10.1080/14786430410001680935.

[25] A.K. Gaharwar, P.J. Schexnailder, G. Schmidt, Nanocomposite Polymer Biomaterials for Tissue Repair of Bone and Cartilage, Researchgate.Net. (2011). https://doi.org/10.1201/b10970-25.

[26] D. Heinegård, åke Oldberg, Structure and biology of cartilage and bone matrix noncollagenous macromolecules, FASEB J. 3 (1989) 2042–2051. https://doi.org/10.1096/fasebj.3.9.2663581.

[27] E.F. Morgan, G.U. Unnikrisnan, A.I. Hussein, Bone mechanical properties in healthy and diseased states, Annu. Rev. Biomed. Eng. 20 (2018) 119–143.

[28] D. Lacroix, Biomechanical aspects of bone repair, in: Bone Repair Biomater., 2009: pp. 106–118. https://doi.org/10.1533/9781845696610.1.106.

[29] J.D. Currey, Bones: Structure and mechanics, 2013. https://doi.org/10.1016/s0021-9290(03)00033-2.

[30] A.S.-C.S. Reviews, U. 2016, Additive manufacturing of biologically-inspired materials, Pubs.Rsc.Org. (n.d.).

[31] M. Grossman, F. Bouville, F. Erni, K. Masania, R. Libanori, A.R. Studart, Mineral Nano-Interconnectivity Stiffens and Toughens Nacre-like Composite Materials, Adv. Mater. 29 (2017). https://doi.org/10.1002/adma.201605039.

[32] J.J. Martin, B.E. Fiore, R.M. Erb, Designing bioinspired composite reinforcement architectures via 3D magnetic printing, Nat. Commun. 6 (2015). https://doi.org/10.1038/ncomms9641.

[33] R.M. Erb, J.S. Sander, R. Grisch, A.R. Studart, Self-shaping composites with programmable bioinspired microstructures, Nat. Commun. 4 (2013). https://doi.org/10.1038/ncomms2666.

[34] N.A. Yaraghi, N. Guarín-Zapata, L.K. Grunenfelder, E. Hintsala, S. Bhowmick, J.M. Hiller, M. Betts, E.L.

Principe, J.Y. Jung, L. Sheppard, R. Wuhrer, J. McKittrick, P.D. Zavattieri, D. Kisailus, A Sinusoidally Architected Helicoidal Biocomposite, Adv. Mater. 28 (2016) 6835–6844. https://doi.org/10.1002/adma.201600786.

[35] M. Mirkhalaf, T. Zhou, F. Barthelat, D.A. Weitz, Simultaneous improvements of strength and toughness in topologically interlocked ceramics, Natl. Acad Sci. 115 (2018) 9128–9133. https://doi.org/10.1073/pnas.1807272115.

[36] J.A. Lewis, B.G. Compton, J.R. Raney, T.J. Ober, Three-Dimensional (3D) Printed Composite Structure and 3D Printable Composite Ink Formulation, 15/117,623, 2016.

[37] P. Zhang, M.A. Heyne, A.C. To, Biomimetic staggered composites with highly enhanced energy dissipation: Modeling, 3D printing, and testing, J. Mech. Phys. Solids. 83 (2015) 285–300. https://doi.org/10.1016/j.jmps.2015.06.015.

[38] F. Libonati, A.E. Vellwock, F. Ielmini, D. Abliz, G. Ziegmann, L. Vergani, Bone-inspired enhanced fracture toughness of de novo fiber reinforced composites, Sci. Rep. 9 (2019). https://doi.org/10.1038/s41598-019-39030-7.

[39] R. Rabiei, S. Bekah, F. Barthelat, CHAPTER 5. Nacre from Mollusk Shells: Inspiration for High-performance Nanocomposites, in: Books.Google.Com, 2012: pp. 113–149. https://doi.org/10.1039/9781849735315-00113.

[40] N. Almqvist, N.H. Thomson, B.L. Smith, G.D. Stucky, D.E. Morse, P.K. Hansma, Methods for fabricating and characterizing a new generation of biomimetic materials, Mater. Sci. Eng. C. 7 (1999) 37–43. https://doi.org/10.1016/S0928-4931(98)00072-1.

[41] Z. Tang, N.A. Kotov, S. Magonov, B. Ozturk, Nanostructured artificial nacre, Nat. Mater. 2 (2003) 413–418. https://doi.org/10.1038/nmat906.

[42] M. Jafarkhani, A. Fazlali, F. Moztarzadeh, Z. Moztarzadeh, M. Mozafari, Fabrication and characterization of PLLA/chitosan/nano calcium phosphate scaffolds by freeze-casting technique, Ind. Eng. Chem. Res. 51 (2012) 9241–9249. https://doi.org/10.1021/ie300173j.

[43] C.M. Andres, N.A. Kotov, Inkjet deposition of layer-by-layer assembled films, J. Am. Chem. Soc. 132 (2010) 14496–14502. https://doi.org/10.1021/ja104735a.

[44] L.J. Bonderer, K. Feldman, L.J. Gauckler, Platelet-reinforced polymer matrix composites by combined gel-casting and hot-pressing. Part I: Polypropylene matrix composites, Compos. Sci. Technol. 70 (2010) 1958–1965. https://doi.org/10.1016/j.compscitech.2010.07.014.

[45] R.M. Erb, R. Libanori, N. Rothfuchs, A.R. Studart, Three Dimensions by Using Low Magnetic Fields, Science (80-.). 335 (2012) 199–204.

[46] H. Le Ferrand, F. Bouville, T.P. Niebel, A.R. Studart, Magnetically assisted slip casting of bioinspired heterogeneous composites, Nat. Mater. 14 (2015) 1172–1179. https://doi.org/10.1038/nmat4419.

[47] S.N.G. Guner, A.F. Dericioglu, Nacre-mimetic epoxy matrix composites reinforced by two-dimensional glass reinforcements, RSC Adv. 6 (2016) 33184–33196. https://doi.org/10.1039/c5ra25049h.

[48] E. Feilden, C. Ferraro, Q. Zhang, E. García-Tuñón, E. D'Elia, F. Giuliani, L. Vandeperre, E. Saiz, 3D Printing Bioinspired Ceramic Composites, Sci. Rep. 7 (2017). https://doi.org/10.1038/s41598-017-14236-9.

[49] D. Mondal, S. Hashemi, E. Diederichs, … H.P.-A.M., U. 2023, 3D printing of biopolymer composites and nanocomposites, Elsevier. (n.d.).

[50] A. Wubneh, E.K. Tsekoura, C. Ayranci, H. Uludağ, Current state of fabrication technologies and materials for bone tissue engineering, Acta Biomater. 80 (2018) 1–30. https://doi.org/10.1016/j.actbio.2018.09.031.

[51] S. Bose, D. Ke, H. Sahasrabudhe, A. Bandyopadhyay, Additive manufacturing of biomaterials, Prog. Mater. Sci. 93 (2018) 45–111. https://doi.org/10.1016/j.pmatsci.2017.08.003.

[52] J.R.C. Dizon, A.H. Espera, Q. Chen, R.C. Advincula, Mechanical characterization of 3D-printed polymers, Addit. Manuf. 20 (2018) 44–67. https://doi.org/10.1016/j.addma.2017.12.002.

[53] H. Wu, W.P. Fahy, S. Kim, H. Kim, N. Zhao, L. Pilato, A. Kafi, S. Bateman, J.H. Koo, Recent developments in polymers/polymer nanocomposites for additive manufacturing, Prog. Mater. Sci. 111 (2020) 100638. https://doi.org/10.1016/j.pmatsci.2020.100638.

[54] B. Tan, S. Gan, X. Wang, W. Liu, X. Li, Applications of 3D bioprinting in tissue engineering: advantages, deficiencies, improvements, and future perspectives, J. Mater. Chem. B. 9 (2021) 5385–5413. https://doi.org/10.1039/d1tb00172h.

[55] M. Pagac, J. Hajnys, Q.P. Ma, L. Jancar, J. Jansa, P. Stefek, J. Mesicek, A review of vat photopolymerization technology: Materials, applications, challenges, and future trends of 3d printing, Polymers (Basel). 13 (2021) 1–20. https://doi.org/10.3390/polym13040598.

[56] T.D. Ngo, A. Kashani, G. Imbalzano, K.T.Q. Nguyen, D. Hui, Additive manufacturing (3D printing): A review of materials, methods, applications and challenges, Compos. Part B Eng. 143 (2018) 172–196. https://doi.org/10.1016/j.compositesb.2018.02.012.

[57] R.K. Gupta, T. Anh Nguyen, Smart Multifunctional Nano-inks: Fundamentals and Emerging Applications, 2022.

[58] S. Fu, Z. Sun, P. Huang, Y. Li, N.H.-N.M. Science, undefined 2019, Some basic aspects of polymer nanocomposites: A critical review, Elsevier. (n.d.).

[59] R.A. Hule, D.J. Pochan, Polymer nanocomposites for biomedical applications, MRS Bull. 32 (2007) 354–358. https://doi.org/10.1557/mrs2007.235.

[60] M. Pracella, M.M.U. Haque, D. Puglia, Morphology and properties tuning of PLA/cellulose nanocrystals bio-nanocomposites by means of reactive functionalization and blending with PVAc, Polymer (Guildf). 55 (2014) 3720–3728. https://doi.org/10.1016/j.polymer.2014.06.071.

[61] D. Mondal, T.W.-J. of the M.B. of Biomedical, undefined 2022, Enhanced mechanical performance of mSLA-printed biopolymer nanocomposites due to phase functionalization, Elsevier. (n.d.).

[62] D. Mondal, Z. Haghpanah, C. Huxman, … S.T.-M.S. and, U. 2021, mSLA-based 3D Printing of Acrylated Epoxidized Soybean Oil-Nano-Hydroxyapatite Composites for Bone Repair, Elsevier. (n.d.).

[63] D. Mondal, A. Srinivasan, P. Comeau, Y.C. Toh, T.L. Willett, Acrylated epoxidized soybean oil/hydroxyapatite-based nanocomposite scaffolds prepared by additive manufacturing for bone tissue engineering, Mater. Sci. Eng. C. 118 (2021). https://doi.org/10.1016/j.msec.2020.111400.

[64] S. Miao, L. Sun, P. Wang, R. Liu, Z. Su, S. Zhang, Soybean oil-based polyurethane networks as candidate biomaterials: Synthesis and biocompatibility, Eur. J. Lipid Sci. Technol. 114 (2012) 1165–1174. https://doi.org/10.1002/ejlt.201200050.

[65] J.F. BURKE, P. DIDISHEIM, D. GOUPIL, J. HELLER, J.B. KANE, J.L. KATZ, S.W. KIM, J.E. LEMONS, M.F. REFOJO, L.S. ROBBLEE, D.C. SMITH, J.D. SWEENEY, R.G. TOMPKINS, J.T. WATSON, P. YAGER, M.L. YARMUSH, Application of Materials in Medicine and Dentistry, in: Biomater. Sci., 1996: pp. 283–388. https://doi.org/10.1016/b978-0-08-050014-0.50012-2.

[66] K.H. Reinert, J.P. Carbone, Synthetic Polymers, in: Encycl. Ecol. Five-Volume Set, 2008: pp. 3461–3472. https://doi.org/10.1016/B978-008045405-4.00432-8.

[67] A. Mohanty, M. Misra, L. Drzal, Natural fibers, biopolymers, and biocomposites, 2005.

[68] C.M. Agrawal, R.B. Ray, Biodegradable polymeric scaffolds for musculoskeletal tissue engineering, J. Biomed. Mater. Res. 55 (2001) 141–150. https://doi.org/10.1002/1097-4636(200105)55:2<141::AID-JBM1000>3.0.CO;2-J.

[69] P. Chandrangsu, C. Rensing, J.D. Helmann, Metal homeostasis and resistance in bacteria, Nat. Rev. Microbiol. 15 (2017) 338–350. https://doi.org/10.1038/nrmicro.2017.15.

[70] K. Gold, B. Slay, M. Knackstedt, A.K. Gaharwar, Antimicrobial Activity of Metal and Metal-Oxide Based Nanoparticles, Adv. Ther. 1 (2018). https://doi.org/10.1002/adtp.201700033.

[71] F. Martinez-Gutierrez, P.L. Olive, A. Banuelos, E. Orrantia, N. Nino, E.M. Sanchez, F. Ruiz, H. Bach, Y. Av-Gay, Synthesis, characterization, and evaluation of antimicrobial and cytotoxic effect of silver and titanium nanoparticles, Nanomedicine Nanotechnology, Biol. Med. 6 (2010) 681–688. https://doi.org/10.1016/j.nano.2010.02.001.

[72] C.M. González-Henríquez, M.A. Sarabia-Vallejos, J. Rodriguez-Hernandez, Polymers for additive manufacturing and 4D-printing: Materials, methodologies, and biomedical applications, Prog. Polym. Sci. 94 (2019) 57–116. https://doi.org/10.1016/j.progpolymsci.2019.03.001.

[73] R.D. Turner, J.R. Wingham, T.E. Paterson, J. Shepherd, C. Majewski, Use of silver-based additives for the development of antibacterial functionality in Laser Sintered polyamide 12 parts, Sci. Rep. 10 (2020). https://doi.org/10.1038/s41598-020-57686-4.

[74] C.M. González-Henríquez, M.A. Sarabia-Vallejos, J.R. Hernandez, Antimicrobial polymers for additive manufacturing, Int. J. Mol. Sci. 20 (2019). https://doi.org/10.3390/ijms20051210.

[75] A. Tamayol, A. Hassani Najafabadi, P. Mostafalu, A.K. Yetisen, M. Commotto, M. Aldhahri, M.S. Abdel-Wahab, Z.I. Najafabadi, S. Latifi, M. Akbari, N. Annabi, S.H. Yun, A. Memic, M.R. Dokmeci, A. Khademhosseini, Biodegradable elastic nanofibrous platforms with integrated flexible heaters for on-demand drug delivery, Sci. Rep. 7 (2017). https://doi.org/10.1038/s41598-017-04749-8.

[76] A.S. Sarvestani, X. He, E. Jabbari, Osteonectin-derived peptide increases the modulus of a bone-mimetic nanocomposite, Eur. Biophys. J. 37 (2008) 229–234. https://doi.org/10.1007/s00249-007-0198-3.

[77] G. Wei, P.X. Ma, Structure and properties of nano-hydroxyapatite/polymer composite scaffolds for bone tissue engineering, Biomaterials. 25 (2004) 4749–4757. https://doi.org/10.1016/j.biomaterials.2003.12.005.

[78] S. Samavedi, A.R. Whittington, A.S. Goldstein, Calcium phosphate ceramics in bone tissue engineering: a review of properties and their influence on cell behavior, Acta Biomater. 9 (2013) 8037–8045.

[79] B. Sitharaman, Nanobiomaterials Handbook, 2016. https://doi.org/10.1201/b10970.

[80] A. Szcześ, L. Hołysz, E. Chibowski, Synthesis of hydroxyapatite for biomedical applications, Adv. Colloid

Interface Sci. 249 (2017) 321–330. https://doi.org/10.1016/j.cis.2017.04.007.

[81] C. Shuai, B. Yang, S. Peng, Z. Li, Development of composite porous scaffolds based on poly(lactide-co-glycolide)/nano-hydroxyapatite via selective laser sintering, Int. J. Adv. Manuf. Technol. 69 (2013) 51–57. https://doi.org/10.1007/s00170-013-5001-2.

[82] J. Yu, Y. Xu, S. Li, G. V. Seifert, M.L. Becker, Three-Dimensional Printing of Nano Hydroxyapatite/Poly(ester urea) Composite Scaffolds with Enhanced Bioactivity, Biomacromolecules. 18 (2017) 4171–4183. https://doi.org/10.1021/acs.biomac.7b01222.

[83] Y. Xia, P.Y. Zhou, X.S. Cheng, Y. Xie, C. Liang, C. Li, S.G. Xu, Selective laser sintering fabrication of nano-hydroxyapatite/poly-ε-caprolactone scaffolds for bone tissue engineering applications, Int. J. Nanomedicine. 8 (2013) 4197–4213. https://doi.org/10.2147/IJN.S50685.

[84] D. Mondal, Z. Haghpanah, C.J. Huxman, S. Tanter, D. Sun, M. Gorbet, T.L. Willett, mSLA-based 3D printing of acrylated epoxidized soybean oil - nano-hydroxyapatite composites for bone repair, Mater. Sci. Eng. C. 130 (2021). https://doi.org/10.1016/j.msec.2021.112456.

[85] P.A. Comeau, T.L. Willett, Triethyleneglycol dimethacrylate addition improves the 3D-printability and construct properties of a GelMA-nHA composite system towards tissue engineering applications, Mater. Sci. Eng. C. 112 (2020). https://doi.org/10.1016/j.msec.2020.110937.

[86] P. Comeau, T. Willett, Printability of Methacrylated Gelatin upon Inclusion of a Chloride Salt and Hydroxyapatite Nano-Particles, Macromol. Mater. Eng. 304 (2019). https://doi.org/10.1002/mame.201900142.

[87] T. Twardowski, Introduction to nanocomposite materials: properties, processing, characterization, Choice Rev. Online. 46 (2008) 46-0317-46–0317. https://doi.org/10.5860/choice.46-0317.

[88] N.W.S. Pinargote, A. Smirnov, N. Peretyagin, A. Seleznev, P. Peretyagin, Direct ink writing technology (3d printing) of graphene-based ceramic nanocomposites: A review, Nanomaterials. 10 (2020) 1–48. https://doi.org/10.3390/nano10071300.

[89] M. Aakyiir, B. Tanner, P.L. Yap, H. Rastin, T.T. Tung, D. Losic, Q. Meng, J. Ma, 3D printing interface-modified PDMS/MXene nanocomposites for stretchable conductors, J. Mater. Sci. Technol. 117 (2022) 174–182. https://doi.org/10.1016/j.jmst.2021.11.048.

[90] J. Zhong, G.X. Zhou, P.G. He, Z.H. Yang, D.C. Jia, 3D printing strong and conductive geo-polymer nanocomposite structures modified by graphene oxide, Carbon N. Y. 117 (2017) 421–426. https://doi.org/10.1016/j.carbon.2017.02.102.

[91] J.A. Lewis, J.E. Smay, J. Stuecker, J. Cesarano, Direct ink writing of three-dimensional ceramic structures, J. Am. Ceram. Soc. 89 (2006) 3599–3609. https://doi.org/10.1111/j.1551-2916.2006.01382.x.

[92] S. Corbel, O. Dufaud, T. Roques-Carmes, Materials for Stereolithography, in: Stereolithography, Springer, Boston, MA, 2011: pp. 141–159. https://doi.org/10.1007/978-0-387-92904-0_6.

[93] M. Instruments, WHITEPAPER 2 A Basic Introduction to Rheology Shear Flow, J Biomech. 35 (2019) 415–435.

[94] J.M. Dealy, K.F. Wissbrun, Introduction to Rheology, in: Melt Rheol. Its Role Plast. Process., Springer Netherlands, 1999: pp. 1–41. https://doi.org/10.1007/978-94-009-2163-4_1.

[95] J.Vlachopoulos, D. Strutt, The role of rheology in polymer extrusion. InNew Technology for Extrusion

Conference 2003 Nov 20 pp. 20-21. Milan: Italy

[96] B.G. Compton, J.A. Lewis, 3D-printing of lightweight cellular composites, Adv. Mater. 26 (2014) 5930–5935. https://doi.org/10.1002/adma.201401804.

[97] J.J. Martin, M.S. Riederer, M.D. Krebs, R.M. Erb, Understanding and overcoming shear alignment of fibers during extrusion, Soft Matter. 11 (2015) 400–405. https://doi.org/10.1039/c4sm02108h.

[98] Z. Ge, A.M. Tawfek, H. Zhang, Y. Yang, H. Yuan, R. Sun, Z. Wang, Influence of an extrusion approach on the fiber orientation and mechanical properties of engineering cementitious composite, Constr. Build. Mater. 306 (2021) 124876. https://doi.org/10.1016/j.conbuildmat.2021.124876.

[99] Z. Yang, Z. Yang, H. Chen, W. Yan, 3D printing of short fiber reinforced composites via material extrusion: Fiber breakage, Addit. Manuf. 58 (2022) 103067. https://doi.org/10.1016/j.addma.2022.103067.

[100] J. Summerscales, Fundamentals of composites manufacturing: materials, methods and applications, Compos. Manuf. 2 (1991) 52–53. https://doi.org/10.1016/0956-7143(91)90160-i.

[101] D.E. Yunus, W. Shi, S. Sohrabi, Y. Liu, Shear induced alignment of short nanofibers in 3D printed polymer composites, Nanotechnology. 27 (2016). https://doi.org/10.1088/0957-4484/27/49/495302.

[102] E. Narimissa, R.K. Gupta, N. Kao, H.J. Choi, M. Jollands, S.N. Bhattacharya, Melt rheological investigation of polylactide-nanographite platelets biopolymer composites, Polym. Eng. Sci. 54 (2014) 175–188. https://doi.org/10.1002/pen.23550.

[103] R.M. Erb, R. Libanori, N. Rothfuchs, A.R. Studart, Composites reinforced in three dimensions by using low magnetic fields, Science (80-.). 335 (2012) 199–204. https://doi.org/10.1126/science.1210822.

[104] T. Nakamoto, S. Kojima, Layered thin film micro parts reinforced with aligned short fibers in laser stereolithography by applying magnetic field, in: J. Adv. Mech. Des. Syst. Manuf., 2012: pp. 849–858. https://doi.org/10.1299/jamdsm.6.849.

[105] T. Nakamoto, O. Kanehisa, Y. Sugawa, Whisker alignment in microparts using laser stereolithography with applied electric field, J. Adv. Mech. Des. Syst. Manuf. 7 (2013) 888–902. https://doi.org/10.1299/jamdsm.7.888.

[106] D. Garcia-Gonzalez, A. Muñoz-Barrutia, Computational insights into the influence of substrate stiffness on collective cell migration, Extrem. Mech. Lett. 40 (2020). https://doi.org/10.1016/j.eml.2020.100928.

[107] J.P. Lewicki, J.N. Rodriguez, C. Zhu, M.A. Worsley, A.S. Wu, Y. Kanarska, J.D. Horn, E.B. Duoss, J.M. Ortega, W. Elmer, R. Hensleigh, R.A. Fellini, M.J. King, 3D-Printing of Meso-structurally Ordered Carbon Fiber/Polymer Composites with Unprecedented Orthotropic Physical Properties, Sci. Rep. 7 (2017). https://doi.org/10.1038/srep43401.

[108] B.G. Compton, J.A. Lewis, 3D-printing of lightweight cellular composites, Adv. Mater. 26 (2014) 5930–5935. https://doi.org/10.1002/adma.201401804.

[109] H.L. Tekinalp, V. Kunc, G.M. Velez-Garcia, C.E. Duty, L.J. Love, A.K. Naskar, C.A. Blue, S. Ozcan, Highly oriented carbon fiber-polymer composites via additive manufacturing, Compos. Sci. Technol. 105 (2014) 144–150. https://doi.org/10.1016/j.compscitech.2014.10.009.

[110] K. Balani, V. Verma, A. Agarwal, R. Narayan, Physical, Thermal, and Mechanical Properties of Polymers, in: Biosurfaces, John Wiley & Sons, Inc, 2015: pp. 329–344.

https://doi.org/10.1002/9781118950623.app1.

[111] W.C. Jr, D. Rethwisch, Callister's materials science and engineering, 2020.

[112] V.P. Cyras, D.A. D'Amico, L.B. Manfredi, Crystallization behavior of polymer nanocomposites, in: Cryst. Multiph. Polym. Syst., 2018: pp. 269–311. https://doi.org/10.1016/B978-0-12-809453-2.00010-4.

[113] A. Baltazar-Y-Jimenez, M. Sain, Effect of bismaleimide reactive extrusion on the crystallinity and mechanical performance of poly(lactic acid) green composites, J. Appl. Polym. Sci. 124 (2012) 3013–3023. https://doi.org/10.1002/app.35331.

[114] E. Barocio, B. Brenken, A. Favaloro, R.B. Pipes, Interlayer fusion bonding of semi-crystalline polymer composites in extrusion deposition additive manufacturing, Compos. Sci. Technol. 230 (2022). https://doi.org/10.1016/j.compscitech.2022.109334.

[115] H. Han, X. Wang, D. Wu, Preparation, crystallization behaviors, and mechanical properties of biodegradable composites based on poly(L-lactic acid) and recycled carbon fiber, Compos. Part A Appl. Sci. Manuf. 43 (2012) 1947–1958. https://doi.org/10.1016/j.compositesa.2012.06.014.

[116] G. Liu, A.J. Müller, D. Wang, Confined Crystallization of Polymers within Nanopores, Acc. Chem. Res. 54 (2021) 3028–3038. https://doi.org/10.1021/acs.accounts.1c00242.

[117] C. Zhang, L. Li, S. Zheng, Formation and confined crystallization of polyethylene nanophases in epoxy thermosets, Macromolecules. 46 (2013) 2740–2753. https://doi.org/10.1021/ma4000682.

[118] J.H. Lee, R.K. Prud'homme, I.A. Aksay, Cure depth in photopolymerization: Experiments and theory, J. Mater. Res. 16 (2001) 3536–3544. https://doi.org/10.1557/JMR.2001.0485.

[119] M. Lebedevaite, J. Ostrauskaite, Influence of photoinitiator and temperature on photocross-linking kinetics of acrylated epoxidized soybean oil and properties of the resulting polymers, Ind. Crops Prod. 161 (2021) 113210. https://doi.org/10.1016/j.indcrop.2020.113210.

[120] H.J. Lee, S.E. Kim, H.W. Choi, C.W. Kim, K.J. Kim, S.C. Lee, The effect of surface-modified nano-hydroxyapatite on biocompatibility of poly(ε-caprolactone)/hydroxyapatite nanocomposites, Eur. Polym. J. 43 (2007) 1602–1608. https://doi.org/10.1016/j.eurpolymj.2007.02.030.

[121] H. Yang, Q. Zhang, M. Guo, C. Wang, R. Du, Q. Fu, Study on the phase structures and toughening mechanism in PP/EPDM/SiO 2 ternary composites, Polymer (Guildf). 47 (2006) 2106–2115. https://doi.org/10.1016/j.polymer.2006.01.076.

[122] J. Kruenate, R. Tongpool, T. Panyathanmaporn, P. Kongrat, Optical and mechanical properties of polypropylene modified by metal oxides, in: Surf. Interface Anal., 2004: pp. 1044–1047. https://doi.org/10.1002/sia.1833.

[123] S. Kango, S. Kalia, A. Celli, J. Njuguna, Y. Habibi, R. Kumar, Surface modification of inorganic nanoparticles for development of organic-inorganic nanocomposites - A review, Prog. Polym. Sci. 38 (2013) 1232–1261. https://doi.org/10.1016/j.progpolymsci.2013.02.003.

[124] M.Z. Rong, M.Q. Zhang, W.H. Ruan, Surface modification of nanoscale fillers for improving properties of polymer nanocomposites: A review, Mater. Sci. Technol. 22 (2006) 787–796. https://doi.org/10.1179/174328406X101247.

[125] Y. Zare, Study of nanoparticles aggregation/agglomeration in polymer particulate nanocomposites by mechanical properties, Compos. Part A Appl. Sci. Manuf. 84 (2016) 158–164.

https://doi.org/10.1016/j.compositesa.2016.01.020.

[126] J. Lim, M.S.K. Chong, J.K.Y. Chan, S.H. Teoh, Polymer powder processing of cryomilled polycaprolactone for solvent-free generation of homogeneous bioactive tissue engineering scaffolds, Small. 10 (2014) 2495–2502. https://doi.org/10.1002/smll.201302389.

[127] S.Y. Tong, Z. Wang, P.N. Lim, W. Wang, E.S. Thian, Uniformly-dispersed nanohydroxapatite-reinforced poly(ε-caprolactone) composite films for tendon tissue engineering application, Mater. Sci. Eng. C. 70 (2017) 1149–1155. https://doi.org/10.1016/j.msec.2016.03.051.

[128] D. Poirier, R.A.L. Drew, M.L. Trudeau, R. Gauvin, Fabrication and properties of mechanically milled alumina/aluminum nanocomposites, Mater. Sci. Eng. A. 527 (2010) 7605–7614. https://doi.org/10.1016/j.msea.2010.08.018.

[129] B. Prabhu, C. Suryanarayana, L. An, R. Vaidyanathan, Synthesis and characterization of high volume fraction Al-Al2O3 nanocomposite powders by high-energy milling, Mater. Sci. Eng. A. 425 (2006) 192–200. https://doi.org/10.1016/j.msea.2006.03.066.

[130] K.L. Lu, R.M. Lago, Y.K. Chen, M.L.H. Green, P.J.F. Harris, S.C. Tsang, Mechanical damage of carbon nanotubes by ultrasound, Carbon N. Y. 34 (1996) 814–816. https://doi.org/10.1016/0008-6223(96)89470-X.

[131] B. Pukánszky, E. Fekete, Aggregation Tendency of Particulate Fillers: Determination and Consequences, Polym. Polym. Compos. 6 (1998) 313–322. https://doi.org/10.1177/147823919800600508.

[132] Q. Li, X. Lei, X. Wang, Z. Cai, P. Lyu, G. Zhang, Hydroxyapatite/Collagen Three-Dimensional Printed Scaffolds and Their Osteogenic Effects on Human Bone Marrow-Derived Mesenchymal Stem Cells, Tissue Eng. - Part A. 25 (2019) 1261–1271. https://doi.org/10.1089/ten.tea.2018.0201.

[133] G. Ruphuy, T. Weide, J.C.B. Lopes, M.M. Dias, M.F. Barreiro, Preparation of nano-hydroxyapatite/chitosan aqueous dispersions: From lab scale to continuous production using an innovative static mixer, Carbohydr. Polym. 202 (2018) 20–28. https://doi.org/10.1016/j.carbpol.2018.08.123.

[134] Z. Hong, X. Qiu, J. Sun, M. Deng, X. Chen, X. Jing, Grafting polymerization of L-lactide on the surface of hydroxyapatite nano-crystals, Polymer (Guildf). 45 (2004) 6699–6706. https://doi.org/10.1016/j.polymer.2004.07.036.

[135] R. Ying, H. Wang, R. Sun, K. Chen, Preparation and properties of a highly dispersed nano-hydroxyapatite colloid used as a reinforcing filler for chitosan, Mater. Sci. Eng. C. 110 (2020) 110689. https://doi.org/10.1016/j.msec.2020.110689.

[136] S. S. Hashemi, D. Mondal, J. Montesano, T.L. Willett, Effects of biopolymer functionalization and nanohydroxyapatite heat treatment on the tensile and thermomechanical properties of Bone-Inspired 3D printable nanocomposite biomaterials, Mater. Des. 225 (2023) 111587. https://doi.org/10.1016/J.MATDES.2023.111587.

[137] M. Šupová, Problem of hydroxyapatite dispersion in polymer matrices: A review, J. Mater. Sci. Mater. Med. 20 (2009) 1201–1213. https://doi.org/10.1007/s10856-009-3696-2.

[138] R.E. Baier, Surface behaviour of biomaterials: The theta surface for biocompatibility, in: J. Mater. Sci. Mater. Med., 2006: pp. 1057–1062. https://doi.org/10.1007/s10856-006-0444-8.

[139] M.W. Hyer, Stress Analysis of Fibre-Reinforced Composite Materials, 2009.

[140] H. Kim, A.A. Abdala, C.W. MacOsko, Graphene/polymer nanocomposites, Macromolecules. 43 (2010) 6515–6530. https://doi.org/10.1021/ma100572e.

[141] Y. Wang, C.S. Lin, Preparation and characterization of maleated polylactide-functionalized graphite oxide nanocomposites, J. Polym. Res. 21 (2014). https://doi.org/10.1007/s10965-013-0334-y.

[142] B.W. Chieng, N.A. Ibrahim, W.M.Z.W. Yunus, M.Z. Hussein, Y.Y. Then, Y.Y. Loo, Effects of graphene nanoplatelets and reduced graphene oxide on poly(lactic acid) and plasticized poly(lactic acid): A comparative study, Polymers (Basel). 6 (2014) 2232–2246. https://doi.org/10.3390/polym6082232.

[143] M.L. Flores-Cedillo, K.N. Alvarado-Estrada, A.J. Pozos-Guillén, J.S. Murguía-Ibarra, M.A. Vidal, J.M. Cervantes-Uc, R. Rosales-Ibáñez, J. V. Cauich-Rodríguez, Multiwall carbon nanotubes/polycaprolactone scaffolds seeded with human dental pulp stem cells for bone tissue regeneration, J. Mater. Sci. Mater. Med. 27 (2016) 1–12. https://doi.org/10.1007/s10856-015-5640-y.

[144] Y. Hosseini, R. Emadi, M. Kharaziha, A. Doostmohammadi, Reinforcement of electrospun poly(ε-caprolactone) scaffold using diopside nanopowder to promote biological and physical properties, J. Appl. Polym. Sci. 134 (2017) 44433. https://doi.org/10.1002/app.44433.

[145] T. Kuilla, S. Bhadra, D. Yao, N.H. Kim, S. Bose, J.H. Lee, Recent advances in graphene based polymer composites, Prog. Polym. Sci. 35 (2010) 1350–1375. https://doi.org/10.1016/j.progpolymsci.2010.07.005.

[146] S.C. Udensi, L.A. Nnanna, Sem Studies of Tensile Fractured Surfaces of Expanded Graphite/Acrylonitrile/Methyl Methacrylate Nanocomposites Prepared via in-Situ Polymerization, Am. J. Mater. Sci. 1 (2012) 123–127. https://doi.org/10.5923/j.materials.20110102.20.

[147] X.S. Sun, Overview of Plant Polymers: Resources, Demands, and Sustainability. Resources, Demands, and Sustainability., in: Handb. Biopolym. Biodegrad. Plast. Prop. Process. Appl., 2013: pp. 1–10. https://doi.org/10.1016/B978-1-4557-2834-3.00001-X.

[148] T.J. Farmer, J.W. Comerford, A. Pellis, T. Robert, Post-polymerization modification of bio-based polymers: maximizing the high functionality of polymers derived from biomass, Polym. Int. 67 (2018) 775–789. https://doi.org/10.1002/pi.5573.

[149] D. Bertomeu, D. García-Sanoguera, O. Fenollar, T. Boronat, R. Balart, Use of eco-friendly epoxy resins from renewable resources as potential substitutes of petrochemical epoxy resins for ambient cured composites with flax reinforcements, Polym. Compos. 33 (2012) 683–692. https://doi.org/10.1002/pc.22192.

[150] A. Llevot, Sustainable Synthetic Approaches for the Preparation of Plant Oil-Based Thermosets, JAOCS, J. Am. Oil Chem. Soc. 94 (2017) 169–186. https://doi.org/10.1007/s11746-016-2932-4.

[151] K. Amulya, R. Katakojwala, S. Ramakrishna, S. Venkata Mohan, Low carbon biodegradable polymer matrices for sustainable future, Compos. Part C Open Access. 4 (2021). https://doi.org/10.1016/j.jcomc.2021.100111.

[152] M.A.R. Meier, J.O. Metzger, U.S. Schubert, Plant oil renewable resources as green alternatives in polymer science, Chem. Soc. Rev. 36 (2007) 1788–1802. https://doi.org/10.1039/b703294c.

[153] M. Meier, Plant oils: The perfect renewable resource for the chemical industry?!, Int. News Fats, Oils Relat. Mater. 24 (2013) 460–463.

[154] H. Pelletier, A. Gandini, Preparation of acrylated and urethanated triacylglycerols, in: Eur. J. Lipid Sci. Technol., 2006: pp. 411–420. https://doi.org/10.1002/ejlt.200501168.

[155] B. Song, W. Chen, Z. Liu, S. Erhan, Compressive properties of epoxidized soybean oil/clay nanocomposites, Int. J. Plast. 22 (2006) 1549–1568. https://doi.org/10.1016/j.ijplas.2005.10.004.

[156] S.C. Mauck, S. Wang, W. Ding, B.J. Rohde, C.K. Fortune, G. Yang, S.K. Ahn, M.L. Robertson, Biorenewable Tough Blends of Polylactide and Acrylated Epoxidized Soybean Oil Compatibilized by a Polylactide Star Polymer, Macromolecules. 49 (2016) 1605–1615. https://doi.org/10.1021/acs.macromol.5b02613.

[157] A. Campanella, J.J.L. Scala, R.P. Wool, Fatty acid-based comonomers as styrene replacements in soybean and castor oil-based thermosetting polymers, J. Appl. Polym. Sci. 119 (2011) 1000–1010. https://doi.org/10.1002/app.32810.

[158] A. Campanella, J.J. La Scala, R.P. Wool, The use of acrylated fatty acid methyl esters as styrene replacements in triglyceride-based thermosetting polymers, Polym. Eng. Sci. 49 (2009) 2384–2392. https://doi.org/10.1002/pen.21486.

[159] J. La Scala, R.P. Wool, Property analysis of triglyceride-based thermosets, Polymer (Guildf). 46 (2005) 61–69. https://doi.org/10.1016/j.polymer.2004.11.002.

[160] D. Mondal, T.L. Willett, Enhanced mechanical performance of mSLA-printed biopolymer nanocomposites due to phase functionalization, J. Mech. Behav. Biomed. Mater. 135 (2022) 105450. https://doi.org/10.1016/j.jmbbm.2022.105450.

[161] W. Liu, T. Xie, R. Qiu, Biobased Thermosets Prepared from Rigid Isosorbide and Flexible Soybean Oil Derivatives, ACS Sustain. Chem. Eng. 5 (2017) 774–783. https://doi.org/10.1021/acssuschemeng.6b02117.

[162] R. Walter, K. Friedrich, V. Privalko, A. Savadori, On modulus and fracture toughness of rigid particulate filled high density polyethylene, J. Adhes. 64 (1997) 87–109. https://doi.org/10.1080/00218469708010533.

[163] Y. Taniguchi, M. Ogawa, W. Gang, H. Saitoh, K. Fujiki, T. Yamauchi, N. Tsubokawa, Preparation of hyperfunctional carbon black by grafting of hyperbranched polyester onto the surface, Mater. Chem. Phys. 108 (2008) 397–402. https://doi.org/10.1016/j.matchemphys.2007.10.013.

[164] Q. Peng, D.M.Y. Lai, E.T. Kang, K.G. Neoh, Preparation of polymer-silicon(100) hybrids via interface-initiated reversible addition-fragmentation chain-transfer (RAFT) polymerization, Macromolecules. 39 (2006) 5577–5582. https://doi.org/10.1021/ma0607362.

[165] H. Skaff, T. Emrick, Reversible addition fragmentation chain transfer (RAFT) polymerization from unprotected cadmium selenide nanoparticles, Angew. Chemie - Int. Ed. 43 (2004) 5383–5386. https://doi.org/10.1002/anie.200453822.

[166] J. Wei, Y. Li, X. Peng, L. Zhang, J. Han, A study on tissue engineering scaffold material of nano-apatite and polyamide composite, in: Trans. - 7th World Biomater. Congr., 2004: p. 827.

[167] H.J. Lee, H.W. Choi, K.J. Kim, S.C. Lee, Modification of hydroxyapatite nanosurfaces for enhanced colloidal stability and improved interfacial adhesion in nanocomposites, Chem. Mater. 18 (2006) 5111–5118. https://doi.org/10.1021/cm061139x.

[168] J.A. Roether, S. Deb, The effect of surface treatment of hydroxyapatite on the properties of a bioactive bone cement, in: J. Mater. Sci. Mater. Med., 2004: pp. 413–418. https://doi.org/10.1023/B:JMSM.0000021112.51065.40.

[169] S.C. D'Andrea, A.Y. Fadeev, Covalent surface modification of calcium hydroxyapatite using n-alkyl- and n-fluoroalkylphosphonic acids, Langmuir. 19 (2003) 7904–7910. https://doi.org/10.1021/la027000s.

[170] S.C. Lee, H.W. Choi, H.J. Lee, K.J. Kim, J.H. Chang, S.Y. Kim, J. Choi, K.S. Oh, Y.K. Jeong, In-situ synthesis of reactive hydroxyapatite nano-crystals for a novel approach of surface grafting polymerization, J. Mater. Chem. 17 (2007) 174–180. https://doi.org/10.1039/b611401f.

[171] Q. Liu, J.R. De Wijn, C.A. Van Blitterswijk, Nano-apatite/polymer composites: Mechanical and physicochemical characteristics, Biomaterials. 18 (1997) 1263–1270. https://doi.org/10.1016/S0142-9612(97)00069-0.

[172] Q. Liu, J.R. De Wijn, C.A. Van Blitterswijk, A study on the grafting reaction of isocyanates with hydroxyapatite particles, J. Biomed. Mater. Res. 40 (1998) 358–364. https://doi.org/10.1002/(SICI)1097-4636(19980605)40:3<358::AID-JBM3>3.0.CO;2-E.

[173] Q. Liu, J.R. De Wijn, C.A. Van Blitterswijk, Covalent bonding of PMMA, PBMA, and poly(HEMA) to hydroxyapatite particles, J. Biomed. Mater. Res. 40 (1998) 257–263. https://doi.org/10.1002/(SICI)1097-4636(199805)40:2<257::AID-JBM10>3.0.CO;2-J.

[174] R. Murugan, S. Ramakrishna, Coupling of therapeutic molecules onto surface modified coralline hydroxyapatite, Biomaterials. 25 (2004) 3073–3080. https://doi.org/10.1016/j.biomaterials.2003.09.089.

[175] C.M. Vaz, R.L. Reis, A.M. Cunha, Use of coupling agents to enhance the interfacial interactions in starch-EVOH/hydroxylapatite composites, Biomaterials. 23 (2002) 629–635. https://doi.org/10.1016/S0142-9612(01)00150-8.

[176] W.L. Tham, W.S. Chow, Z.A.M. Ishak, The effect of 3-(trimethoxysilyl) propyl methacrylate on the mechanical, thermal, and morphological properties of poly(methyl methacrylate)/ hydroxyapatite composites, J. Appl. Polym. Sci. 118 (2010) 218–228. https://doi.org/10.1002/app.32111.

[177] Y. Uyama, K. Kato, Y. Ikada, Surface Modification of Polymers by Grafting, Adv. Polym. Sci. 137 (1998) 1067–1072. https://doi.org/10.1007/3-540-69685-7_1.

[178] L. Borum, O.C. Wilson, Surface modification of hydroxyapatite. Part II. Silica, Biomaterials. 24 (2003) 3681–3688. https://doi.org/10.1016/S0142-9612(03)00240-0.

[179] L. Borum-Nicholas, O.C. Wilson, Surface modification of hydroxyapatite. Part I. Dodecyl alcohol, Biomaterials. 24 (2003) 3671–3679. https://doi.org/10.1016/S0142-9612(03)00239-4.

[180] H. Tanaka, M. Futaoka, R. Hino, Surface modification of calcium hydroxyapatite with pyrophosphoric acid, J. Colloid Interface Sci. 269 (2004) 358–363. https://doi.org/10.1016/j.jcis.2003.07.039.

[181] H. Tanaka, M. Futaoka, R. Hino, K. Kandori, T. Ishikawa, Structure of synthetic calcium hydroxyapatite particles modified with pyrophosphoric acid, J. Colloid Interface Sci. 283 (2005) 609–612. https://doi.org/10.1016/j.jcis.2004.09.013.

[182] J.E. Barralet, M. Tremayne, K.J. Lilley, U. Gbureck, Modification of calcium phosphate cement with α-hydroxy acids and their salts, Chem. Mater. 17 (2005) 1313–1319. https://doi.org/10.1021/cm048803z.

[183] C. Lung, Z. Sarfraz, A. Habib, … A.K.-J. of the, U. 2016, Effect of silanization of hydroxyapatite fillers on physical and mechanical properties of a bis-GMA based resin composite, Elsevier. (n.d.).

[184] J.R. Jones, Reprint of: Review of bioactive glass: From Hench to hybrids, Acta Biomater. 23 (2015) S53–S82. https://doi.org/10.1016/j.actbio.2015.07.019.

[185] R. Larry, L. Hench, The story of Bioglass, J Mater Sci Mater Med. 17 (2006) 967–978. https://doi.org/10.1007/s10856-006-0432-z.

[186] M. Reiter, Z. Major, A combined experimental and simulation approach for modelling the mechanical behaviour of heterogeneous materials using rapid prototyped microcells: A novel two-component rapid prototyping system was used to produce real 3D microcell models for various he, Virtual Phys. Prototyp. 6 (2011) 111–120. https://doi.org/10.1080/17452759.2011.586949.

[187] M. Chwal, A. Muc, FEM micromechanical modeling of nanocomposites with carbon nanotubes, Rev. Adv. Mater. Sci. 60 (2021) 342–351. https://doi.org/10.1515/rams-2021-0027.

[188] P.D. Spanos, A. Kontsos, A multiscale Monte Carlo finite element method for determining mechanical properties of polymer nanocomposites, Probabilistic Eng. Mech. 23 (2008) 456–470. https://doi.org/10.1016/j.probengmech.2007.09.002.

[189] A. Bahmani, G. Li, T.L. Willett, J. Montesano, Three-dimensional microscopic assessment of randomly distributed representative volume elements for high fiber volume fraction unidirectional composites, Compos. Struct. 192 (2018) 153–164. https://doi.org/10.1016/j.compstruct.2018.02.075.

[190] T. Desai, P. Keblinski, S.K. Kumar, Molecular dynamics simulations of polymer transport in nanocomposites, J. Chem. Phys. 122 (2005) 134910. https://doi.org/10.1063/1.1874852.

[191] P.K. Singh, K. Sharma, Molecular dynamics simulation of glass transition behavior of polymer based nanocomposites, J. Sci. Ind. Res. (India). 77 (2018) 592–595.

[192] G.D. Smith, D. Bedrov, L. Li, O. Byutner, A molecular dynamics simulation study of the viscoelastic properties of polymer nanocomposites, J. Chem. Phys. 117 (2002) 9478–9490. https://doi.org/10.1063/1.1516589.

[193] F. Liu, N. Hu, H. Ning, Y. Liu, Y. Li, L. Wu, Molecular dynamics simulation on interfacial mechanical properties of polymer nanocomposites with wrinkled graphene, Comput. Mater. Sci. 108 (2015) 160–167. https://doi.org/10.1016/j.commatsci.2015.06.023.

[194] C. Pelissou, J. Baccou, Y. Monerie, F. Perales, Determination of the size of the representative volume element for random quasi-brittle composites, Int. J. Solids Struct. 46 (2009) 2842–2855. https://doi.org/10.1016/j.ijsolstr.2009.03.015.

[195] M.M. Aghdam, S.R. Falahatgar, Micromechanical modeling of interface damage of metal matrix composites subjected to transverse loading, Compos. Struct. 66 (2004) 415–420. https://doi.org/10.1016/j.compstruct.2004.04.063.

[196] M.M. Aghdam, S.R. Falahatgar, M. Gorji, Micromechanical consideration of interface damage in fiber reinforced Ti-alloy under various combined loading conditions, Compos. Sci. Technol. 68 (2008) 3406–3411. https://doi.org/10.1016/j.compscitech.2008.09.028.

[197] M.J. Mahmoodi, M.M. Aghdam, M. Shakeri, Micromechanical modeling of interface damage of metal matrix composites subjected to off-axis loading, Mater. Des. 31 (2010) 829–836. https://doi.org/10.1016/j.matdes.2009.07.048.

[198] M. Ahmadi, R. Ansari, S. Rouhi, Fracture behavior of the carbon nanotube/carbon fiber/polymer multiscale composites under bending test–A stochastic finite element method, Mech. Adv. Mater. Struct. 26 (2019) 1169–1177. https://doi.org/10.1080/15376494.2018.1432790.

[199] M. Mirkhalaf, F. Barthelat, Nacre-like materials using a simple doctor blading technique: Fabrication,

testing and modeling, J. Mech. Behav. Biomed. Mater. 56 (2016) 23–33. https://doi.org/10.1016/J.JMBBM.2015.11.010.

[200] M.K. Kassa, A.B. Arumugam, Micromechanical modeling and characterization of elastic behavior of carbon nanotube-reinforced polymer nanocomposites: A combined numerical approach and experimental verification, Polym. Compos. 41 (2020) 3322–3339. https://doi.org/10.1002/pc.25622.

[201] Y.J. Liu, X.L. Chen, Evaluations of the effective material properties of carbon nanotube-based composites using a nanoscale representative volume element, Mech. Mater. 35 (2003) 69–81. https://doi.org/10.1016/S0167-6636(02)00200-4.

[202] X.L. Chen, Y.J. Liu, Square representative volume elements for evaluating the effective material properties of carbon nanotube-based composites, Comput. Mater. Sci. 29 (2004) 1–11. https://doi.org/10.1016/S0927-0256(03)00090-9.

[203] M. Malagù, M. Goudarzi, A. Lyulin, E. Benvenuti, A. Simone, Diameter-dependent elastic properties of carbon nanotube-polymer composites: Emergence of size effects from atomistic-scale simulations, Compos. Part B Eng. 131 (2017) 260–281. https://doi.org/10.1016/j.compositesb.2017.07.029.

[204] A.R. Alian, S.I. Kundalwal, S.A. Meguid, Multiscale modeling of carbon nanotube epoxy composites, Polymer (Guildf). 70 (2015) 149–160. https://doi.org/10.1016/j.polymer.2015.06.004.

[205] M.K. Kassa, A.B. Arumugam, Micromechanical modeling and characterization of elastic behavior of carbon nanotube-reinforced polymer nanocomposites: A combined numerical approach and experimental verification, Polym. Compos. 41 (2020) 3322–3339. https://doi.org/10.1002/pc.25622.

[206] M.M. Shokrieh, R. Mosalmani, A.R. Shamaei, A combined micromechanical-numerical model to simulate shear behavior of carbon nanofiber/epoxy nanocomposites, Mater. Des. 67 (2015) 531–537. https://doi.org/10.1016/j.matdes.2014.10.077.

[207] K.N. Spanos, S.K. Georgantzinos, N.K. Anifantis, Investigation of stress transfer in carbon nanotube reinforced composites using a multi-scale finite element approach, Compos. Part B Eng. 63 (2014) 85–93. https://doi.org/10.1016/j.compositesb.2014.03.020.

[208] M.A. Maghsoudlou, R. Barbaz Isfahani, S. Saber-Samandari, M. Sadighi, Effect of interphase, curvature and agglomeration of SWCNTs on mechanical properties of polymer-based nanocomposites: Experimental and numerical investigations, Compos. Part B Eng. 175 (2019) 107119. https://doi.org/10.1016/j.compositesb.2019.107119.

[209] A. Bahmani, G. Li, T.L. Willett, J. Montesano, Three-dimensional microscopic assessment of randomly distributed representative volume elements for high fiber volume fraction unidirectional composites, Compos. Struct. 192 (2018) 153–164.

[210] M.A. Eltaher, A. Wagih, Micromechanical modeling of damage in elasto-plastic nanocomposites using unit cell representative volume element and cohesive zone model, Ceram. Int. 46 (2020) 10469–10480. https://doi.org/10.1016/j.ceramint.2020.01.046.

[211] G. Bao, J.W. Hutchinson, R.M. McMeeking, Particle reinforcement of ductile matrices against plastic flow and creep, Acta Metall. Mater. 39 (1991) 1871–1882. https://doi.org/10.1016/0956-7151(91)90156-U.

[212] S. Qu, T. Siegmund, Y. Huang, P.D. Wu, F. Zhang, K.C. Hwang, A study of particle size effect and interface fracture in aluminum alloy composite via an extended conventional theory of mechanism-based strain-gradient plasticity, Compos. Sci. Technol. 65 (2005) 1244–1253.

https://doi.org/10.1016/j.compscitech.2004.12.029.

[213] Y. Wang, Z.M. Huang, Analytical micromechanics models for elastoplastic behavior of long fibrous composites: A critical review and comparative study, Materials (Basel). 11 (2018). https://doi.org/10.3390/ma11101919.

[214] S. Asiri, A. Wagih, M.A. Eltaher, Predictive model for spherical indentation on elastoplastic nanocomposites: Loading and unloading behavior, Ceram. Int. 45 (2019) 3088–3100. https://doi.org/10.1016/j.ceramint.2018.10.199.

[215] C. Le Thanh, L. V. Tran, T. Vu-Huu, H. Nguyen-Xuan, M. Abdel-Wahab, Size-dependent nonlinear analysis and damping responses of FG-CNTRC micro-plates, Comput. Methods Appl. Mech. Eng. 353 (2019) 253–276. https://doi.org/10.1016/j.cma.2019.05.002.

[216] P.A. Comeau, T. Willett, An Alternative Approach to the Surface Methacrylation of Non-stoichiometric Hydroxyapatite Nanoparticles for Use in Bone-Inspired Composites, Front. Mater. 6 (2019). https://doi.org/10.3389/fmats.2019.00263.

[217] Z. Bal, T. Kaito, F. Korkusuz, H. Yoshikawa, Bone regeneration with hydroxyapatite-based biomaterials, Emergent Mater. 3 (2020) 521–544. https://doi.org/10.1007/s42247-019-00063-3.

[218] A. Bahmani, G. Li, T.L. Willett, J. Montesano, Three-dimensional micromechanical assessment of bio-inspired composites with non-uniformly dispersed inclusions, Compos. Struct. 212 (2019) 484–499. https://doi.org/10.1016/j.compstruct.2019.01.056.

[219] A. Bahmani, P.A. Comeau, J. Montesano, T.L. Willett, Extrudable hydroxyapatite/plant oil-based biopolymer nanocomposites for biomedical applications: Mechanical testing and modeling, Mater. Des. 174 (2019). https://doi.org/10.1016/j.matdes.2019.107790.

[220] M. Amirmaleki, J. Samei, D.E. Green, I. van Riemsdijk, L. Stewart, 3D micromechanical modeling of dual phase steels using the representative volume element method, Mech. Mater. 101 (2016) 27–39. https://doi.org/10.1016/j.mechmat.2016.07.011.

[221] S. Bargmann, B. Klusemann, … J.M.-P. in M., undefined 2018, Generation of 3D representative volume elements for heterogeneous materials: A review, Elsevier. (n.d.).

[222] S.L. Omairey, P.D. Dunning, S. Sriramula, Development of an ABAQUS plugin tool for periodic RVE homogenisation, Eng. Comput. 35 (2019) 567–577. https://doi.org/10.1007/s00366-018-0616-4.

[223] A. Sheidaei, M. Baniassadi, M. Banu, P. Askeland, M. Pahlavanpour, N. Kuuttila, F. Pourboghrat, L.T. Drzal, H. Garmestani, 3-D microstructure reconstruction of polymer nano-composite using FIB-SEM and statistical correlation function, Compos. Sci. Technol. 80 (2013) 47–54. https://doi.org/10.1016/j.compscitech.2013.03.001.

[224] N. Rao, K. O'Brien, N. Rao, K. O'Brien, Mechanical Properties of Solid Polymers, in: Des. Data Plast. Eng., 1998: pp. 1–22. https://doi.org/10.3139/9783446402447.001.

[225] J. Lemaitre, Handbook of Materials Behavior Models, Three-Volume Set: Nonlinear Models and Properties, 2001.

[226] D.R. Mears, K.D. Pae, J.A. Sauer, Effects of hydrostatic pressure on the mechanical behavior of polyethylene and polypropylene, J. Appl. Phys. 40 (1969) 4229–4237. https://doi.org/10.1063/1.1657180.

[227] K.D. Pae, D.R. Mears, J.A. Sauer, Stress–strain behavior of polypropylene under high pressure, J. Polym.

Sci. Part B Polym. Lett. 6 (1968) 773–778. https://doi.org/10.1002/pol.1968.110061103.

[228] K. Matsushige, S. V. Radcliffe, E. Baer, The mechanical behaviour of polystyrene under pressure, J. Mater. Sci. 10 (1975) 833–845. https://doi.org/10.1007/BF01163078.

[229] A.W. Christiansen, E. Baer, S. V Radcliffe, The mechanical behaviour of polymers under high pressure, Philos. Mag. 24 (1971) 451–467. https://doi.org/10.1080/14786437108227400.

[230] J. Yuan, A. Hiltner, E. Baer, D. Rahrig, The effect of high pressure on the mechanical behavior of short fiber composites, Polym. Eng. Sci. 24 (1984) 844–850. https://doi.org/10.1002/pen.760241103.

[231] S.K. Bhateja, The Effects of Hydrostatic Pressure on the Mechanical Behavior of Polymers, J. Macromol. Sci. Part C. 13 (1975) 1–75. https://doi.org/10.1080/15321797508068145.

[232] S. Rabinowitz, I.M. Ward, J.S.C. Parry, The effect of hydrostatic pressure on the shear yield behaviour of polymers, J. Mater. Sci. 5 (1970) 29–39. https://doi.org/10.1007/bf02427181.

[233] A.S. Argon, The physics of deformation and fracture of polymers, Cambridge University Press, Cambridge, 2010. https://doi.org/10.1017/CBO9781139033046.

[234] S.K. Bhateja, The Effects of Hydrostatic Pressure on the Mechanical Behavior of Polymers, J. Macromol. Sci. Part C. 13 (1975) 1–75. https://doi.org/10.1080/15321797508068145.

[235] E. Jones Parry, D. Tabor, Pressure dependence of the shear modulus of various polymers, J. Mater. Sci. 9 (1974) 289–292. https://doi.org/10.1007/BF00550953.

[236] K. Rouf, M.J. Worswick, J. Montesano, Experimentally verified dual-scale modelling framework for predicting the strain rate-dependent nonlinear anisotropic deformation response of unidirectional non-crimp fabric composites, Compos. Struct. 303 (2023) 116384. https://doi.org/10.1016/j.compstruct.2022.116384.

[237] F. Sharifpour, J. Montesano, R. Talreja, Micromechanical assessment of local failure mechanisms and early-stage ply crack formation in cross-ply laminates, Compos. Sci. Technol. 220 (2022) 109286. https://doi.org/10.1016/j.compscitech.2022.109286.

[238] R.C. Batra, G. Gopinath, J.Q. Zheng, Material parameters for pressure-dependent yielding of unidirectional fiber-reinforced polymeric composites, in: Compos. Part B Eng., Elsevier, 2012: pp. 2594–2604. https://doi.org/10.1016/j.compositesb.2011.12.005.

[239] D. Pulungan, A. Yudhanto, S. Goutham, G. Lubineau, R. Yaldiz, W. Schijve, Characterizing and modeling the pressure- and rate-dependent elastic-plastic-damage behavior of polypropylene-based polymers, Polym. Test. 68 (2018) 433–445. https://doi.org/10.1016/j.polymertesting.2018.02.024.

[240] G. Han, Z. Guan, X. Li, W. Zhang, S. Du, Microscopic progressive damage simulation of unidirectional composite based on the elastic-plastic theory, J. Reinf. Plast. Compos. 34 (2015) 232–247. https://doi.org/10.1177/0731684414567745.

[241] Y. Chen, Y. Zhao, S. Ai, C. He, Y. Tao, Y. Yang, D. Fang, A constitutive model for elastoplastic-damage coupling effect of unidirectional fiber-reinforced polymer matrix composites, Compos. Part A Appl. Sci. Manuf. 130 (2020) 105736. https://doi.org/10.1016/j.compositesa.2019.105736.

[242] R. Seltzer, A.P. Cisilino, P.M. Frontini, Y.W. Mai, Determination of the DruckerPrager parameters of polymers exhibiting pressure-sensitive plastic behaviour by depth-sensing indentation, Int. J. Mech. Sci. 53 (2011) 471–478. https://doi.org/10.1016/j.ijmecsci.2011.04.002.

[243] D.C. Drucker, W. Prager, Soil mechanics and plastic analysis or limit design, Q. Appl. Math. 10 (1952) 157–165. https://doi.org/10.1090/qam/48291.

[244] E. Öztekin, S. Pul, M. Hüsem, Experimental determination of Drucker-Prager yield criterion parameters for normal and high strength concretes under triaxial compression, Constr. Build. Mater. 112 (2016) 725–732. https://doi.org/10.1016/j.conbuildmat.2016.02.127.

[245] W. Chen, Plasticity in reinforced concrete, J. Ross Publishing., 2007.

[246] A.S. Khan, S. Huang, Continuum theory of plasticity, John Wiley & Sons, 1995.

[247] J. Bergström, Mechanics of Solid Polymers: Theory and Computational Modeling, 2015. https://doi.org/10.1016/C2013-0-15493-1.

[248] V. Dhinakaran, K. V. Surendar, M.S.H. Riyaz, M. Ravichandran, Review on study of thermosetting and thermoplastic materials in the automated fiber placement process, in: Mater. Today Proc., 2020: pp. 812–815. https://doi.org/10.1016/j.matpr.2019.12.355.

[249] Y. Zeng, Mechanical Characterization and Computational Modeling of Snap-cure Epoxy, 2020.

[250] M.J. Marks, R.V. Snelgrove, Effect of conversion on the structure-property relationships of amine-cured epoxy thermosets, ACS Appl. Mater. Interfaces. 1 (2009) 921–926. https://doi.org/10.1021/am900030u.

[251] B. Ellis, M.S. Found, J.R. Bell, Influence of cure treatment on extent of reaction and glassy modulus for BADGE-DDM epoxy resin, J. Appl. Polym. Sci. 82 (2001) 1265–1276. https://doi.org/10.1002/app.1960.

[252] C. Li, A. Strachan, Molecular dynamics predictions of thermal and mechanical properties of thermoset polymer EPON862/DETDA, Polymer (Guildf). 52 (2011) 2920–2928. https://doi.org/10.1016/j.polymer.2011.04.041.

[253] O. Sindt, J. Perez, J.F. Gerard, Molecular architecture-mechanical behaviour relationships in epoxy networks, Polymer (Guildf). 37 (1996) 2989–2997. https://doi.org/10.1016/0032-3861(96)89396-7.

[254] X.P. Morelle, J. Chevalier, C. Bailly, T. Pardoen, F. Lani, Mechanical characterization and modeling of the deformation and failure of the highly crosslinked RTM6 epoxy resin, Mech. Time-Dependent Mater. 21 (2017) 419–454. https://doi.org/10.1007/s11043-016-9336-6.

[255] D.E. Packham, Polymer science dictionary, Compos. Sci. Technol. 38 (1990) 289–290. https://doi.org/10.1016/0266-3538(90)90063-b.

[256] R. Brown, Handbook of Polymer Testing: Physical Methods, 1999.

[257] T. Boyce, J. Edwards, N. Scarborough, Allograft bone: The influence of processing on safety and performance, Orthop. Clin. North Am. 30 (1999) 571–581. https://doi.org/10.1016/S0030-5898(05)70110-3.

[258] A.J. Harmata, S. Uppuganti, M. Granke, S.A. Guelcher, J.S. Nyman, Compressive fatigue and fracture toughness behavior of injectable, settable bone cements, J. Mech. Behav. Biomed. Mater. 51 (2015) 345–355. https://doi.org/10.1016/j.jmbbm.2015.07.027.

[259] T.G. Vladkova, Surface engineered polymeric biomaterials with improved biocontact properties, Int. J. Polym. Sci. 2010 (2010). https://doi.org/10.1155/2010/296094.

[260] J.F. Mano, R.A. Sousa, L.F. Boesel, N.M. Neves, R.L. Reis, Bioinert, biodegradable and injectable

polymeric matrix composites for hard tissue replacement: State of the art and recent developments, Compos. Sci. Technol. 64 (2004) 789–817. https://doi.org/10.1016/j.compscitech.2003.09.001.

[261] Z. Ozdemir, A. Ozdemir, G.B. Basim, Application of chemical mechanical polishing process on titanium based implants, Mater. Sci. Eng. C. 68 (2016) 383–396. https://doi.org/10.1016/j.msec.2016.06.002.

[262] X. Lin, X. Xiao, Y. Wang, C. Gu, C. Wang, J. Chen, H. Liu, J. Luo, T. Li, D. Wang, S. Fan, Biocompatibility of Bespoke 3D-Printed Titanium Alloy Plates for Treating Acetabular Fractures, Biomed Res. Int. 2018 (2018). https://doi.org/10.1155/2018/2053486.

[263] R. Trombetta, J.A. Inzana, E.M. Schwarz, S.L. Kates, H.A. Awad, 3D Printing of Calcium Phosphate Ceramics for Bone Tissue Engineering and Drug Delivery, Ann. Biomed. Eng. 45 (2017) 23–44. https://doi.org/10.1007/s10439-016-1678-3.

[264] S. Singh, C. Prakash, S. Ramakrishna, 3D printing of polyether-ether-ketone for biomedical applications, Eur. Polym. J. 114 (2019) 234–248. https://doi.org/10.1016/j.eurpolymj.2019.02.035.

[265] H. Le Ferrand, F. Bouville, T.P. Niebel, A.R. Studart, Magnetically assisted slip casting of bioinspired heterogeneous composites, Nat. Mater. 14 (2015) 1172–1179. https://doi.org/10.1038/nmat4419.

[266] R.M. Erb, R. Libanori, N. Rothfuchs, A.R. Studart, Composites reinforced in three dimensions by using low magnetic fields, Science (80-.). 335 (2012) 199–204. https://doi.org/10.1126/SCIENCE.1210822.

[267] X. Ye, J. He, S. Wang, Q. Han, D. You, B. Feng, F. Zhao, J. Yin, M. Yu, H. Wang, H. Yang, A hierarchical vascularized engineered bone inspired by intramembranous ossification for mandibular regeneration, Int. J. Oral Sci. 14 (2022). https://doi.org/10.1038/s41368-022-00179-z.

[268] X. Fan, F. Wang, Q. Gao, Y. Zhang, F. Huang, R. Xiao, J. Qin, H. Zhang, X. Shi, G. Zhang, Nature inspired hierarchical structures in nano-cellular epoxy/graphene-Fe3O4 nanocomposites with ultra-efficient EMI and robust mechanical strength, J. Mater. Sci. Technol. 103 (2021) 177–185. https://doi.org/10.1016/j.jmst.2021.06.030.

[269] C. Feng, J. Xue, X. Yu, D. Zhai, R. Lin, M. Zhang, L. Xia, X. Wang, Q. Yao, J. Chang, C. Wu, Co-inspired hydroxyapatite-based scaffolds for vascularized bone regeneration, Acta Biomater. 119 (2021) 419–431. https://doi.org/10.1016/j.actbio.2020.11.010.

[270] X. Dong, B.W. Chua, T. Li, W. ZHAI, Multi-Directional Freeze Casting of Porous Ceramics with Bone-Inspired Microstructure, SSRN Electron. J. (2022). https://doi.org/10.2139/ssrn.4145564.

[271] Y. Shanjani, Y. Hu, R.M. Pilliar, E. Toyserkani, Mechanical characteristics of solid-freeform-fabricated porous calcium polyphosphate structures with oriented stacked layers, Acta Biomater. 7 (2011) 1788–1796. https://doi.org/10.1016/j.actbio.2010.12.017.

[272] R. Yunus Basha, S.K. Sampath, M. Doble, Design of biocomposite materials for bone tissue regeneration, Mater. Sci. Eng. C. 57 (2015) 452–463. https://doi.org/10.1016/j.msec.2015.07.016.

[273] A.G. Tsai, M.S. Reich, J. Bensusan, T. Ashworth, R.E. Marcus, O. Akkus, A fatigue loading model for investigation of iatrogenic subtrochanteric fractures of the femur, Clin. Biomech. 28 (2013) 981–987. https://doi.org/10.1016/j.clinbiomech.2013.09.009.

[274] Z. Gu, J. Fu, H. Lin, Y. He, Development of 3D bioprinting: From printing methods to biomedical applications, Asian J. Pharm. Sci. 15 (2020) 529–557. https://doi.org/10.1016/j.ajps.2019.11.003.

[275] M. Torre, S.M. Giannitelli, E. Mauri, M. Trombetta, A. Rainer, Additive manufacturing of biomaterials,

in: Adv. Chem. Eng., 2021: pp. 233–260. https://doi.org/10.1016/bs.ache.2021.03.003.

[276] J.A. Lewis, Direct ink writing of 3D functional materials, Adv. Funct. Mater. 16 (2006) 2193–2204. https://doi.org/10.1002/adfm.200600434.

[277] K.A. van Kampen, E. Olaret, I.C. Stancu, L. Moroni, C. Mota, Controllable four axis extrusion-based additive manufacturing system for the fabrication of tubular scaffolds with tailorable mechanical properties, Mater. Sci. Eng. C. 119 (2021). https://doi.org/10.1016/j.msec.2020.111472.

[278] J.A. Gardner, T. Nethercott-Garabet, N. Kaill, R.I. Campbell, G.A. Bingham, D.S. Engstrøm, N.O. Balc, Aligning material extrusion direction with mechanical stress via 5-axis tool paths, in: Solid Free. Fabr. 2018 Proc. 29th Annu. Int. Solid Free. Fabr. Symp. - An Addit. Manuf. Conf. SFF 2018, 2020: pp. 2005–2019.

[279] D. Lei, B. Luo, Y. Guo, D. Wang, H. Yang, S. Wang, H. Xuan, A. Shen, Y. Zhang, Z. Liu, C. He, F.L. Qing, Y. Xu, G. Zhou, Z. You, 4-Axis printing microfibrous tubular scaffold and tracheal cartilage application, Sci. China Mater. 62 (2019) 1910–1920. https://doi.org/10.1007/s40843-019-9498-5.

[280] S. Xiong, Y. Chen, W. Jia, X. Yang, K. Liu, C. Li, G. Ling, Optimization of the co-axial dispensing nozzle of a 3D bioprinter for the fabrication of tubular structures with micro-channel encapsulation, J. Micromechanics Microengineering. 31 (2021). https://doi.org/10.1088/1361-6439/abe09a.

[281] Q. Gao, Z. Liu, Z. Lin, J. Qiu, Y. Liu, A. Liu, Y. Wang, M. Xiang, B. Chen, J. Fu, Y. He, 3D Bioprinting of Vessel-like Structures with Multilevel Fluidic Channels, ACS Biomater. Sci. Eng. 3 (2017) 399–408. https://doi.org/10.1021/acsbiomaterials.6b00643.

[282] I. Holland, J. Logan, J. Shi, C. McCormick, D. Liu, W. Shu, 3D biofabrication for tubular tissue engineering, Bio-Design Manuf. 1 (2018) 89–100. https://doi.org/10.1007/s42242-018-0013-2.

[283] F. Zhang, K. Cao, A. Zaeri, R. Zgeib, C. Buckley, Y. Ma, R.C. Chang, Design, fabrication, and characterization of tubular scaffolds by way of a melt electrowriting process, Addit. Manuf. 62 (2023). https://doi.org/10.1016/j.addma.2022.103383.

[284] J.E. Smay, J. Cesarano, J.A. Lewis, Colloidal inks for directed assembly of 3-D periodic structures, Langmuir. 18 (2002) 5429–5437. https://doi.org/10.1021/la0257135.

[285] Q. Guo, R. Thomann, W. Gronski, R. Staneva, R. Ivanova, B. Stu, Nanostructures, semicrytalline morphology, and nanoscale confinement effect on the crystallization kinetics in self-organized block copolymer/thermoset blends, ACS Publ. 36 (2003) 3635–3645. https://doi.org/10.1021/ma0340154.

[286] A.A. Griffits, The phenomena of rupture and flow in solids, Masinovedenie. 4 (1995) 9–14. https://doi.org/10.1098/rsta.1921.0006.

[287] P. Christöfl, C. Czibula, T. Seidlhofer, M. Berer, A. Macher, E. Helfer, T. Schrank, G. Oreski, C. Teichert, G. Pinter, Morphological characterization of semi-crystalline POM using nanoindentation, Int. J. Polym. Anal. Charact. 26 (2021) 692–706. https://doi.org/10.1080/1023666X.2021.1968122.

[288] Y. Kong, J.N. Hay, The enthalpy of fusion and degree of crystallinity of polymers as measured by DSC, Eur. Polym. J. 39 (2003) 1721–1727. https://doi.org/10.1016/S0014-3057(03)00054-5.

[289] M. Doumeng, L. Makhlouf, F. Berthet, O. Marsan, K. Delbé, J. Denape, F. Chabert, A comparative study of the crystallinity of polyetheretherketone by using density, DSC, XRD, and Raman spectroscopy techniques, Polym. Test. 93 (2021). https://doi.org/10.1016/j.polymertesting.2020.106878.

[290] P. Sriamornsak, N. Thirawong, Use of back-scattered electron imaging as a tool for examining matrix structure of calcium pectinate, Int. J. Pharm. 267 (2003) 151–156. https://doi.org/10.1016/j.ijpharm.2003.08.005.

[291] J. Vlachopoulos, D.S.-N.T. for Extrusion, undefined 2003, The role of rheology in polymer extrusion, Polydynamics.Com. (n.d.).

[292] C.W. Macosko, Rheology Principles, Meas. Appl. (1994).

[293] Y. Bouligand, Twisted fibrous arrangements in biological materials and cholesteric mesophases, Tissue Cell. 4 (1972) 189–217. https://doi.org/10.1016/S0040-8166(72)80042-9.

[294] T. Li, J. Chang, Y. Zhu, C.W.-A.H. Materials, undefined 2020, 3D printing of bioinspired biomaterials for tissue regeneration, Wiley Online Libr. 9 (2020). https://doi.org/10.1002/adhm.202000208.

[295] I.T. Ozbolat, M. Hospodiuk, Current advances and future perspectives in extrusion-based bioprinting, Biomaterials. 76 (2016) 321–343. https://doi.org/10.1016/j.biomaterials.2015.10.076.

[296] D. Behera, A.K. Banthia, Synthesis, characterization, and kinetics study of thermal decomposition of epoxidized soybean oil acrylate, J. Appl. Polym. Sci. 109 (2008) 2583–2590. https://doi.org/10.1002/app.28350.

[297] T.W. Sun, Y.J. Zhu, F. Chen, F.F. Chen, Y.Y. Jiang, Y.G. Zhang, J. Wu, Ultralong hydroxyapatite nanowires/collagen scaffolds with hierarchical porous structure, enhanced mechanical properties and excellent cellular attachment, Ceram. Int. 43 (2017) 15747–15754. https://doi.org/10.1016/j.ceramint.2017.08.137.

[298] R.J. Kane, R.K. Roeder, Effects of hydroxyapatite reinforcement on the architecture and mechanical properties of freeze-dried collagen scaffolds, J. Mech. Behav. Biomed. Mater. 7 (2012) 41–49. https://doi.org/10.1016/j.jmbbm.2011.09.010.

[299] J.E. Trachtenberg, J.K. Placone, B.T. Smith, J.P. Fisher, A.G. Mikos, Extrusion-based 3D printing of poly(propylene fumarate) scaffolds with hydroxyapatite gradients, J. Biomater. Sci. Polym. Ed. 28 (2017) 532–554. https://doi.org/10.1080/09205063.2017.1286184.

[300] Q. Yao, B. Wei, Y. Guo, C. Jin, X. Du, C. Yan, J. Yan, W. Hu, Y. Xu, Z. Zhou, Y. Wang, L. Wang, Design, construction and mechanical testing of digital 3D anatomical data-based PCL–HA bone tissue engineering scaffold, J. Mater. Sci. Mater. Med. 26 (2015). https://doi.org/10.1007/s10856-014-5360-8.

[301] J.D. de Bruijn, C.P.A.T. Klein, K. de Groot, C.A. van Blitterswijk, The ultrastructure of the bone-hydroxyapatite interface in vitro, J. Biomed. Mater. Res. 26 (1992) 1365–1382. https://doi.org/10.1002/jbm.820261008.

[302] A.L. Rosa, M.M. Beloti, P.T. Oliveira, R. Van Noort, Osseointegration and osseoconductivity of hydroxyapatite of different microporosities, J. Mater. Sci. Mater. Med. 13 (2002) 1071–1075. https://doi.org/10.1023/A:1020305008042.

[303] T. Guo, J.P. Ringel, C.G. Lim, L.G. Bracaglia, M. Noshin, H.B. Baker, D.A. Powell, J.P. Fisher, Three dimensional extrusion printing induces polymer molecule alignment and cell organization within engineered cartilage, J. Biomed. Mater. Res. - Part A. 106 (2018) 2190–2199. https://doi.org/10.1002/jbm.a.36426.

[304] M. Spoerk, C. Holzer, J. Gonzalez-Gutierrez, Material extrusion-based additive manufacturing of polypropylene: A review on how to improve dimensional inaccuracy and warpage, J. Appl. Polym. Sci.

137 (2020). https://doi.org/10.1002/app.48545.

[305] L.A. Northcutt, S. V. Orski, K.B. Migler, A.P. Kotula, Effect of processing conditions on crystallization kinetics during materials extrusion additive manufacturing, Polym. (United Kingdom). 154 (2018) 182–187. https://doi.org/10.1016/j.polymer.2018.09.018.

[306] Z.M. Li, L. Li, K.Z. Shen, M.B. Yang, R. Huang, In situ poly(ethylene terephthalate) microfibers- and shear-induced non-isothermal crystallization of isotactic polypropylene by on-line small angle X-ray scattering, Polymer (Guildf). 46 (2005) 5358–5367. https://doi.org/10.1016/j.polymer.2005.04.016.

[307] A. Das, A.E.C. Marnot, J.J. Fallon, S.M. Martin, E.G. Joseph, M.J. Bortner, Material Extrusion-Based Additive Manufacturing with Blends of Polypropylene and Hydrocarbon Resins, ACS Appl. Polym. Mater. 2 (2020) 911–921. https://doi.org/10.1021/acsapm.9b01127.

[308] A.A. Griffits, The phenomena of rupture and flow in solids, Masinovedenie. (1995) 9–14. https://doi.org/10.1098/rsta.1921.0006.

[309] L.E. Nielsen, Cross-Linking–Effect on Physical Properties of Polymers, J. Macromol. Sci. Part C. 3 (1969) 69–103. https://doi.org/10.1080/15583726908545897.

[310] M.F. Drumm, C.W.H. Dodge, L.E. Nielsen, Cross Linking of a Phenol-Formaldehyde Novolac - Determiantion by Dynamic-Mechanical Measurements, Ind. Eng. Chem. 48 (1956) 76–81. https://doi.org/10.1021/ie50553a026.

[311] T.G. Fox, S. Loshaek, Influence of molecular weight and degree of crosslinking on the specific volume and glass temperature of polymers, J. Polym. Sci. 15 (1955) 371–390. https://doi.org/10.1002/pol.1955.120158006.

[312] T.A. Tip, Interpreting DSC curves; Part 2: Isothermal measurements, Interpreting. (2000) 1–20.

[313] M. Toft, The Effect of Crystalline Morphology on The Glass Transition and Enthalpic Relaxation in Poly (Ether-Ether-Ketone), 2011.

[314] Y. Zare, K.Y. Rhee, D. Hui, Influences of nanoparticles aggregation/agglomeration on the interfacial/interphase and tensile properties of nanocomposites, Compos. Part B Eng. 122 (2017) 41–46. https://doi.org/10.1016/j.compositesb.2017.04.008.

[315] V. Campana, G. Milano, E. Pagano, M. Barba, C. Cicione, G. Salonna, W. Lattanzi, G. Logroscino, Bone substitutes in orthopaedic surgery: from basic science to clinical practice, J. Mater. Sci. Mater. Med. 25 (2014) 2445–2461. https://doi.org/10.1007/s10856-014-5240-2.

[316] M.F. Moreau, Y. Gallois, M.F. Baslé, D. Chappard, Gamma irradiation of human bone allografts alters medullary lipids and releases toxic compounds for osteoblast-like cells, Biomaterials. 21 (2000) 369–376. https://doi.org/10.1016/S0142-9612(99)00193-3.

[317] J.S. Silber, D.G. Anderson, S.D. Daffner, B.T. Brislin, J.M. Leland, A.S. Hilibrand, A.R. Vaccaro, T.J. Albert, Donor site morbidity after anterior iliac crest bone harvest for single-level anterior cervical discectomy and fusion, Spine (Phila. Pa. 1976). 28 (2003) 134–139. https://doi.org/10.1097/00007632-200301150-00008.

[318] J.D. Currey, Hierarchies in biomineral structures, Science (80-.). 309 (2005) 253–254. https://doi.org/10.1126/science.1113954.

[319] O.A. Tertuliano, J.R. Greer, The nanocomposite nature of bone drives its strength and damage resistance,

Nat. Mater. 15 (2016) 1195–1202. https://doi.org/10.1038/nmat4719.

[320] M.A. Meyers, J. McKittrick, P.-Y. Chen, Structural biological materials: critical mechanics-materials connections, Science. 339 (2013) 773–779. https://doi.org/10.1126/science.1220854.

[321] H. Gao, B. Ji, I.L. Jäger, E. Arzt, P. Fratzl, Materials become insensitive to flaws at nanoscale: Lessons from nature, Proc. Natl. Acad. Sci. U. S. A. 100 (2003) 5597–5600. https://doi.org/10.1073/pnas.0631609100.

[322] L. Cheng, K. Shoma Suresh, H. He, R.S. Rajput, Q. Feng, S. Ramesh, Y. Wang, S. Krishnan, S. Ostrovidov, G. Camci-Unal, M. Ramalingam, 3d printing of micro-and nanoscale bone substitutes: A review on technical and translational perspectives, Int. J. Nanomedicine. 16 (2021) 4289–4319. https://doi.org/10.2147/IJN.S311001.

[323] Z. Gu, J. Fu, H. Lin, Y. He, Development of 3D bioprinting: From printing methods to biomedical applications, Asian J. Pharm. Sci. 15 (2020) 529–557. https://doi.org/10.1016/j.ajps.2019.11.003.

[324] L. Ouyang, C.B. Highley, W. Sun, J.A. Burdick, A Generalizable Strategy for the 3D Bioprinting of Hydrogels from Nonviscous Photo-crosslinkable Inks, Adv. Mater. 29 (2017). https://doi.org/10.1002/adma.201604983.

[325] G. Gao, A.F. Schilling, K. Hubbell, T. Yonezawa, D. Truong, Y. Hong, G. Dai, X. Cui, Improved properties of bone and cartilage tissue from 3D inkjet-bioprinted human mesenchymal stem cells by simultaneous deposition and photocrosslinking in PEG-GelMA, Biotechnol. Lett. 37 (2015) 2349–2355. https://doi.org/10.1007/s10529-015-1921-2.

[326] X. Cui, K. Breitenkamp, M.G. Finn, M. Lotz, D.D. D'Lima, Direct human cartilage repair using three-dimensional bioprinting technology, Tissue Eng. - Part A. 18 (2012) 1304–1312. https://doi.org/10.1089/ten.tea.2011.0543.

[327] B. Huber, K. Borchers, G.E.M. Tovar, P.J. Kluger, Methacrylated gelatin and mature adipocytes are promising components for adipose tissue engineering, J. Biomater. Appl. 30 (2016) 699–710. https://doi.org/10.1177/0885328215587450.

[328] S. Knowlton, B. Yenilmez, S. Anand, S. Tasoglu, Photocrosslinking-based bioprinting: Examining crosslinking schemes, Bioprinting. 5 (2017) 10–18. https://doi.org/10.1016/j.bprint.2017.03.001.

[329] C. Yang, J. Li, C. Zhu, Q. Zhang, J. Yu, J. Wang, Q. Wang, J. Tang, H. Zhou, H. Shen, Advanced antibacterial activity of biocompatible tantalum nanofilm via enhanced local innate immunity, Acta Biomater. 89 (2019) 403–418. https://doi.org/10.1016/j.actbio.2019.03.027.

[330] A.E. Jakus, A.L. Rutz, S.W. Jordan, A. Kannan, S.M. Mitchell, C. Yun, K.D. Koube, S.C. Yoo, H.E. Whiteley, C.P. Richter, R.D. Galiano, W.K. Hsu, S.R. Stock, E.L. Hsu, R.N. Shah, Hyperelastic "bone": A highly versatile, growth factor-free, osteoregenerative, scalable, and surgically friendly biomaterial, Sci. Transl. Med. 8 (2016). https://doi.org/10.1126/scitranslmed.aaf7704.

[331] S.H. Lee, H. Shin, Matrices and scaffolds for delivery of bioactive molecules in bone and cartilage tissue engineering, Adv. Drug Deliv. Rev. 59 (2007) 339–359. https://doi.org/10.1016/j.addr.2007.03.016.

[332] E.J. Anderson, M.L. Knothe Tate, Design of tissue engineering scaffolds as delivery devices for mechanical and mechanically modulated signals, Tissue Eng. 13 (2007) 2525–2538. https://doi.org/10.1089/ten.2006.0443.

[333] K. Parratt, N. Yao, Nanostructured Biomaterials and Their Applications, Nanomaterials. 3 (2013) 242–

271. https://doi.org/10.3390/nano3020242.

[334] J. Jeevanandam, A. Barhoum, Y.S. Chan, A. Dufresne, M.K. Danquah, Review on nanoparticles and nanostructured materials: History, sources, toxicity and regulations, Beilstein J. Nanotechnol. 9 (2018) 1050–1074. https://doi.org/10.3762/bjnano.9.98.

[335] R.L. Yang, Y.J. Zhu, F.F. Chen, D.D. Qin, Z.C. Xiong, Bioinspired Macroscopic Ribbon Fibers with a Nacre-Mimetic Architecture Based on Highly Ordered Alignment of Ultralong Hydroxyapatite Nanowires, ACS Nano. 12 (2018) 12284–12295. https://doi.org/10.1021/acsnano.8b06096.

[336] F. Chen, Y.J. Zhu, Large-Scale Automated Production of Highly Ordered Ultralong Hydroxyapatite Nanowires and Construction of Various Fire-Resistant Flexible Ordered Architectures, ACS Nano. 10 (2016) 11483–11495. https://doi.org/10.1021/acsnano.6b07239.

[337] C. Yu, W. Zhu, B. Sun, D. Mei, M. Gou, S. Chen, Modulating physical, chemical, and biological properties in 3D printing for tissue engineering applications, Appl. Phys. Rev. 5 (2018). https://doi.org/10.1063/1.5050245.

[338] Y. Yang, Q. Zhang, T. Xu, H. Zhang, M. Zhang, L. Lu, Y. Hao, J.Y.H. Fuh, X. Zhao, Photocrosslinkable nanocomposite ink for printing strong, biodegradable and bioactive bone graft, Biomaterials. 263 (2020). https://doi.org/10.1016/j.biomaterials.2020.120378.

[339] A. Bhattacharyya, G. Janarthanan, I. Noh, Nano-biomaterials for designing functional bioinks towards complex tissue and organ regeneration in 3D bioprinting, Addit. Manuf. 37 (2021). https://doi.org/10.1016/j.addma.2020.101639.

[340] A. Zengin, J.P.O. Castro, P. Habibovic, S.H. Van Rijt, Injectable, self-healing mesoporous silica nanocomposite hydrogels with improved mechanical properties, Nanoscale. 13 (2021) 1144–1154. https://doi.org/10.1039/d0nr07406c.

[341] J. Liu, Q. Dai, M.D. Weir, A. Schneider, C. Zhang, G.D. Hack, T.W. Oates, K. Zhang, A. Li, H.H.K. Xu, Biocompatible nanocomposite enhanced osteogenic and cementogenic differentiation of periodontal ligament stem cells in vitro for periodontal regeneration, Materials (Basel). 13 (2020) 1–22. https://doi.org/10.3390/ma13214951.

[342] D. Rana, T.S.S. Kumar, M. Ramalingam, Impact of nanotechnology on 3D bioprinting, J. Bionanoscience. 11 (2017) 1–6. https://doi.org/10.1166/jbns.2017.1417.

[343] A. Bhatt, A. Anbarasu, Nanoscale Biomaterials for 3D printing, IOSR J. Pharm. Biol. Sci. 12 (2017) 80–86. https://doi.org/10.9790/3008-1203068086.

[344] P. Fucile, I. Onofrio, I. Papallo, V. Gallicchio, A. Rega, V. D'Antò, G. Improta, R. de Santis, A. Gloria, T. Russo, Strategies for the design of additively manufactured nanocomposite scaffolds for hard tissue regeneration, Acta IMEKO. 9 (2020) 53–59. https://doi.org/10.21014/acta_imeko.v9i4.739.

[345] M. Domingos, F. Chiellini, A. Gloria, L. Ambrosio, P. Bartolo, E. Chiellini, Effect of process parameters on the morphological and mechanical properties of 3D Bioextruded poly(1-caprolactone) scaffolds, Rapid Prototyp. J. 18 (2012) 56–67. https://doi.org/10.1108/13552541211193502.

[346] S.C. Mauck, S. Wang, W. Ding, B.J. Rohde, C.K. Fortune, G. Yang, S.K. Ahn, M.L. Robertson, Biorenewable Tough Blends of Polylactide and Acrylated Epoxidized Soybean Oil Compatibilized by a Polylactide Star Polymer, Macromolecules. 49 (2016) 1605–1615. https://doi.org/10.1021/acs.macromol.5b02613.

[347] A. Khan, M.H. Shamsi, T.S. Choi, Correlating dynamical mechanical properties with temperature and clay composition of polymer-clay nanocomposites, Comput. Mater. Sci. 45 (2009) 257–265. https://doi.org/10.1016/j.commatsci.2008.09.027.

[348] J. Chen, Y. Yu, J. Chen, H. Li, J. Ji, D. Liu, Chemical modification of palygorskite with maleic anhydride modified polypropylene: Mechanical properties, morphology, and crystal structure of palygorskite/polypropylene nanocomposites, Appl. Clay Sci. 115 (2015) 230–237. https://doi.org/10.1016/j.clay.2015.07.012.

[349] Y.T. Huang, M. Imura, Y. Nemoto, C.H. Cheng, Y. Yamauchi, Block-copolymer-assisted synthesis of hydroxyapatite nanoparticles with high surface area and uniform size, Sci. Technol. Adv. Mater. 12 (2011) 45005. https://doi.org/10.1088/1468-6996/12/4/045005.

[350] A.S.M. Mohd Zaffarin, S.-F. Ng, M.H. Ng, H. Hassan, E. Alias, Nano-Hydroxyapatite as a Delivery System for Promoting Bone Regeneration In Vivo: A Systematic Review, Nanomaterials. 11 (2021) 2569. https://doi.org/10.3390/nano11102569.

[351] O.Y. Rogulska, N.A. Trufanova, Y.A. Petrenko, N. V. Repin, V.P. Grischuk, N.O. Ashukina, S.Y. Bondarenko, G. V. Ivanov, E.A. Podorozhko, V.I. Lozinsky, A.Y. Petrenko, Generation of bone grafts using cryopreserved mesenchymal stromal cells and macroporous collagen-nanohydroxyapatite cryogels, J. Biomed. Mater. Res. - Part B Appl. Biomater. (2021). https://doi.org/10.1002/jbm.b.34927.

[352] D. Slota, M. Gląb, B. Tyliszczak, T.E.L. Dogulas, K. Rudnicka, K. Miernik, M.M. Urbaniak, P. Rusek-Wala, A. Sobczak-upiec, Composites based on hydroxyapatite and whey protein isolate for applications in bone regeneration, Materials (Basel). 14 (2021). https://doi.org/10.3390/ma14092317.

[353] H. Song, Y. Zhang, Z. Zhang, S. Xiong, X. Ma, Y. Li, Hydroxyapatite/nell-1 nanoparticles electrospun fibers for osteoinduction in bone tissue engineering application, Int. J. Nanomedicine. 16 (2021) 4321–4332. https://doi.org/10.2147/IJN.S309567.

[354] Q. Liu, J.R. De Wijn, K. De Groot, C.A. Van Blitterswijk, Surface modification of nano-apatite by grafting organic polymer, Biomaterials. 19 (1998) 1067–1072. https://doi.org/10.1016/S0142-9612(98)00033-7.

[355] A.J. Crosby, J.Y. Lee, Polymer nanocomposites: The "nano" effect on mechanical properties, Polym. Rev. 47 (2007) 217–229. https://doi.org/10.1080/15583720701271278.

[356] S. Saadatmand Hashemi, D. Mondal, H. Patil, J. Montesano, T.L. Willett, Effect of Increased Shear during Extrusion-Based 3D Printing on the Mechanical Properties of 3D Printable Nanocomposite Biomaterials, Compos. Part B Eng. Submitted (2022).

[357] S.S. Hashemi, M. Asgari, A. Rasoulian, An experimental study of nonlinear rate-dependent behaviour of skeletal muscle to obtain passive mechanical properties, Proc. Inst. Mech. Eng. Part H J. Eng. Med. 234 (2020) 590–602. https://doi.org/10.1177/0954411920909705.

[358] M.D. Abràmoff, P.J. Magalhães, S.J. Ram, Image processing with imageJ, Biophotonics Int. 11 (2004) 36–41. https://doi.org/10.1201/9781420005615.ax4.

[359] B.M. Cromer, E.B. Coughlin, A.J. Lesser, Evaluation of a new processing method for improved nanocomposite dispersions, Nanocomposites. 1 (2015) 152–159. https://doi.org/10.1179/2055033215Y.0000000009.

[360] S.R. Gallagher, Digital image processing and analysis with imagej, Curr. Protoc. Essent. Lab. Tech. 2014 (2014) A.3C.1-A.3C.29. https://doi.org/10.1002/9780470089941.eta03cs9.

[361] S.J. Underwood, J.M. Gorham, Challenges and approaches for particle size analysis on micrographs of nanoparticles loaded onto textile surfaces, NIST Spec. Publ. 1200-22. (2017) 13. https://doi.org/10.6028/NIST.SP.1200-22.

[362] G. J., A. C. H., R.B. M., Automatic detection and counting of Callosobruchus maculatus (Fab.) Eggs on Vigna radiata seeds, using ImageJ, J. Appl. Biol. Biotechnol. (2021). https://doi.org/10.7324/jabb.2021.9219.

[363] H. Elias, Macromolecules· 1: Volume 1: Structure and Properties, 2012.

[364] T. Attia, M. Grynpas, T. Willett, Ribose pre-treatment can protect the fatigue life of γ-irradiation sterilized bone, Cell Tissue Bank. 20 (2019) 287–295. https://doi.org/10.1007/s10561-019-09767-6.

[365] N. Dunne, Mechanical properties of bone cements, in: Orthop. Bone Cem., 2008: pp. 233–264. https://doi.org/10.1533/9781845695170.3.233.

[366] R.Y. Hong, Q. Chen, Dispersion of inorganic nanoparticles in polymer matrices: Challenges and solutions, Adv. Polym. Sci. 267 (2014) 1–38. https://doi.org/10.1007/12_2014_286.

[367] A. Dorigato, Y. Dzenis, A. Pegoretti, Filler aggregation as a reinforcement mechanism in polymer nanocomposites, Mech. Mater. 61 (2013) 79–90. https://doi.org/10.1016/j.mechmat.2013.02.004.

[368] Y. Hu, Y. Shao, Z. Liu, X. He, B. Liu, Effect of short-chain branching on the tie chains and dynamics of bimodal polyethylene: Molecular dynamics simulation, Eur. Polym. J. 103 (2018) 312–321. https://doi.org/10.1016/j.eurpolymj.2018.01.006.

[369] M.A. Kennedy, A.J. Peacock, M.D. Failla, J.C. Lucas, L. Mandelkern, Tensile Properties of Crystalline Polymers: Random Copolymers of Ethylene, Macromolecules. 28 (1995) 1407–1421. https://doi.org/10.1021/ma00109a012.

[370] D.T. Gentekos, R.J. Sifri, B.P. Fors, Controlling polymer properties through the shape of the molecular-weight distribution, Nat. Rev. Mater. 4 (2019) 761–774. https://doi.org/10.1038/s41578-019-0138-8.

[371] T. Kida, T. Kimura, A. Eno, K. Janchai, M. Yamaguchi, Y. Otsuki, T. Kimura, T. Mizukawa, T. Murakami, K. Hato, T. Okawa, Effect of ultra-high-molecular-weight molecular chains on the morphology, crystallization, and mechanical properties of polypropylene, Polymers (Basel). 13 (2021). https://doi.org/10.3390/polym13234222.

[372] F.G. Hamad, R.H. Colby, S.T. Milner, Onset of Flow-Induced Crystallization Kinetics of Highly Isotactic Polypropylene, Macromolecules. 48 (2015) 3725–3738. https://doi.org/10.1021/acs.macromol.5b00386.

[373] O.O. Mykhaylyk, P. Chambon, C. Impradice, J.P.A. Fairclough, N.J. Terrill, A.J. Ryan, Control of structural morphology in shear-induced crystallization of polymers, Macromolecules. 43 (2010) 2389–2405. https://doi.org/10.1021/ma902495z.

[374] J.M. Sadler, A.P.T. Nguyen, F.R. Toulan, J.P. Szabo, G.R. Palmese, C. Scheck, S. Lutgen, J.J. La Scala, Isosorbide-methacrylate as a bio-based low viscosity resin for high performance thermosetting applications, J. Mater. Chem. A. 1 (2013) 12579–12586. https://doi.org/10.1039/c3ta12918g.

[375] N. Mohd, M. Razali, M. Ghazali, N.A.K.- Materials, undefined 2022, 3D-Printed Hydroxyapatite and Tricalcium Phosphates-Based Scaffolds for Alveolar Bone Regeneration in Animal Models: A Scoping Review, Mdpi.Com. (2022). https://doi.org/10.3390/ma15072621.

[376] H.Y. Ahmed, N. Safwat, R. Shehata, E. Hillal Althubaiti, S. Kareem, A. Atef, S.H. Qari, A.H. Aljahani,

A. Suliman Al-Meshal, M. Youssef, R. Sami, Synthesis of Natural Nano-Hydroxyapatite from Snail Shells and Its Biological Activity: Antimicrobial, Antibiofilm, and Biocompatibility, Mdpi.Com. 12 (2022). https://doi.org/10.3390/membranes12040408.

[377] A. Szcześ, L. Hołysz, E. Chibowski, Synthesis of hydroxyapatite for biomedical applications, Adv. Colloid Interface Sci. 249 (2017) 321–330. https://doi.org/10.1016/j.cis.2017.04.007.

[378] J. Lu, H. Yu, C. Chen, Biological properties of calcium phosphate biomaterials for bone repair: A review, RSC Adv. 8 (2018) 2015–2033. https://doi.org/10.1039/c7ra11278e.

[379] W. Habraken, P. Habibovic, M. Epple, M. Bohner, Calcium phosphates in biomedical applications: Materials for the future?, Mater. Today. 19 (2016) 69–87. https://doi.org/10.1016/j.mattod.2015.10.008.

[380] L.L. Hench, Bioceramics: From Concept to Clinic, J. Am. Ceram. Soc. 74 (1991) 1487–1510. https://doi.org/10.1111/j.1151-2916.1991.tb07132.x.

[381] N. Tran, T.J. Webster, Nanotechnology for bone materials, Wiley Interdiscip. Rev. Nanomedicine Nanobiotechnology. 1 (2009) 336–351. https://doi.org/10.1002/wnan.23.

[382] T.J. Webster, C. Ergun, R.H. Doremus, R.W. Siegel, R. Bizios, Enhanced functions of osteoblasts on nanophase ceramics, Biomaterials. 21 (2000) 1803–1810. https://doi.org/10.1016/S0142-9612(00)00075-2.

[383] N. Reznikov, M. Bilton, L. Lari, M.M. Stevens, R. Kröger, Fractal-like hierarchical organization of bone begins at the nanoscale, Science (80-.). 360 (2018). https://doi.org/10.1126/science.aao2189.

[384] W.J. Landis, M.J. Song, A. Leith, L. McEwen, B.F. McEwen, Mineral and organic matrix interaction in normally calcifying tendon visualized in three dimensions by high-voltage electron microscopic tomography and graphic image reconstruction, J. Struct. Biol. 110 (1993) 39–54. https://doi.org/10.1006/jsbi.1993.1003.

[385] E.A. McNally, H.P. Schwarcz, G.A. Botton, A.L. Arsenault, A model for the ultrastructure of bone based on electron microscopy of ion-milled sections, PLoS One. 7 (2012). https://doi.org/10.1371/journal.pone.0029258.

[386] G. Ruphuy, T. Weide, J.C.B. Lopes, M.M. Dias, M.F. Barreiro, Preparation of nano-hydroxyapatite/chitosan aqueous dispersions: From lab scale to continuous production using an innovative static mixer, Carbohydr. Polym. 202 (2018) 20–28. https://doi.org/10.1016/j.carbpol.2018.08.123.

[387] S. Kang, A. Haider, K.C. Gupta, H. Kim, I. Kang, Chemical Bonding of Biomolecules to the Surface of Nano-Hydroxyapatite to Enhance Its Bioactivity, Coatings. 12 (2022). https://doi.org/10.3390/coatings12070999.

[388] M.S. Islam, M. Todo, Effects of sintering temperature on the compressive mechanical properties of collagen/hydroxyapatite composite scaffolds for bone tissue engineering, Mater. Lett. 173 (2016) 231–234. https://doi.org/10.1016/j.matlet.2016.03.028.

[389] S. Tabassum, Role of substitution in bioceramics, in: Handb. Ion. Substituted Hydroxyapatites, Woodhead Publishing, 2019: pp. 117–148. https://doi.org/10.1016/B978-0-08-102834-6.00005-7.

[390] J. Chen, B. Liu, X. Gao, D. Xu, A review of the interfacial characteristics of polymer nanocomposites containing carbon nanotubes, RSC Adv. 8 (2018) 28048–28085. https://doi.org/10.1039/c8ra04205e.

[391] Y.Z.-C.P.A.A.S. and, undefined 2016, Study of nanoparticles aggregation/agglomeration in polymer

particulate nanocomposites by mechanical properties, Elsevier. (n.d.).

[392] Y. Zare, H. Garmabi, F. Sharif, Optimization of mechanical properties of PP/Nanoclay/CaCO3 ternary nanocomposite using response surface methodology, J. Appl. Polym. Sci. 122 (2011) 3188–3200. https://doi.org/10.1002/app.34378.

[393] Y. Zare, H. Garmabi, Nonisothermal crystallization and melting behavior of PP/nanoclay/CaCO 3 ternary nanocomposite, J. Appl. Polym. Sci. 124 (2012) 1225–1233. https://doi.org/10.1002/app.35134.

[394] G.S. Martynková, K. Cech Barabaszova, M. Šupová, G. Simha Martynková, K. Barabaszová, Effect of nanofillers dispersion in polymer matrices: a review, Ingentaconnect.Com. 3 (2010) 1–25. https://doi.org/10.1166/sam.2011.1136.

[395] L. Casarrubios, M.C. Matesanz, S. Sánchez-Salcedo, D. Arcos, M. Vallet-Regí, M.T. Portolés, Nanocrystallinity effects on osteoblast and osteoclast response to silicon substituted hydroxyapatite, J. Colloid Interface Sci. 482 (2016) 112–120. https://doi.org/10.1016/j.jcis.2016.07.075.

[396] D. Mondal, T.L. Willett, Enhanced mechanical performance of mSLA-printed biopolymer nanocomposites due to phase functionalization, J. Mech. Behav. Biomed. Mater. 135 (2022). https://doi.org/10.1016/j.jmbbm.2022.105450.

[397] P. Comeau, T. Willett, Impact of Side Chain Polarity on Non-Stoichiometric Nano-Hydroxyapatite Surface Functionalization with Amino Acids, Sci. Rep. 8 (2018) 12700. https://doi.org/10.1038/s41598-018-31058-5.

[398] J. Zhang, Z. Jia, D. Jia, D. Zhang, A. Zhang, Chemical functionalization for improving dispersion and interfacial bonding of halloysite nanotubes in epoxy nanocomposites, High Perform. Polym. 26 (2014) 734–743. https://doi.org/10.1177/0954008314528226.

[399] W. Zou, Z. jie Du, Y. xin Liu, X. Yang, H. quan Li, C. Zhang, Functionalization of MWNTs using polyacryloyl chloride and the properties of CNT-epoxy matrix nanocomposites, Compos. Sci. Technol. 68 (2008) 3259–3264. https://doi.org/10.1016/j.compscitech.2008.08.011.

[400] W.L. Tham, W.S. Chow, Z.A.M. Ishak, The effect of 3-(trimethoxysilyl) propyl methacrylate on the mechanical, thermal, and morphological properties of poly(methyl methacrylate)/ hydroxyapatite composites, J. Appl. Polym. Sci. 118 (2010) 218–228. https://doi.org/10.1002/app.32111.

[401] O.G. Cisneros-Pineda, W. Herrera Kao, M.I. Loría-Bastarrachea, Y. Veranes-Pantoja, J. V. Cauich-Rodríguez, J.M. Cervantes-Uc, Towards optimization of the silanization process of hydroxyapatite for its use in bone cement formulations, Mater. Sci. Eng. C. 40 (2014) 157–163. https://doi.org/10.1016/j.msec.2014.03.064.

[402] A. Hussein, S. Ramasundaram, B. Kim, A novel method for fabricating bioinspired layered nanocomposites using aligned graphene oxide/PVDF and their micromechanical modeling, Mater. Today Commun. 24 (2020). https://doi.org/10.1016/j.mtcomm.2020.101050.

[403] G. Kickelbick, Hybrid materials: synthesis, characterization, and applications, 2007.

[404] M. Šupová, G.S. Martynková, K. Barabaszová, Effect of nanofillers dispersion in polymer matrices: A review, Sci. Adv. Mater. 3 (2011) 1–25. https://doi.org/10.1166/sam.2011.1136.

[405] P. Feng, S. Peng, C. Shuai, C. Gao, W. Yang, S. Bin, A. Min, In situ generation of hydroxyapatite on biopolymer particles for fabrication of bone scaffolds owning bioactivity, ACS Publ. 12 (2020) 46755. https://doi.org/10.1021/acsami.0c13768.

[406] R. Sun, L. Li, H. Zhang, J.Y.-P. Composites, undefined 2020, Effect of hydrogen functionalization on interfacial behavior of defective-graphene/polymer nanocomposites, Wiley Online Libr. 41 (2019) 1291–1298. https://doi.org/10.1002/pc.25454.

[407] W. Zou, Z. Du, Y. Liu, X. Yang, H. Li, C.Z.-C.S. and, undefined 2008, Functionalization of MWNTs using polyacryloyl chloride and the properties of CNT–epoxy matrix nanocomposites, Elsevier. (n.d.).

[408] J. Cha, J. Kim, S. Ryu, S.H.-C.P.B. Engineering, undefined 2019, Comparison to mechanical properties of epoxy nanocomposites reinforced by functionalized carbon nanotubes and graphene nanoplatelets, Elsevier. (n.d.).

[409] G. Balasundaram, M. Sato, T.J. Webster, Using hydroxyapatite nanoparticles and decreased crystallinity to promote osteoblast adhesion similar to functionalizing with RGD, Biomaterials. 27 (2006) 2798–2805. https://doi.org/10.1016/j.biomaterials.2005.12.008.

[410] S. Wang, S. Wen, M. Shen, R. Guo, X. Cao, J. Wang, X. Shi, Aminopropyltriethoxysilane-mediated surface functionalization of hydroxyapatite nanoparticles: synthesis, characterization, and in vitro toxicity assay., Int. J. Nanomedicine. 6 (2011) 3449–3459.

[411] S. Rehman, K. Khan, M. Mujahid, S. Nosheen, Synthesis of nano-hydroxyapatite and its rapid mediated surface functionalization by silane coupling agent, Mater. Sci. Eng. C. 58 (2016) 675–681. https://doi.org/10.1016/j.msec.2015.09.014.

[412] S. Yadav, S. Gangwar, An Investigation of Experimental Dental Restorative Composites Filled with Nano-Hydroxyapatite Treated with Different Silanes, Silicon. 13 (2021) 1127–1137. https://doi.org/10.1007/s12633-020-00502-5.

[413] A. Buasri, N. Chaiyut, C. Kritsanakun, C. Phatkun, T. Khunsri, Preparation and properties of nanocomposites based on poly (lactic acid) and modified TiO 2, in: Adv. Mater. Res., 2012: pp. 519–522. https://doi.org/10.4028/www.scientific.net/AMR.463-464.519.

[414] J. Ha, Y. Song, N. Song, J.S. Yun, D. Lee, Designing an interpenetrating network of silane-functionalized nanocomposites for enhanced particle dispersity and interfacial bonding strength, Ceram. Int. 48 (2022) 1827–1835. https://doi.org/10.1016/j.ceramint.2021.09.264.

[415] M.C. Rodrigues, T.A. Xavier, V.E. Arana-Chavez, R.R. Braga, Polymer-based material containing calcium phosphate particles functionalized with a dimethacrylate monomer for use in restorative dentistry, J. Biomater. Appl. 31 (2017) 871–877. https://doi.org/10.1177/0885328216680116.

[416] E.H. Alosaimi, I. Hotan Alsohaimi, H. M. A. Hassan, Q. Chen, S. Melhi, A. Abdelaziz Younes, Towards superior permeability and antifouling performance of sulfonated polyethersulfone ultrafiltration membranes modified with sulfopropyl methacrylate functionalized SBA-15, Chinese J. Chem. Eng. 53 (2023) 89–100. https://doi.org/10.1016/J.CJCHE.2021.09.019.

[417] B. Safaei, R. Moradi-Dastjerdi, Z. Qin, F. Chu, Frequency-dependent forced vibration analysis of nanocomposite sandwich plate under thermo-mechanical loads, Compos. Part B Eng. 161 (2019) 44–54. https://doi.org/10.1016/j.compositesb.2018.10.049.

[418] F. Ebrahimi, A. Seyfi, Wave dispersion analysis of embedded MWCNTs-reinforced nanocomposite beams by considering waviness and agglomeration factors, Waves in Random and Complex Media. (2021). https://doi.org/10.1080/17455030.2021.1883148.

[419] R. Shokri-Oojghaz, R. Moradi-Dastjerdi, H. Mohammadi, K. Behdinan, Stress distributions in

nanocomposite sandwich cylinders reinforced by aggregated carbon nanotube, Polym. Compos. 40 (2019) E1918–E1927. https://doi.org/10.1002/pc.25206.

[420] S. Lee, J. Jung, S. Ryu, Applicability of interface spring and interphase models in micromechanics for predicting effective stiffness of polymer-matrix nanocomposite, Extrem. Mech. Lett. 49 (2021) 101489. https://doi.org/10.1016/j.eml.2021.101489.

[421] Y. Zare, K.Y. Rhee, A Simulation Work for the Influences of Aggregation/Agglomeration of Clay Layers on the Tensile Properties of Nanocomposites, JOM. 71 (2019) 3989–3995. https://doi.org/10.1007/s11837-019-03768-2.

[422] S. Mohanty, S.K. Nayak, Effect of clay exfoliation and organic modification on morphological, dynamic mechanical, and thermal behavior of melt-compounded polyamide-6 nanocomposites, Polym. Compos. 28 (2007) 153–162. https://doi.org/10.1002/pc.20284.

[423] A.R. Annappa, S. Basavarajappa, J.P. Davim, Effect of organoclays on mechanical properties of glass fiber-reinforced epoxy nanocomposite, Polym. Bull. 79 (2022) 5085–5103. https://doi.org/10.1007/s00289-021-03759-x.

[424] Y.W. Mai, Z.Z. Yu, Polymer nanocomposites, 2006. https://doi.org/10.1016/b978-0-08-100037-3.00008-0.

[425] R. Krishnamoorti, R.A. Vaia, Polymer nanocomposites, J. Polym. Sci. Part B Polym. Phys. 45 (2007) 3252–3256. https://doi.org/10.1002/polb.21319.

[426] C. Zhan, G. Yu, Y. Lu, L. Wang, E. Wujcik, S. Wei, Conductive polymer nanocomposites: a critical review of modern advanced devices, J. Mater. Chem. C. 5 (2017) 1569–1585. https://doi.org/10.1039/c6tc04269d.

[427] S. Fu, Z. Sun, P. Huang, Y. Li, N. Hu, Some basic aspects of polymer nanocomposites: A critical review, Nano Mater. Sci. 1 (2019) 2–30. https://doi.org/10.1016/j.nanoms.2019.02.006.

[428] E. Reynaud, C. Gauthier, J. Perez, Nanophases in polymers, Rev. Metall. Cah. D'Informations Tech. 96 (1999) 169–176. https://doi.org/10.1051/metal/199996020169.

[429] J. Mehta, P.P. Das, S. Mehta, V. Chaudhary, S. Gupta, N. Gupta, M.L. Rinawa, P. Gupta, Effect of nanofillers and nanotoxicity on the performance of composites: Influencing factors, future scope, challenges and applications, Polym. Compos. 43 (2022) 3335–3349. https://doi.org/10.1002/pc.26635.

[430] M. Naffakh, A.M. Díez-Pascual, C. Marco, G.J. Ellis, M.A. Gómez-Fatou, Opportunities and challenges in the use of inorganic fullerene-like nanoparticles to produce advanced polymer nanocomposites, Prog. Polym. Sci. 38 (2013) 1163–1231. https://doi.org/10.1016/j.progpolymsci.2013.04.001.

[431] A. Kausar, I. Rafique, B. Muhammad, Aerospace Application of Polymer Nanocomposite with Carbon Nanotube, Graphite, Graphene Oxide, and Nanoclay, Polym. - Plast. Technol. Eng. 56 (2017) 1438–1456. https://doi.org/10.1080/03602559.2016.1276594.

[432] S.Y. Fu, X.Q. Feng, B. Lauke, Y.W. Mai, Effects of particle size, particle/matrix interface adhesion and particle loading on mechanical properties of particulate-polymer composites, Compos. Part B Eng. 39 (2008) 933–961. https://doi.org/10.1016/j.compositesb.2008.01.002.

[433] M.K. Hausmann, P.A. Rühs, G. Siqueira, J. Läuger, R. Libanori, T. Zimmermann, A.R. Studart, Dynamics of Cellulose Nanocrystal Alignment during 3D Printing, ACS Nano. 12 (2018) 6926–6937. https://doi.org/10.1021/acsnano.8b02366.

[434] G. Siqueira, D. Kokkinis, R. Libanori, M.K. Hausmann, A.S. Gladman, A. Neels, P. Tingaut, T. Zimmermann, J.A. Lewis, A.R. Studart, Cellulose Nanocrystal Inks for 3D Printing of Textured Cellular Architectures, Adv. Funct. Mater. 27 (2017). https://doi.org/10.1002/adfm.201604619.

[435] H. Jahandideh, J.R. Macairan, A. Bahmani, M. Lapointe, N. Tufenkji, Fabrication of graphene-based porous materials: traditional and emerging approaches, Chem. Sci. 13 (2022) 8924–8941. https://doi.org/10.1039/d2sc01786e.

[436] F.H. Gojny, M.H.G. Wichmann, B. Fiedler, K. Schulte, Influence of different carbon nanotubes on the mechanical properties of epoxy matrix composites - A comparative study, Compos. Sci. Technol. 65 (2005) 2300–2313. https://doi.org/10.1016/j.compscitech.2005.04.021.

[437] X. Li, H. Gao, W.A. Scrivens, D. Fei, X. Xu, M.A. Sutton, A.P. Reynolds, M.L. Myrick, Nanomechanical characterization of single-walled carbon nanotube reinforced epoxy composites, Nanotechnology. 15 (2004) 1416–1423. https://doi.org/10.1088/0957-4484/15/11/005.

[438] E.J. García, A.J. Hart, B.L. Wardle, A.H. Slocum, Fabrication and nanocompression testing of aligned carbon-nanotube-polymer nanocomposites, Adv. Mater. 19 (2007) 2151–2156. https://doi.org/10.1002/adma.200700237.

[439] R. Rafiee, Carbon Nanotube-Reinforced Polymers: From Nanoscale to Macroscale, 2017. https://doi.org/10.1016/C2016-0-00371-6.

[440] M. Chwał, A. Muc, Design of reinforcement in nanoand microcomposites, Materials (Basel). 12 (2019). https://doi.org/10.3390/ma12091474.

[441] P. Jojibabu, Y.X. Zhang, B.G. Prusty, A review of research advances in epoxy-based nanocomposites as adhesive materials, Int. J. Adhes. Adhes. 96 (2020). https://doi.org/10.1016/j.ijadhadh.2019.102454.

[442] F. Gardebien, J.L. Brédas, R. Lazzaroni, Molecular dynamics simulations of nanocomposites based on poly(ε-caprolactone) grafted on montmorillonite clay, J. Phys. Chem. B. 109 (2005) 12287–12296. https://doi.org/10.1021/jp045122i.

[443] K. Baek, W. Lee, H. Shin, M. Cho, Multiscale study on determining representative volume elements size for mechanical behaviours of complex polymer nanocomposites with nanoparticulate agglomerations, Compos. Struct. 253 (2020). https://doi.org/10.1016/j.compstruct.2020.112796.

[444] R. Hill, Elastic properties of reinforced solids: Some theoretical principles, J. Mech. Phys. Solids. 11 (1963) 357–372. https://doi.org/10.1016/0022-5096(63)90036-X.

[445] J. Qu, M. Cherkaoui, Fundamentals of Micromechanics of Solidss, John Wiley and Sons, 2007. https://doi.org/10.1002/9780470117835.

[446] H. Hosseini-Toudeshky, B. Anbarlooie, J. Kadkhodapour, Micromechanics stress-strain behavior prediction of dual phase steel considering plasticity and grain boundaries debonding, Mater. Des. 68 (2015) 167–176. https://doi.org/10.1016/j.matdes.2014.12.013.

[447] S. S. Hashemi, D. Mondal, J. Montesano, T.L. Willett, Enhanced Dispersion and Interfacial Bonding of Nanoparticles in 3D Printable Nanocomposite Materials: Innovative Surface Functionalization and Processing Techniques for Nanohydroxyapatite Particles, To Be Submitt. (2023).

[448] J.L. Katz, P. Spencer, Y. Wang, A. Misra, O. Marangos, L. Friis, On the anisotropic elastic properties of woods, J. Mater. Sci. 43 (2008) 139–145. https://doi.org/10.1007/s10853-007-2121-9.

[449] F. Sharifpour, J. Montesano, R. Talreja, Assessing the effects of ply constraints on local stress states in cross-ply laminates containing manufacturing induced defects, Compos. Part B Eng. 199 (2020). https://doi.org/10.1016/j.compositesb.2020.108227.

[450] A. Abedini, C. Butcher, M.J. Worswick, Fracture Characterization of Rolled Sheet Alloys in Shear Loading: Studies of Specimen Geometry, Anisotropy, and Rate Sensitivity, Exp. Mech. 57 (2017) 75–88. https://doi.org/10.1007/s11340-016-0211-9.

[451] J. Peirs, P. Verleysen, J. Degrieck, Novel Technique for Static and Dynamic Shear Testing of Ti6Al4V Sheet, Exp. Mech. 52 (2012) 729–741. https://doi.org/10.1007/s11340-011-9541-9.

[452] A. Abedini, C. Butcher, M.J. Worswick, Fracture Characterization of Rolled Sheet Alloys in Shear Loading: Studies of Specimen Geometry, Anisotropy, and Rate Sensitivity, Exp. Mech. 57 (2017) 75–88. https://doi.org/10.1007/S11340-016-0211-9/FIGURES/11.

[453] C. Butcher, A. Abedini, Shear confusion: Identification of the appropriate equivalent strain in simple shear using the logarithmic strain measure, Int. J. Mech. Sci. 134 (2017) 273–283. https://doi.org/10.1016/j.ijmecsci.2017.10.005.

[454] K. Willam, Plasticity in reinforced concrete, Comput. Methods Appl. Mech. Eng. 31 (1982) 363. https://doi.org/10.1016/0045-7825(82)90016-0.

[455] E. Öztekin, S. Pul, M. Hüsem, Experimental determination of Drucker-Prager yield criterion parameters for normal and high strength concretes under triaxial compression, Constr. Build. Mater. 112 (2016) 725–732. https://doi.org/10.1016/j.conbuildmat.2016.02.127.

[456] F. Taheri-Behrooz, E. Pourahmadi, A 3D RVE model with periodic boundary conditions to estimate mechanical properties of composites, Struct. Eng. Mech. 72 (2019) 713–722. https://doi.org/10.12989/sem.2019.72.6.713.

[457] R.S. Bay, C.L. Tucker, Stereological measurement and error estimates for three-dimensional fiber orientation, Polym. Eng. Sci. 32 (1992) 240–253. https://doi.org/10.1002/pen.760320404.

[458] M. Gupta, K.K. Wang, Fiber orientation and mechanical properties of short-fiber-reinforced injection-molded composites: Simulated and experimental results, Polym. Compos. 14 (1993) 367–382. https://doi.org/10.1002/pc.750140503.

[459] M. Hori, S. Nemat-Nasser, On two micromechanics theories for determining micro-macro relations in heterogeneous solids, Mech. Mater. 31 (1999) 667–682. https://doi.org/10.1016/S0167-6636(99)00020-4.

[460] L. Bouaoune, Y. Brunet, A. El Moumen, T. Kanit, H. Mazouz, Random versus periodic microstructures for elasticity of fibers reinforced composites, Compos. Part B Eng. 103 (2016) 68–73. https://doi.org/10.1016/j.compositesb.2016.08.026.

[461] D. Pahr, H.J. Böhm, T.U. Wien, D.H. Pahr, H.J. Böhm, Assessment of mixed uniform boundary conditions for predicting the mechanical behavior of elastic and inelastic discontinuously reinforced composites, Researchgate.Net. 00 (2008) 1–12. https://doi.org/10.3970/cmes.2008.034.117.

[462] S. Hazanov, C. Huet, Order relationships for boundary conditions effect in heterogeneous bodies smaller than the representative volume, J. Mech. Phys. Solids. 42 (1994) 1995–2011. https://doi.org/10.1016/0022-5096(94)90022-1.

[463] J.J. Espadas-Escalante, N.P. van Dijk, P. Isaksson, A study on the influence of boundary conditions in computational homogenization of periodic structures with application to woven composites, Compos.

Struct. 160 (2017) 529–537. https://doi.org/10.1016/j.compstruct.2016.10.082.

[464] D. Sokołowski, M. Kamiński, Homogenization of carbon/polymer composites with anisotropic distribution of particles and stochastic interface defects, Acta Mech. 229 (2018) 3727–3765. https://doi.org/10.1007/s00707-018-2174-7.

[465] S. Jansson, Homogenized nonlinear constitutive properties and local stress concentrations for composites with periodic internal structure, Int. J. Solids Struct. 29 (1992) 2181–2200. https://doi.org/10.1016/0020-7683(92)90065-2.

[466] A. Fritsch, L. Dormieux, C. Hellmich, J. Sanahuja, Mechanical behavior of hydroxyapatite biomaterials: An experimentally validated micromechanical model for elasticity and strength, J. Biomed. Mater. Res. - Part A. 88 (2009) 149–161. https://doi.org/10.1002/jbm.a.31727.

[467] R. Chollakup, R. Tantatherdtam, S. Ujjin, K. Sriroth, Pineapple leaf fiber reinforced thermoplastic composites: Effects of fiber length and fiber content on their characteristics, J. Appl. Polym. Sci. 119 (2011) 1952–1960. https://doi.org/10.1002/app.32910.

[468] P.B. Anand, A. Lakshmikanthan, M.P.G. Chandrashekarappa, C.P. Selvan, D.Y. Pimenov, K. Giasin, Experimental Investigation of Effect of Fiber Length on Mechanical, Wear, and Morphological Behavior of Silane-Treated Pineapple Leaf Fiber Reinforced Polymer Composites, Fibers. 10 (2022). https://doi.org/10.3390/fib10070056.

[469] C.C. Chamis, MECHANICS OF LOAD TRANSFER AT THE INTERFACE., Compos Mater. v (1974) 31–77.

[470] Y. Zare, Study of nanoparticles aggregation/agglomeration in polymer particulate nanocomposites by mechanical properties, Compos. Part A Appl. Sci. Manuf. 84 (2016) 158–164. https://doi.org/10.1016/j.compositesa.2016.01.020.

Appendices.

Shear stress state investigation in biopolymer matrix mini-shear tests

Calculation the principal strains for the shown strain field and comparing with the obtained principal strains:

$$\varepsilon_{max}=(\varepsilon_x+\varepsilon_y)/2+(((\varepsilon_x-\varepsilon_y)/2)^2+(\gamma_{xy}/2)^2)^{0.5}$$

$$\varepsilon_{min}=(\varepsilon_x+\varepsilon_y)/2-(((\varepsilon_x-\varepsilon_y)/2)^2+(\gamma_{xy}/2)^2)^{0.5}$$

$\varepsilon_{x=}$ -0.0023, $\varepsilon_{y=0.0026}$, $\gamma_{xy=2}$ $\varepsilon_{xy=0.0204}$ → ε_{max} = **0.0106**, ε_{min} = **-0.0103**

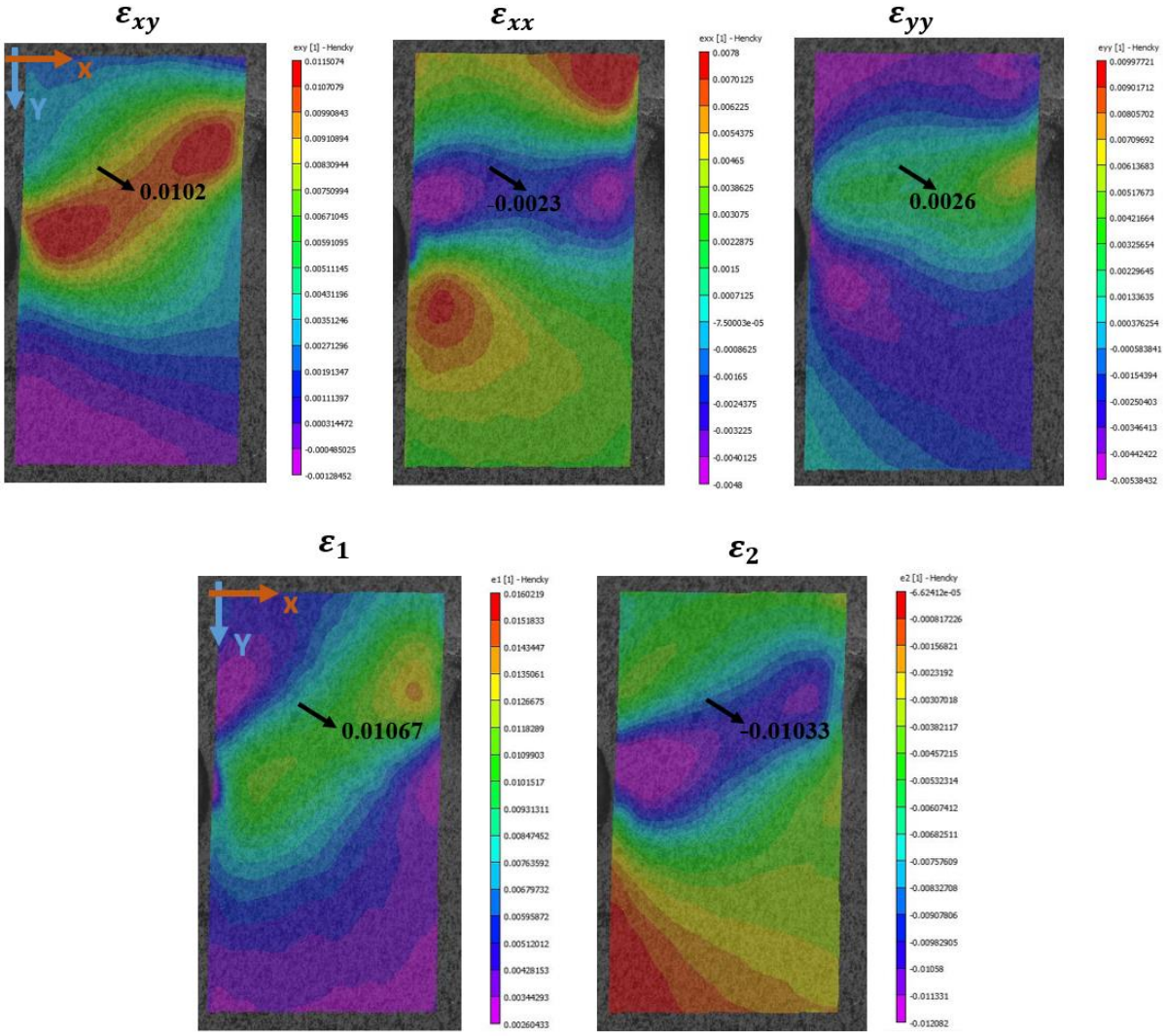


Fig. a.1. The DIC captured shear strain, normal strain and principal strain fields occurring in the shear specimen.

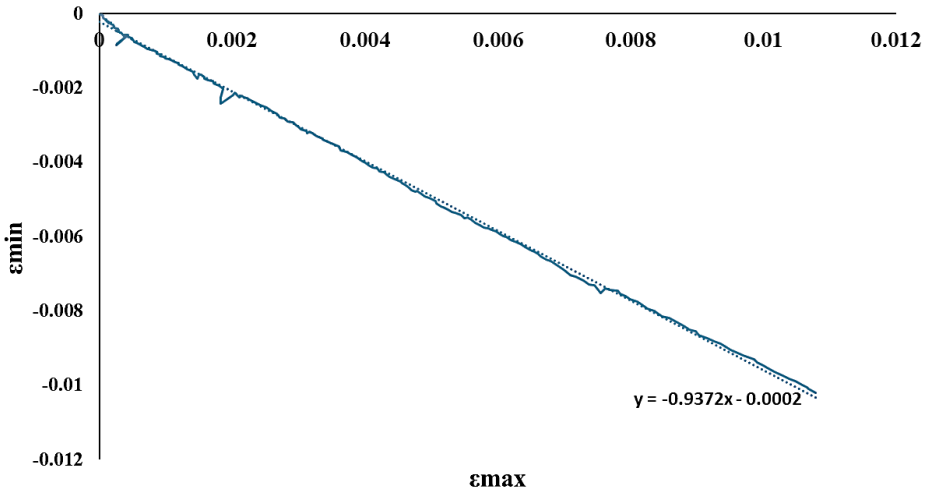


Fig. a.2. Comparing the ε_{max}/ ε_{min} during the uniaxial shear test in the centre of the mini shear sample

According to Levy-Mises equations for simple shear stress the theoretical proportion of min principal shear stress to max principal shear stress should satisfy following equation ($\varepsilon_2/\ \varepsilon_1 = -1$).

By graphing the maximum strain (ε_{max}) against the minimum strain (ε_{min}) measured at the center of the mini shear sample (printed with optimized support structures), it is evident that the ratio of $\varepsilon_2/\ \varepsilon_1$ is approximately -0.94, aligning with the findings reported in the literature [452].

RVE Assessments

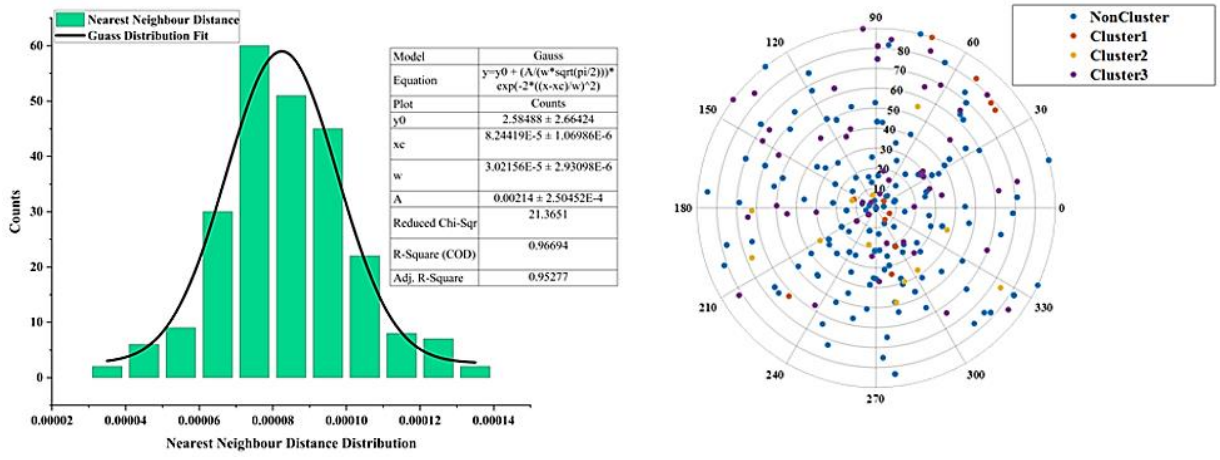


Fig. a.3. RVE assessments, a) Distribution of nearest neighbor distances in, b) Demonstraing randomly oriented inclusions in a representative RVE

Mesh Sensitivity Analysis:

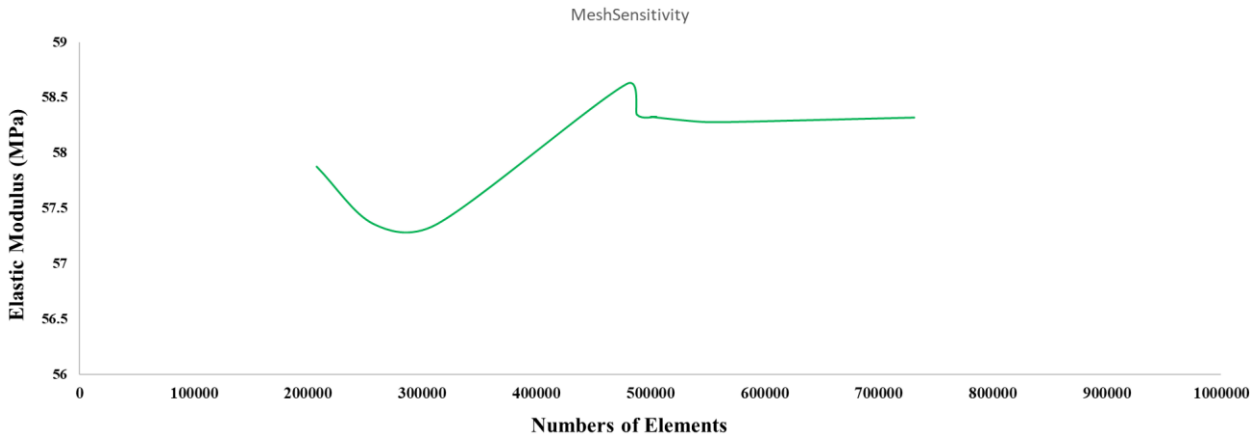


Fig. a.4. Mesh sensitivity analysis